Identification of Model and Grid Parameters
for
Incompressible Turbulent Flows

Dissertation
zur Erlangung des Doktorgrades
der Mathematisch-Naturwissenschaftlichen Fakultäten
der Georg-August-Universität zu Göttingen

vorgelegt von

Xiaoqin Zhang
aus
Jiangsu, China

Göttingen 2007

D7
Referent: Prof. Dr. G. Lube
Korreferent: Prof. Dr. T. Hohage
Tag der mündlichen Prüfung: 09. Oct. 2007

Table of Contents

List of Figures

List of Tables

Chapter 1

Introduction

1.1 Problem statement

An incompressible flow is described by the Navier-Stokes equations (NSE) and the continuity equation, see [1], [96], [105] and [129]. Consider the bounded domain $\Omega \subset \mathbb{R}^d$, $d \in \{2, 3\}$ and the time interval $I = [0, T]$. The density ρ and kinematic viscosity ν are assumed to be constant. The basic incompressible model for the velocity $\mathbf{u}$ and pressure p reads:

$$\frac{\partial \mathbf{u}}{\partial t} + \nabla \cdot (\mathbf{u} \otimes \mathbf{u}) - \nabla \cdot (2\nu \mathbb{S}(\mathbf{u})) + \nabla p \;=\; \mathbf{f} \quad \text{in } \Omega \times [0, T], \tag{1.1}$$

$$\nabla \cdot \mathbf{u} \;=\; 0 \quad \text{in } \Omega \times [0, T], \tag{1.2}$$

where $\mathbf{f}$ is a body force. $\mathbb{S}$ is the symmetric Reynolds rate of strain tensor

$$\mathbb{S}(\mathbf{u}) = \frac{\nabla \mathbf{u} + \nabla \mathbf{u}^{\mathrm{T}}}{2}. \tag{1.3}$$

In this thesis, we focus on turbulent flows. Turbulent flow is a great scientific and technological challenge in the area of computational fluid dynamics (CFD). A turbulent flow is always a three-dimensional problem, the solution is random, i.e, the velocity at a certain location changes from one instant to another. As shown in Fig. 1.1-1.2 for a plane channel flow, the instantaneous velocity in streamwise direction is not constant in both homogeneous directions, streamwise x and spanwise z directions. The velocity at one position varies all the time. Hence, statistical approaches are needed to handle the numerical results of turbulent flow. For stationary turbulence, the mean profile does not vary with time, such as flow in a plane channel. Furthermore, turbulent flow has a wide range of scales, the ratio between the largest lengthscale L and the smallest scale η (Kolmogorov scale) is proportional to $Re^{3/4}$, where Re is the Reynolds number. In fluid mechanics it is a dimensionless measure of the ratio of inertial forces and viscous forces, it is given by

$$Re = \frac{UL}{\nu}, \tag{1.4}$$

1
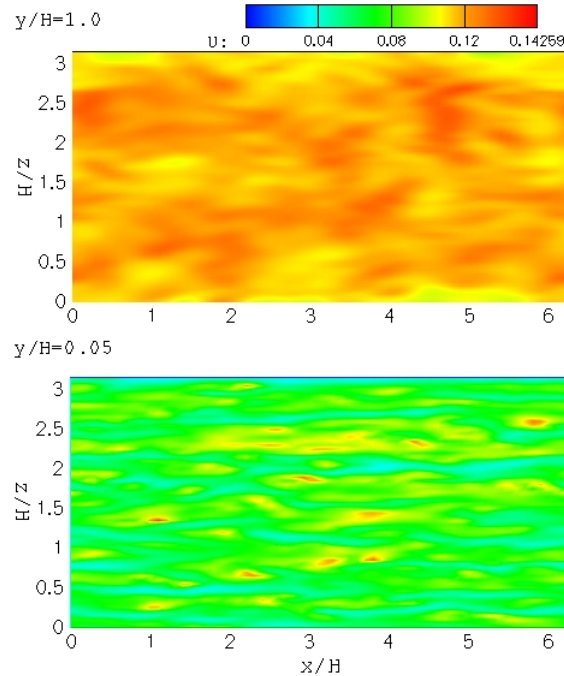
Figure 1.1: The instantaneous streamwise velocity at the center of the channel ($y/H = 1.0$) and close to the wall ($y^+ \approx 20$).
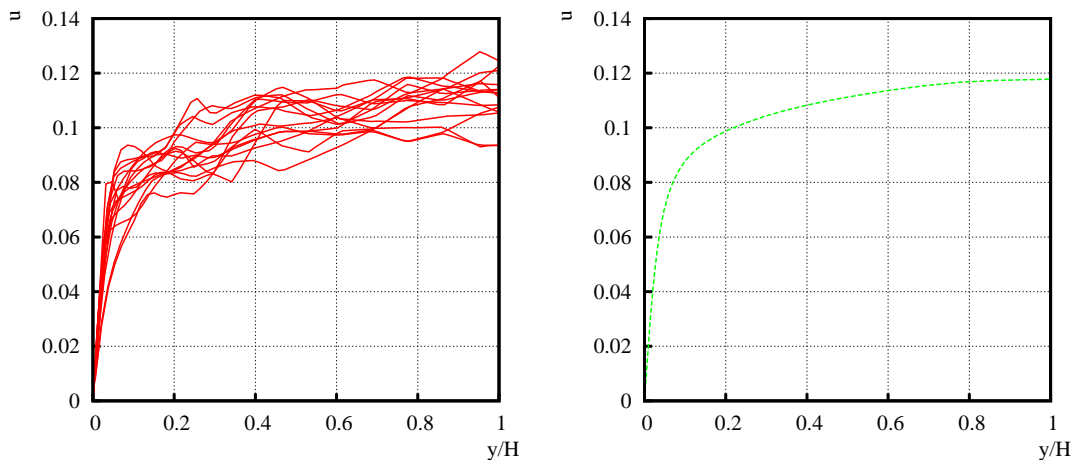
Figure 1.2: Velocity profiles of a half channel: (left) instantaneous velocities at the same streamwise position for 15 time positions, (right) space and time averaged mean velocity.

with the mean velocity U, the characteristic length L and kinematic viscosity $\nu = \mu/\rho$, where μ is the dynamic viscosity and ρ is the density of the flow.

The so-called direct numerical simulation (DNS) is an approach which resolves numerically

all the scales. It requires a very fine mesh, the number of temporal and spatial degrees of freedom is in the order of Re^4. Thus the computational cost of DNS is extremely high. As a consequence, it is restricted to low and moderate Reynolds number flows so far. For our simulations DNS is not practicable. A brief overview is given in [96], Chapter 9.

The theory of self similarity (Kolmogorov, 1941) says that the large eddies of the flow are dependent on the flow geometry, while smaller eddies are self similar with a universal character. This leads to the main idea of large eddy simulation (LES), that is to solve only for the large eddies explicitly and model the effect of the smaller and more universal eddies on the larger ones. Thus, in LES the large scale (resolved scale) motions of the flow are resolved, the effect of the smaller scales (the so-called *sub-grid scales*, also as unresolved scales) are modeled using a sub-grid scale (SGS) model. In practical simulations, filtered Navier-Stokes equations with an additional sub-grid scale stress term are solved for the large scales. Smagorinsky model [110] and dynamic Smagorinsky model by Germano [34] and Lilly [76] are the commonly used SGS models. With LES, the turbulent flow can be solved on a grid coarsened by a factor of 4 to 8 in each space direction and also larger time steps are allowed, cf. [114].

As an alternative to classical LES, Hughes *et al.* [49] proposed the concept of variational multiscale methods by considering an additional separation between the large and small resolved scales, see also [40], [50] and [51].

The Reynolds averaged Navier-Stokes (RANS) model (e.g. the Spalart-Allmaras one-equation model, see Section 3.2.3) is a method which solves only for the mean velocity field. In recent years, hybrid LES/RANS method becomes a very popular approach, for instance, detached eddy simulation (DES) based on the Spalart-Allmaras model [114] and extra-large eddy simulation (XLES) [69]. The idea is to use a model which reduces to RANS in boundary layers and behaves like a LES in regions of separated flow, where the switch is based on the turbulent length scale. The computational cost and degree of modeling of DNS, LES and RANS are shown in Fig. 1.3. No modeling is used in DNS, however, the price to pay is the extremely high computational cost due to the requirement of a very fine mesh. In RANS, all scales are modeled. LES is an approach in between, it is attractive to researchers and engineers since the large scales can be resolved at an acceptable computational cost, although LES is much closer to DNS than to RANS regarding its computational costs.

In this work, the numerical simulations are based on the DLR-THETA-code of the German Aerospace Center (DLR). It is a finite volume code on collocated grids (see Chapter 2) for incompressible flows. Most of the turbulence models, which are considered here, have been implemented by the author. Results of other groups with application of finite volume codes (e.g., at the Stanford Center for Turbulence Research with the CDP-α-code) to turbulent flows encouraged the author to apply the DLR-THETA-code.

The goal of this thesis is twofold:

- to study the behavior of some basic turbulence models in the DLR-THETA-code, and

- to calibrate model and grid parameters for some LES and hybrid LES/RANS models
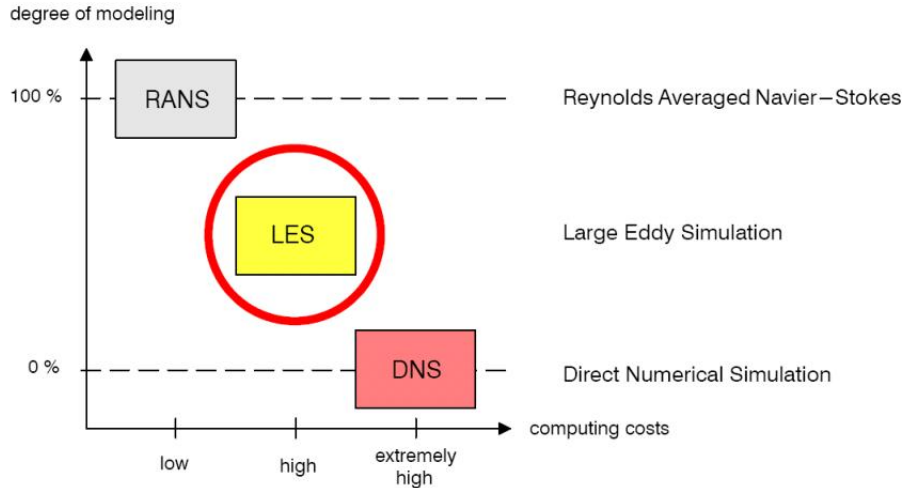
Figure 1.3: Computational costs of DNS, LES and RANS, cf. Breuer [10].

for standard three-dimensional benchmark problems.

More precisely, we consider problems with increasing complexity of the flow,

- decaying homogeneous isotropic turbulence (DHIT) with three homogeneous directions,

- plane channel flow with two homogeneous directions (statistically one-dimensional problem),

- flow over a backward-facing step with one homogeneous direction (statistically two-dimensional problem).

Let us discuss the calibration problem for a typical example. In LES, we use a scale separation operator to subdivide the scales into filtered scales and unresolved scales. Only the filtered scales are solved and the unresolved scales are modeled by a sub-grid stress term of the so-called *eddy-viscosity* ν_t. In the classical LES proposed by Smagorinsky (1963), the (constant) kinematic viscosity ν in (1.1) is replaced by $\nu + \nu_t$ with the eddy-viscosity

$$\nu_t = (C_S \Delta)^2 |S|. \tag{1.5}$$

Here $|S| = (2\mathbb{S} : \mathbb{S})^{1/2} = (2\sum_{i,j=1}^d \mathbb{S}_{ij}\mathbb{S}_{ij})^{1/2}$ is the characteristic filtered rate of strain tensor, C_S the model coefficient and Δ the filter width. The parameters C_S and Δ (more precisely, the ratio Δ/h with the mesh size h) play an important role in the modeling. In wall bounded flows, the wall unit distance $y^+(1)$ at the first grid point away from the wall is also an important variable. The corresponding values at these nodes are used to compute the shear stress at the wall. To evaluate the turbulence models and to adapt the grid to get solutions

which have better agreement with DNS or experimental results, it is necessary to study the parameters concerned in this kind of problem. C_S and Δ as the model parameters and $y^+(1)$ as the grid parameter are the quantities that we want to identify, for instance, in the case of plane channel flow.

The basic idea of our approach is to treat the calibration of parameters as an optimization problem. To this goal, we consider a least-square error functional measuring the difference between our numerical results and data stemming either from DNS or experiments. As only statistically averaged values are useful for turbulent flows, these functionals are based on first and second order statistics of the flow problems under consideration. In the case of the (statistically one-dimensional) plane channel flow, the mean streamwise velocity component (averaged in streamwise and spanwise directions and in time) represents the expected value of the random velocity fields. A reasonable approach is to compare the first order statistics for LES and DNS, the latter on a much finer grid. Moverover, second order statistics (as the root-mean-square values) will be considered (see Chapter 5).

1.2 Optimization techniques for parameter identification

As already mentioned, it is useful to consider the calibration problem of some basic turbulence problems within the framework of optimization problems. For a review of such techniques, we refer to the special issue [79] of GAMM-Mitteilungen, in particular to the paper [58] and the references given there. Let us critically review the basic adjoint approach for an abstract nonlinear stationary model problem and discuss it with respect to our problem. Formally, a quasi-stationary turbulent flow can be seen as such a model.

The state variable u is considered as a sum $u \in \hat{V} := u + V$ of a function describing Dirichlet data and a function of a Hilbert space V. The unknown parameter vector q belongs to the control space $Q := \mathbb{R}^{n_p}$. In an abstract form, we consider the following equation for the state variable

$$A(q, u) = f \quad \text{in} \quad \Omega. \tag{1.6}$$

Here $f \in W$ is a continuous source term, $A(q, u)$ is a nonlinear operator acting on $\hat{V} \times Q$ with values in the Hilbert space W. Let $A(q, u)$ be twice continuously differentiable with respect to u and q.

Let $C : \hat{V} \to Z$ be a linear observation operator mapping the state variable u into the space of measurements $Z := \mathbb{R}^{n_m}$ with $n_m \geq n_p$. $< \cdot, \cdot >_Z$ and $\| \cdot \|_Z$ denote the Euclidean scalar product of Z and the corresponding norm, respectively. The value of parameters q is estimated using a set of measurements $\hat{C} \in Z$. Using the least-square approach, we obtain a constrained optimization problem with the cost functional $J : V \to \mathbb{R}$,

$$\text{Minimize} \quad J(q, u) := \frac{1}{2} \|C(u) - \hat{C}\|_Z^2, \tag{1.7}$$

under constraint (1.6).

Let us assume that there exists a unique solution to the optimization problem (1.6)-(1.7). Provided the existence of an open set $Q_0 \subset Q$ containing the optimal solution and a solution operator $S : Q_0 \to \hat{V}$, i.e. $u = S(q)$, we can define the reduced cost functional $j : Q_0 \to \mathbb{R}$ by $j(q) = J(q, S(q))$. By denoting the reduced observation opterator $c(q) := C(S(q))$, we obtain an unconstraint optimization problem

$$\text{Minimize} \quad j(q) = \frac{1}{2}\|c(q) - \hat{C}\|_Z^2, \quad q \in Q_0. \tag{1.8}$$

The first-order necessary condition for the optimality of the solution of (1.8) is

$$j'(q) = 0. \tag{1.9}$$

The unconstraint optimization problem (1.8) is solved iteratively by starting with an initial value q^0 and updating $q^{k+1} = q^k + \delta q^k$, where δq^k is the solution of the linear problem

$$H_k \delta q^k = -j'(q^k). \tag{1.10}$$

H_k is an approximation of the Hessian $\nabla^2 j(q^k)$ of the reduced cost functional j. To compute the first and second derivatives of the reduced cost functional, we introduce the Lagrangian $\mathcal{L} : Q \times \hat{V} \times \hat{V} \to \mathbb{R}$,

$$\mathcal{L}(q, u, \lambda) = J(q, u) + \lambda(f - A(q, u)), \tag{1.11}$$

with a Lagrange multiplier λ. Then the first derivative of $j(q)$ is given by

$$j'(q) = \partial_q \mathcal{L}(q, u, \lambda), \tag{1.12}$$

if for a given $q \in Q$ the state variable $u \in \hat{V}$ satisfies the state equation

$$\partial_\lambda \mathcal{L}(q, u, \lambda) = 0, \tag{1.13}$$

and if $\lambda \in \hat{V}$ fulfills the adjoint state equation

$$\partial_u \mathcal{L}(q, u, \lambda) = 0. \tag{1.14}$$

To this end, the solution to the optimization problem (1.9) is the solution to the following Karush-Kuhn-Tucker system

$$\partial_\lambda \mathcal{L}(q, u, \lambda) = 0, \tag{1.15}$$
$$\partial_u \mathcal{L}(q, u, \lambda) = 0, \tag{1.16}$$
$$\partial_q \mathcal{L}(q, u, \lambda) = 0. \tag{1.17}$$

There are different methods to approximate the matrix H_k, which leads to different optimization algorithms. Typical algorithms are Gauß-Newton method, full Newton method

and Quasi-Newton method. We denote $G_k = c'(q^k)$ as the Jacobian matrix of the reduced observation operator $c(q^k)$. By using Gauß-Newton method the Hessian is expressed as

$$H_k = G_k^{\mathrm{T}} G_k. \tag{1.18}$$

This algorithm converges very slowly when the least square residual $\|C(u^k) - \hat{C}\|$ is large. The full Newton method includes a matrix $M_k \in \mathbb{R}^{n_p} \times \mathbb{R}^{n_p}$ to approximate the Hessian

$$H_k = G_k^{\mathrm{T}} G_k + M_k. \tag{1.19}$$

The full Newton method shows better convergence property. However, the calculation of the matrix M_k, which needs the evaluation of the second derivative of $A(q, u)$ in the direction of the solution to a tangent problem, is very expensive. The Quasi-Newton method uses a rather simple formula to compute M_k, it gives better convergence than Gauß-Newton method and only some calculations of the gradient vectors are required.

Clearly, this framework can be applied to the discretized reduced optimization problem

$$\text{Minimize} \qquad j_h(q_h, u_h) = \frac{1}{2} \|c_h(q_h) - \hat{C}\|_Z^2, \qquad q_h \in Q, \tag{1.20}$$

where the discrete state variable u_h is subject to the discrete state equation

$$A_h(q_h, u_h) = f_h, \tag{1.21}$$

on $\hat{V}_h := \hat{u}_h + V_h$, $V_h \subset V$ and with $f_h \in W_h \subset W$, h being the grid spacing.

The approach can be generalized to time-dependent problems. Please note that our model problem (1.1)-(1.2) is non-stationary. This makes the optimization problem and solution techniques much more expensive. In particular, the solution of parameter identification problems in this framework is very expensive. Sophisticated tools such as an *a-posteriori*-based optimization approach can reduce the computational costs, e.g. Becker and Vexler in [4], Becker, Braack and Vexler [5], etc.

The mathematical foundation of the described approach to optimization problems is still in its infancy. Rannacher and Vexler [100] studied an error for symmetric elliptic problems. They derived an *a priori* error estimate for the finite element Galerkin discretization of parameter identification problems. The nonsymmetric case of elliptic problems is considered by Becker and Vexler [4]. Scalar parabolic problems are studied e.g. in Meidner and Vexler [82]. The application to the laminar incompressible Navier-Stokes problem is studied in Hinze and Kunisch [48]. A parameter identification problem for the compressible Navier-Stokes problem is discussed in [5].

This review of optimization problems and of parameter identification problems for partial differential equation suggests that the application of this adjoint approach to our calibration problem for turbulent flow problems is not feasible at the moment. Let us summarize some critical items of dealing with parameter identification problems governed by the incompressible Navier-Stokes equations in the turbulent regime:

- To the best of our knowledge, there exists no theory for the optimization of turbulent flows governed by the incompressible Navier-Stokes model. Main problems occur from the strong nonlinearity of turbulent viscosity models. Moreover, the existing theory is not applicable as usually, only pointwise measurements are available (with the exception of Rannacher and Vexler [100] for simple diffusion problem). For nonlinear turbulence models, writing down the adjoint and in particular of the formulas for the second derivative is very cumbersome. For parameter identification problems for the steady state RANS equation with a one- or two-equation turbulence model, it is not clear whether, in particular, the full Newton method does converge for an arbitrary initial guess. Therefore, "simple" methods for solving the optimization problem are still of practical relevance.

- The simulation of turbulent flows with a statistically steady solution using a turbulence resolving model requires long time intervals. Recent optimization tools for time-dependent problems would be extremely expensive regarding both CPU time and memory consumptions. In particular, one forward calculation of the plane channel flow on a grid with 64^3 grid points and 14000 time steps requires a CPU time of one week on a single processor. Moreover, the application of adjoint optimization tools in the DLR-THETA-code would require major modification within the code (similar to the DLR-TAU code for compressible flow [29]).

- It remains unclear how the calibration of grid parameters can be incorporated into the optimization framework. For the Smagorinsky model, the mesh size directly appears in the momentum equation, as the filter width Δ is related to the grid spacing for Δ/h fixed. Then the calibration of C_S is also affected by the underlying mesh. It should be pointed out that the issue of grid-converged solution for LES is still a delicate question, in particular for complex problems (see [126]). Another question is the role of the resolution of the near-wall region in LES, e.g. the role of $y^+(1)$ for wall-bounded flows. In particular, the application of highly anisotropic meshes as typically used for wall-bounded flows has not been considered for optimization procedures yet.

It is not the goal of this thesis to develop an appropriate theory of parameter identification for turbulent incompressible flows. As conclusion of the reasons discussed just before, we will apply a rather simple approach to the least-square minimization of the cost functional (1.8). As a basic step, a series of numerical simulations of some turbulence models for a given flow problem will provide look-up tables for the least-square error functional depending on relevant model and grid parameters as a basis for further systematic considering. In some cases, a Newton type method is feasible to determine optimized parameters.

1.3   Survey and main results

At the end of the introduction, a short overview of what will be dealt with in this thesis is presented. It is organized as follows.

First, a description of the DLR-THETA-code for laminar flow is presented in Chapter 2. The incompressible Navier-Stokes equation is introduced, followed by the spatial discretization with finite volume method on collocated grids and the time discretization using the generalized trapezoidal rule and backward differentiation formulae. The projection method is used to decouple the velocity and pressure in the arising coupled system. A convergence test is presented to test the convergence rate both in space and in time.

Chapter 3 is devoted to turbulence modeling. Different formulations of a scale separation operator lead to different turbulence models. Statistical averaging leads to the unsteady Reynolds-averaged Navier-Stokes (URANS) model. In particular, the one-equation turbulence of Spalart-Allmaras and the two-equation $k - \omega$ turbulence model together with the SST-modification of Menter are introduced. Filtering procedures lead to large eddy simulation (LES). Some variants of the classical Smagorinsky subgrid scale model are considered. Finally, we introduce hybrid LES/RANS models which try to combine advantages of both methods. In particular, the detached eddy simulation (DES) model based on the Spalart-Allmaras model and the XLES model based on the SST model are presented.

Then we start with the application of the DLR-THETA-code and the turbulence models to basic benchmark problems mentioned in Section 1.1. In Chapter 4, we will give numerical results for the basic Smagorinsky LES model applied to the decaying homogeneous isotropic turbulence (DHIT). For this rather simple benchmark problem, expected values of the flow are constant for fixed time and therefore not of interest. Of principal interest is the turbulent kinetiv energy. More precisely, we consider the energy spectrum and make comparison with the experimental data from Comte-Bellot & Corrsin (1966). The least-square error
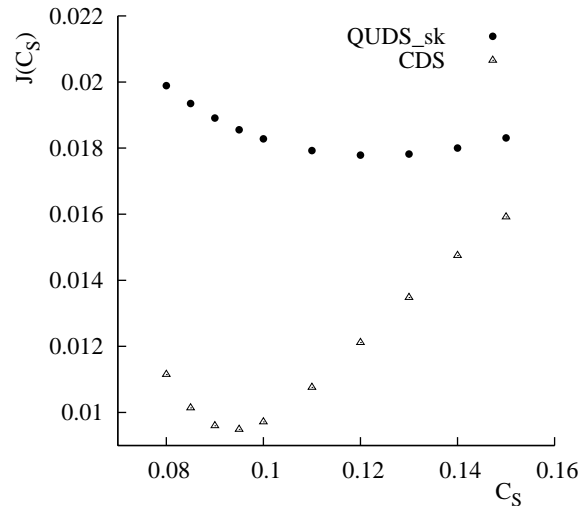
Figure 1.4: The value of the error functional for DHIT.

functional (1.7) is based on the energy spectrum. For this benchmark problem, we study the influence of the discretization schemes of the DLR-THETA-code first. It turns out that
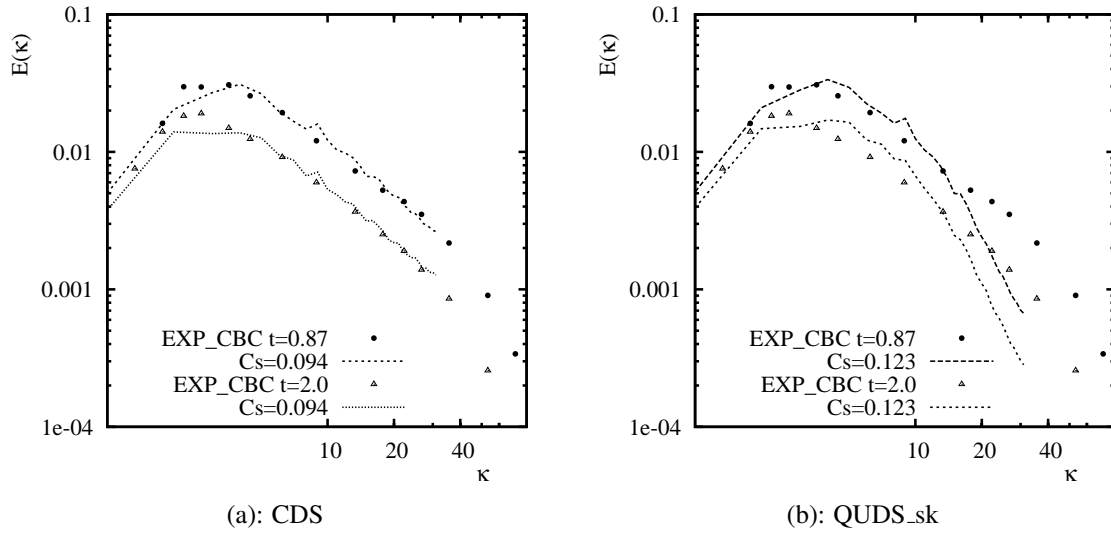
Figure 1.5: Energy spectra at the corresponding best C_S for DHIT.

only the central difference scheme (CDS) and quadratic upwind scheme with nonlinear term treated in the skew symmetric form (QUDS_sk) are of interest, with clear preference to CDS. Then we consider the influence of the model parameter C_S of the Smagorinsky model (1.5) and of the ratio Δ/h. It is shown that the ratio $\Delta/h = 2$ gives the best results. In the next step, we identify the model parameter C_S for CDS-scheme and QUDS_sk-scheme by using a Newton-type method. The value which makes the error functional $J(C_S)$ (see Fig. 1.4) minimal is considered as the optimal one. The results show that C_S depends on the schemes. The optimal values are $C_S = 0.094$ for CDS and $C_S = 0.123$ for QUDS_sk. The optimized values of C_S give the best least-square fits of the energy spectra on the finest equidistant mesh (with 64^3 mesh points) as shown in Fig. 1.5. A clear preference of the CDS-scheme can be observed from Fig. 1.4 and Fig. 1.5.

The plane channel flow at the moderate Reynolds number $Re_\tau = 395$ based on the friction velocity and channel halfwidth is studied in Chapter 5. It is an often studied test case for wall-bounded flows with two homogeneous directions. As already discussed in Section 1.1 we compare the LES resolution with DNS data for the mean velocity and second order statistics, such as kinetic energy and root mean square (rms) values. Two LES are considered, SMG: classical Smagorinsky model (1.5), and SMG-MOD: classical Smagorinsky model with modified filter width, [122]. Both variants are considered with a van Driest damping function which shrinks the Smagorinsky term in the vicinity of the walls. A proper resolution of this part of the boundary layer is accomplished via an anisotropic mesh refinement towards the boundary. In particular, the distance of the mesh points nearest the wall is a very important grid parameter. The calibration of the Smagorinsky model parameter C_S and grid parameter $y^+(1)$ is performed by forcing the error functional of the mean velocity J_u and kinetic energy J_k (Fig. 1.6) to reach a minimum. However, as already mentioned in Section
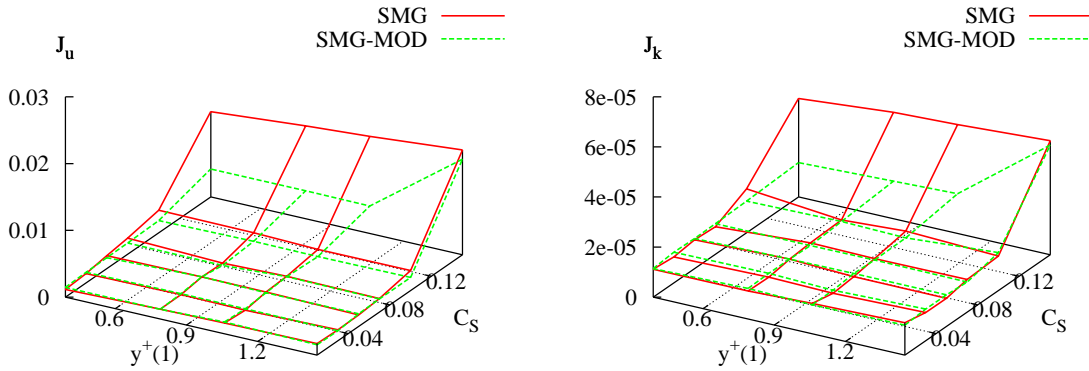
Figure 1.6: The error functionals of the mean velocity and kinetic energy for plane channel flow.
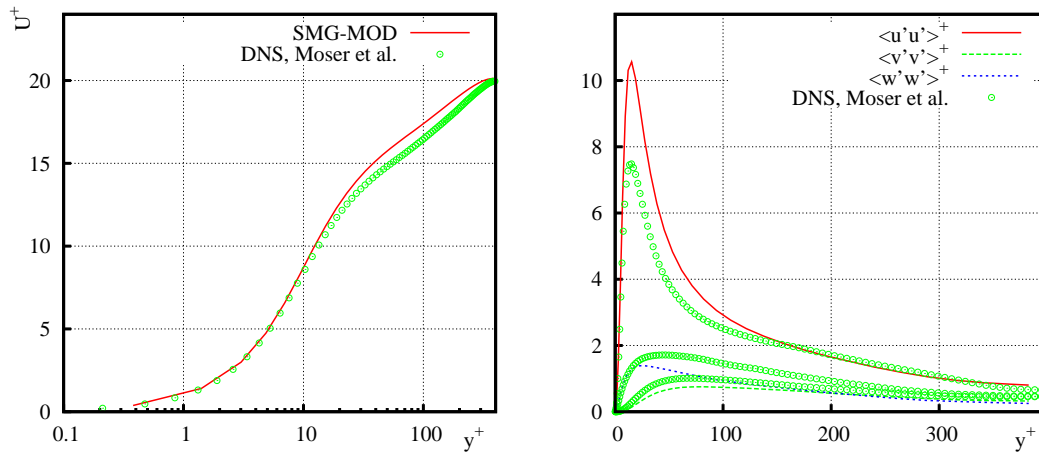
Figure 1.7: Mean velocity and fluctuations of channel flow at $C_S = 0.05$ on mesh with $y^+(1)$.

1.2, the simulation is very time-consuming. So it is too expensive to use the Newton-type method as in Chapter 4. From the simulations we have performed, it is found that the DLR-THETA-code is quite robust with respect to the grid parameter $y^+(1) \in [0, 2.0]$, no obvious dependence can be observed at proper C_S. An additional consideration of the error functionals in the discrete maximum norm give no clear preference of C_S value. Surprisingly, even no turbulence model ($C_S = 0$), a quasi-DNS, gives very convincing results as the anisotropically adapted mesh resolves the boundary layer region very well. As for DHIT, the central difference scheme (CDS) clearly outperforms upwind type discretization schemes. On the other hand, the calibration results would allow to use the Smagorinsky constant C_S optimized

11

for DHIT. Fig. 1.7 shows the mean velocity and fluctuations in wall units for $C_S = 0.05$ and $y^+(1) = 0.39$ with SMG-MOD.

The approach with the Smagorinsky LES model together with a proper anisotropic resolution of the boundary layers is not feasible for higher Reynolds number. As a remedy, we will present in Chapter 6 the numerical results for hybrid models of LES/RANS for DHIT and plane channel flow. Typical variants are the detached-eddy simulation combined with the Spalart-Allmaras RANS model leading to the SADES method and the extra-large-eddy simulation (XLES) based on a RANS model of $k - \omega$ type. These methods may be considered as hybrid domain decomposition method. The major problem is to guarantee a smooth transition between the RANS and LES region. As a starting point, the basic benchmark problems of Chapters 4 and 5 at moderate Reynolds numbers are reconsidered. First the model constant C_{DES} is calibrated for SADES with DHIT. The energy spectrum has the best agreement with the experimental data when $C_{DES} = 0.67$, it is very close to the value given by Shur *et al.* [109]. Fig. 1.8 gives the energy spectra of SADES in comparison with SMG and the experimental data. Then the SADES is applied to the channel flow at $Re_\tau = 395$.

(a): Grid 32^3 (b): Grid 64^3

Figure 1.8: Energy spectra of SADES and SMG for DHIT.

In particular, the second order statistics are even better predicted than by LES in Chapter 5, see Fig. 1.9. As a conclusion, the SADES approach may be considered as alternative to the Smagorinsky LES model for turbulent flows at moderately large Reynolds numbers.

Finally, we consider the channel flow at the high Reynolds number $Re_\tau = 4800$. It turns out that the hybrid LES/RANS method with a proper resolved anisotropic mesh in the wall regions is too expensive for the simulation on a single processor. As alternative, wall modeled LES (Smagorinsky model with wall functions and SADES with wall functions) are used. One plot of the Smagorinsky model with wall functions is shown in Fig. 1.10. It turns out that an eddy-viscosity correction proposed by Kalitzin *et al.* [61], Medic *et al.* [81] and

Figure 1.9: Mean velocity and fluctuations of channel flow for SADES.

Figure 1.10: Mean velocity and fluctuations of WSMG $Re_\tau = 4800$.

Templeton *et al.* [117] allows a reasonable prediction of the friction velocity.

The conclusions of the thesis are addressed in Chapter 7. As an outlook, we present some first results and open problems for the turbulent flow over a backward-facing step at $Re_h = 5100$ based on the step height h and the inlet free stream velocity. This is a flow with only one homogeneous direction, hence it is a statistically two-dimensional flow. Due to the sudden expansion of the channel (Fig. 7.1), the flow separates after the step. The reattachment length in the recirculation region is of interest. From a physical point of view, the flow recovery in the reattachment region is important. Moreover, results and open questions are discussed.

In the Appendices we collect some basic mathematical tools of the thesis. The properties of the linear multistep methods, the solvers for large algebraic problems as well as the Fourier

transform used for computing the energy spectrum may be found as supportive materials of the proceeding work.

Chapter 2

Numerical methods for laminar flow in the DLR-THETA-code

In this chapter numerical methods used in the DLR-THETA-code are presented. The DLR-THETA-code is an incompressible flow solver of the Finite Volume Method (FVM). It uses the libraries of the DLT-TAU code for preprocessing and adaptation. During preprocessing the dual-grid data is generated. The flow solver is based on the projection method which is used to decouple the velocity and pressure. Since the unknowns of pressure and velocity are located at the same nodes, spurious oscillation of the pressure may appear. Thus, introduction of some stabilization is necessary. The multigrid method is adopted to solve the pressure Poisson equation. Iterative solvers (e.g. GMRES) are used to solve the arising convection-diffusion problems for the velocity field.

2.1 The incompressible Navier-Stokes equations

Consider the bounded domain $\Omega \subset \mathbb{R}^d$, $d \in \{2, 3\}$ and the time interval $I = [0, T]$. The basic incompressible Navier-Stokes equations (NSE) for the velocity $\mathbf{u}$ and the pressure p read:

$$\partial_t \mathbf{u} + \nabla \cdot (\mathbf{u} \otimes \mathbf{u}) + \nabla p - \nu \Delta \mathbf{u} = \mathbf{f} \quad \text{in } \Omega \times (0, T], \tag{2.1}$$

$$\nabla \cdot \mathbf{u} = 0 \quad \text{in } \Omega \times (0, T], \tag{2.2}$$

$$\mathbf{u}(0, \cdot) = \mathbf{u}_0 \quad \text{in } \Omega, \tag{2.3}$$

with the kinematic viscosity ν and body force $\mathbf{f}$.

Let $\mathbf{n}$ be the unit normal vector on the boundary $\Gamma = \partial \Omega$ pointing outward. Γ_W is the no-slip boundary with $\mathbf{u} \cdot \mathbf{n} = 0$. Γ_{in} and Γ_{out} are the inflow and outflow boundary, respectively, with $\mathbf{u} \cdot \mathbf{n} < 0$ and $\mathbf{u} \cdot \mathbf{n} > 0$, respectively, as shown in Fig. 2.1 for a plane channel flow. We prescribe a no-slip boundary condition on walls

$$\mathbf{u} = \mathbf{0} \quad \text{on } \Gamma_W \times [0, T], \tag{2.4}$$
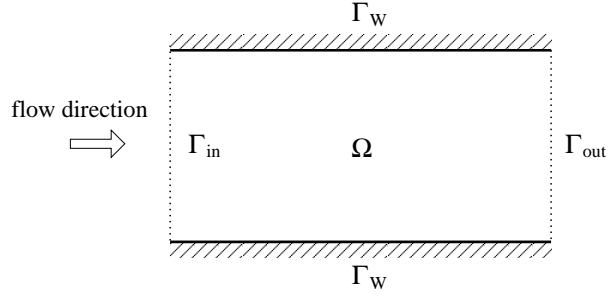
Figure 2.1: A sketch of domain Ω.

and the following inflow and outflow boundary conditions

$$\mathbf{u} = \mathbf{u}_{in} \quad \text{on } \Gamma_{in} \times [0, T], \tag{2.5}$$

$$(\nu \nabla \mathbf{u} - p\mathbb{I}) \cdot \mathbf{n} = 0 \quad \text{on } \Gamma_{out} \times [0, T], \tag{2.6}$$

with the unit tensor $\mathbb{I}$ and $\Gamma = \Gamma_W \cup \Gamma_{in} \cup \Gamma_{out}$.

The initial condition (2.3) must satisfy the continuity equation (2.2). The total kinetic energy k and the rate of dissipation ϵ in the flow are defined as

$$k : = \int_\Omega \left(\frac{1}{2}|\mathbf{u}|^2\right) \mathrm{d}\mathbf{x} = \frac{1}{2}\|\mathbf{u}\|_2^2, \tag{2.7}$$

$$\epsilon : = \nu \int_\Omega \left(|\nabla \mathbf{u}|^2\right) \mathrm{d}\mathbf{x} = \nu\|\nabla \mathbf{u}\|_2^2, \tag{2.8}$$

where the notation $\|\cdot\|_2$ is the norm in $L^2(\Omega)$, the Hilbert space of square integrable functions.

It is well-known that there exists a weak solution of the nonstationary NSE model (2.1)-(2.6) in two and three dimensions. In the literature, the analysis of (2.1)-(2.6) is very often given for (homogeneous) Dirichlet boundary conditions, i.e., for $\partial\Omega = \Gamma_w$. A weak solution of the problem fulfills the *a-priori* estimate

$$k(t) + \int_0^t \epsilon(\tau)\mathrm{d}\tau = \int_0^t p(\tau)\mathrm{d}\tau, \quad \forall \tau \in (0, t) \tag{2.9}$$

with the total kinetic energy k and dissipation rate ϵ as defined in (2.7) and (2.8), respectively, and with

$$p(\tau) = \int_\Omega \mathbf{f}(\tau)\mathbf{u}(\tau)\mathrm{d}x. \tag{2.10}$$

Such results can be extended to mixed boundary conditions (2.4)-(2.6) if $\Gamma_w \cup \Gamma_{in} \neq \emptyset$. The uniqueness of a weak nonstationary solution is only proven for the two-dimensional case. However, the existence of a classical solution to the nonstationary NSE in 3D is still an open problem, see e.g. [33] and [111]. It is a challenge to prove the uniqueness of the weak solution in 3D or the existence of a classical solution in 3D of NSE. More results can be found in [7, 33, 103, 111].

2.2 Discretization in space using finite volume method

In the following part we focus on the finite volume method (cf. [32] and [65]) to discretize the equations of incompressible flow in space. The inviscid and viscid fluxes are introduced and calculated with upwind or central difference schemes.

2.2.1 Primary grid and dual grid

The primary grid is a set of polyedric elements (cells) $C = \{C_m\}_{m=1}^{\#C}$. Each cell is either a tetrahedron, a prism, a hexahedron or a pyramid in 3D, and there exists no overlap or gap between two cells. Fig. 2.2 provides an illustration for the two-dimensional case. Note that regular elements, such as hexahedra or prisms in the three-dimensional case, are employed in the region very close to the wall. Remote from the wall where the viscous terms are small, more flexible elements such as tetrahedra are used.

Γ_w
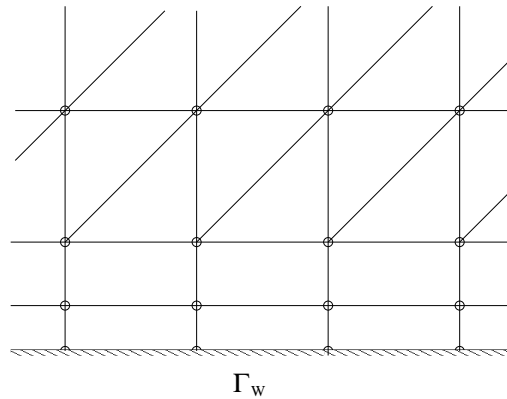
Figure 2.2: Sketch of a primary grid.

The governing equations are solved on the so-called *dual-grid*. A cell in the dual grid is also called control volume (CV). The dual grid has to be determined from the primary grid during the preprocess. The aim is to associate a control volume with the corresponding primary grid node. The finite volume method seeks a solution which is piecewise constant with respect to the dual grid.

Each face of the dual grid is associated with one edge of the primary grid. For the sake of clarity we study a two-dimensional sketch in Fig. 2.3. We use the following notations:

- Let $\mathcal{B} = (B_i)_{i=1}^{\#B}$ be the set of all cells of the dual grid.

- Let primary grid nodes P_i and P_j be connected by primary grid edge $\overline{P_i P_j}$.

- Denote $\mathcal{F}^{ij} = \{C_\alpha\}$ ($\alpha = 1, 2, \cdots$) the set of primary grid cells having a common line with $\overline{P_i P_j}$. To be more precise, we define

$$\mathcal{F}^{ij} = \{C \in C \mid \mu_{d-2}(\overline{C} \cap \overline{P_i P_j}) > 0\}$$

with μ_{d-2} denoting the $(d-2)$-dimensional measure in $\mathbb{R}^d$, e.g., the length of a curvilinear segment for $d = 3$.

- Denote $N^{ij} = \#\mathcal{F}^{ij}$ the number of primary grid cells adjacent to $\overline{P_i P_j}$.
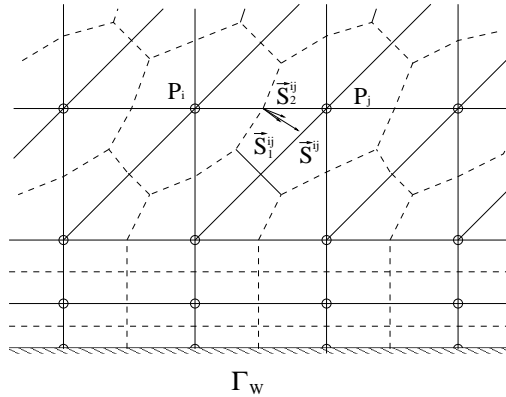
Figure 2.3: Sketch of a dual grid (dashed lines) with corresponding primary grid.

In the sequel we characterize a (d-1)-dimensional surface element with surface measure $\mu_{d-1}(\mathcal{A}) = S$ by the normal vector $\vec{S}$ with $|\vec{S}| = S$. Then the dual grid face $\vec{S}^{ij}$ associated with the primary grid edge $\overline{P_i P_j}$ is defined as follows:

- The triangular facets $\vec{S}_\alpha^{ij}$ with ($\alpha = 1, 2, \ldots, N^{ij}$) are determined by the mid points of cells and cell faces of the primary grid cells C_α in $\mathcal{F}^{ij}$.

- The dual grid face $\vec{S}^{ij}$ associated to $\overline{P_i P_j}$ is then given by $\vec{S}^{ij} = \bigcup_{\alpha=1}^{N^{ij}} \vec{S}_\alpha^{ij}$.

Given a primary grid $C = \{C_m\}_{m=1}^{\#C}$, denote $\mathcal{E}(C) = \{E_l\}_{l=1}^{\#\mathcal{E}}$ the set of all edges $\overline{P_i P_j}$ with P_i, P_j being grid nodes in C. Then during the preprocess for all faces $E = \overline{P_i P_j} \in \mathcal{E}$ the corresponding dual grid face $\vec{S}^{ij}$ is computed and stored in a data structure. This data structure provides an iterator for sequential data access.

When the unknowns of pressure and velocity are located at the same nodes as shown above, it is called nonstaggered (collocated) grid; otherwise it is called staggered grid. In a staggered grid the pressure and velocity are stored on different nodes, and two sets of control volumes are required. A staggered grid makes the code more complicated especially in the case of unstructured grids. However, the drawback of using nonstaggered grid is that spurious

pressure oscillations may occur due to the decoupling of pressure and velocity (cf. Section 2.3.2). For details of the variable arrangement on the grid, the reader is referred to [32].

Moreover, in a wall bounded turbulent flow, a finer grid in wall-normal direction should be used in the near-wall region in order to resolve the near-wall stress. Far away from the wall the grid can be coarser. Therefore, large aspect ratio may be used close to the wall.

2.2.2 FVM for the incompressible Navier-Stokes equations

Let B_i be a dual cell of domain Ω with $\overline{\Omega} = \bigcup_{B_i \in \mathcal{B}} \overline{B}_i$, $\mathcal{B}$ is the set of all cells of the dual grid. $\mathbf{u}_i$ and p_i are the discrete velocity and pressure located at the center of the control volume B_i. The weighting functions are chosen to be

$$\mathbf{v} = \sum_i \mathbf{v}_i, \quad q = \sum_i q_i, \tag{2.11}$$

where

$$\mathbf{v}_i = \mathbf{1} \quad \text{and} \quad q_i = 1 \qquad \text{in } B_i, \tag{2.12}$$

and zero elsewhere. Test the equations (2.1) and (2.2) by $\mathbf{v}_i$ and q_i, respectively, then integrate over all control volumes

$$\sum_{B_i \in \mathcal{B}} \int_{B_i} \mathbf{v}_i \frac{\partial \mathbf{u}_i}{\partial t} \mathrm{d}x + \sum_{B_i \in \mathcal{B}} \int_{B_i} \mathbf{v}_i \nabla \cdot (\mathbf{u}_i \otimes \mathbf{u}_i) \mathrm{d}x + \sum_{B_i \in \mathcal{B}} \int_{B_i} \mathbf{v}_i \nabla p_i \mathrm{d}x$$

$$- \sum_{B_i \in \mathcal{B}} \int_{B_i} \mathbf{v}_i \nu \Delta \mathbf{u}_i \mathrm{d}x = \sum_{B_i \in \mathcal{B}} \int_{B_i} \mathbf{v}_i \mathbf{f}_i \mathrm{d}x, \tag{2.13}$$

$$\sum_{B_i \in \mathcal{B}} \int_{B_i} q_i \nabla \cdot \mathbf{u}_i \mathrm{d}x = 0. \tag{2.14}$$

Applying the Gauss' theorem to the convective term and viscous term and setting $\mathbf{v}_i = \mathbf{1}$ and $q_i = 1$, we obtain a system of ordinary differential and algebraic equations:

$$\sum_{B_i \in \mathcal{B}} \int_{B_i} \frac{\partial \mathbf{u}_i}{\partial t} \mathrm{d}x + \sum_{B_i \in \mathcal{B}} \int_{\partial B_i} (\mathbf{u}_i \otimes \mathbf{u}_i) \cdot \mathbf{n}_i \mathrm{d}\sigma + \sum_{B_i \in \mathcal{B}} \int_{B_i} \nabla p_i \mathrm{d}x$$

$$- \sum_{B_i \in \mathcal{B}} \int_{\partial B_i} \nu \nabla \mathbf{u}_i \cdot \mathbf{n}_i \mathrm{d}\sigma = \sum_{B_i \in \mathcal{B}} \int_{B_i} \mathbf{f}_i \mathrm{d}x, \tag{2.15}$$

$$\sum_{B_i \in \mathcal{B}} \int_{\partial B_i} \mathbf{u}_i \cdot \mathbf{n}_i \mathrm{d}\sigma = 0, \tag{2.16}$$

where ∂B_i denotes the boundary of B_i and $\mathbf{n}_i$ is the unit normal vector pointing outward to this boundary ∂B_i.

Using FVM, one typically integrates the NSE in space in conservative form, so that the volume integrals with divergence terms are transformed into surface integrals of the corresponding fields flux on the cell interfaces. How the fluxes are calculated is unspecified by

the FVM, as long as they satisfy two principles: conservation and consistency. The former requires that the flux from cell B_i to neighbor cell B_j through their common side is opposite to the flux from B_j to B_i. The latter, roughly speaking, requires that the numerical error on the flux evaluation is $O(h)$, if h is the size of the largest cell in the mesh. The method is conservative by construction, as long as the surface integrals are the same for the CVs sharing the boundary.

The remaining volume integrals in (2.15) can be calculated in a very simple way since one approximates the source term $\mathbf{f}$ by a piecewise constant on each CV. Using the volume ΔV_i of each CV B_i, we obtain, e.g.,

$$\sum_{B_i \in \mathcal{B}} \int_{B_i} \mathbf{f}_i \mathrm{d}x = \sum_{B_i \in \mathcal{B}} \mathbf{f}_i \Delta V_i, \tag{2.17}$$

where $\mathbf{f}_i$ is the corresponding value at the center of the CV B_i. The integration of the pressure gradient is done as

$$\sum_{B_i \in \mathcal{B}} \int_{B_i} \nabla p_i \mathrm{d}x = \sum_{B_i \in \mathcal{B}} \nabla p_i \Delta V_i. \tag{2.18}$$

Furthermore, the left hand side of (2.16) is actually the mass flux which will be introduced later on in Section 2.2.4.

2.2.3 Definition of inviscid and viscid fluxes

The surface integrals in (2.15) are specified as fluxes. The convective term is defined as the inviscid flux across the boundary of B_i,

$$\mathbf{Q}_{B_i}^i = \int_{\partial B_i} (\mathbf{u}_i \otimes \mathbf{u}_i) \cdot \mathbf{n}_i \mathrm{d}\sigma = \sum_j \int_{S_{ij}} (\mathbf{u}_i \otimes \mathbf{u}_i) \cdot \mathbf{n}_{ij} \mathrm{d}\sigma, \tag{2.19}$$

and the diffusive term as the viscid flux across ∂B_i,

$$\mathbf{Q}_{B_i}^v = -\int_{\partial B_i} \nu \nabla \mathbf{u}_i \cdot \mathbf{n}_i \mathrm{d}\sigma = -\sum_j \int_{S_{ij}} \nu \nabla \mathbf{u}_i \cdot \mathbf{n}_{ij} \mathrm{d}\sigma. \tag{2.20}$$

where j denotes the neighbors of i those share one primary edge with i, S_{ij} the interface between cell i and j with $\partial B_i = \sum_j S_{ij}$ and $\mathbf{n}_{ij}$ the unit normal vector on S_{ij} pointing from i to j. The evaluation of the viscid fluxes requires the gradients on the cell sides. These kind of fluxes, themselves expressed as functions of some gradients, may require a cell-centered evaluation of the gradients. For details, we refer to Section 2.2.4.

Fluxes across inner faces

In the DLR-THETA-code, the computation of the fluxes is performed within a loop over all faces. For an interface S_{ij} of the dual grid corresponding to the edge $E = \overline{P_i P_j}$ with normal

vector $\mathbf{n}_{ij}$, and $S_{ij} \cap \Gamma_W = \emptyset$, we define the inviscid flux across S_{ij} as

$$\mathbf{Q}^i_{S_{ij}} = \int_{S_{ij}} (\mathbf{u}_i \otimes \mathbf{u}_i) \cdot \mathbf{n}_{ij} \mathrm{d}\sigma, \tag{2.21}$$

and the viscid flux across S_{ij}

$$\mathbf{Q}^v_{S_{ij}} = -\int_{S_{ij}} \nu \nabla \mathbf{u}_i \cdot \mathbf{n}_{ij} \mathrm{d}\sigma. \tag{2.22}$$

The contribution of the fluxes to the control volume B_i is $\mathbf{Q}^i_{S_{ij}}$ and $\mathbf{Q}^v_{S_{ij}}$, while with opposite sign to the control volume B_j for keeping conservation of the fluxes.

Fluxes across boundary faces

We consider $B \in \mathcal{B}$ with $\overline{B} \cap \Gamma_W \neq \emptyset$, with Γ_W the no-slip boundary of $\mathcal{B}$ as shown in Fig. 2.2, and study the fluxes across Γ_W. The inviscid flux across Γ_W vanishes since $\mathbf{u} = 0$ on the wall. We define the viscid flux across Γ_W

$$\mathbf{Q}^v_{\partial B \cap \Gamma_W} = -\int_{\partial B \cap \Gamma_W} \nu \nabla \mathbf{u}_i \cdot \mathbf{n}_i \mathrm{d}\sigma. \tag{2.23}$$

The fluxes across the inflow boundary Γ_{in} are as follows

$$\mathbf{Q}^i_{\partial B \cap \Gamma_{in}} = \int_{\Gamma_{in}} (\mathbf{u}_i \otimes \mathbf{u}_i) \cdot \mathbf{n}_i \mathrm{d}\sigma, \tag{2.24}$$

$$\mathbf{Q}^v_{\partial B \cap \Gamma_{in}} = -\int_{\Gamma_{in}} \nu \nabla \mathbf{u}_i \cdot \mathbf{n}_i \mathrm{d}\sigma, \tag{2.25}$$

and the fluxes across the outflow boundary Γ_{out} have the following forms

$$\mathbf{Q}^i_{\partial B \cap \Gamma_{out}} = \int_{\Gamma_{out}} (\mathbf{u}_i \otimes \mathbf{u}_i) \cdot \mathbf{n}_i \mathrm{d}\sigma, \tag{2.26}$$

$$\mathbf{Q}^v_{\partial B \cap \Gamma_{out}} = -\int_{\Gamma_{out}} \nu \nabla \mathbf{u}_i \cdot \mathbf{n}_i \mathrm{d}\sigma, \tag{2.27}$$

where $\mathbf{u}_i$ and $\mathbf{n}_i$ are the velocity and the corresponding unit normal vector at the boundaries.

2.2.4 Calculation and linearization of fluxes

The calculation of volume integrals can be treated as in (2.17) and (2.18). For the surface integrals, further approximations are necessary since the values of the integrand, $\mathbf{u} \otimes \mathbf{u}$ in the convective and $\nabla \mathbf{u}$ in the diffusive fluxes, are not available at the cell-face center. Therefore,

interpolation and numerical differentiation have to be used to compute the cell-face values of variables and their derivatives through the nodal values.

To evaluate the convective terms, we use four different spatial discretization schemes: first-order upwind difference scheme (UDS), second-order central difference scheme (CDS), second-order linear upwind difference scheme (LUDS) and quadratic upwind difference scheme (QUDS), see also in [32]. The diffusive term is discretized with the second-order central difference scheme in the DLR-THETA-code.
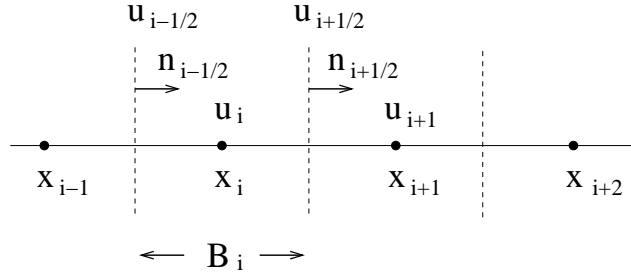
Figure 2.4: Control volume B_i in 1D.

Let us briefly explain the spatial discretization schemes used in the present study by considering a one-dimensional situation as in Fig. 2.4. In the finite volume approach, the first derivative of $\mathbf{u}$ may be discretized as

$$\left.\frac{\partial \mathbf{u}}{\partial x}\right|_i = \frac{1}{h_B}(\mathbf{u}_{i+1/2} - \mathbf{u}_{i-1/2}), \tag{2.28}$$

here i denotes an index of a cell B_i and h_B is a suitable length scale associated with the dual grid cell. Since $\mathbf{u}_i$ is located at the center of the ith cell, $\mathbf{u}_{i+1/2}$ and $\mathbf{u}_{i-1/2}$ are obtained by interpolations. In the case of CDS, $\mathbf{u}_{i+1/2}$ is interpolated as

$$\mathbf{u}_{i+1/2} = \frac{1}{2}(\mathbf{u}_i + \mathbf{u}_{i+1}). \tag{2.29}$$

In the case of the three upwind schemes, $\mathbf{u}_{i+1/2}$ is expressed as

$$\begin{aligned}\mathbf{u}_{i+1/2} =\ &\max(0, s_{i+1/2})\left[g_1\mathbf{u}_{i+1} - g_2\mathbf{u}_{i-1} + (1 - g_1 + g_2)\mathbf{u}_i\right]\\ &- \min(0, s_{i+1/2})\left[g_1\mathbf{u}_i - g_2\mathbf{u}_{i+2} + (1 - g_1 + g_2)\mathbf{u}_{i+1}\right],\end{aligned} \tag{2.30}$$

where $s_{i+1/2}$ is the sign of the projection of velocity $\mathbf{u}$ on the outward normal vector of the face between ith and $(i + 1)$th cells, that is,

$$s_{i+1/2} = \begin{cases} 1, & \text{if } \mathbf{u}_{i+1/2} \cdot \mathbf{n}_{i+1/2} \geq 0, \\ -1, & \text{if } \mathbf{u}_{i+1/2} \cdot \mathbf{n}_{i+1/2} < 0. \end{cases} \tag{2.31}$$

For UDS, LUDS and QUDS, the coefficients g_1 and g_2 are given by

UDS: $g_1 = g_2 = 0,$

LUDS: $g_1 = 0, g_2 = 1/2,$

QUDS: $g_1 = 3/8, g_2 = 1/8.$

These four schemes are sketched in Fig. 2.5 and Fig. 2.6 for the one-dimensional case. We can easily read that the central difference scheme takes the mean velocity of both sides to approximate the velocity at the face of the control volume. The upwind scheme uses the velocity at upstream point, linear upwind scheme approximates linearly with two upstream points and quadratic upwind scheme adopts two points from upstream and one point downstream to perform a quadratic interpolation.
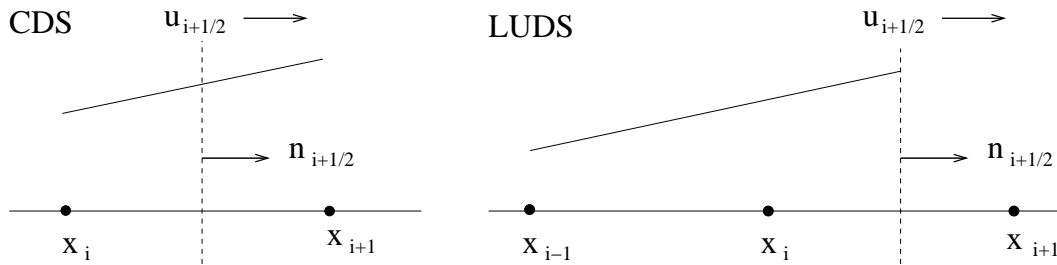
Figure 2.5: Central and linear upwind difference scheme.
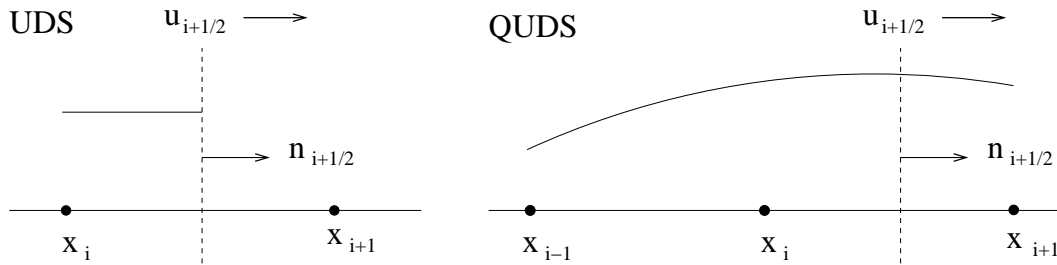
Figure 2.6: Upwind and quadratic upwind difference scheme.

The next step is to calculate the velocity and velocity gradient at the boundary of the dual cells using the different schemes explained above. To this goal one has to linearize the convective flux terms and to take into account potential modifications of the flux terms for the multi-dimensional case.

The convective fluxes are nonlinear terms, so linearization is necessary. The most widely used approach is the Picard-iteration scheme, i.e. the approximation of nonlinear terms is calculated by a product of an 'old' (from the preceding time iteration) and a 'new' value, cf. [32]. The mass flux through the cell face is computed using the velocity from the previous

iteration, the convective fluxes are linearized as follows,

$$\mathbf{Q}^i_{S_{ij}} = \int_{S_{ij}} (\mathbf{u}^{n+1}_i \otimes \mathbf{u}^n_i) \cdot \mathbf{n}_{ij} d\sigma = \dot{m}^n_{S_{ij}} \mathbf{u}^{n+1}_{S_{ij}}, \tag{2.32}$$

with the mass flux through S_{ij}

$$\dot{m}^n_{S_{ij}} = \int_{S_{ij}} \mathbf{u}^n_{S_{ij}} \cdot \mathbf{n}_{ij} d\sigma. \tag{2.33}$$

For some time discretization scheme which will be introduced in Section 2.3, the nonlinear term needs a special treatment in order to keep the order of accuracy. Further details will be given in Section 2.3.3.

Let us now consider modifications of the flux terms for the multi-dimensional case, see Fig. 2.7. In the DLR-THETA-code the convective fluxes through a face S are split into two parts: the flux calculated with upstream velocity and the correction part. We define the upstream and downstream points as follows

$$\begin{cases} P_u = P_i, P_d = P_j, & \text{if } \dot{m}_S = \dot{m}_{S_{ij}} > 0, \\ P_u = P_j, P_d = P_i, & \text{otherwise.} \end{cases} \tag{2.34}$$

Here $\dot{m}_S$ is the mass flux. In function `add_i_c_im_mom_fluxes()`, the first part of convective flux is computed,

$$F_u = \dot{m}_S \mathbf{u}_u. \tag{2.35}$$

In function `add_i_c_ex_mom_fluxes()` of the DLR-THETA-code, the correction is made for different discretization schemes to the convective flux,

$$F_{cor} = \frac{1}{2} \dot{m}_S [\alpha(\mathbf{u}_d - \mathbf{u}_u) - \beta \nabla \mathbf{u}_u \cdot \mathbf{l}], \tag{2.36}$$

where $\mathbf{u}_u$ and $\mathbf{u}_d$ are upstream and downstream velocity, respectively. $\mathbf{l}$ is the distance between the node $\mathbf{u}_u$ and its neighbor, α and β are parameters for discretization schemes listed in Table 2.1.

	α	β	convective flux $\mathbf{Q}^i_{S_{ij}} = F_u + F_{cor}$
UDS	0	0	$\dot{m}_S \mathbf{u}_u$
CDS	1	0	$\frac{1}{2}\dot{m}_S(\mathbf{u}_u + \mathbf{u}_d)$
LUDS	0	1	$\dot{m}_S(\mathbf{u}_u + \frac{1}{2}\nabla \mathbf{u}_u \cdot \mathbf{l})$
QUDS	0.5	0.5	$\frac{1}{4}\dot{m}_S(\mathbf{u}_d + 3\mathbf{u}_u + \nabla \mathbf{u}_u \cdot \mathbf{l})$

Table 2.1: Table of parameters and convective fluxes of discretization schemes.

If we assume $\nabla \mathbf{u}_i \cdot \mathbf{l} = \mathbf{u}_i - \mathbf{u}_{i-1}$, we can show that the same approximation of velocity is used as in equation (2.30).
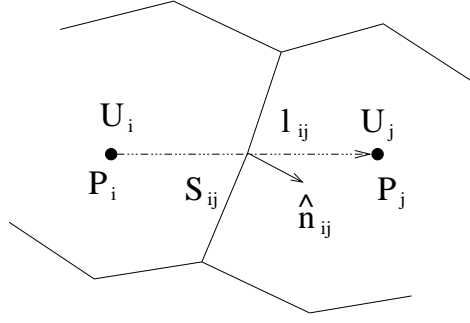
Figure 2.7: The cell face S_{ij}.

Similarly, the diffusive fluxes are also split into two parts: the implicit part and the explicit part. In function `add_i_d_im_mom_fluxes()`, the implicit part is treated,

$$F_{d1} = \nu_m(\mathbf{u}|_{P_j} - \mathbf{u}|_{P_i})n_l, \tag{2.37}$$

and the explicit part is computed in function `add_i_d_ex_mom_fluxes()`,

$$F_{d2} = \nu_m \left(\nabla \mathbf{u}_m \cdot \hat{\mathbf{n}} + \nabla \mathbf{u}_m \cdot (\hat{\mathbf{n}} - n_l \mathbf{l}) \right), \tag{2.38}$$

where the mean values are $\nabla \cdot \mathbf{u}_m = \frac{1}{2}(\nabla \cdot \mathbf{u}|_{P_i} + \nabla \cdot \mathbf{u}|_{P_j})$, $\nu_m = \nu|_{P_i} + \nu|_{P_j}$ and $\nabla \mathbf{u}_m = \nabla \mathbf{u}|_{P_i} + \nabla \mathbf{u}|_{P_j}$, $\hat{\mathbf{n}}$ is the normal vector with length scale of S_{ij} and $n_l = \frac{\hat{\mathbf{n}} \cdot \hat{\mathbf{n}}}{\mathbf{l} \cdot \hat{\mathbf{n}}}$. Then the diffusive flux is

$$\mathbf{Q}^{\nu}_{S_{ij}} = F_{d1} + F_{d2}. \tag{2.39}$$

The first term of (2.38) gives the flux through the cell face in the orthogonal direction, the second term represents the nonorthogonal part. When the line connecting cell centers P_i and P_j is orthogonal to the cell face, the second term vanishes due to zero vector $\mathbf{n} - n_l \mathbf{l}$.

2.2.5 Implementation of boundary conditions

In this work we only consider no-slip boundary condition (2.4) at the wall and inflow/outflow boundary conditions (2.5)-(2.6). Let N denote the number of all nodes in domain Ω, N_{inner} and N_{bdry} represent the number of inner nodes and boundary nodes, respectively. We have the original grid as sketched in Fig. 2.8, where the full line is the primary grid and the dashed line denotes the dual grid.

During preprocessing, the boundary nodes at the wall are shifted toward inner nodes along the primary edges, which connect the boundary nodes and the first inner nodes next to the boundary, one third of the lengths. These new inner nodes are denoted as P, all original inner nodes remain fixed. N_{bdry} additional nodes are added at the position of the original boundary nodes, which are small circles in Fig. 2.9 and denoted as P_A. Now we have N inner nodes
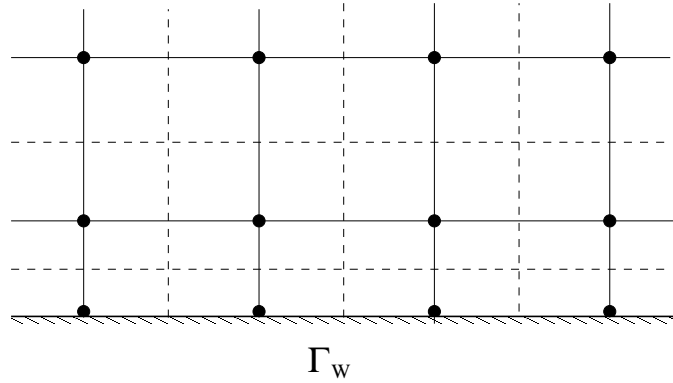
Figure 2.8: The original grid of the boundary part.
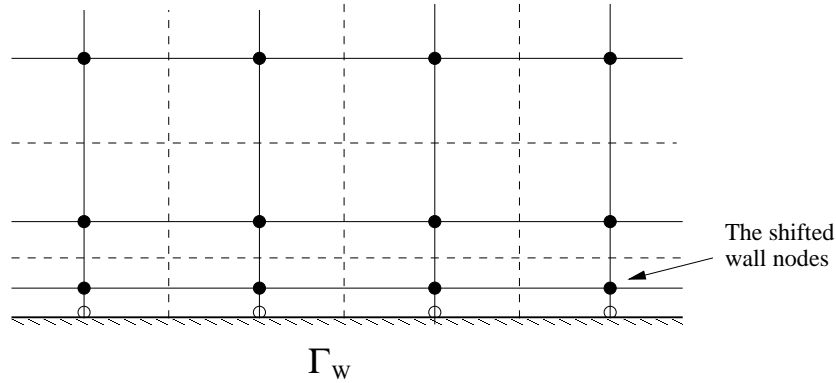
Figure 2.9: The shifted grid of the boundary part.

and N_{bdry} boundary nodes, i.e., N_{bdry} more inner nodes are implemented near the boundary to generate a new mesh.

In the course of calculation, the no-slip boundary condition is imposed on the additional nodes P_A. The boundary fluxes require a special treatment, they must either be known or be expressed as a combination of interior values and boundary data. Since there are no nodes outside the boundary, these approximations must be performed based on one-sided differences or extrapolations.

In the DLR-THETA-code, the convective fluxes are zero at impermeable walls and symmetry planes, products of the mass fluxes and mean velocity at the inflow boundary. They are treated fully implicitly at the outflow boundary as follows

$$\mathbf{Q}^i_{\partial B \cap \Gamma_{out}} = \dot{m}|_{\Gamma_{out}}(\mathbf{u}|_{\Gamma_{out}} + \mathbf{l} \cdot \nabla \mathbf{u}|_{\Gamma_{out}}). \qquad (2.40)$$

where $\mathbf{l}$ is the length vector of the edge which connects the boundary node and the shifted node. The velocity gradient at the boundary needs to be specified to evaluate the diffusive fluxes. One sided approximations for normal gradients are used. Inhomogeneous parts of

the diffusive fluxes at the inflow boundary have the following form

$$\mathbf{Q}^{vi}_{\partial B \cap \Gamma_{in}} = -\nu_m \mathbf{u}|_{\Gamma_{in}} n_l \quad \text{with } n_l = \sqrt{\frac{\mathbf{n} \cdot \mathbf{n}}{\mathbf{l} \cdot \mathbf{l}}}, \tag{2.41}$$

homogeneous parts are

$$\mathbf{Q}^{vh}_{\partial B \cap \Gamma_{in}} = -\nu_m (\mathbf{n} \cdot (\nabla \mathbf{u}|_{\Gamma_{in}} + \nabla \cdot \mathbf{u}|_{\Gamma_{in}} \mathbf{I}) + \nabla \mathbf{u}|_{\Gamma_{in}} \cdot \mathbf{t} - n_l \mathbf{u}|_{\Gamma_{in}}), \tag{2.42}$$

and $\mathbf{t} = \mathbf{n} - n_l \mathbf{l}$ is the tangential vector of the boundary face. The diffusive fluxes are described at the outflow boundary fully implicitly, they are given as

$$\mathbf{Q}^{v}_{\partial B \cap \Gamma_{out}} = -\nu_m (\mathbf{n} \cdot (\nabla \mathbf{u}|_{\Gamma_{out}} + \nabla \cdot \mathbf{u}|_{\Gamma_{out}} \mathbf{I}) + \nabla \mathbf{u}|_{\Gamma_{out}} \cdot \mathbf{t} + n_l \nabla \mathbf{u}|_{\Gamma_{out}} \cdot \mathbf{l}). \tag{2.43}$$

To output the solution, all the shifted nodes P are removed and the solutions at P_A are copied to P. The output data is given on the same grid as the original one.

2.2.6 Convergence test in space

The convergence rate of the spatial discretization QUDS, LUDS, UDS and CDS for the problem (2.1)-(2.2) is tested. The error analysis of upwind-discretizations based on FVM for the incompressible NSE is studied by Angermann [2], and an approximation technique for the nonlinear convective term is investigated. We consider the computational domain $\Omega = [0, 1] \times [0, 1]$ with the following exact solution $(\mathbf{u}, p)$:

$$u(x, y, t) = \pi \sin(2\pi y) \sin^2(\pi x) \sin t, \tag{2.44}$$
$$v(x, y, t) = -\pi \sin(2\pi x) \sin^2(\pi y) \sin t, \tag{2.45}$$
$$p(x, y, t) = \pi \cos(\pi x) \sin(\pi y) \sin t. \tag{2.46}$$

Then the source term is given by $\mathbf{f} = \mathbf{u}_t - \nu \nabla^2 \mathbf{u} + \mathbf{u} \nabla \mathbf{u} + \nabla p$. Rectangular cells with mesh sizes $h = 1/40, 1/80, 1/160$ and $1/320$ are used. The time step of the time-stepping scheme BDF(2) (see Section 2.3) is set to $\delta t = 0.0005$. It is small enough that the temporal error does not disturb the spatial error. Two different viscosities are considered, $\nu = 1.0$ and $\nu = 10^{-6}$.

Assume ϕ is the quantity of interest, then the discrete L^2-norm of the error between the exact solution $\phi(x, y, t^k)$ and the discrete solution $\phi_h(x, y, t^k)$ at time $t = t^k$ is defined as

$$e^k_\phi = h \left(\sum_{i,j=0}^{N} \left[\phi(x_i, y_j, t^k) - \phi_h(x_i, y_j, t^k) \right]^2 \right)^{1/2}, \tag{2.47}$$

where N is the number of discrete points in one direction, $N = 40, 80, 160$ and 320 for four grids, respectively. The theory for parabolic problems suggest estimates in $L^\infty(L^2(\Omega))$. A suitable numerical approximation is given by

$$e_\phi := \max_{k=0,\dots,M} e^k_\phi = \max_{k=0,\dots,M} h \left(\sum_{i,j=0}^{N} \left[\phi(x_i, y_j, t^k) - \phi_h(x_i, y_j, t^k) \right]^2 \right)^{1/2}. \tag{2.48}$$
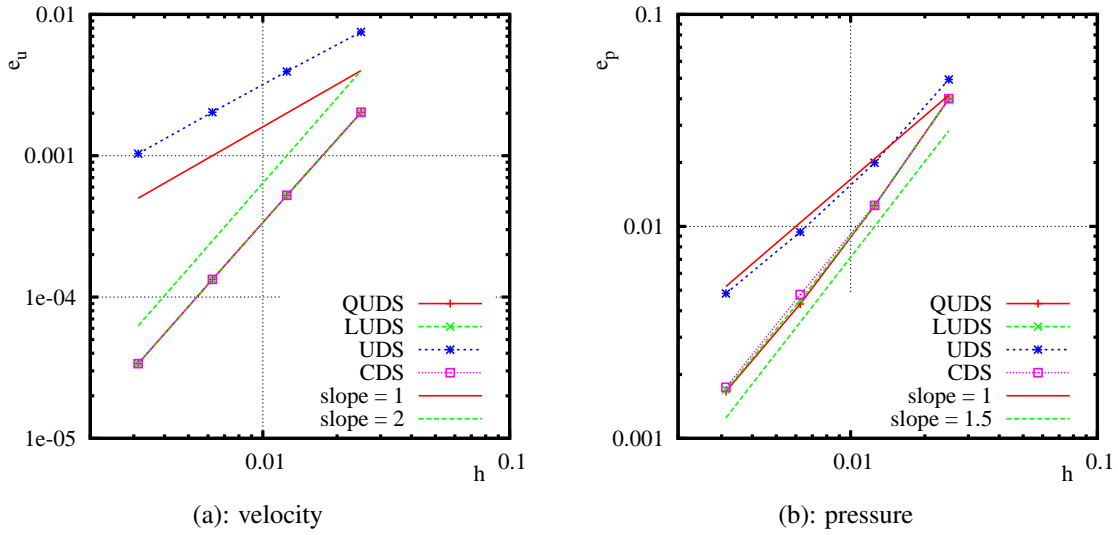
Figure 2.10: Errors in the L^2-norm at $\nu = 1.0$.
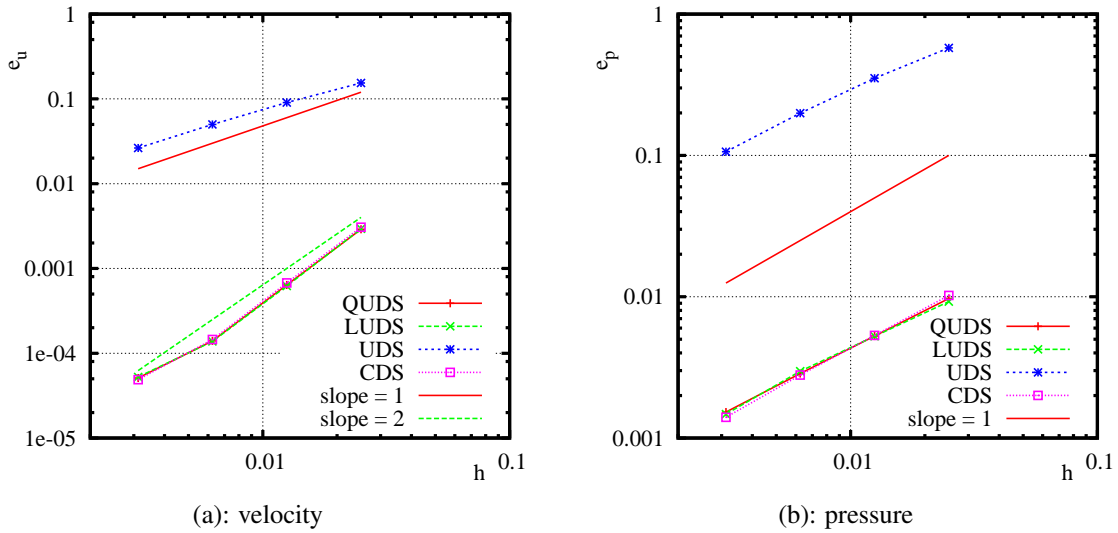
Figure 2.11: Errors in the L^2-norm at $\nu = 10^{-6}$.

As e_ϕ^k increases with k, it is useful to consider $e_\phi = e_\phi^M$, i.e., the error at $t^M = T$.

The errors of the velocity and pressure at time $T = 1.0$ in the discrete L^2-norms are shown in Fig. 2.10 and 2.11. Obviously, for both viscosities a second order convergence rate on the velocity is obtained for QUDS, LUDS and CDS. UDS gives the convergence rate of order $O(h)$. The pressure converges with order one except that it has convergence rate of order $O(h^{3/2})$ at the large viscosity $\nu = 1.0$ for QUDS, LUDS and CDS.

2.3 Discretization in time and projection method

To solve the system of the incompressible Navier-Stokes equations (2.1)-(2.2), fractional-step methods provide an efficient approach. The main idea of projection methods is to separate the calculation of velocity and pressure, meanwhile the divergence free constraint (2.2) is fulfilled via a projection step.

Let us remind that after semidiscretization of (2.1)-(2.2) in space we obtained the coupled system (2.15) and (2.16), which suffers from two major problems:

- (2.15) is a large system of ordinary differential equations (ODE) which is stiff and dissipative, (for an explanation see Appendix A).

- (2.16) is a linear system of algebraic equations which acts as side condition of the ODE-system (2.15).

In the following, we combine the presentation of the projection method with the time discretization of the ODE-system (2.15).

2.3.1 Time discretization with linear multistep methods

For the sake of simplicity, the governing ODE-system (2.15) is written in the form of

$$\frac{d\mathbf{u}}{dt} = \mathbf{F}(t, \mathbf{u}), \qquad t \in [0, T], \tag{2.49}$$

where $\mathbf{F}$ stands for all other terms (convective, diffusive, source terms and pressure gradient). Let $0 = t_0 < t_1 < \ldots < t_N = T$ be the sequence of discretization nodes, $I_n = [t_n, t_{n+1}]$ be the subintervals with $n = 0, 1, \ldots, N$. For simplicity, assume that the equidistant time step is given by

$$\delta t = \delta t_n := t_{n+1} - t_n. \tag{2.50}$$

Denote $\mathbf{u}^n := \mathbf{u}(t_n), \ldots, \mathbf{u}^{n+s} := \mathbf{u}(t_{n+s})$ and $\mathbf{F}^{n+s} := \mathbf{F}(t_{n+s}, \mathbf{u}(t_{n+s}))$. To approximate the solution of the large and stiff ODE-system (2.49), the multistep methods are formulated as follows,

$$\sum_{s=0}^{p} \alpha_s \mathbf{u}^{n+s} = \delta t \phi(t_n, \mathbf{u}^n, \ldots, \mathbf{u}^{n+s}; \delta t), \quad n = 0, 1, \ldots, N - p. \tag{2.51}$$

For these p-step (p≥1) methods, $\alpha_0, \ldots, \alpha_p$ are constants and ϕ is an appropriate method function. If the function ϕ is a linear function, i.e.,

$$\sum_{s=0}^{p} \alpha_s \mathbf{u}^{n+s} = \delta t \sum_{s=0}^{p} \beta_s \mathbf{F}^{n+s}, \tag{2.52}$$

with constants β_s, for $s = 0, \ldots, p$, the method is called *linear multistep method*.

29

The reader who is interested in the properties of the linear multistep methods is referred to Appendix A.

Here, we present two examples of linear multistep methods which are used in the DLR-THETA-code.

Example 2.1 *A one-step method is a special case of the multistep methods. By setting $p = 1$, $\alpha_0 = -1$, $\alpha_1 = 1$, $\beta_1 = \theta$ and $\beta_0 = 1 - \theta$ in (2.52), the so-called θ-scheme or generalized trapezoidal rule is obtained*

$$\mathbf{u}^{n+1} - \mathbf{u}^n = \delta t[(1 - \theta)\mathbf{F}^n + \theta\mathbf{F}^{n+1}] \tag{2.53}$$

with parameter $\theta \in [0, 1]$. The values $\theta = 0$ and $\theta = 1$ represent the explicit and implicit Euler scheme, respectively, $\theta = 1/2$ leads to the Crank-Nicolson method.

The θ-scheme has first order accuracy for $0 \leq \theta \leq 1$ and second order accuracy for $\theta = 1/2$. Moreover, the implicit Euler scheme $\theta = 1$ is A-stable, so it is well-suited for stiff ODE-systems (2.49). For details, see Appendix A.

For the one-step θ-scheme, there exists in the DLR-THETA-code a mixed implicit-explicit implementation of different terms. This usually leads to an upper limit of the time step size δt. For the simple transport equation

$$\partial_t u + b\partial_x u = 0, \tag{2.54}$$

with constant velocity b, the Courant-Friedrichs-Levy (CFL) parameter is defined as

$$CFL = \frac{b\delta t}{h}, \tag{2.55}$$

where δt is the time step, h the characteristic mesh size and b the characteristic velocity. The physical meaning of the CFL parameter is a measure, in characteristic grid spacings, of how far a wave can travel through the flow in a single time step. For the problem (2.54) the necessary and sufficient condition for an explicit scheme to be stable is that the CFL number fulfills the so-called CFL condition:

$$|CFL| \leq 1. \tag{2.56}$$

The time step size δt is restricted for a given mesh. However, the CFL condition constraint is not necessary for implicit schemes. For details, we refer to Appendix A.

This one-step method has low accuracy, therefore it is natural to look for higher order methods with good stability properties. As described in Appendix A, there are no A-stable linear multistep methods of order greater than 2. A remedy is to look for A(α)-stable linear multistep methods of higher order with sufficiently large α. It turns out that such schemes can be obtained by taking $\beta_0 = \ldots = \beta_{p-1} = 0$ and $\beta_p = 1$ in (2.52), i.e.,

$$\sum_{s=0}^{p} \alpha_s \mathbf{u}^{n+s} = \delta t \mathbf{F}^{n+p}. \tag{2.57}$$

Example 2.2 *The so-called* backward differentiation formulae *(shortly, BDF) are implicit multistep methods, which can be derived by approximating the derivative at node t_{n+1} directly through a backward polynomial interpolation based on the derivatives at the $p + 1$ nodes $t_{n+1}, t_n, \ldots, t_{n-p+1}$. The polynomial $\mathbf{q}(t)$ satisfies the following differential equation*

$$\mathbf{q}'(t_{n+p}) = \mathbf{F}(t_{n+p}, \mathbf{u}_{n+p}).$$

After some calculation, one obtains the BDF-scheme

$$\sum_{s=1}^{p} \frac{1}{s} \nabla^s \mathbf{u}_{n+1} = \delta t \mathbf{F}_{n+1} \tag{2.58}$$

with

$$\nabla^0 \mathbf{u}_s = \mathbf{u}_s, \qquad \nabla^s \mathbf{u}_s = \nabla^{s-1} \mathbf{u}_s - \nabla^{s-1} \mathbf{u}_{s-1}.$$

We reformulate (2.58) as follows

$$\sum_{s=0}^{p} \alpha_s \mathbf{u}^{n+1-s} = \delta t \mathbf{F}^{n+1}. \tag{2.59}$$

The coefficients of BDF methods are listed for $p \leq 6$ in Table 2.2.

p	α_0	α_1	α_2	α_3	α_4	α_5	α_6
1	1	-1	0	0	0	0	0
2	3/2	-2	1/2	0	0	0	0
3	11/6	-3	3/2	-1/3	0	0	0
4	25/12	-4	3	-4/3	1/4	0	0
5	137/60	-5	5	-10/3	5/4	-1/5	0
6	147/60	-6	15/2	-20/3	15/4	-6/5	1/6

Table 2.2: Coefficients of zero-stable BDF methods for $p = 1, 2, \ldots, 6$.

In particular, for p=1 and p=2 we obtain,

BDF(1): $\mathbf{u}^{n+1} - \mathbf{u}^n = \delta t \mathbf{F}^{n+1}$,

BDF(2): $\frac{3}{2} \mathbf{u}^{n+1} - 2 \mathbf{u}^n + \frac{1}{2} \mathbf{u}^{n-1} = \delta t \mathbf{F}^{n+1}$.

The one-step BDF method is simply the backward Euler method (see Example 2.1 with $\theta = 1$), which is first order accurate. The two-step BDF method, denoted as BDF(2), will be later on used in the following form,

$$\frac{3 \mathbf{u}^{n+1} - 4 \mathbf{u}^n + \mathbf{u}^{n-1}}{2 \delta t} = \mathbf{F}^{n+1}. \tag{2.60}$$

The BDF(2) method is second order accurate. Please note that the BDF(1) and BDF(2) are A-stable, i.e., A(α)-stable with $\alpha = \pi/2$ (see Appendix A).

2.3.2 Projection method

The projection scheme is a method of discretizing equation (2.1)-(2.2) in time so that the computation of velocity and pressure can be decoupled. There are several projection methods, namely the pressure-correction method (see [17, 37, 116, 120]), the velocity-correction method (e.g. [43]) and the consistent splitting method (for instance [30] as Gauge method, also [44]). In this thesis, we only consider the pressure-correction method.

The pressure-correction method was first proposed by Chorin [17] and Temam [116] in the late 1960s. The idea is to solve the momentum equation for an intermediate velocity by ignoring the pressure gradient and projecting the velocity back to the space of the incompressible vector fields. In 1979, Goda [37] suggested to include an old value of the pressure gradient since it was observed that the pressure gradient is obviously missing in the previous approach. For instance, considering the Navier-Stokes problem after semi-discretization with the θ-scheme in time, the pressure-correction method of the system (2.1)-(2.2) reads:

$$\frac{\mathbf{u}^* - \mathbf{u}^n}{\delta t_n} + \nabla \cdot (\theta \mathbf{u}^* \otimes \mathbf{u}^* + (1 - \theta)\mathbf{u}^n \otimes \mathbf{u}^n) + \nabla p^n$$

$$-\nu\Delta(\theta\mathbf{u}^* + (1 - \theta)\mathbf{u}^n) = \mathbf{f}^n, \tag{2.61}$$

$$\nabla \cdot \nabla \delta p^{n+1} = \frac{\omega}{\delta t_n}\nabla \cdot \mathbf{u}^*, \tag{2.62}$$

$$p^{n+1} = p^n + \delta p^{n+1}, \tag{2.63}$$

$$\mathbf{u}^{n+1} = \mathbf{u}^* - \frac{\delta t_n}{\omega}\nabla\delta p^{n+1}. \tag{2.64}$$

This is the so-called *standard incremental pressure-correction scheme*, (cf. [42]). The source term $\mathbf{f}$ is simply taken from the previous time step. The pressure gradient is treated explicitly in the momentum equation (2.61), which is a vector-valued stationary diffusion-advection-reaction equation with a nonlinear advection term.

In (2.62) and (2.64) $\omega \in [1, 2]$ is the projection weighting factor which is used in the DLR-THETA-code to improve convergence. Boundary conditions for $\mathbf{u}^*$ subject to equation (2.61) are simply chosen to be the boundary conditions for the final velocity $\mathbf{u}^{n+1}$ of this time step. Chorin's original *non-incremental pressure-correction scheme* can be derived from (2.61)-(2.64) by omitting ∇p^n, replacing δp^{n+1} by p^{n+1} and setting $\omega = 1$.

As a result, at each time step, one only needs to solve a vector-valued advection-diffusion-reaction equation and a Poisson equation separately for velocity and pressure instead of the coupled system. This is done by first ignoring the incompressibility condition (2.2) and taking the pressure gradient explicitly, computing an intermediate velocity $\mathbf{u}^*$ using the momentum equation, which may lead to $\nabla \cdot \mathbf{u}^* \neq 0$, and then projecting $\mathbf{u}^*$ back to the space of incompressible vector fields to obtain $\mathbf{u}^{n+1}$ and p^{n+1}, with $\nabla \cdot \mathbf{u}^{n+1} = 0$.

For BDF(2), the projection scheme of the NSE system (2.1)-(2.2) is written as follows:

$$\frac{3\mathbf{u}^* - 4\mathbf{u}^n + \mathbf{u}^{n-1}}{2\delta t_n} + \nabla \cdot (\mathbf{u}^* \otimes \mathbf{u}^*) + \nabla p^n - \nu \Delta \mathbf{u}^* \;=\; \mathbf{f}^n, \tag{2.65}$$

$$\nabla \cdot \nabla \delta p^{n+1} \;=\; \frac{3\omega}{2\delta t_n} \nabla \cdot \mathbf{u}^*, \tag{2.66}$$

$$p^{n+1} \;=\; p^n + \delta p^{n+1}, \tag{2.67}$$

$$\mathbf{u}^{n+1} \;=\; \mathbf{u}^* - \frac{2\delta t_n}{3\omega} \nabla \delta p^{n+1}. \tag{2.68}$$

We use the same treatment to pressure and source term as in the θ-scheme. The previous velocity $\mathbf{u}^n$ and also the preprevious velocity $\mathbf{u}^{n-1}$ are included in the first sub-step. After solving the decoupled momentum and Poisson equations, a projection is performed to correct the velocity in the second sub-step.

It is shown in [42] that the nonstationary Stokes problem is second order accurate on the velocity in the L^2-norm, the pressure has first order convergence rate in L^∞-norm. Let $\hat{\mathbf{u}}_{\delta t}$ and $\hat{p}_{\delta t}$ be the continuous solutions to the Stokes problem of (2.1)-(2.2) at discrete point δt. Define the following discrete norms in a Hilbert space E,

$$\| \phi_{\delta t} \|_{l^2(E)} := \left(\delta t \sum_{k=0}^{N} \| \phi^k \|_E^2 \right)^{1/2} \approx \int_0^T \| \phi \|_E^2 \, \mathrm{d}t, \tag{2.69}$$

$$\| \phi_{\delta t} \|_{l^\infty(E)} := \max_{0 \le k \le N} (\| \phi^k \|_E). \tag{2.70}$$

The error estimate is given by E and Liu [30], Shen [108] and Guermond [41] as

$$\| \hat{\mathbf{u}}_{\delta t} - \mathbf{u}_{\delta t} \|_{l^2([L^2(\Omega)]^d)} + \| \hat{\mathbf{u}}_{\delta t} - \mathbf{u}^*_{\delta t} \|_{l^2([L^2(\Omega)]^d)} \;\lesssim\; (\delta t)^2, \tag{2.71}$$

$$\| \hat{p}_{\delta t} - p_{\delta t} \|_{l^\infty([L^2(\Omega)])} + \| \hat{\mathbf{u}}_{\delta t} - \mathbf{u}^*_{\delta t} \|_{l^\infty([H^1(\Omega)]^d)} \;\lesssim\; \delta t. \tag{2.72}$$

However, the artificial Neumann boundary condition

$$\nabla \delta p^{n+1} \cdot \mathbf{n}|_{\Gamma_W} = 0 \tag{2.73}$$

enforced on the pressure induces the numerical boundary layer and limits the accuracy of the scheme, an example will be given in the convergence test in time.

To overcome the problem of the boundary layer, Timmermans, Minev and Van De Vosse [120] (1996) proposed a modification to the correction step by adding a divergence term $\nu \nabla \cdot \mathbf{u}^*$ to the pressure difference, which is the so-called *rotational incremental pressure-correction scheme*. By doing so, a consistent boundary condition is obtained for the pressure. The convergence rate of the pressure is improved, it is of order $3/2$ in L^2-norm. For details of these projection methods, we refer to [42]. Please note that the influence of the viscosity ν and of the nonlinear convective term $\nabla \cdot (\mathbf{u} \otimes \mathbf{u})$ is not considered in the study [42].

Convergence test in time

We take the same test case as on p. 27 to test the convergence of the spatial discretization. Rectangular cells with sufficiently small mesh size $h = 1/320$ are used. The time step size of the BDF(2) scheme is in the range of $[5 \times 10^{-4}, 10^{-1}]$.
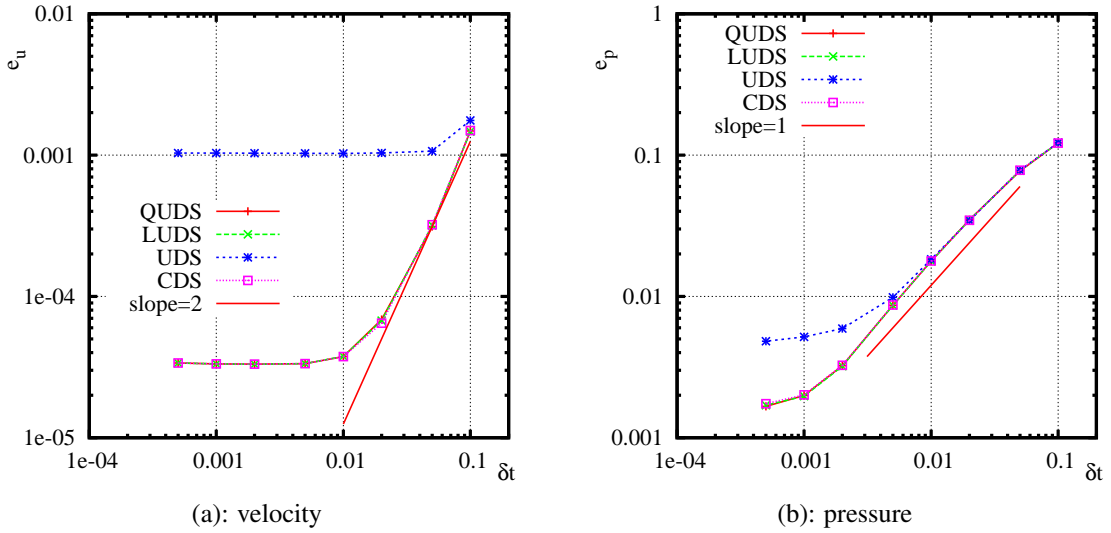
Figure 2.12: Errors in the L^2-norm at $v = 1.0$.
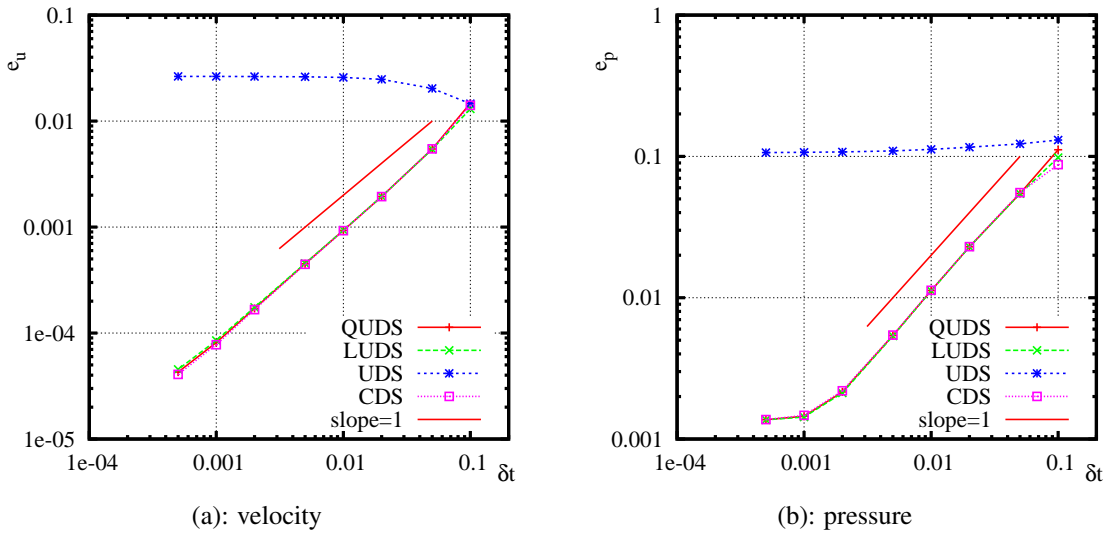
Figure 2.13: Errors in the L^2-norm at $v = 10^{-6}$.

(a): $\nu = 1.0$ (b): $\nu = 10^{-6}$
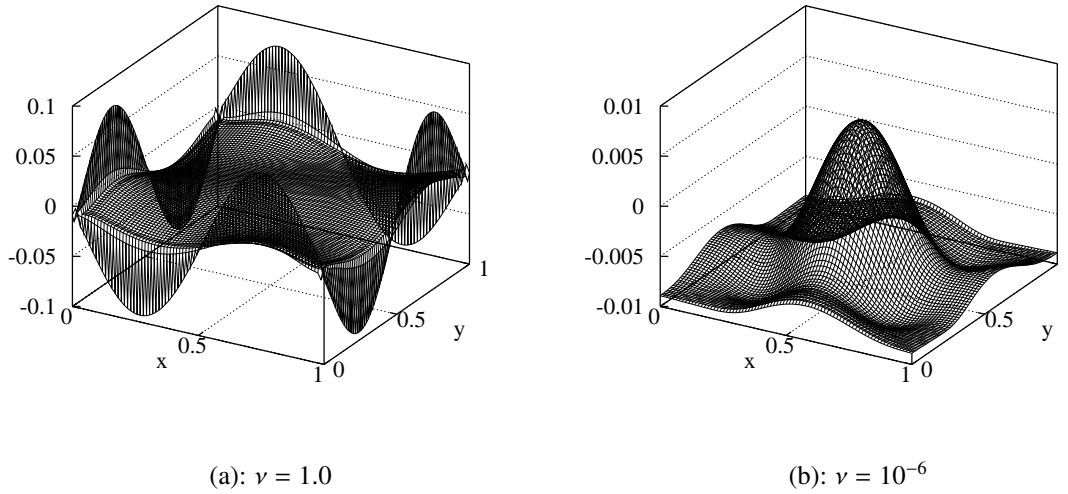
Figure 2.14: Pressure error field.

The same error estimate in the L^2-norm is used as in (2.48) at time $T = 1.0$. The errors e_u and e_p are reported in Fig. 2.12-2.13 for two different viscosities. For large viscosity $\nu = 1.0$, the velocities converge with second order at large time step sizes to a constant for QUDS, LUDS and CDS. The reason could be that the error in time reaches the spatial error at small time step sizes. There is no convergence for UDS except for the smallest time step. The pressure has first order convergence for all the four discretization schemes. For the small viscosity $\nu = 10^{-6}$, the rate of convergence of both velocity and pressure has first order for QUDS, LUDS and CDS. UDS does not give convergence for both velocity and pressure at all. Thus UDS is not acceptable for small ν. Furthermore, we can see obvious boundary layers for the pressure in Fig. 2.14 (left) for $\nu = 1.0$. It is well-known that the thickness of the boundary layer is of order $O(\nu^{1/2})$. So it disappears for small ν, see Fig. 2.14 (right).

2.3.3   Treatment of transport step

Combining the FVM (see Section 2.2) and the θ-scheme used in the projection system (2.61) within domain Ω with $\overline{\Omega} = \bigcup_{B_i \in \mathcal{B}} \overline{B}_i$ and applying Gauss' theorem to the convective term

35

and the viscous term, we get the weak form of the transport equation,

$$\sum_{B_i \in \mathcal{B}} \int_{B_i} \frac{\mathbf{u}_i^* - \mathbf{u}_i^n}{\delta t_n} \mathrm{d}x + \sum_{B_i \in \mathcal{B}} \int_{\partial B_i} (\theta \mathbf{u}_i^* \otimes \mathbf{u}_i^*) \cdot \mathbf{n}_i \mathrm{d}\sigma$$

$$+ \sum_{B_i \in \mathcal{B}} \int_{\partial B_i} ((1-\theta)\mathbf{u}_i^n \otimes \mathbf{u}_i^n) \cdot \mathbf{n}_i \mathrm{d}\sigma + \sum_{B_i \in \mathcal{B}} \int_{B_i} \nabla p_i^n \mathrm{d}x$$

$$- \sum_{B_i \in \mathcal{B}} \int_{\partial B_i} \nu \nabla (\theta \mathbf{u}_i^* + (1-\theta)\mathbf{u}_i^n) \cdot \mathbf{n}_i \mathrm{d}\sigma \quad = \quad \sum_{B_i \in \mathcal{B}} \int_{B_i} \mathbf{f}_i^n \mathrm{d}x, \qquad (2.74)$$

where ∂B_i denotes the surface of B_i and $\mathbf{n}_i$ is the unit outward normal vector.

To solve for the intermediate velocity $\mathbf{u}^*$, linearizing the convective term in momentum equation yields

$$\sum_{B_i \in \mathcal{B}} \int_{B_i} \frac{\mathbf{u}_i^* - \mathbf{u}_i^n}{\delta t_n} \mathrm{d}x + \sum_{B_i \in \mathcal{B}} \int_{\partial B_i} (\theta \mathbf{u}_i^* \otimes \mathbf{u}_i^n) \cdot \mathbf{n}_i \mathrm{d}\sigma$$

$$+ \sum_{B_i \in \mathcal{B}} \int_{\partial B_i} ((1-\theta)\mathbf{u}_i^n \otimes \mathbf{u}_i^n) \cdot \mathbf{n}_i \mathrm{d}\sigma + \sum_{B_i \in \mathcal{B}} \int_{B_i} \nabla p_i^n \mathrm{d}x$$

$$- \sum_{B_i \in \mathcal{B}} \int_{\partial B_i} \nu \nabla (\theta \mathbf{u}_i^* + (1-\theta)\mathbf{u}_i^n) \cdot \mathbf{n}_i \mathrm{d}\sigma \quad = \quad \sum_{B_i \in \mathcal{B}} \int_{B_i} \mathbf{f}_i^n \mathrm{d}x. \qquad (2.75)$$

The linearization holds for $\theta \in [0, 1]$. However, in order to get second order accuracy for the Crank-Nicolson method ($\theta = 1/2$), one should replace $\mathbf{u}_i^n \otimes \mathbf{u}_i^n$ in the third integral on the left hand side of (2.75) by $\mathbf{u}_i^n \otimes \mathbf{u}_i^*$. The fully discretized version of the transport step for the BDF(2)-variant can be derived in a similar way.

Due to the nonlinearity, (2.74) can not be solved directly. The only choice is to solve it iteratively. Iteration must be continued within each time step until a tolerance is reached, i.e., more than only one linearization cycle (2.75) should be performed. In the current DLR-THETA version used in this work, this iteration is not possible.

Without loss of generality the linearized discretized equations (2.75) in space with FVM are presented in coefficient form, which follows the terminology used in [32]. The discretized equations can be formulated as

$$A_P^{\mathbf{u}} \mathbf{u}_P^* + \sum_l A_l^{\mathbf{u}} \mathbf{u}_l^* = Q_{\mathbf{u}}^{n+1}. \qquad (2.76)$$

In equation (2.76) P denotes the index of an arbitrary node, l is the index of all neighbor points related to P. The source term $Q_{\mathbf{u}}^{n+1}$ contains all the other terms depending on $\mathbf{u}^n$ and p^n in (2.75).

(2.76) is a large linear algebraic system. In general, one can use iterative solution techniques to solve this kind of problems, for instance, Krylov type (e.g. GMRES) solvers with or without preconditioning. For details of Krylov type solvers we refer to Appendix B.1.

Since the pressure used in the iterations is obtained from the previous time step, the velocities $\mathbf{u}^*$ computed from (2.75) usually do not satisfy the continuity equation. To enforce the incompressibility, corrections to the velocities are needed. To this aim modifications of the pressure field are required. How to get a divergence free velocity by solving a pressure Poisson equation is described in the next section.

2.3.4 Treatment of projection step

Through the transport equation in Section 2.3.3, an intermediate velocity is obtained. Please keep in mind that the velocity, in general, does not satisfy the continuity equation

$$\nabla \cdot \mathbf{u}^* = 0. \tag{2.77}$$

To enforce the continuity, the projection step is performed to project the velocity $\mathbf{u}^*$ back to the set of divergence free fields. The pressure Poisson equation (2.62) is established for a pressure correction. The weak form of (2.62) is written as follows,

$$\sum_{B_i \in \mathcal{B}} \int_{\partial B_i} \nabla \delta p_i^{n+1} \cdot \mathbf{n}_i \mathrm{d}\sigma = \sum_{B_i \in \mathcal{B}} \int_{\partial B_i} \frac{\omega}{\delta t_n} \mathbf{u}_i^* \cdot \mathbf{n}_i \mathrm{d}\sigma, \tag{2.78}$$

where the pressure correction δp_i^{n+1} and the velocity can be updated in the domain,

$$
\begin{aligned}
p_i^{n+1} &= p_i^n + \delta p_i^{n+1}, & (2.79)\\
\mathbf{u}_i^{n+1} &= \mathbf{u}_i^* - \frac{\delta t_n}{\omega} \nabla \delta p_i^{n+1}, \quad \forall B_i \in \mathcal{B}. & (2.80)
\end{aligned}
$$

If δp^{n+1} is the solution of (2.78) then $\mathbf{u}^{n+1}$ is divergence free.

It turns out that the pressure shows often spurious oscillations when a collocated arrangement of the mesh is used. Here we will show for the one-dimensional case why the problem occurs. Recall the pressure Poisson equation at an arbitrary time step $n + 1$ in case of using the θ-scheme

$$\nabla \cdot \nabla \delta p^{n+1} = \frac{\omega}{\delta t_n} \nabla \cdot \mathbf{u}^*. \tag{2.81}$$

Please note that the Laplacian operator in the pressure equation is a product of the divergence and gradient operator. The former stems from the continuity equation, while the latter comes from the momentum equation. It is important that the consistency of the operators is maintained during numerical approximations.

For simplicity we denote $\tilde{p} := \delta p^{n+1}$ and constant $C := \frac{\omega}{\delta t_n}$. Assume the grid has uniform grid spacing h, (2.81) can be written as

$$\frac{\mathrm{d}}{\mathrm{d}x_i}\left(\frac{\mathrm{d}\tilde{p}}{\mathrm{d}x_i}\right) = C\frac{\mathrm{d}u_i^*}{\mathrm{d}x_i}. \tag{2.82}$$

As an example, we only consider difference schemes. First we take a forward difference scheme for the pressure term and a backward difference scheme for the velocity. Applying the backward difference scheme to the outer difference operator in (2.82), we obtain

$$\frac{\left(\frac{d\tilde{p}}{dx}\right)_i - \left(\frac{d\tilde{p}}{dx}\right)_{i-1}}{h} = \frac{C}{h}(u_i^* - u_{i-1}^*). \tag{2.83}$$

For the pressure derivative, we use a forward difference scheme,

$$\frac{\frac{\tilde{p}_{i+1}-\tilde{p}_i}{h} - \frac{\tilde{p}_i-\tilde{p}_{i-1}}{h}}{h} = \frac{C}{h}(u_i^* - u_{i-1}^*). \tag{2.84}$$

It is actually a central difference approximation since it is a product of the forward and backward difference approximation for the second derivative, i.e.,

$$\frac{\tilde{p}_{i+1} - 2\tilde{p}_i + \tilde{p}_{i-1}}{h^2} = \frac{C}{h}(u_i^* - u_{i-1}^*). \tag{2.85}$$

Now we consider a central difference approximation for both the divergence and the gradient operators. Approximating the outer and inner difference operator in (2.82) leads to

$$\frac{\frac{\tilde{p}_{i+2}-\tilde{p}_i}{2h} - \frac{\tilde{p}_i-\tilde{p}_{i-2}}{2h}}{2h} = \frac{C}{2h}(u_{i+1}^* - u_{i-1}^*). \tag{2.86}$$

The system can be reformulated as

$$\frac{\tilde{p}_{i+2} - 2\tilde{p}_i + \tilde{p}_{i-2}}{(2h)^2} = \frac{C}{2h}(u_{i+1}^* - u_{i-1}^*). \tag{2.87}$$

The equation (2.87) has the same form as equation (2.85) except that it involves nodes of spacing $2h$. It splits into two independent systems, one with even i and one with odd i. They give different solutions, so a checkboard pressure distribution could be produced. For an explanation in the two-dimensional case the reader is referred to [32].

The same problem may occur if the finite volume approach is used to calculate the fluxes across a CV face by linear interpolation of the two neighbor nodes. Thus, stabilization is necessary for the pressure Poisson equation. Therefore, a stabilization term developed by Rhie and Chow [102] is introduced into the pressure Poisson equation (PPE) (2.62). The new PPE is written as follows

$$\nabla \cdot \nabla \delta p^{n+1} + S(p^{n+1}) = \frac{\omega}{\delta t_n}\nabla \cdot \mathbf{u}^* + S(p^n), \tag{2.88}$$

where $S(p^n)$ and $S(p^{n+1})$ possess the same form. They are treated explicitly with p^n and implicitly with p^{n+1}, respectively.

The stabilization terms in Eq. (2.88) are formulated with the difference between the interpolated pressure gradient and the gradient calculated at the cell faces. They have the following general form at the face S_{ij} between node P_i and node P_j (see Fig. 2.7),

$$S|_{S_{ij}} = \frac{1}{l_n}\left[(p_j - p_i) - \frac{\nabla p|_i + \nabla p|_j}{2} \cdot \mathbf{l}_{ij}\right]. \tag{2.89}$$

Here $\mathbf{l}_{ij}$ is the vector pointing from P_i to P_j, $l_n = \mathbf{n} \cdot \mathbf{l}_{ij}$ with unit outward normal vector $\mathbf{n}$ on interface S_{ij}.

Let us give an explanation of the impact of the pressure stabilization for the one-dimensional case by using a Taylor expansion of the pressure at $x = x_i$ and $x = x_j = x_i + \Delta x$,

$$p_j \quad = \quad p_i + p'_i(x_j - x_i) + \frac{1}{2}p''|_i(x_j - x_i)^2 + O(\Delta x^3), \tag{2.90}$$

$$p_i \quad = \quad p_j + p'_j(x_i - x_j) + \frac{1}{2}p''|_j(x_i - x_j)^2 + O(\Delta x^3), \tag{2.91}$$

$$p''|_j \quad = \quad p''|_i + p'''|_i(x_j - x_i) + O(\Delta x^2). \tag{2.92}$$

Subtracting (2.90) by (2.91) and moving the pressure and first derivative terms to the left hand side lead to

$$p_j - p_i - \frac{1}{2}(p'_i + p'_j)\Delta x = \frac{1}{4}(p''|_i - p''|_j)\Delta x^2 + O(\Delta x^3). \tag{2.93}$$

For the one-dimensional case, $l_n = \Delta x$. By inserting (2.92) into (2.93), we obtain

$$S|_{S_{ij}} = -\frac{1}{4}p'''|_i\Delta x^2 + o(\Delta x^2). \tag{2.94}$$

The stabilization term (2.94) is proportional to the third derivative of the pressure. It vanishes when the pressure is a linear or quadratic function. If the pressure oscillates rapidly the third derivative is large. Then the pressure stabilization term will activate and smooth out the pressure.

The PPE leads to a large, linear and symmetric algebraic system. Within the DLR-THETA-code, one can use Krylov type solvers or multigrid solvers. Due to the symmetry of the algebraic problem, multigrid is the preferred method. If the multigrid method is switched on, the iterative solver is only used on the coarsest grid. For details of the multigrid method, we refer to Appendix B.2.

The pressure Poisson equation is treated in the DLR-THETA-code with the following pseudo-code.

---
solver_ mg() in lin_ mg_ solver.c

- compute_ ax()

- FOR(step = 0; step < nsteps; step++)

    - IF(mode > 0), go down to the next coarser gird
        * Jacobi pre-smoothing
        * var_ data = var_ data − > succ

  * dgrid = dgrid − > succ
  ⇒ restrict_ residuals()

– ELSE IF(mode < 0), go up to the next finer grid

  ⇒ prolong_ correction()
  * var_ data = var_ data − > pred
  * dgrid = dgrid − > pred
  * Jacobi post-smoothing

– ELSE, solve exactly on the coarsest grid

  * lin_ solver.c (BCGS, GMRES, JACOBI, CG)

2.3.5   Control flow of the DLR-THETA-code

Finally, let us briefly show how the solution of the projection method for the nonstationary Navier-Stokes equations is organized within the DLR-THETA-code.

The Navier-Stokes equations are solved within inner iterations and outer iterations. The time stepping is performed within the outer iterations of the DLR-THETA-code. For each time step the inner iteration is called, where the momentum and pressure Poisson equations are solved in space. The control flow is as follows:

| control flow of the DLR-THETA-code |

- **Physical time steps: FOR** $\tau = 1, \ldots, T =n\_ timestep$ **DO**
  (do_ timeintegration() in time_integration.c)

    - **Inner iterations: FOR** $i = 1, \ldots, I =n\_ inner\_ loop$ **DO**

        · Solve momentum equation ⇒ Solve (*velocity*)
            * explicit fluxes are computed and added to the flux
              (flux.c and eqn_momentum.c)
            * implicit fluxes are calculated and summed up
              (flux.c and eqn_momentum.c)
        · Projection step ⇒ Solve (*pressure gradient*)
        · Update pressure and velocity
    - **ENDDO**

- **ENDDO**

Chapter 3

Turbulence modeling

When the Reynolds number Re is increased to a critical number, the system (2.1)-(2.2) becomes a turbulent problem. The solution to the turbulent flows is three-dimensional, time-dependent and random-like. Furthermore, there is a large range of timescales and lengthscales. Regarding to the largest scales, the smallest timescale (i.e. Kolmogorov scale) decreases as $Re^{-1/2}$, and the smallest lengthscale as $Re^{-3/4}$.

A direct numerical simulation (DNS) would exceed the capacity of our computer power. For the three approaches we consider in this work, the Reynolds averaged Navier-Stokes (RANS) model, large eddy simulation (LES) and hybrid LES/RANS methods, turbulence models are needed. The RANS model is a method which solves the mean momentum equation (also denoted as Reynolds equation) for the mean velocity field, all scales are modeled. In LES, the large scales are resolved and the influence of the small scales are modeled into the large scales. In hybrid LES/RANS methods, the solution flow is separated into a RANS-like in the boundary layer region and an LES-like in the separated flow region according to the turbulent length scale.

3.1 Scale separation

As mentioned before, it is out of our computer capacity to solve all the scales with DNS. Some methods have been developed to reduce the cost of the simulation of turbulent flows. The main idea is to use a scale separation operator to separate the scales of interest (resolved scales) from others (unresolved scales) and to compute only the resolved scales in the simulation. The averaging and filtering approaches are the two main scale separation methods, cf. Chapter 2 of [106].

In general, a scale separation operator $\mathcal{T}$ is applied to a variable $\phi(\mathbf{x}, t)$ with time t and space coordinate $\mathbf{x}$. The following decomposition is obtained

$$\phi = \bar{\phi} + \phi', \tag{3.1}$$

where $\bar{\phi} = \mathcal{T}(\phi)$ is the resolved part of ϕ, and ϕ' denotes the unresolved part. In this work, the variable ϕ represents the velocity field $\mathbf{u}$ and the pressure p.

We require that the scale separation operator has the important properties that it is linear and that operator and differentiation commute. More precisely, the following assumptions should be valid:

Assumption 3.0.1 *The scale separation operater $\mathcal{T}$ has the following properties*

$$\textit{Linearity}: \qquad \overline{c\phi + \psi} = c\bar{\phi} + \bar{\psi}, \quad c \in \mathbb{R}$$

$$\textit{Commutativity with differentiation w.r.t. } x_j: \qquad \overline{\frac{\partial \phi}{\partial x_j}} = \frac{\partial}{\partial x_j} \bar{\phi}$$

$$\textit{Commutativity with differentiation w.r.t. } t: \qquad \overline{\frac{\partial \phi}{\partial t}} = \frac{\partial}{\partial t} \bar{\phi}$$

$$\textit{Projection identity}: \qquad \bar{\bar{\phi}} = \bar{\phi}$$

The property of projection identity implies that application of the operator to the unresolved part is zero, i.e., $\overline{\phi'} = 0$.

In general, there is no commutativity with respect to the nonlinear terms. In particular, applying the operator to a product we have

$$
\begin{aligned}
\overline{\phi\psi} &= \overline{(\bar{\phi} + \phi')(\bar{\psi} + \psi')} \\
&= \overline{\bar{\phi}\bar{\psi} + \phi'\bar{\psi} + \bar{\phi}\psi' + \phi'\psi'} \\
&= \bar{\phi}\bar{\psi} + \overline{\phi'\psi'}.
\end{aligned}
\tag{3.2}
$$

The last term is zero only if the two quantities ϕ and ψ are uncorrelated, i.e., the correlation of these two is zero. The definition of the two-point correlation is referred to Section 4.2. Furthermore, the root mean square (rms) of the velocity $\mathbf{u} = (u, v, w)^{\mathrm{T}}$ for three-dimensional problem is defined as

$$u_{rms} = \sqrt{\frac{1}{3}(\overline{u'u'} + \overline{v'v'} + \overline{w'w'})}.
\tag{3.3}$$

3.2 The Reynolds averaged Navier-Stokes model

In RANS models, a statistical procedure is employed as the scale separation operator to resolve an averaged turbulent motion. In comparison with DNS, the cost of computation with RANS is reduced significantly.

The Reynolds equation is obtained by taking the mean of the momentum equation. To solve the mean velocity, the Reynolds stress is modeled by the turbulent viscosity model, where the eddy-viscosity can be obtained from turbulent quantities such as k, ω or $\tilde{\nu}$, which satisfy transport equations. Models of approximating the eddy-viscosity by two turbulent quantities,

which are solved from two scalar equations respectively, are called two-equation models, e.g. $k - \epsilon$ model and $k - \omega$ model. The Spalart-Allmaras is a one-equation model, which uses only one turbulent quantity to simulate the eddy-viscosity.

3.2.1 Statistical averaging

For an ensemble of N identical flow experiments with initial and boundary conditions that differ by random infinitesimal perturbations, the random velocity and pressure can be decomposed into a mean component and a turbulent fluctuation component via Reynolds decomposition,

$$\mathbf{u} = \langle \, \mathbf{u} \, \rangle + \mathbf{u}', \qquad p = \langle \, p \, \rangle + p', \tag{3.4}$$

here $\langle \, \cdot \, \rangle$ denotes the averaging filter as defined in the following:

Definition 3.1 *The ensemble averaging filter over an ensemble of N flow experiments is defined by*

$$\langle \, \mathbf{u} \, \rangle_N \;\; = \;\; \frac{1}{N} \sum_{i=1}^{N} \mathbf{u}^{(i)}(x, y, z, t).$$

Therein, denote $\mathbf{u}^{(i)}$ the solution of the ith flow experiment where the inflow boundary conditions U_{in} and the shape of the boundary Γ_{in} are disturbed by small changes which are random with a probability function which is independent and identically distributed.
The time averaging filter $\langle \, \cdot \, \rangle_{(t, t+\Delta t)}$ over the interval $(t, t + \Delta t)$ is defined by

$$\langle \, \mathbf{u} \, \rangle_{(t, t+\Delta t)}(x, y, z) \;\; = \;\; \frac{1}{\Delta t} \int_{t}^{t+\Delta t} \mathbf{u}(x, y, z, s) \, \mathrm{d}s.$$

The space averaging filter, e.g. in the homogeneous z-coordinate direction over the interval $(z, z + \Delta z)$ is given by

$$\langle \, \mathbf{u} \, \rangle_{(z, z+\Delta z)}(x, y, t) \;\; = \;\; \frac{1}{\Delta z} \int_{z}^{z+\Delta z} \mathbf{u}(x, y, r, t) \, \mathrm{d}r.$$

Remark 3.2 *The ensemble averaging concept is only of theoretical interest: It would require to setup a large number of N very similar flow experiments, or to run a numerical simulation on N workstations with randomly perturbed inflow conditions.*
On the other hand, the concept of time-averaging and space-averaging (over homogeneous flow directions) allows to consider only one flow experiment (or simulation).

3.2.2 The RANS equations

Applying the ensemble averaging operator to the governing equations (1.1)-(1.2) of the incompressible flows yields the so-called Reynolds Averaged Navier-Stokes equations (RANS

equations) as follows,

$$\langle\,\partial_t\mathbf{u}\,\rangle + \langle\,\nabla\cdot(\mathbf{u}\otimes\mathbf{u})\,\rangle + \langle\,\nabla p\,\rangle - \langle\,\nabla\cdot(2\nu\mathbb{S}(\mathbf{u}))\,\rangle \;=\; \langle\,\mathbf{f}\,\rangle, \tag{3.5}$$

$$\langle\,\nabla\cdot\mathbf{u}\,\rangle \;=\; 0. \tag{3.6}$$

Using the commutativity w.r.t. the space and the non-commutativity w.r.t. the nonlinear expression (3.2) of the operator, the nonlinear term can be written as

$$\langle\,\nabla\cdot(\mathbf{u}\otimes\mathbf{u})\,\rangle = \nabla\cdot\langle\,\mathbf{u}\otimes\mathbf{u}\,\rangle = \nabla\cdot(\langle\,\mathbf{u}\,\rangle\otimes\langle\,\mathbf{u}\,\rangle) + \nabla\cdot\langle\,\mathbf{u}'\otimes\mathbf{u}'\,\rangle. \tag{3.7}$$

It is sufficient to have $\mathbf{f} = \langle\,\mathbf{f}\,\rangle$ and we define the mean velocity and pressure as $\mathbf{U} = \langle\,\mathbf{u}\,\rangle$ and $P = \langle\,p\,\rangle$. Since the other terms are linear, the RANS equations read

$$\partial_t\mathbf{U} + \nabla\cdot(\mathbf{U}\otimes\mathbf{U}) + \nabla P - \nabla\cdot(2\nu\mathbb{S}(\mathbf{U}) - \langle\,\mathbf{u}'\otimes\mathbf{u}'\,\rangle) \;=\; \mathbf{f}, \tag{3.8}$$

$$\nabla\cdot\mathbf{U} \;=\; 0, \tag{3.9}$$

with Reynolds rate of strain tensor

$$\mathbb{S}(\mathbf{U}) = \frac{\nabla\mathbf{U} + \nabla\mathbf{U}^{\mathrm{T}}}{2}. \tag{3.10}$$

The Reynolds stress tensor is defined as

$$\tau = \langle\,\mathbf{u}'\otimes\mathbf{u}'\,\rangle. \tag{3.11}$$

For a general three-dimensional flow, there are four independent equations governing the mean velocity and mean pressure. However, these four equations contain more than four unknowns. In addition to $\mathbf{U}$ and P (four unknowns), there are also six independent components for the symmetric Reynolds stress tensor. These equations are unclosed, that is, they cannot be solved unless the Reynolds stresses are somehow determined in terms of $\mathbf{U}$ and P.

To close the problem, we must specify the Reynolds stress. Boussinesq proposed a so-called *turbulent-viscosity hypothesis* or *eddy-viscosity hypothesis* which assumes that

$$\tau = -2\nu_t\mathbb{S}(\mathbf{U}) + \frac{2}{3}kI, \tag{3.12}$$

where ν_t is the *turbulent-viscosity* or *eddy-viscosity*. The last term $\frac{2}{3}kI$ ensures the trace of τ to be correct for the incompressible flows. k is the turbulent kinetic energy per unit mass, defined as

$$k = \frac{1}{2}\langle\,\mathbf{u}'\cdot\mathbf{u}'\,\rangle = \frac{1}{2}\sum_{i=1}^{d}\langle\,u_i'u_i'\,\rangle. \tag{3.13}$$

We introduce the effective viscosity ν_e to be

$$\nu_e = \nu + \nu_t. \tag{3.14}$$

Using (3.12) and (3.14), the RANS equations can be rewritten as

$$\partial_t \mathbf{U} + \nabla \cdot (\mathbf{U} \otimes \mathbf{U}) + \nabla(P + \frac{2}{3}k) - \nabla \cdot (2\nu_e \mathbb{S}(\mathbf{U})) = \mathbf{f}, \tag{3.15}$$

$$\nabla \cdot \mathbf{U} = 0. \tag{3.16}$$

There are two possibilities to treat the term $\frac{2}{3}\nabla k$ arising in (3.15). It can be absorbed by the pressure gradient term or by the source term at the right hand side

$$P^* = P + \frac{2}{3}k, \qquad \text{or} \qquad \mathbf{f}^* = \mathbf{f} - \frac{2}{3}k. \tag{3.17}$$

3.2.3 The Spalart-Allmaras model

The Spalart-Allmaras one-equation model (see [113]) uses only one equation of the viscosity $\tilde{\nu}$ to compute the eddy-viscosity directly from

$$\nu_t = \tilde{\nu} f_{v1}, \qquad f_{v1} = \frac{\chi^3}{\chi^3 + c_{v1}^3}, \qquad \chi = \frac{\tilde{\nu}}{\nu}. \tag{3.18}$$

Here ν is the kinematic viscosity. $\tilde{\nu}$ satisfies the following transport equation,

$$\partial_t \tilde{\nu} + (\mathbf{U} \cdot \nabla)\tilde{\nu} - \nabla \cdot \left(\frac{\nu + \tilde{\nu}}{\sigma} \nabla \tilde{\nu}\right) - \frac{c_{b2}}{\sigma} \nabla \tilde{\nu} \cdot \nabla \tilde{\nu} = P_\nu - \epsilon_\nu, \tag{3.19}$$

where the production term P_ν and destruction term ϵ_ν are defined as

$$P_\nu = c_{b1} \tilde{S} \tilde{\nu}, \qquad \epsilon_\nu = c_{w1} f_w \left(\frac{\tilde{\nu}}{d}\right)^2, \tag{3.20}$$

with the wall distance d and

$$\tilde{S} = \Omega + \frac{\tilde{\nu}}{\kappa^2 d^2} f_{v2}, \qquad f_{v2} = 1 - \frac{\chi}{1 + \chi f_{v1}}. \tag{3.21}$$

Here Ω is the magnitude of the vorticity defined as follows

$$\Omega = \sqrt{2\Omega(\mathbf{U}) : \Omega(\mathbf{U})}, \qquad \Omega(\mathbf{U}) = \frac{\nabla \mathbf{U} - \nabla \mathbf{U}^T}{2}. \tag{3.22}$$

The function f_w (see Fig. 3.1) is given by

$$f_w = g \left(\frac{1 + c_{w3}^6}{g^6 + c_{w3}^6}\right)^{1/6}, \qquad g = r + c_{w2}(r^6 - r), \qquad r = \frac{\tilde{\nu}}{\tilde{S} \kappa^2 d^2}. \tag{3.23}$$

The constants are

$$c_{b1} = 0.1355, \quad \sigma = 2/3, \quad c_{b2} = 0.622, \quad \kappa = 0.41,$$
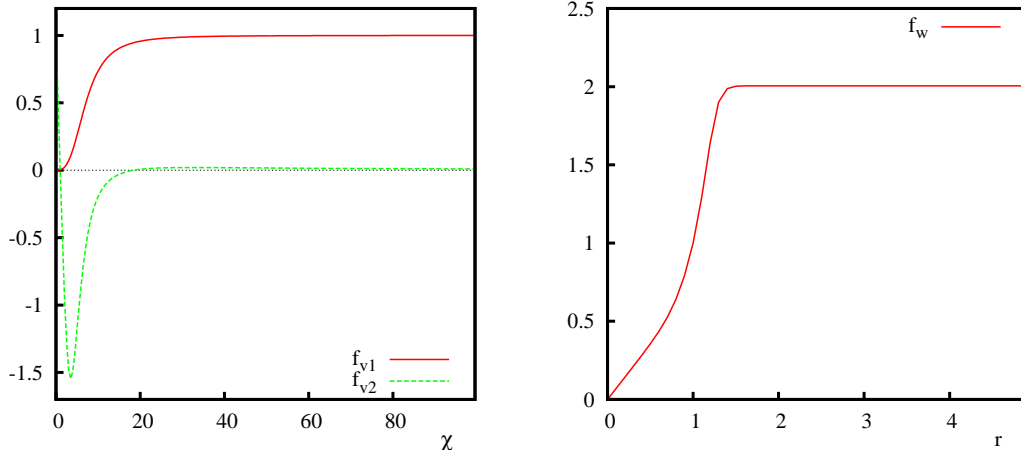
Figure 3.1: Sketch of f_{v1}, f_{v2} and f_w in the Spalart-Allmaras model.

$$c_{w1} = \frac{c_{b1}}{\kappa^2} + \frac{1 + c_{b2}}{\sigma}, \quad c_{w2} = 0.3, \quad c_{w3} = 2.0, \quad c_{v1} = 7.1.$$

This is the standard Spalart-Allmaras model in the RANS framework. Edwards and Chandra [31] proposed a modification regarding the near-wall behavior. The new formulations are given by

$$\tilde{S} = \left(\frac{1}{\chi} + f_{v1} \right) \sqrt{2\mathbb{S}(\mathbf{U}) : \nabla\mathbf{U} - \frac{2}{3}(\nabla \cdot \mathbf{U})^2}, \tag{3.24}$$

$$r = \tanh\left(\frac{\tilde{\nu}}{\max(\tilde{S}, 10^{-12})\kappa^2 d^2} \right) / \tanh(1.0), \tag{3.25}$$

to avoid negative values of $\tilde{S}$ and to make the computations more stable. Moreover, we limit $\chi = \max(\tilde{\nu}/\nu, 10^{-12})$ for numerical reasons. Later we will introduce a modified Spalart-Allmaras model for the detached-eddy simulation approach.

3.2.4 The $k - \omega$ model

The Wilcox $k - \omega$ model

If the Wilcox $k - \omega$ model (see [129]) is employed to close the problem (3.15)-(3.16), the turbulent viscosity is related to the production of turbulent kinetic energy k and dissipation per unit turbulent kinetic energy ω through the following expression,

$$\nu_t = \frac{k}{\omega}. \tag{3.26}$$

Here k and ω are determined from the two coordinate-invariant semi-empirical transport equations,

$$\partial_t k + (\mathbf{U} \cdot \nabla)k - \nabla \cdot (\nu_k \nabla k) = P_k - \beta_k k\omega, \tag{3.27}$$

$$\partial_t \omega + (\mathbf{U} \cdot \nabla)\omega - \nabla \cdot (\nu_\omega \nabla \omega) = \frac{\gamma}{\nu_t} P - \beta_\omega \omega^2, \tag{3.28}$$

with viscosities

$$\nu_k = \nu + \nu_t \sigma_k, \qquad \nu_\omega = \nu + \nu_t \sigma_\omega, \tag{3.29}$$

and production rate P_k of turbulent energy given by

$$P_k = 2\nu_t \mathbb{S}(\mathbf{U}) : \mathbb{S}(\mathbf{U}). \tag{3.30}$$

Different variants of the above model arise from different approaches to determine the model coefficients σ_k, σ_ω, γ and β_ω. For the standard Wilcox $k - \omega$ model [128] the constants have the following values

$$\sigma_k = 0.5, \quad \sigma_\omega = 0.5, \quad \gamma = 0.55555556, \quad \beta_\omega = 0.07521. \tag{3.31}$$

To this end, the system of equations for $\mathbf{U}$, P, k, ω and ν_t reads

$$\partial_t \mathbf{U} + \nabla \cdot (\mathbf{U} \otimes \mathbf{U}) + \nabla P - \nabla \cdot (2\nu_e \mathbb{S}(\mathbf{U})) = \mathbf{f}, \tag{3.32}$$

$$\nabla \cdot \mathbf{U} = 0, \tag{3.33}$$

$$\partial_t k + (\mathbf{U} \cdot \nabla)k - \nabla \cdot (\nu_k \nabla k) = P_k - \beta_k k\omega, \tag{3.34}$$

$$\partial_t \omega + (\mathbf{U} \cdot \nabla)\omega - \nabla \cdot (\nu_\omega \nabla \omega) = \frac{\gamma}{\nu_t} P - \beta_\omega \omega^2, \tag{3.35}$$

$$\nu_t = \frac{k}{\omega}. \tag{3.36}$$

The algorithm for solving this system can be done in three steps:

- for a given starting value ν_t, solve (3.32) and (3.33) for $\mathbf{U}$ and P with the projection method (Section 2.3.4),

- solve the two coupled scalar equations (3.34) and (3.35) for k and ω,

- update ν_t using (3.36) and repeat the three steps until the tolerance is reached.

Another well-known two-equation model is the $k - \epsilon$ model (see, for instance [86]). This model requires modification in order to apply it to the viscous near-wall region. One modification is to use wall functions, cf. [86, 96], which rely on the existence of a logarithmic region in the velocity profile.

As compared to the $k - \epsilon$ model, the $k - \omega$ model is superior in its treatment of the viscous near-wall region and also doing better in dealing with the effects of the streamwise pressure gradients. It does not need any wall damping functions, thus there is no need of wall distance calculation. However, the drawback of this model is that the results depend on the free-stream value of the turbulence variables, in particular of ω, see [68].

The Menter SST model

Menter [84] proposed a blending function of the Wilcox $k - \omega$ model in boundary layer and the standard $k - \epsilon$ model in the outer part of the boundary layer. The modified transport equations for k and ω are

$$\partial_t k + (\mathbf{U} \cdot \nabla)k - \nabla \cdot (\nu_k \nabla k) = P_k - \beta_k k\omega, \tag{3.37}$$

$$\partial_t \omega + (\mathbf{U} \cdot \nabla)\omega - \nabla \cdot (\nu_\omega \nabla \omega) = \frac{\gamma}{\nu_t}P - \beta_\omega \omega^2 + 2(1 - F_1)\frac{\sigma_{\omega 2}}{\omega}\nabla k \cdot \nabla \omega. \tag{3.38}$$

The last term in the right hand side of (3.38) did not appear in (3.27)-(3.28). It is the so-called *cross-diffusion* term, which acts as a switch from $k - \omega$ to $k - \epsilon$. The coefficients $\phi \in \{\sigma_k, \sigma_\omega, \gamma, \beta_k\}$ are defined by a blending formula

$$\phi = F_1 \phi_1 + (1 - F_1)\phi_2, \tag{3.39}$$

where ϕ_1 are coefficients at inner layer from $k - \omega$ model and ϕ_2 at outer layer from $k - \epsilon$ model given by

Inner layer: $\quad \sigma_{k1} = 0.85, \quad \sigma_{\omega 1} = 0.5, \quad \gamma_1 = 0.555556, \quad \beta_{\omega 1} = \beta_k\left(\gamma_1 + \frac{\sigma_{\omega 1}\kappa^2}{\sqrt{\beta_k}}\right),$

Outer layer: $\quad \sigma_{k2} = 1.0, \quad \sigma_{\omega 2} = 0.857, \quad \gamma_2 = 0.44, \quad \beta_{\omega 2} = \beta_k\left(\gamma_2 + \frac{\sigma_{\omega 2}\kappa^2}{\sqrt{\beta_k}}\right),$

with $\kappa = 0.41, \beta_k = 0.09$ and the blending function F_1 (see Fig. 3.2) is given by
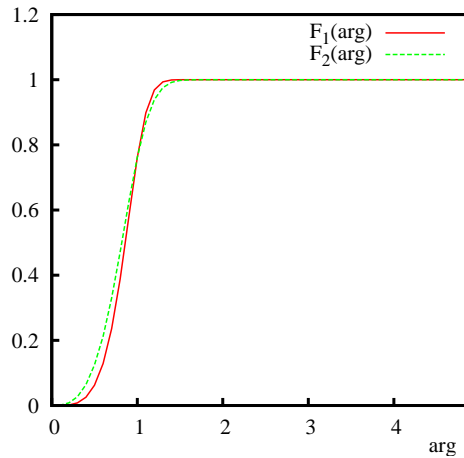
Figure 3.2: Sketch of the blending functions in the Menter SST model.

$$F_1 = \tanh(arg_1^4), \quad arg_1 = \min\left(\max\left(\frac{\sqrt{k}}{\beta_k\omega d}, \frac{500\nu}{d^2\omega}\right), \frac{4\sigma_{\omega 2}k}{CD_{k\omega}d^2}\right),$$

$$CD_{k\omega} = \max\left(2\frac{\sigma_{\omega 2}}{\omega}\nabla k \cdot \nabla \omega, 10^{-20}\right).$$

The eddy-viscosity is computed from the shear-stress correction

$$\nu_t = \min\left(\frac{k}{\omega}, \frac{a_1 k}{\Omega F_2}\right),\tag{3.40}$$

with

$$F_2 = \tanh(arg_2^2), \quad arg_2 = \max\left(\frac{2\sqrt{k}}{\beta_k \omega d}, \frac{500\nu}{d^2\omega}\right),$$

and the vorticity

$$\Omega = \sqrt{2\Omega(\mathbf{U}) : \Omega(\mathbf{U})}, \qquad \Omega(\mathbf{U}) = \frac{\nabla \mathbf{U} - \nabla \mathbf{U}^{\mathrm{T}}}{2}.\tag{3.41}$$

Here $a_1 = 0.31$ is the Bradshaw constant. In this model, the wall distance d is required.

3.3 LES model

Different from RANS, a filter is used in LES as the scale separation operator to filter out the small scales. The effect of the small scales on the large scales is modeled and only large scales are resolved. In this section the classical Smagorinsky model is introduced.

3.3.1 Filtering

In LES a low-pass spatial filtering operator is performed to separate the scales into filtered scales, which can be adequately resolved on a relatively coarse grid, and residual components (or subgrid-scales, SGS). The general filtering operation (introduced by Leonard (1974)) is represented in the physical space as a convolution integral. The filtered part $\bar{\phi}(\mathbf{x}, t)$ of a space-time variable $\phi(\mathbf{x}, t)$ is defined as

$$\bar{\phi}(\mathbf{x}, t) = \int G_\Delta(\mathbf{r}, \mathbf{x})\phi(\mathbf{x} - \mathbf{r}, t)d\mathbf{r},\tag{3.42}$$

where integration is over the entire flow domain. $G_\Delta(\mathbf{r}, \mathbf{x})$ is a filter kernel which is associated with the filter width Δ. The filter function satisfies the normalization condition

$$\int G_\Delta(\mathbf{r}, \mathbf{x})d\mathbf{r} = 1.\tag{3.43}$$

This convolution is denoted symbolically by

$$\bar{\phi} = G_\Delta * \phi.\tag{3.44}$$

49

Then variables, e.g. the velocity and pressure, can be decomposed into a filtered part and a residual part, i.e.,

$$\mathbf{u}(\mathbf{x}, t) = \bar{\mathbf{u}}(\mathbf{x}, t) + \mathbf{u}'(\mathbf{x}, t), \tag{3.45}$$

$$p(\mathbf{x}, t) = \bar{p}(\mathbf{x}, t) + p'(\mathbf{x}, t). \tag{3.46}$$

We assume the filtering possesses the properties in Assumption 3.0.1. However, the commutation property does not hold when the wall is approaching in the wall-bounded turbulent flow. For analysis of the commutation error we refer to [56].

Three filters are often used in LES for performing the spatial scale separation, cf. [96]. In the one-dimensional case, the convolution kernel $G_\Delta(r)$ and the corresponding transfer function $\hat{G}_\Delta(\kappa)$ (see Fig. 3.3) are:

- box filter:

$$G_\Delta(x, r) = \begin{cases} \frac{1}{\Delta}, & \text{if } | r | \leq \frac{\Delta}{2} \\ 0, & \text{otherwise} \end{cases}, \quad \hat{G}_\Delta(\kappa) = \frac{\sin(\kappa\Delta/2)}{\kappa\Delta/2},$$

- Gaussian filter:

$$G_\Delta(x, r) = (\frac{\gamma}{\pi\Delta^2})^{1/2} \exp(\frac{-\gamma | r |^2}{\Delta^2}), \quad \hat{G}_\Delta(\kappa) = \exp(\frac{-\Delta^2\kappa^2}{4\gamma}), \quad \gamma = 6,$$

- sharp cutoff filter:

$$G_\Delta(x, r) = \frac{\sin(\pi r/\Delta)}{\pi r}, \quad \hat{G}_\Delta(\kappa) = \begin{cases} 1, & \text{if } \kappa \leq \pi/\Delta \\ 0, & \text{otherwise} \end{cases}.$$
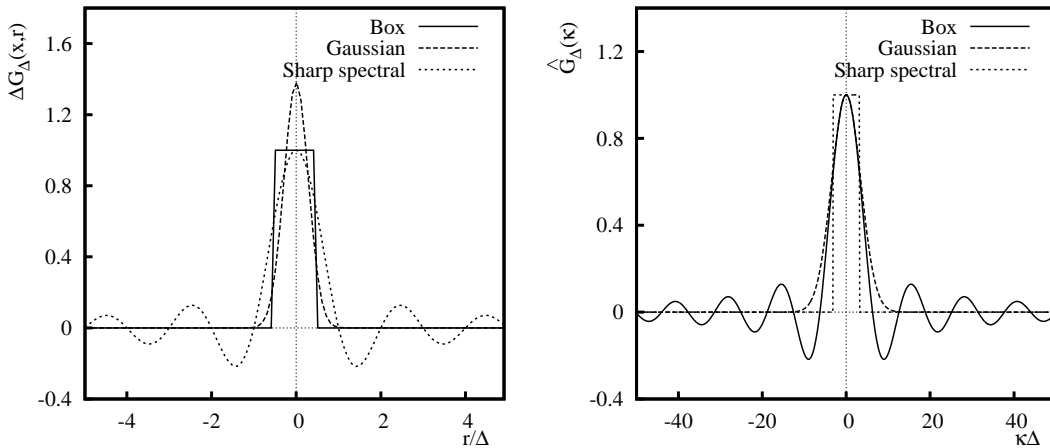
Figure 3.3: Filters $G_\Delta(\frac{r}{\Delta})$ and filter transfer functions $\hat{G}_\Delta(\kappa)$.

3.3.2 The Smagorinsky model

A classical SGS model is proposed by Smagorinsky (1963) [110]. Applying the filtering to the incompressible Navier-Stokes equation and using the property of the filtering, we obtain

$$\partial_t \bar{\mathbf{u}} + \nabla \cdot (\bar{\mathbf{u}} \otimes \bar{\mathbf{u}}) + \nabla \bar{p} - \nabla \cdot \left(2\nu \mathbb{S}(\bar{\mathbf{u}}) - \overline{\mathbf{u}' \otimes \mathbf{u}'} \right) = \mathbf{f}, \tag{3.47}$$
$$\nabla \cdot \bar{\mathbf{u}} = 0. \tag{3.48}$$

Using the turbulent-viscosity hypothesis (3.12), the SGS stress tensor is approximated by

$$\tau := \overline{\mathbf{u}' \otimes \mathbf{u}'} = -2\nu_t \mathbb{S}(\bar{\mathbf{u}}). \tag{3.49}$$

Then the filtered Navier-Stokes equation is written as

$$\partial_t \bar{\mathbf{u}} + \nabla \cdot (\bar{\mathbf{u}} \otimes \bar{\mathbf{u}}) + \nabla \bar{p} - \nabla \cdot (2(\nu + \nu_t)\mathbb{S}(\bar{\mathbf{u}})) = \mathbf{f}, \tag{3.50}$$
$$\nabla \cdot \bar{\mathbf{u}} = 0, \tag{3.51}$$

whereas, the eddy-viscosity is given by

$$\nu_t = l_S^2 |S| = (C_S \Delta)^2 |S|, \tag{3.52}$$

with $|S| = (2\mathbb{S}(\mathbf{U}) : \mathbb{S}(\mathbf{U}))^{1/2}$ the characteristic filtered rate of strain. l_S is the Smagorinsky lengthscale which is proportional to the filter width Δ through the Smagorinsky constant C_S. It should be noted that the value of the constant C_S can be problem dependent. Lilly [75] gave an approximation $C_S = 0.17$ by assuming an inertial-range Kolmogorov spectrum for isotropic turbulence. This value has turned out to be too large for most flows so that often smaller values are used, e.g., Deardorff [25] uses $C_S = 0.1$ for a plane channel flow.

Δ is often taken as the cubic root of the cell volumes, $\Delta = V_c^{1/3}$ with V_c being the volume of control volumes. In the paper by Travin *et al.* [122], they define a new subgrid length scale Δ, which depends not only on Δx, Δy and Δz, but also on the wall distance d. Set the maximum local grid spacing

$$\Delta_{max} = \max\{\Delta x, \Delta y, \Delta z\}. \tag{3.53}$$

Away from the wall, the grid is quite isotropic, Δ is bounded from above by Δ_{max}. In the near-wall region, the behavior of Δ should not follow the radical decreasing of the wall normal mesh size, so it limits to the wall distance d. To fit these two limits, Δ is defined as a function of d and Δ_{max} by

$$\Delta = \Delta_T := \min\{\max[C_w d, C_w \Delta_{max}, \Delta_{wn}], \Delta_{max}\}, \tag{3.54}$$

where Δ_{wn} is the grid size in wall-normal direction, and $C_w = 0.15$ is an empirical constant.

The Smagorinsky model introduces too much diffusion into the flow. Near the walls the turbulent viscosity ν_t has to be reduced to account for the anisotropy of the turbulence. This is treated by replacing C_S in (3.50) by $C_S D(y^+)$,

$$\nu_t = (C_s D(y^+)\Delta)^2 |S|, \tag{3.55}$$

where the van Driest damping function

$$D(y^+) = 1 - e^{-y^+/A^+}, \qquad A^+ = 26, \tag{3.56}$$

is proposed by van Driest (1956) [125]. $y^+ = u_\tau y/\nu$ is the distance in wall units with friction velocity u_τ. However, for small y^+ this yields $\nu_t \sim (y^+)^2$, while ν_t should behave like $(y^+)^3$.
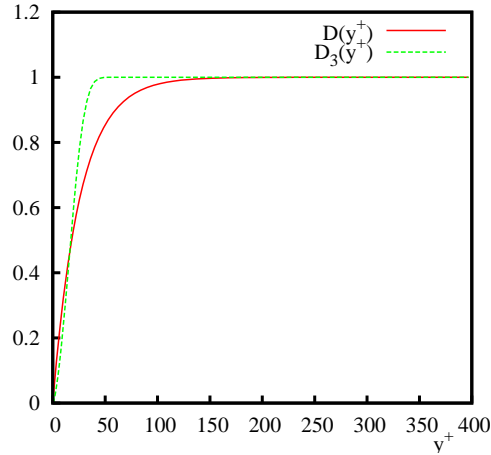
Figure 3.4: Damping functions.

The alternative formula of the damping function (Piomelli, Moin and Ferziger [95]) is given by

$$D_3(y^+) = \left(1 - e^{-\left(y^+/A^+\right)^3}\right)^{1/2}, \tag{3.57}$$

which is used in some literature, e.g., in [46] and [122]. From Fig. 3.4, we can see that the damping functions are activated only in the near-wall region.

The Smagorinsky model is often used for its simplicity, however it has drawbacks since the parameter C_S has to be calibrated and its optimal value may vary with the type of flow, the Reynolds number or the discretization scheme.

Remark 3.3 *The constant C_S used in large eddy simulation is not universal. Germano et al. (1991) [34] and Lilly (1992) [76] developed a dynamical model to compute the coefficient dynamically as a function of space and time.*

3.4 Hybrid LES/RANS model

The drawback of using LES at high Reynolds number is that it requires a very fine mesh in the near-wall region, thus the computational cost is high. On the other hand, the treatment of massive separation is difficult with RANS. To get rid of these limitations, hybrid methods of

using RANS in the near-wall region and LES away from the wall have been developed. In this section we will present two hybrid methods, the detached eddy simulation (DES) based on the Spalart-Allmaras model and extra-large eddy simulation (XLES).

For wall bounded flows at higher Reynolds number, it is too expensive to resolve the eddies in the near-wall region. Wall models (see Chapter 6) are introduced to serve as approximate boundary conditions for resolving the important eddies of the outer flow with rather coarse meshes in wall normal direction.

3.4.1   DES model

A popular hybrid approach is the detached eddy simulation (DES), which has drawn most attention in recent years. It was first proposed by Spalart *et al.* (1997) [114] based on a modification of the Spalart-Allmaras (SA) model (see Section 3.2.3), here called SADES. The length scale d in the destruction term and in the local deformation rate $\tilde{S}$ is replaced by

$$\tilde{d} = \min(d, C_{DES}\Delta) \quad \text{with} \quad \Delta = \max(\Delta x, \Delta y, \Delta z). \tag{3.58}$$

When the destruction term is balanced with the production term, the eddy-viscosity is adjusted to the scale with $\tilde{S}$,

$$\tilde{\nu} \sim \tilde{S}\tilde{d}^2, \tag{3.59}$$

which is analogous to the Smagorinsky model.

wall

RANS

LES
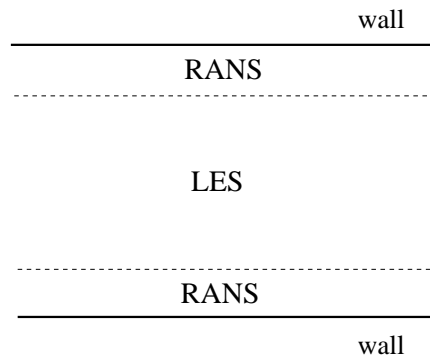
RANS

wall

Figure 3.5: The near-wall RANS region and LES region away from the wall.

In a wall bounded flow simulation, $\tilde{d} = d$ in the near-wall region, which means that the RANS mode is used. In a region away from the wall $\tilde{d} = C_{DES}\Delta$, the LES mode is switched on, see Fig. 3.5. Shur *et al* [109] calibrated the constant C_{DES} based on the simulation of DHIT. They recommended the value of 0.65.

3.4.2 XLES model

The extra-large eddy simulation model is a hybrid method introduced by Kok *et al* in [69]. The XLES formulation is based on a composition of the RANS $k - \omega$ turbulence model and the k-equation SGS model. Two transport equations are included for the kinetic energy k and the specific dissipation ω,

$$\partial_t k + (\mathbf{U} \cdot \nabla)k - \nabla \cdot (\nu_k \nabla k) \quad = \quad P_k - \epsilon, \tag{3.60}$$

$$\partial_t \omega + (\mathbf{U} \cdot \nabla)\omega - \nabla \cdot (\nu_\omega \nabla \omega) \quad = \quad P_\omega - \beta_\omega \omega^2 + CD_{k\omega}, \tag{3.61}$$

with viscosities

$$\nu_k = \nu + \nu_t \sigma_k, \qquad \nu_\omega = \nu + \nu_t \sigma_\omega. \tag{3.62}$$

The production terms P_k, P_ω and the cross-diffusion term $CD_{k\omega}$ are given by

$$P_k \quad = \quad \nu_t |S|^2, \tag{3.63}$$

$$P_\omega \quad = \quad \alpha_\omega |S|^2, \tag{3.64}$$

$$CD_{k\omega} \quad = \quad \frac{\sigma_d}{\omega} \max(\nabla k \cdot \nabla \omega, 10^{-20}), \tag{3.65}$$

with $|S|^2 = 2\mathbb{S}(\mathbf{U}) : \mathbb{S}(\mathbf{U})$. The difference between RANS and LES mode lies in the modeling of the eddy-viscosity and dissipation. For the RANS mode, the following length scale is used

$$l_{RANS} = \frac{\sqrt{k}}{\omega}, \qquad \nu_t = l_{RANS} \sqrt{k}, \qquad \epsilon = \beta_k \frac{k^{3/2}}{l_{RANS}}, \tag{3.66}$$

and

$$l_{LES} = C_1 \Delta, \qquad \nu_t = l_{LES} \sqrt{k}, \qquad \epsilon = C_2 \frac{k^{3/2}}{\Delta}, \tag{3.67}$$

for the LES mode, with Δ the filter width. The composition of the RANS and LES models is obtained by a composite length scale l_{XLES}

$$l_{XLES} = \min\{l_{RANS}, l_{LES}\}, \tag{3.68}$$

so that

$$\nu_t = l_{XLES} \sqrt{k}, \qquad \epsilon = \beta_k \frac{k^{3/2}}{l_{XLES}}, \tag{3.69}$$

or

$$\nu_t = \min\left(\frac{k}{\omega}, C_1 \Delta \sqrt{k}\right), \qquad \epsilon = \max\left(\beta_k \omega k, C_2 \frac{k^{3/2}}{\Delta}\right). \tag{3.70}$$

The constants are set to be

$$\beta_k = 0.09, \qquad \beta_\omega = 0.075, \qquad \alpha_\omega = 0.55,$$

$$\sigma_k = 2/3, \qquad \sigma_\omega = 0.5, \qquad \sigma_d = 0.5.$$

The coefficient $C_1 = 0.06$ was calibrated in the LES model for the decaying homogeneous turbulence in [69], and $C_2 = \beta_k / C_1$ for the switch of ν_t and ϵ simultaneously. A different $C_1 = 0.07$ is used in [24]. According to the length scale (3.68), the flow solutions are dynamically divided into RANS and LES regions. The RANS mode is switched on when $l_{RANS} < l_{LES}$, the $k - \omega$ model is used. Otherwise, the LES mode is applied.

Chapter 4

Decaying homogeneous isotropic turbulence at $Re_\lambda = 150$

Decaying homogeneous isotropic turbulence (DHIT) can be modeled with randomly stirred turbulence in a cubic periodic box. It is a basic turbulence benchmark problem with three homogeneous directions. Many empirical constants, for instance, the Smagorinsky constant, are estimated from the homogeneous turbulence data by adjusting the value of constants to reach the best agreement with the experimental data available in the literature.

We apply the classical Smagorinsky subgrid-scale (SGS) model to DHIT and consider the effects of the discretization schemes and forms of nonlinear terms to the numerical results. Having the evaluation of those aspects we select the methods, which provide best results with respect to the second order statistics associated with the energy spectrum, to calibrate the Smagorinsky constant C_S in the SGS model.

4.1 Test case description

DHIT can be created in a wind-tunnel with a uniform stream passing through a grid, which is normal to the steady flow. The flow in a frame moving with mean velocity U_0 is statistically stationary and (in the center of the flow) statistics vary only in the streamwise direction. In this moving frame the turbulence is (to an adequate approximation) homogeneous. Without mean velocity, the homogeneous turbulence decays for the reason that there is no production of turbulent kinetic energy, as it is shown in Fig. 4.1 for one of our simulations.

The earliest study of grid turbulence can be referred to Comte-Bellot & Corrsin (1966). Probably the best known data of decaying isotropic turbulence are provided by the grid turbulence experiments of Comte-Bellot & Corrsin (1971, denoted henceforth as CBC), see [19]. They measured the turbulent kinetic energy, decay rate, correlation functions and one- or three-dimensional energy spectra at three locations in a closed circuit wind tunnel (sketched in Fig. 4.2). The test section is about 10 [m] long, with a cross-section 1.0 [m] × 1.3 [m]. A slight
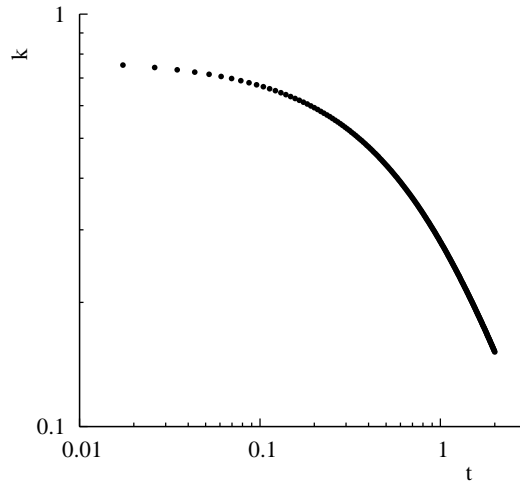
Figure 4.1: Decay of turbulent kinetic energy at $C_S = 0.094$ with CDS.

contraction (1.27:1) was located 18 mesh lengths downstream of the grid. Turbulence was generated using a grid space of $M = 5.08$ [cm] in a uniform mean flow of velocity $U_0 = 10$ [m/s], yielding a Reynolds number of $U_0 M / \nu = 34,000$. Data were reported at downstream stations: $U_0 t / M = 42$, 98 and 171.
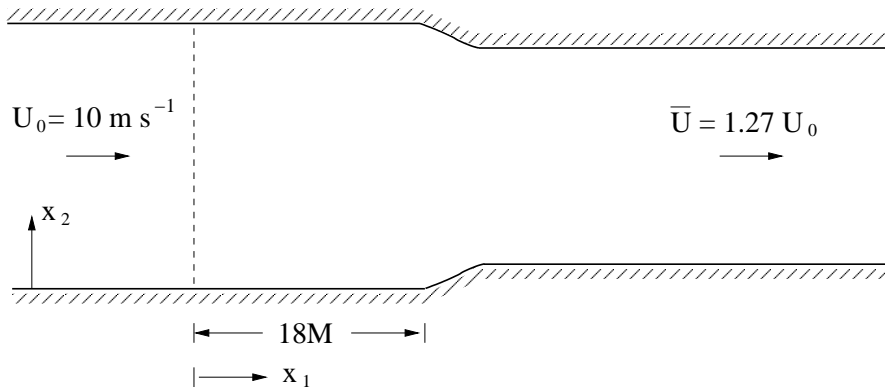
Figure 4.2: Sketch of upstream end of wind-tunnel test section.

Remark 4.1 *Two important limitations of CBC data for the purpose of testing LES are that only second-order spectra are reported, and that the Taylor scale Reynolds number is low ($Re_\lambda \sim 150$), where $Re_\lambda = \frac{u_{rms}\lambda}{\nu}$ with root mean square (rms) velocity u_{rms} and Taylor scale λ, cf. p. 198 in [96]. More recent measurements in decaying grid turbulence are reported in Kang et al. [60]. They updated the results of CBC (1971) based on turbulence at higher Reynolds number and provided more data and details of interest in studies of LES. In this study we use CBC experiment data as our reference data.*

The decay of the normal stresses and kinetic energy k have a power law form, e.g.,

$$k \sim (\frac{x - x_0}{M})^{-n},$$

where x is the coordinate with the virtual origin x_0, and M is mesh spacing. The decay exponent n of the power law is found to be $1.16 \leq n \leq 1.37$, which depends on the initial conditions such as grid spacing, Reynolds number, solidity, grid rod shape and surface roughness, from CBC data. Mohamed and LaRue [85] suggest that $n = 1.30$ ($x_0 = 0$) with a rms variation of 0.024 gives consistency with all of the data that belong to the homogeneous isotropic region. This value does not depend on the initial conditions.

To study numerical solution of DHIT, our computational domain is set to be a cubic box of side length L. In a numerical simulation of decaying turbulence, the size of computational domain gives an upper bound on the size of the largest scales in the flow. This is consistent with the observation in most experiments that the large scales of motion are of the same order as the size of the experimental apparatus. For the grid turbulence of the CBC experiment the large eddies are on the order of $M = 5.08$ [cm] in size. To capture a statistically significant number of the large eddies in our box, we must have $L > M$. Here we take $L = 2\pi$ [cm].

The initial velocity is generated from the energy spectrum by using the fast Fourier transform (FFT) tool, see Appendix C.2. The energy spectrum has been taken from experimental data at the first test section up to the cut-off value of the wave number that depends upon the grid size. The number of modes (wave numbers κ) and grids are specified to generate the velocity field on equidistant grids with 32^3 points and 64^3 points. In our problem a periodic boundary condition is imposed at one pair of boundary faces. The other boundaries are set to be symmetry planes since using periodic boundary condition in all direction is not possible yet with the DLR-THETA-code.

The numerical model used in this study is the classical Smagorinsky SGS model, see Section 3.3.2. As explained therein, the Smagorinsky constant is flow type dependent. It is one of the model parameters that we will identify in this thesis.

To compare the results with the experimental data from Comte-Bellot and Corrsin (CBC), we study the solution at time $t = 0.87$ and $t = 2.0$, where the following relation between the time t_{CBC} from the experiments of CBC and the physical time t in the computation is given,

$$t = (t_{CBC} - 42)\frac{M/U_0}{L_{ref}/U_{ref}}. \tag{4.1}$$

Here $L_{ref} = 11M/2\pi = 8.9$ [cm] and $U_{ref} = 27.19$ [cm/s] are the reference length scale and reference velocity, respectively. The computation starts at $t = 0$ whereas $t_{CBC} = 42$. The time step size is $\delta t = 0.0087$. All data are scaled by the values of L_{ref} and U_{ref}.

In the present work we will consider the influence of the following factors to DHIT: solver parameters, such as the formulation of nonlinear term, discretization schemes of the convective term and model parameters, e.g., the filterwidth and LES model coefficient.

All results presented in this Chapter are obtained with the DLR-THETA-code and implementation of the Smagorinsky model by the author.

4.2 Energy spectrum for DHIT

The incompressible flow is described by the Navier-Stokes equations (2.1)-(2.2). By setting the source term $\mathbf{f} = 0$, the NSE for DHIT are written as

$$\partial_t \mathbf{u} + \nabla \cdot (\mathbf{u} \otimes \mathbf{u}) + \nabla p - \nu \Delta \mathbf{u} \;=\; 0 \quad \text{in } \Omega \times (0, T], \tag{4.2}$$

$$\nabla \cdot \mathbf{u} \;=\; 0 \quad \text{in } \Omega \times (0, T]. \tag{4.3}$$

We consider the flow confined in a cubical box $\Omega = [0, L]^3$ of side length L with two periodic boundaries and four symmetric boundaries of Ω. The Fourier transform of the velocity vector field is

$$\hat{\mathbf{u}}(\boldsymbol{\kappa}, t) = \int_\Omega \mathbf{u}(\mathbf{x}, t) e^{-i\boldsymbol{\kappa} \cdot \mathbf{x}} \mathrm{d}\mathbf{x}, \tag{4.4}$$

and the inverse transform

$$\mathbf{u}(\mathbf{x}, t) = \frac{1}{L^3} \sum_{\boldsymbol{\kappa}} \hat{\mathbf{u}}(\boldsymbol{\kappa}, t) e^{i\boldsymbol{\kappa} \cdot \mathbf{x}}, \tag{4.5}$$

with the discrete wavenumber $\boldsymbol{\kappa} = (\kappa_1, \kappa_2, \kappa_3) \in \mathbb{R}^3$, where $\kappa_i = \frac{2\pi n_i}{L}$, $n_i \in \mathbb{N}$. Details of the Fourier transform are given in Appendix C.1.

As mentioned in Section 3.3, the velocities can be decomposed into filtered velocities and fluctuations, i.e., $\mathbf{u}(\mathbf{x}, t) = \langle\, \mathbf{u}(\mathbf{x}, t)\, \rangle + \mathbf{u}'(\mathbf{x}, t)$. The spatial average of the component $u_i(\mathbf{x}, t)$ is defined by

$$\langle\, u_i(\mathbf{x}, t)\, \rangle = \frac{1}{L^3} \int_0^L \int_0^L \int_0^L u_i(x, y, z, t) \mathrm{d}x\mathrm{d}y\mathrm{d}z. \tag{4.6}$$

Since the turbulent flow is homogeneous and isotropic, the first order statistics, i.e. the mean velocity $\langle\, \mathbf{u}\, \rangle$, is constant everywhere at a fixed time. The interesting property of DHIT is the second order statistics, such as the kinetic energy. Assume $\mathbf{r}$ is a shift of $\mathbf{x}$ in position. Then the two-point correlation

$$R_{jk}(\mathbf{r}, t) = \langle u'_j(\mathbf{x}, t) u'_k(\mathbf{x} + \mathbf{r}, t) \rangle \tag{4.7}$$

is independent of $\mathbf{x}$ due to homogeneity. The velocity spectrum $\boldsymbol{\Phi}(\boldsymbol{\kappa}, t)$ can be defined by the Fourier transform as

$$\Phi_{jk}(\boldsymbol{\kappa}, t) = \frac{1}{(2\pi)^3} \int_{\mathbb{R}^3} e^{-i\boldsymbol{\kappa} \cdot \mathbf{r}} R_{jk}(\mathbf{r}, t) \mathrm{d}\mathbf{r}, \tag{4.8}$$

and the inverse transform is

$$R_{jk}(\mathbf{r}, t) = \int_{\mathbb{R}^3} e^{i\boldsymbol{\kappa} \cdot \mathbf{r}} \Phi_{jk}(\boldsymbol{\kappa}, t) \mathrm{d}\mathbf{r}. \tag{4.9}$$

Then the turbulent kinetic energy $k = \frac{1}{2}\langle \mathbf{u}' \cdot \mathbf{u}' \rangle$ can be written as

$$k = \frac{1}{2}\sum_{i=1}^{3} R_{ii}(\mathbf{0}, t) = \int_0^\infty E(\kappa, t)\mathrm{d}\kappa, \tag{4.10}$$

where the spectrum $E(\kappa, t)$ of the turbulent kinetic energy is a useful quantity. It has the form

$$E(\kappa, t) = \iiint_{-\infty}^{\infty} \frac{1}{2}\sum_{i=1}^{3} \Phi_{ii}(\boldsymbol{\kappa}, t)\delta(|\boldsymbol{\kappa}| - \kappa))\mathrm{d}\boldsymbol{\kappa}, \tag{4.11}$$

where $\delta(\cdot)$ is the Dirac delta function. The energy spectrum function $E(\kappa, t)$ is real and non-negative, it represents the contribution of all wavenumbers $|\boldsymbol{\kappa}|$ in the range $\kappa \le |\boldsymbol{\kappa}| < \kappa + \mathrm{d}\kappa$ to the turbulent kinetic energy. For the decaying homogeneous turbulence, the dissipation rate ϵ related to $E(\kappa, t)$ is given by

$$\epsilon = \int_0^\infty \nu\kappa^2 E(\kappa, t)\mathrm{d}\kappa. \tag{4.12}$$

The kinetic energy k enters the turbulence at the largest scales of motion. The large eddies are not stable and break up, and the energy is transfered successively to smaller and smaller scales until at the smallest scales, finally the energy is dissipated into heat by viscous motion. Following Richardson (1922), this process is called *energy cascade*.

Kolmogorov gave a more detailed and quantitative analysis of high Reynolds number turbulence in [70]. He separated turbulence into two ranges, universal equilibrium range and energy-containing range by lengthscale l_{EI}. The lengthscale l_{DI} splits the universal equilibrium range into two subranges: dissipation range and inertial subrange. This picture is sketched in Fig. 4.3. *Kolmogorov's hypothesis of local isotropy* assumes statistical homogeneity and isotropy in a small space-time domain, here 'local isotropy' means isotropy only at small scales ($l \ll l_0$). For locally isotropic turbulence, the statistics of the small-scale motions ($l < l_{EI}$) are uniquely determined by the viscosity ν and the dissipation rate ϵ according to *Kolmogorov's first similarity hypothesis. Kolmogorov's second similarity hypothesis* says that in the inertial subrange ($l_{DI} < l < l_{EI}$) the statistics are uniquely determined by ϵ and does not depend on ν.

The remaining question is how the turbulent kinetic energy is distributed among the eddies of different sizes. This is done for homogeneous turbulence by considering the energy spectrum function $E(\kappa, t)$, in which the wavenumber $\kappa = 2\pi/l$ corresponds to the motion of lengthscale l. The energy and dissipation rate in the wavenumber range (κ_a, κ_b) are

$$k_{(\kappa_a,\kappa_b)} = \int_{\kappa_a}^{\kappa_b} E(\kappa, t)\mathrm{d}\kappa, \qquad \epsilon_{(\kappa_a,\kappa_b)} = \int_{\kappa_a}^{\kappa_b} 2\nu\kappa^2 E(\kappa, t)\mathrm{d}\kappa. \tag{4.13}$$

Following Kolmogorov's first similarity hypothesis the spectrum is a universal function of ϵ and ν in the universal equilibrium range ($\kappa > \kappa_{EI} \equiv 2\pi/l_{EI}$). Kolmogorov's second similarity hypothesis predicts that in the inertial range ($\kappa_{EI} < \kappa < \kappa_{DI} \equiv 2\pi/l_{DI}$) the spectrum is

$$E(\kappa, t) = C\epsilon^{2/3}\kappa^{-5/3}, \tag{4.14}$$

59
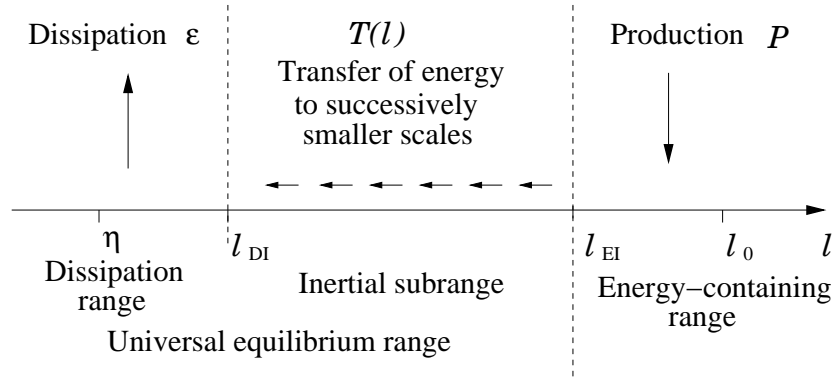
Figure 4.3: Eddy sizes l (on a logarithmic scale) and the energy cascade at very high Reynolds number.

where $C = 1.5$ is a universal Kolmogorov constant. This is the famous Kolmogorov $-\frac{5}{3}$ spectrum. Due to $\kappa \sim 1/l$, large scales correspond to small wave numbers and vice versa. The amount of energy in the high wavenumbers decreases as κ increases, whereas the dissipation in the low wavenumbers decreases as κ decreases toward zero.

From the two-point correlation, the following characteristic integral lengthscale can be defined,

$$L_{11}(\mathbf{x}, t) = \frac{1}{R_{11}(0, \mathbf{x}, t)} \int_0^\infty R_{11}(\mathbf{e}_1 r, \mathbf{x}, t) \mathrm{d}r, \tag{4.15}$$

where $\mathbf{e}_1$ represents the unit vector in the x direction. If $h = l_{EI} = \frac{1}{6}L_{11}$, the energy in the filtered velocity field $\frac{1}{2}\langle \mathbf{u}^2 \rangle$ is approximately 80% of the total energy, cf. [96], Chapter 6. Thus the bulk of kinetic energy k is contained in the large scale motions, which correspond to small wavenumbers.

To compute the energy spectrum $E(\kappa, t)$ by a spectral approach, one can solve the system of ordinary differential equations in spectral space by applying a Fourier transform to the NSE. The reader who is interested in this approach is referred to [26, 105].

The method we use here is to compute the discrete filtered velocity field $\langle \mathbf{u}(\mathbf{x}, t) \rangle$ with FVM on a discretized domain and to get the discrete filtered Fourier transform $\langle \hat{\mathbf{u}}(\kappa, t) \rangle$ of the velocity by using the FFT (see Appendix C.2). The energy spectrum is obtained from

$$E(\kappa, t) = \sum_{\kappa-1/2 < |\mathbf{q}| \leq \kappa+1/2} \frac{1}{2} \langle \hat{\mathbf{u}}(\mathbf{q}, t) \rangle \cdot \langle \hat{\mathbf{u}}^*(\mathbf{q}, t) \rangle. \tag{4.16}$$

Here $\langle \hat{\mathbf{u}}^*(\mathbf{q}, t) \rangle$ is the complex conjugation of $\langle \hat{\mathbf{u}}(\mathbf{q}, t) \rangle$.

4.3   Solver and model parameters affecting the solution

Numerical errors in LES arise due to

- discretization errors,

- aliasing errors (which emerge from the method of computation of the nonlinear term by taking products in physical space on a discrete level), and

- errors in the subgrid-scale turbulence model.

They are difficult to analyse because of nonlinear interactions between these errors. Here we refer to the careful discussion in [36] and [90] where low and higher order schemes are analyzed. It is shown there that the discretization error may outweight the contribution from the SGS force. Moreover, the aliasing error is the leading source at highest wavenumbers where any energy above the wavenumber cutoff incorrectly "folds over" into the resolved spectrum. The numerical error becomes dominant for low-order schemes.

In Section 4.4, we will analyse the influence of the following aspects of the low order finite volume discretization on the resolution of DHIT:

- discretization scheme for the nonlinear fluxes,

- formulation of the nonlinear term.

In Section 4.5, we will consider the influence of the following grid and model parameters:

- mesh size h,

- Smagorinsky constant C_S,

- filter width to mesh size ratio Δ/h.

All these parameters influence the dissipation of the scheme, but in different means. On the one hand, dissipation is explicitly due to the subgrid-scale model. One the other hand, there is dissipation associated implicitly with the numerical discretization scheme.

- Dissipation of the numerical scheme which has three sources:

  – Numerical error associated with a discrete scheme for space and time discretization (The time discretization error is negligibly small for this test case),

  – Regarding the spatial discretization error, the formulation of the nonlinear fluxes is also important. This error is associated with the aliasing error (cf. [90]),

– Artificial viscosity associated with discretization scheme for the numerical fluxes. This artificial viscosity depends on the type of flux discretization scheme and mesh size h (If the mesh is not Cartesian, then the grid arrangement like anisotropy also becomes an improtant issue).

- Dissipation of the subgrid-scale model depending on:

  – type of SGS model (here only Smagorinsky model considered),

  – Smagorinsky constant C_S ($\nu_t \sim C_S^2$),

  – filter width Δ ($\nu_t \sim \Delta^2$). Therein, Δ depends on the mesh size h and on the ratio Δ/h chosen.

- Scale of resolved physics:

  – The smallest flow features resolved are limited by the mesh size h,

  – The question how the filter width Δ is related to the resolved flow physics is still not solved, see [97].

To rule out some schemes which cannot provide appropriate results, we define the following error functional. Let the measurement $\hat{C}(q, \langle \mathbf{u} \rangle)$ be the energy spectrum. By considering the discrete L^2-fitting of the energy spectrum to the CBC data at time $t = 0.87$ and $t = 2.0$, the error functional is defined as,

$$J(q) = \left(\sum_{i=1}^{N/2-1} \left[\left(E(\kappa_i, q) - E_{exp}(\kappa_i) \right)^2_{t=0.87} + \left(E(\kappa_i, q) - E_{exp}(\kappa_i) \right)^2_{t=2.0} \right] \right)^{1/2}, \quad (4.17)$$

where κ_i is wavenumber. N is the number of mesh points in each direction, $N = 64$ for grid 64^3 and $N = 32$ for grid 32^3. q is the control parameter (scheme) under consideration.

4.4 Influence of solver parameters

First of all, we will investigate the influence of the discretization schemes, UDS, LUDS, QUDS and CDS and the formulations of the nonlinear term, i.e., divergence form and skew-symmetric form, on DHIT.

4.4.1 Influence of discretization schemes for the convective fluxes

Here the influence of the discretization scheme for the convective fluxes is considered. We fix the following settings:

- Smagorinsky constant $C_S = 0.1$ and $C_S = 0.17$,

- ratio of filter width to mesh size Δ/h=2,

- nonlinear term in divergence form.

The following four schemes are considered (for details, see Section 2.2.4):

- upwind difference scheme (UDS),

- central difference scheme (CDS),

- linear upwind difference scheme (LUDS),

- quadratic upwind difference scheme (QUDS).

	UDS	LUDS	QUDS	CDS
grid 64^3, $C_S = 0.1$	2.871762e-02	2.465593e-02	2.164382e-02	1.003162e-02
grid 64^3, $C_S = 0.17$	3.184311e-02	2.296563e-02	2.119606e-02	1.791940e-02
grid 32^3, $C_S = 0.1$	3.583124e-02	2.147239e-02	1.761466e-02	1.624498e-02
grid 32^3, $C_S = 0.17$	4.095476e-02	2.724673e-02	2.442006e-02	1.973222e-02

Table 4.1: Error functional (4.17) of the energy spectra for UDS, CDS, LUDS and QUDS.

The energy spectra with respect to wavenumber at time $t = 0.87$ and $t = 2.0$ are shown in Fig. 4.4 at $C_S = 0.1$ and Fig. 4.5 at $C_S = 0.17$ on grid 32^3 and 64^3, respectively. From these figures we can see that the energy spectra with CDS have quite good agreement with CBC data at $C_S = 0.1$, and for the finer grid 64^3 the agreement is even better. Without surprise, UDS leads to much more overdissipation since it is only a first order scheme in space. Moreover LUDS is very dissipative, too. Taking the discretization schemes as the control parameters, the values of the error functional (4.17) for these cases are listed in Table 4.1. It also shows that UDS and LUDS have larger deviation from the experimental data than QUDS and CDS. So they will not be considered in further study. The other upwind scheme QUDS behaves also rather dissipative, but as a quadratic upwind scheme, it is worth being studied further.

For the standard case of $C_S = 0.17$, all schemes are over-dissipative, especially in the region where the wavenumber is around the cutoff wavenumber, but recall that $Δ/h = 2$ is chosen.

4.4.2 Influence of formulations for the nonlinear terms

The form of the nonlinear terms can affect the numerical and aliasing errors, so that the particular choice of discretization of these terms may stabilize and reduce the aliasing error. There have been several studies (see for example [9], [18] and [90]) in which the nonlinear terms are evaluated using a skew-symmetric form. This form is equivalent to the divergence form and advective form analytically but not numerically. The skew-symmetric form is

(a): t=0.87, grid 32^3

(b): t=0.87, grid 64^3

(c): t=2.0, grid 32^3

(d): t=2.0, grid 64^3
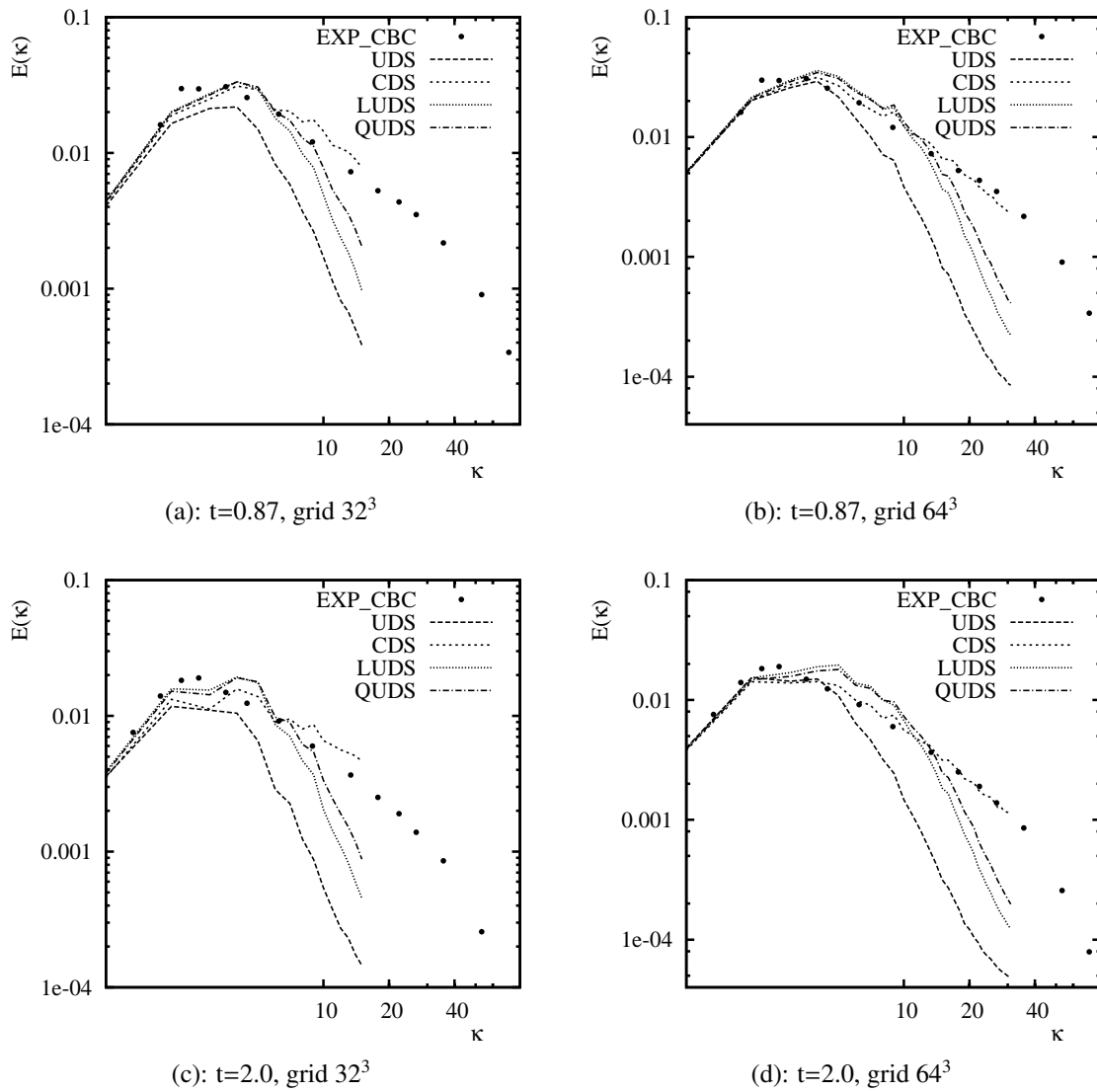
Figure 4.4: Energy spectra for UDS, CDS, LUDS and QUDS at $C_S = 0.1$.

the most robust one compared with the conservative and nonconservative form reported by Blaisdell *et al* [9].

Two different formulations of the nonlinear terms are investigated. In the Navier-Stokes equations, the filtering of the nonlinear term $\partial u_i u_j / \partial x_j$ creates a closure problem in LES. The form of the nonlinear term has a significant influence on the discretization error. There
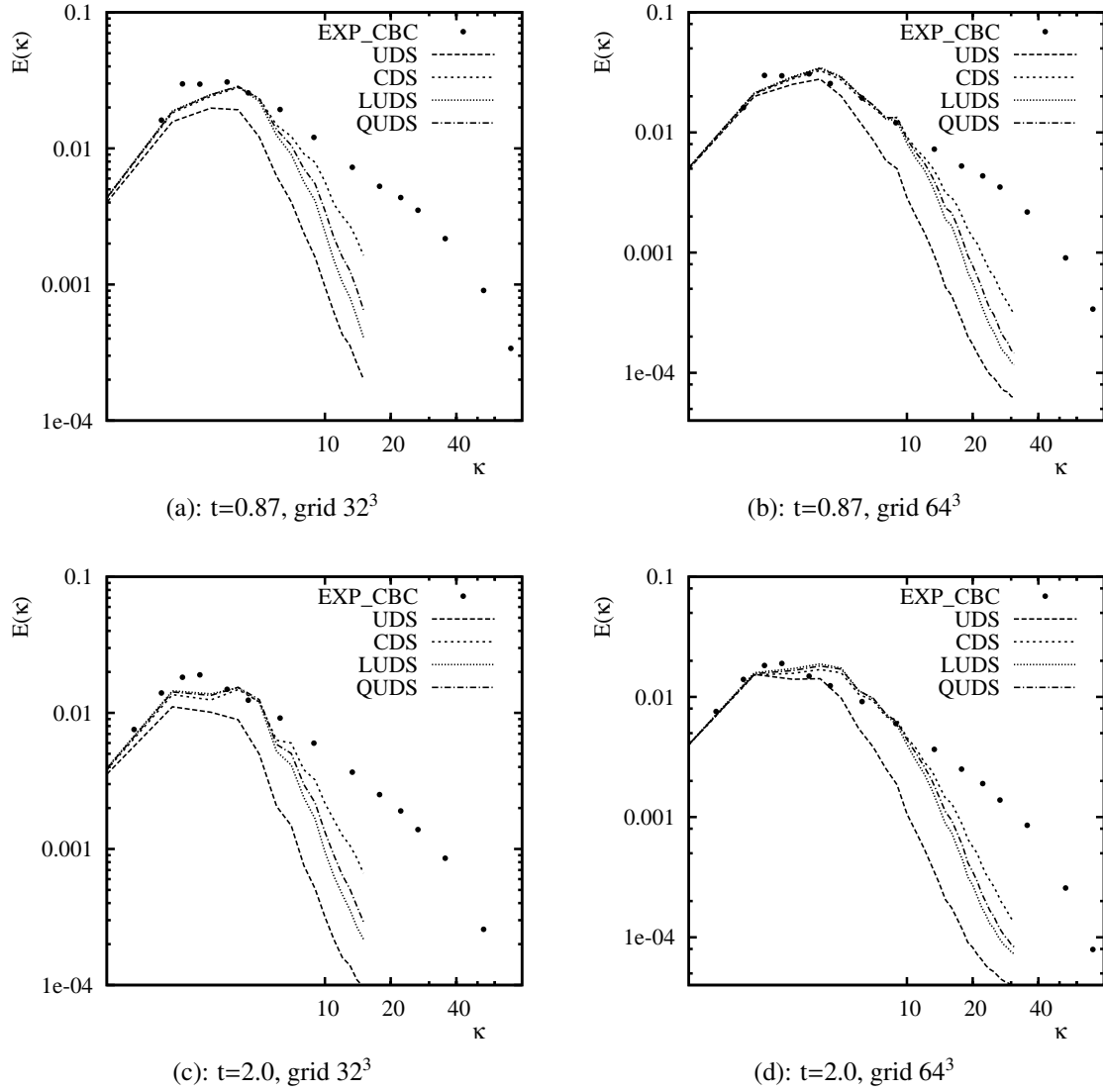
Figure 4.5: Energy spectra for UDS, CDS, LUDS and QUDS at $C_S = 0.17$.

are three analytically but not numerically equivalent forms of the nonlinear term, see [90]:

$$N_i^d = \frac{\partial(u_i u_j)}{\partial x_j}, \qquad \text{divergence or conservative form,} \qquad (4.18)$$

$$N_i^a = u_j \frac{\partial u_i}{\partial x_j} + u_i \frac{\partial u_j}{\partial x_j}, \quad \text{advective or convective form,} \qquad (4.19)$$

$$N_i^s = \frac{1}{2}(N_i^d + N_i^a), \qquad \text{skew-symmetric form.} \qquad (4.20)$$

We fix the following settings:
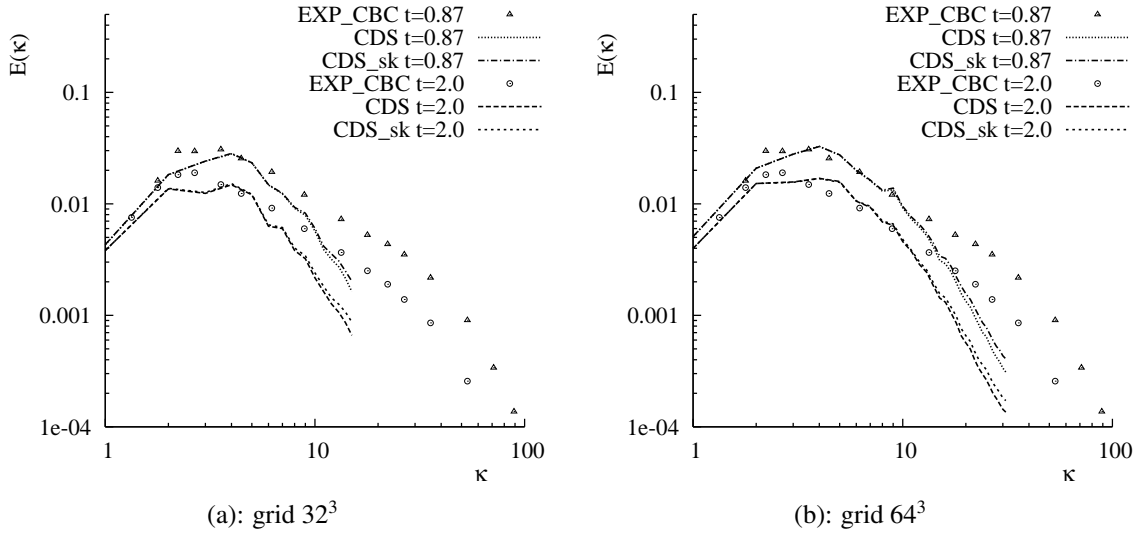
Figure 4.6: Energy spectra with CDS and skew-symmetric form at $C_S = 0.17$.
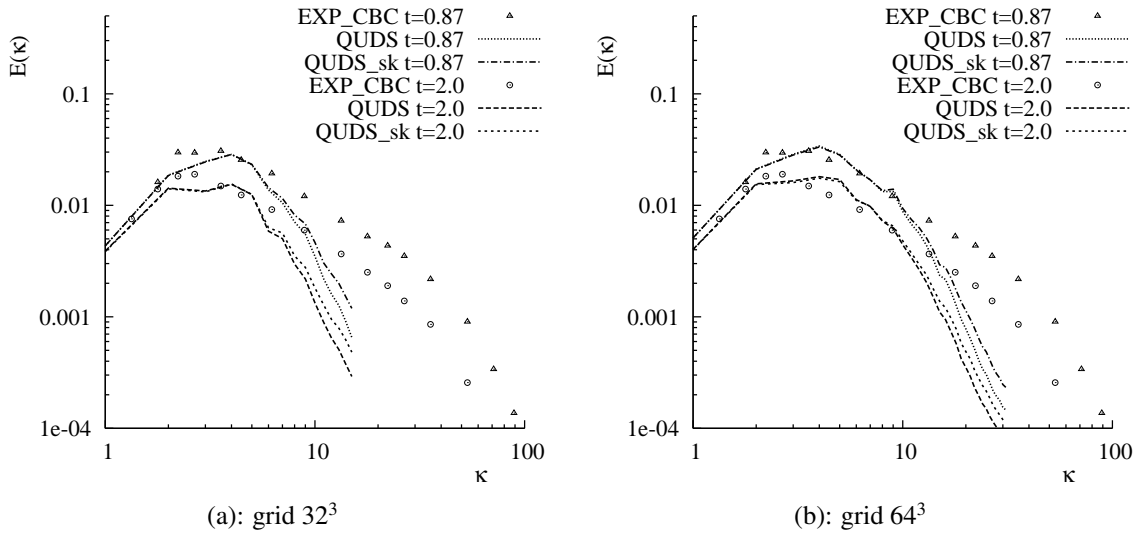
Figure 4.7: Energy spectra with QUDS and skew-symmetric form at $C_S = 0.17$.

- Smagorinsky constant $C_S = 0.1$ and $C_S = 0.17$,

- ratio of filter width to mesh size $\Delta/h=2$,

- discretization schemes for the convective fluxes: CDS and QUDS,

and we vary the formulation for the nonlinear term:

(a): grid 32^3

(b): grid 64^3
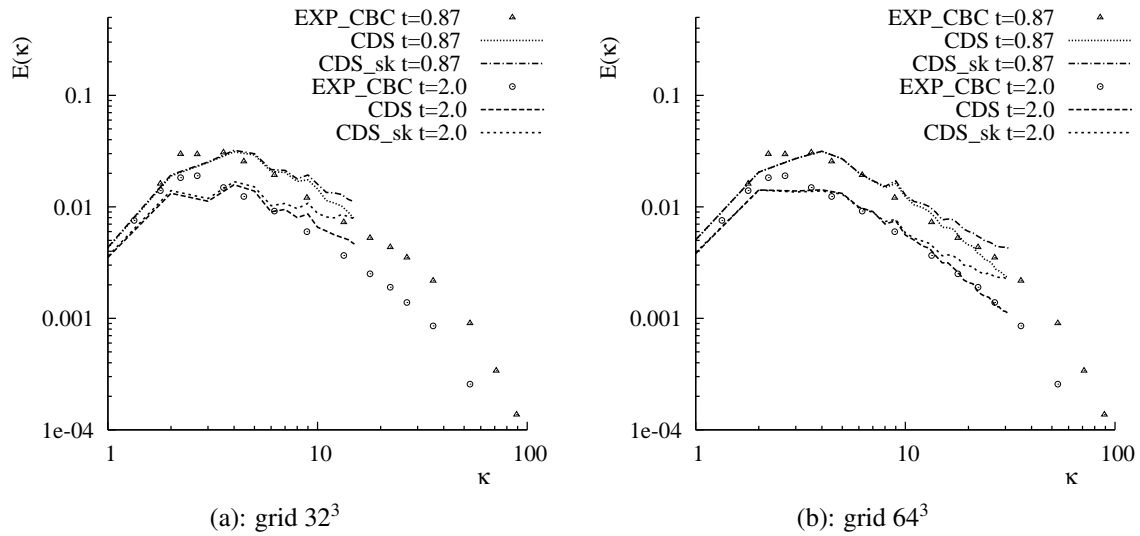
Figure 4.8: Energy spectra with CDS and skew-symmetric form at $C_S = 0.1$.

(a): grid 32^3

(b): grid 64^3
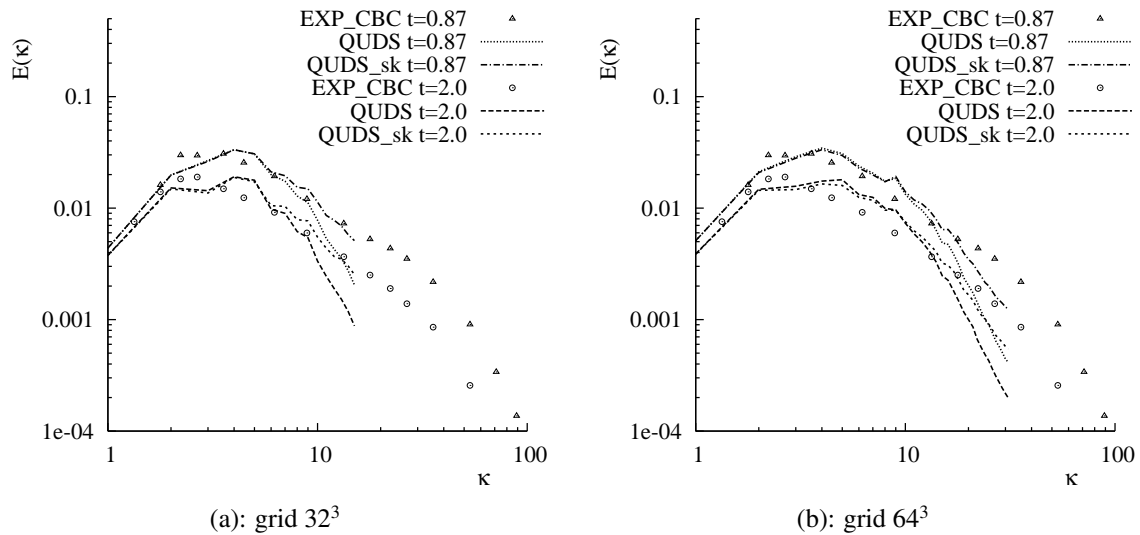
Figure 4.9: Energy spectra with QUDS and skew-symmetric form at $C_S = 0.1$.

- divergence form,

- skew-symmetric form.

The skew-symmetric term is implemented explicitly into the DLR-THETA-code. The energy spectra are plotted in Fig. 4.6-4.9, where the scheme with the skew-symmetric form for the nonlinear terms implemented is denoted with "_sk" and the divergence form is represented

	QUDS	CDS	QUDS_sk	CDS_sk
grid 64^3, $C_S = 0.1$	2.164382e-02	1.003162e-02	1.828027e-02	1.315465e-02
grid 64^3, $C_S = 0.17$	2.119606e-02	1.791940e-02	1.920937e-02	1.707439e-02
grid 32^3, $C_S = 0.1$	1.761466e-02	1.624498e-02	1.509031e-02	2.339599e-02
grid 32^3, $C_S = 0.17$	2.442006e-02	1.973222e-02	2.172800e-02	1.870902e-02

Table 4.2: Error functional (4.17) of the energy spectra for CDS(_sk) and QUDS(_sk).

by the discretization schemes without any index.

The numerical solution of CDS_sk is not dissipative enough at large wavenumbers, but for QUDS_sk better agreement to the CBC data can be achieved at $C_S = 0.1$ at large wavenumbers. For the upwind scheme, the concept of flux vector enforces the nonlinear term to be written in the conservative or divergence form, whereas central difference scheme does not. The specific form of the nonlinear term may have significant influence on the simulation result. From this point of view the skew-symmetric form is not a proper choice to improve the simulation result with the central difference scheme. Here CDS and QUDS_sk give the best results. We will proceed our studies with these two schemes.

A comparison of Fig. 4.6-4.7 to Fig. 4.8-4.9 shows again that $C_S = 0.17$ is not a proper value for this case, although the values of the error functional present a small improvement of CDS_sk compared with CDS in Table 4.2 for $C_S = 0.17$. It is a parameter which has strong influence to the results and needs to be optimized.

4.5 Influence of model parameters

The ratio of the filter width and mesh size Δ/h and the Smagorinsky constant C_S are considered as model parameters for DHIT.

4.5.1 Influence of filter size and grid convergence

In this section we will consider the influence of Δ/h on the numerical solutions. Let us start with some results from the literature. Ghosal [36] presented a method of analysis of the numerical errors in LES from a random field with a von Kármán energy spectrum. It is found that for an eighth-order finite difference scheme, the numerical errors are several orders of magnitude smaller than the subgrid force throughout the whole wavenumber range of interest by implementing the LES with a filter to grid width ratio of 2. For a second-order numerical scheme, Ghosal found that the filterwidth must be at least four times of the grid spacing.

In [35], Geurts and Fröhlich contrasted the gradually increased resolution at constant Δ with grid refinement and at fixed ratio Δ/h in a turbulent mixing layer. They identify suitable

ratios Δ/h which allow for a clear separation of the numerical and modeling effects, i.e., without losing a large amount of physical details to keep computational cost at a feasible level. If Δ/h is large it leads to comparably small numerical effects but comparably large computational cost for capturing scales up to order Δ. If Δ/h is small then large amount of physical informations is contained in the numerical solution at small computational cost. To compromise numerical and modeling effects, a suitable Δ/h is chosen in [35] to be $\Delta/h \in \{1, 2, 4\}$. If we keep Δ fixed and let Δ/h increase when refine the grid, the solution to the modeled LES will asymptotically lead to results close to a direct numerical simulation.

If we keep Δ constant while refine h, then the subgrid scale viscosity v_t does not change due to $v_t \sim (C_S \Delta)^2$. However, the dissipation of the numerical scheme (both numerical error and artificial viscosity) ceases when decreasing h, so this is a first step of a grid convergence study.

We fix the following settings:

- for CDS: $C_S = 0.1$ with divergence form (CDS),

- for QUDS: $C_S = 0.1$ with skew-symmetric form (QUDS_sk).

We compare the following three cases:

- $\Delta/h = 2$ for grid 32^3, ($h = L/32$, $\Delta = L/16$),

- $\Delta/h = 2$ for grid 64^3, ($h = L/64$, $\Delta = L/32$),

- $\Delta/h = 4$ for grid 64^3, ($h = L/64$, $\Delta = L/16$).

	CDS	QUDS_sk
grid 64^3, $\Delta/h = 2$	1.003162e-02	1.828027e-02
grid 64^3, $\Delta/h = 4$	2.062899e-02	2.107595e-02
grid 32^3, $\Delta/h = 2$	1.973222e-02	2.172800e-02

Table 4.3: Error functional (4.17) of the energy spectra for Δ/h.

The energy spectra of CDS and QUDS_sk at $C_S = 0.1$ are given in Fig. 4.10. For $\Delta/h = 2$, the energy spectra with finer grid give better prediction to the CBC data than that ones with coarse grid. This means if one refines the grid and keeps Δ/h fixed a DNS is eventually approached. For fixed Δ with refinement of the grid, i.e., with increasing Δ/h, better resolutions are obtained for small wavenumbers (large scales), but no good resolution at large wavenumbers (small scales). It is clearly shown in Table 4.3 of the error functional that the finer grid with $\Delta/h = 2$ for both CDS and QUDS_sk gives better results.
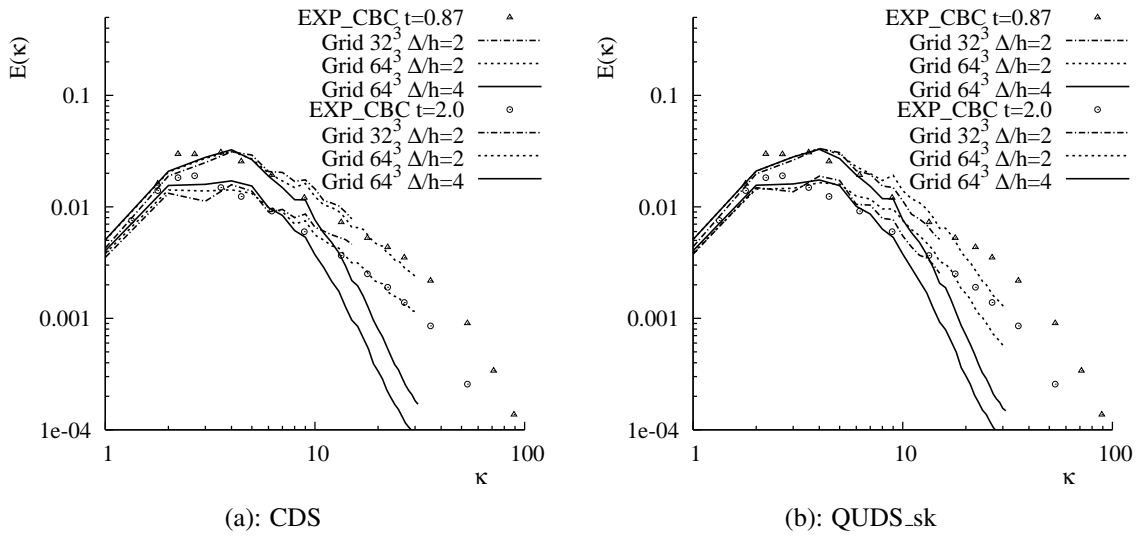
Figure 4.10: Energy spectra at $C_S = 0.1$ for Δ/h.

4.5.2 Role of subgrid-scale model

Now we consider the influence of the Smagorinsky constant C_S of the Smagorinsky model. The DHIT case is the classical benchmark to calibrate this constant.

We fix the following settings:

- ratio $\Delta/h = 2$ for fixed mesh with 64^3 points,

- CDS with divergence form (CDS) and QUDS with skew-symmetric form (QUDS_sk).

We vary Smagorinsky constant:

- $C_S = 0.85$,

- $C_S = 0.1$,

- $C_S = 0.17$.

As it can be seen from Fig. 4.11-4.12, the Smagorinsky constant has significant influence on the solution: the smaller the Smagorinsky constant, the smaller the dissipation at large wavenumbers.

4.5.3 Parameter identification

In Sections 4.4.1-4.5.2, the influence of different schemes and parameters to the simulation of DHIT has been discussed. Let us summarize all the aspects here:

(a): t=0.87

(b): t=2.0
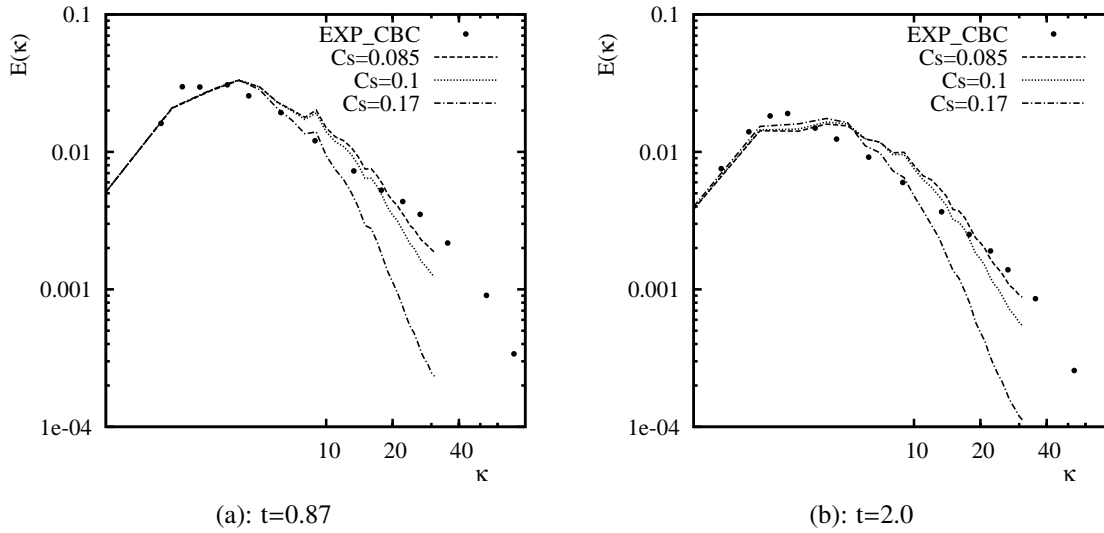
Figure 4.11: Energy spectra on grid 64^3 with QUDS_sk.

(a): t=0.87

(b): t=2.0
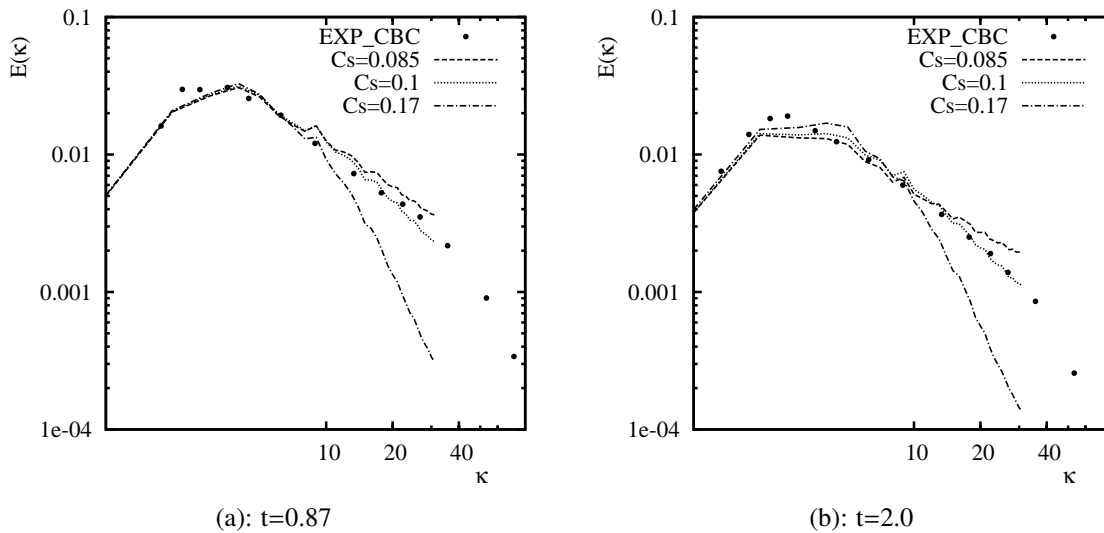
Figure 4.12: Energy spectra on grid 64^3 with CDS.

- The results of UDS and LUDS are too dissipative at large wavenumbers.

- Applying skew-symmetric form of the nonlinear term brings improvement to QUDS but not to CDS.

- The ratio of $\Delta/h = 2$ seems to be a better choice than $\Delta/h = 4$.

- Results of grid 64^3 gives better agreement to the CBC data than those of grid 32^3.
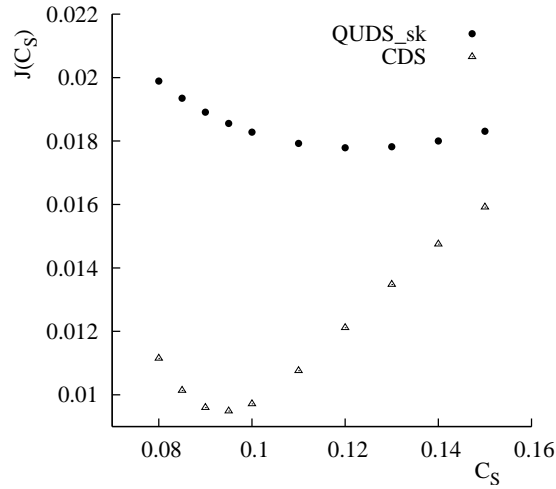
Figure 4.13: The values of error functional (4.21) for DHIT.

C_S	CDS	QUDS_sk
0.08	1.115063e-02	1.989151e-02
0.09	9.599141e-03	1.890759e-02
0.095	9.487918e-03	1.855574e-02
0.1	9.712883e-03	1.828027e-02
0.11	1.076020e-02	1.792614e-02
0.12	1.211416e-02	1.778672e-02
0.13	1.347669e-02	1.782159e-02
0.14	1.474920e-02	1.800351e-02
0.15	1.591452e-02	1.830773e-02

Table 4.4: Error functional (4.21) of the energy spectra for C_S.

To identify the Smagorinsky constant C_S with this test case, we use those schemes which produce best results. Here we set $\Delta/h = 2$ for grid 64^3 and consider QUDS with skew-symmetric form (QUDS_sk) for the nonlinear term and CDS with divergence form (CDS). By setting $q = C_S$, the error functional (4.17) is written as

$$J(C_S) = \left(\sum_{i=1}^{N/2-1} \left[\left(E(\kappa_i, C_S) - E_{exp}(\kappa_i) \right)^2_{t=0.87} + \left(E(\kappa_i, C_S) - E_{exp}(\kappa_i) \right)^2_{t=2.0} \right] \right)^{1/2}, \qquad (4.21)$$

with $N = 64$. For different C_S, the values of the error functional are shown in Fig. 4.13 and in Table 4.4. Evidently, the error of CDS is smaller than that of QUDS_sk. To get the constant C_S where the error functional reaches the minimum, a necessary condition is

$$\frac{\mathrm{d}J(C_S)}{\mathrm{d}C_S} = 0. \qquad (4.22)$$

Denote

$$Q(C_S) := \frac{dJ(C_S)}{dC_S} = 0, \qquad (4.23)$$

the problem now is to find the solution to $Q(C_S) = 0$. The typical approach is the Newton type method, where the solution can be obtained iteratively,

$$C_S^{n+1} = C_S^n - \frac{Q(C_S^n)}{Q'(C_S^n)}. \qquad (4.24)$$

The next task is to compute $Q(C_S^n)$ and its first derivative, which is the second derivative of $J(C_S)$. Obviously $J(C_S)$ is not a given analytical function and computing its derivative would require solving the corresponding adjoint problem, see Section 1.2. Instead, here we use the finite difference to approximate the first and second derivatives. Applying the central difference scheme, we obtain

$$Q(C_S^n) = \left. \frac{dJ(C_S)}{dC_S} \right|_{C_S^n} \approx \frac{J(C_S^n + \delta C_S) - J(C_S^n - \delta C_S)}{2\delta C_S}, \qquad (4.25)$$

$$Q'(C_S^n) = \left. \frac{d^2 J(C_S)}{dC_S^2} \right|_{C_S^n} \approx \frac{J(C_S^n + \delta C_S) - 2J(C_S^n) + J(C_S^n - \delta C_S)}{(\delta C_S)^2}. \qquad (4.26)$$

For one Newton step one needs to solve three Navier-Stokes problems.

From Fig. 4.13 we see that the minima are reached in the vicinity of $C_S = 0.095$ for CDS and $C_S = 0.12$ for QUDS_sk, respectively. Taking these two as starting values C_S^0 and setting $\delta C_S = 0.002$, we compute $J(C_S)$ at $C_S^0 + \delta C_S$ and $C_S^0 - \delta C_S$. Iterations are carried out by

(a): CDS
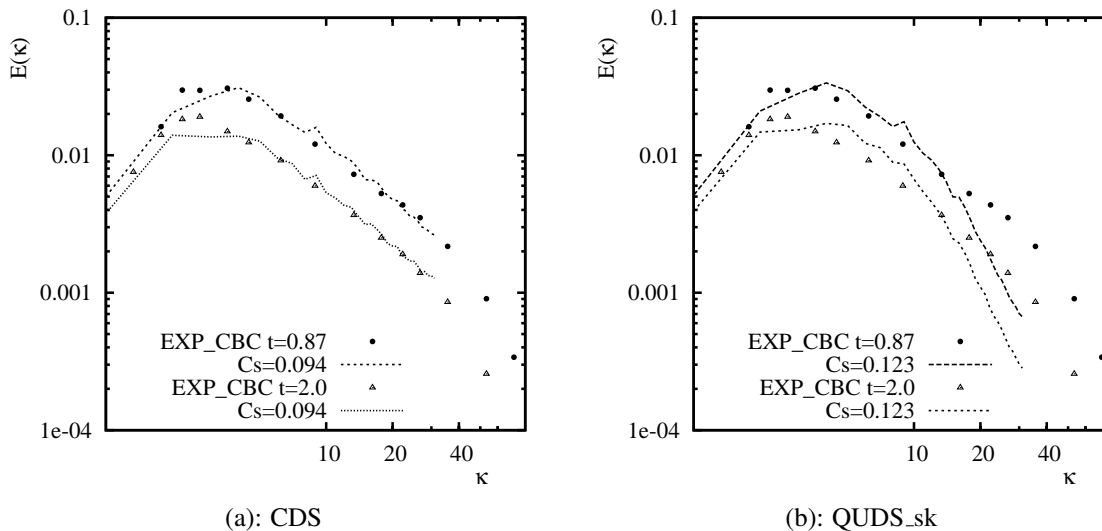
(b): QUDS_sk

Figure 4.14: Energy spectra at the corresponding best C_S.

using (4.24) together with (4.25) and (4.26). Finally, we get the optimal values $C_S = 0.094$

$(J(C_S) = 9.481012e - 03)$ for CDS and $C_S = 0.123$ $(J(C_S) = 1.778043e - 02)$ for QUDS_sk after a few iterations. Obviously, the constant depends on the discretization schemes which we use. The energy spectra of the best C_S are shown in Fig. 4.14 for both schemes.

Although $C_S = 0.123$ gives the minimal error functional for QUDS_sk, the deviation is still quite large compared with the experimental data. The error functional of QUDS_sk at optimized C_S is almost double of the one of CDS.

Let us summarize the results:

- Best results for CDS: $C_S = 0.094$ with optimized $J(C_S) = 9.481012e - 03$,

- Best results for QUDS_sk: $C_S = 0.123$ with optimized $J(C_S) = 1.778043e - 02$.

Chapter 5

Channel flow at moderate Reynolds number $Re_\tau = 395$

Turbulent channel flow is a standard test case for wall bounded flows. A turbulent channel flow of Reynolds number $Re_\tau = 395$ based on friction velocity and the channel halfwidth is studied in this chapter. In this flow, the mean velocity vector is parallel to the wall, hence there is only one nonhomogeneous direction, i.e., the wall normal direction. The flow is homogeneous in spanwise and streamwise directions. Even only one direction of homogeneity less, the simulation is much more complicated than DHIT.

5.1   Description of the flow

In the past decades, several numerical simulations of the turbulent channel flow have been investigated using large-eddy simulation (LES) and direct numerical simulation (DNS). Numerous studies have been performed to the turbulent channel, for instance, by Piomelli *et al.* [94] for approximation of boundary conditions with LES, by Iliescu and Fischer [53] with rational LES and detached-eddy simulation (DES) by Nikitin *et al.* [89]. It has been served as a test case for variational multiscale LES in [39]. The difficulty in such a wall-bounded flow is that it requires a very fine mesh in the near-wall region. Cheaper alternatives may be considered by using appropriate near-wall models, see Section 6.4.2. Moreover, the DNS data by Moser *et al.* [88] serves as a useful benchmark in simulations. Here they are used as reference data.

A channel is a rectangular duct of length L and height $2H$, as sketched in Fig. 5.1. It is sufficiently long ($L \gg H$) and has a large aspect ratio ($b \gg H$), such that at a certain distance from the entrance, the mean velocity profile and statistics are independent of streamwise position x and also of spanwise z. The channel flow becomes fully developed turbulent at $x \geq 30H$, see Wilcox [129]. The mid-plane is located at $y = H$, $y = 0$ and $y = 2H$ are the bottom and top walls, respectively. The mean velocity is denoted by $\mathbf{U} = (U, V, W)$ and mean

75
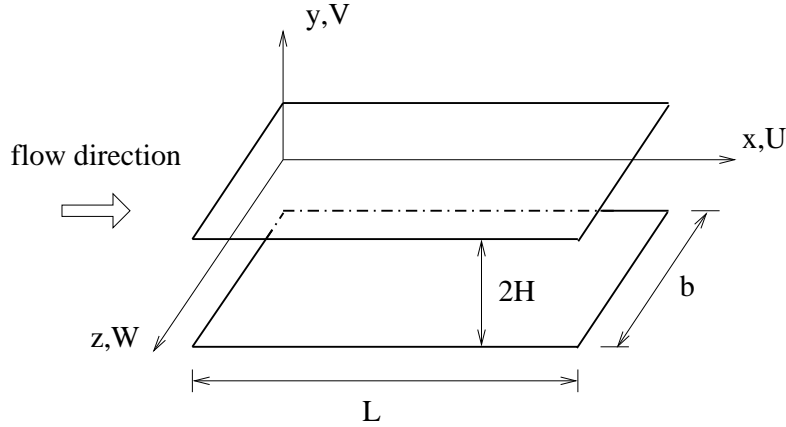
Figure 5.1: Sketch of a 3D channel.

pressure by P. $U_c = U|_{y=H}$ is the centerline velocity and U_{bulk} is the bulk velocity defined by

$$U_{\text{bulk}} \equiv \frac{1}{H} \int_0^H U \mathrm{d}y. \tag{5.1}$$

Assume u_τ is the friction velocity related to the shear stress at the wall. The definition will be given later in this section. The Reynolds numbers characterizing the flow are defined as

$$Re_{\text{bulk}} \equiv \frac{2HU_{\text{bulk}}}{\nu}, \qquad Re_c \equiv \frac{HU_c}{\nu}, \qquad Re_\tau \equiv \frac{u_\tau H}{\nu}. \tag{5.2}$$

Turbulent flow occurs at high Reynolds number ($Re_{\text{bulk}} > 3000$), while laminar flow occurs at low Reynolds number ($Re_{\text{bulk}} < 1350$).The transition between laminar and turbulent flow is often indicated by a critical Reynolds number (Re_{crit}), which depends on the exact flow configuration and can be determined in experiments, cf. [91].

The governing equations for incompressible flow using the Smagorinsky SGS model have been described in Section 3.3.2. By denoting the filtered velocity $\mathbf{U} = \bar{\mathbf{u}}$ and pressure $P = \bar{p}$, they are written as follows (setting $\rho = 1$):

$$\partial_t \mathbf{U} + \nabla \cdot (\mathbf{U} \otimes \mathbf{U}) + \nabla P - \nabla \cdot (2\nu_e \mathbb{S}(\mathbf{U})) = \mathbf{f}, \tag{5.3}$$
$$\nabla \cdot \mathbf{U} = 0. \tag{5.4}$$

with the strain rate tensor of the resolved velocity field

$$\mathbb{S}(\mathbf{U}) = \frac{\nabla(\mathbf{U}) + \nabla(\mathbf{U})^\mathrm{T}}{2}. \tag{5.5}$$

The effective viscosity is given by

$$\nu_e = \nu + \nu_t, \tag{5.6}$$

and the turbulent viscosity by

$$\nu_t = (C_S D(y^+)\Delta)^2 |S|, \tag{5.7}$$

with the classical van Driest damping function

$$D(y^+) = 1 - \exp\left(-\frac{y^+}{A^+}\right), \qquad A^+ = 26. \tag{5.8}$$

A typical choice of the filter width is $\Delta = (\Delta x \Delta y \Delta z)^{1/3}$, with Δx, Δy and Δz being the grid spacing in x, y and z, respectively. C_S is the Smagorinsky constant.

The flow is driven by a pressure gradient, which is constant taken to be

$$\mathbf{f} = \rho(\frac{u_\tau^2}{H}, 0, 0)^\mathrm{T} \quad \text{with } \rho = 1. \tag{5.9}$$

Since the width b of the channel is large compared with H, the flow is statistically independent of z, all the quantities associated with z are zero, i.e., $W = 0$ and $\partial(\cdot)/\partial z = 0$. In the *fully developed* region (large x), in which velocity statistics no longer change with x, the channel is considered statistically stationary and statistically one-dimensional with velocity statistics depending only on y, $U = U(y)$ and $\partial(\cdot)/\partial x = 0$. Substituting these terms into the mean continuity equation

$$\nabla \cdot \mathbf{U} = \frac{\partial U}{\partial x} + \frac{\partial V}{\partial y} + \frac{\partial W}{\partial z} = 0 \tag{5.10}$$

with boundary conditions at the walls leads to $V = 0$. The mean velocity of the turbulent channel flow is in x direction and varies in the cross-stream y direction. With the decomposition of the velocity and pressure (3.45) and (3.46) in mind and (u', v', w') being the fluctuating velocity, the filtered NSE (5.3) for time-independent flow reduce to

$$-\frac{\partial P}{\partial x} = \frac{\partial}{\partial y}\left(\langle u'v'\rangle - \nu\frac{\partial U(y)}{\partial y}\right), \tag{5.11}$$

$$-\frac{\partial P}{\partial y} = \frac{\partial\langle v'v'\rangle}{\partial y}. \tag{5.12}$$

Differentiating the second equation with respect to x gives $\partial_x\partial_y P = \partial_y\partial_x P = -\partial_y(\partial_x\langle v'v'\rangle) = 0$ since $\partial(\cdot)/\partial x = 0$. Denoting the pressure at the wall by P_w, $\partial_x P = \partial_x P_w$ is constant across the flow. Then the equation (5.11) can be written as

$$\frac{\mathrm{d}\tau}{\mathrm{d}y} = \frac{\mathrm{d}P_w}{\mathrm{d}x}, \tag{5.13}$$

with the total shear stress defined by

$$\tau(y) = \nu\frac{\partial U(y)}{\partial y} - \langle u'v'\rangle. \tag{5.14}$$

In Eq. (5.14) the first term in the right hand side is the viscous stress $\nu\frac{\partial U(y)}{\partial y}$, the second term is the Reynolds stress $-\langle u'v'\rangle$. At the walls the Reynolds stress is zero due to no-slip boundary

condition, so the viscous stress is the only contribution to the total stress. In the region away from the walls the Reynolds stress dominates while the viscous stress is negligibly small compared with the Reynolds stress.

τ is a function of only y and P_w is a function of only x, so both terms in (5.13) are constant. The shear stress is antisymmetric about the mid-plane. The solutions for $\tau(y)$ and dP_w/dx can be expressed in terms of the *wall shear stress* $\tau_w = \tau|_{y=0}$ as

$$- \frac{dP_w}{dx} = \frac{\tau_w}{H}, \qquad \tau(y) = \tau_w\left(1 - \frac{y}{H}\right). \tag{5.15}$$

Therefore the total shear stress is a linear function of y. The *friction velocity* is defined by

$$u_\tau \equiv \sqrt{\tau_w}. \tag{5.16}$$

The Reynolds shear stress is given by the turbulent-viscosity hypothesis as follows,

$$- \langle u'v'\rangle = \nu_t \frac{dU(y)}{dy}. \tag{5.17}$$

Assume the pressure gradient in the left hand side of the equation (5.11) is negligibly small, we obtain

$$\frac{d}{dy}\left((\nu + \nu_t)\frac{dU}{dy}\right) = 0. \tag{5.18}$$

Integrating over y of (5.18) leads to

$$(\nu + \nu_t)\frac{dU}{dy} = (\nu + \nu_t)\frac{dU}{dy}\bigg|_{wall} = \tau_w, \tag{5.19}$$

as we know that the turbulent viscosity ν_t is zero at the wall. The dimensionless velocity, wall distance (distance in wall units) and viscosity are defined by

$$U^+ = \frac{U}{u_\tau}, \qquad y^+ = \frac{u_\tau y}{\nu}, \qquad \nu_t^+ = \frac{\nu_t}{\nu}. \tag{5.20}$$

Please note that y^+ is similar to a local Reynolds number. It is identical to Re_τ at the center of the channel. Different layers or regions are defined based on y^+, see Table 7.1 in [96]. Having the above nondimensionalization and $\tau_w = u_\tau^2$, (5.19) can be rewritten as

$$(1 + \nu_t^+)\frac{dU^+}{dy} = 1. \tag{5.21}$$

Assume $\nu_t^+ = \kappa y^+$ and be aware that ν_t^+ is sufficiently small close the vicinity of the wall and $\nu_t^+ \gg 1$ away from the wall, we arrive at the famous law of the wall, viz,

$$U^+ = \begin{cases} y^+, & \text{if } y^+ \leq 11.06 \\ \frac{1}{\kappa}\ln y^+ + B, & \text{if } y^+ > 11.06 \end{cases} \tag{5.22}$$

with $B = 5.2$ a dimensionless integration constant, $\kappa = 0.41$ the von Karman constant. The name *log-law* stems from the fact that the streamwise velocity in the log-layer ($y^+ > 30$) varies logarithmically with the wall unit distance. In the literature, it is shown that the law of the wall has excellent agreement with the DNS data for $y^+ > 30$, except near the channel's mid-plane. An approximative solution, which is in good agreement with the DNS data also for $y^+ < 30$, is given by Reichardt's law [101],

$$U^+ = \frac{1}{\kappa}\ln(1 + 0.4y^+) + 7.8\left[1 - e^{-\frac{y^+}{11}} - \frac{y^+}{11}e^{-\frac{y^+}{3}}\right]. \tag{5.23}$$

5.2   Statistical averaging for turbulent channel flow

The solution to turbulent flows is random (see Fig. 1.1 and 1.2) due to the sensitivity of turbulent flows to perturbations that unavoidably appear in the initial conditions, boundary conditions and material properties. When the channel flow becomes fully developed, the velocity is statistically stationary. For a precise description, we refer to Definition 5.2 below. It turns out that the statistics of the flow are independent of the spanwise z and streamwise x coordinates. In this channel flow simulation, statistics are collected in two homogeneous directions, streamwise x- and spanwise z-direction, and a time interval which starts after the flow reaches statistically steady state.

Recall that the velocity field $\mathbf{u}(\mathbf{x}, t)$ in a turbulent boundary layer flow can be decomposed into a mean part $\langle\,\mathbf{u}\,\rangle$, which is time-independent, and into a fluctuation denoted by $\mathbf{u}'$, i.e.,

$$\mathbf{u}(\mathbf{x}, t) = \langle\,\mathbf{u}\,\rangle + \mathbf{u}'(\mathbf{x}, t), \tag{5.24}$$

where the mean of the fluctuation is zero, i.e.,

$$\langle\,\mathbf{u}'\,\rangle = \mathbf{0}. \tag{5.25}$$

Definition 5.1 *The time averaging filter $\langle\,\cdot\,\rangle_{(t,t+\Delta t)}$ over the interval $(t, t + \Delta t)$ is defined by*

$$\langle\,\mathbf{u}\,\rangle_t = \langle\,\mathbf{u}\,\rangle_{(t,t+\Delta t)} = \frac{1}{\Delta t}\int_t^{t+\Delta t}\mathbf{u}(x, y, z, t)\,\mathrm{d}t.$$

The space averaging filter $\langle\,\cdot\,\rangle_{(x,x+\Delta x)\times(z,z+\Delta z)}$ in the homogeneous (streamwise) x-coordinate direction and the (spanwise) z-coordinate direction over the interval $(x, x + \Delta x) \times (z, z + \Delta z)$ is given by

$$\langle\,\mathbf{u}\,\rangle_s = \langle\,\mathbf{u}\,\rangle_{(x,x+\Delta x)\times(z,z+\Delta z)} = \frac{1}{\Delta x\Delta z}\int_x^{x+\Delta x}\int_z^{z+\Delta z}\mathbf{u}(x, y, z, t)\,\mathrm{d}z\mathrm{d}x.$$

Definition 5.2 *A turbulent channel flow is called fully developed and statistically steady (statistically converged) if the following limit values exist*

$$\lim_{\Delta t\to\infty}\langle\,\mathbf{u}\,\rangle_{(t,t+\Delta t)}\,, \qquad \lim_{\Delta z\to\infty}\langle\,\mathbf{u}\,\rangle_{(x,x+\Delta x)\times(z,z+\Delta z)},$$

where in the following we keep Δx constant and sufficiently large.

After a certain time (resp. after a certain streamwise distance from the channel entrance) and if the spanwise extent of the domain is large enough, then the flow becomes statistically steady. The following theorem now states that averaging over time and/or over the homogeneous coordinate directions give the same solution, which is therefore two-dimensional and steady-state.

Theorem 5.3 (Ergodic theorem (Birkhoff, 1931)) *Consider a fully developed turbulent boundary layer flow, which is homogeneous in (spanwise) z-coordinate direction. Then*

$$\lim_{\Delta t \to \infty} \langle\, \mathbf{u}\, \rangle_{(t,t+\Delta t)} \;=\; \lim_{\Delta z \to \infty} \langle\, \mathbf{u}\, \rangle_{(x,x+\Delta x)\times(z,z+\Delta z)} \equiv \overline{\mathbf{u}}(y).$$

As both time-averaging and space-averaging (over homogeneous directions) are the same, we may define the statistical averaging operator $\langle\,\cdot\,\rangle$ by

$$\overline{\mathbf{u}}(y) \;\equiv\; \langle\, \mathbf{u}\, \rangle \;=\; \lim_{\Delta t \to \infty} \langle\, \mathbf{u}\, \rangle_{(t,t+\Delta t)} \;=\; \lim_{\Delta z \to \infty} \langle\, \mathbf{u}\, \rangle_{(x,x+\Delta x)\times(z,z+\Delta z)}. \tag{5.26}$$

However, in numerical simulations Δz is a finite value given by the spanwise extent of the computational domain and Δt has to be chosen sufficient large (see below). We combine both time and space averaging operators to approximate the statistics,

$$\langle\, \mathbf{u}\, \rangle \;=\; \langle\, \langle\, \mathbf{u}\, \rangle_s\, \rangle_t \;=\; \langle\, \langle\, \mathbf{u}\, \rangle_{(x,x+\Delta x)\times(z,z+\Delta z)}\, \rangle_{(t,t+\Delta t)}. \tag{5.27}$$

In the simulation, we run THETA and let the flow develop to reach the statistically steady state till time T_{start}. We now have to approximate the time and space filter operations. This is done as follows: First, sum up each velocity component u, v, w and their products uu, vv, ww and uv for each time step at those points where their y-coordinates are the same, it means that the summation is done on each (xz) plane which is parallel to the wall. Second, average them on this (xz) plane and on the time interval $[T_{\text{start}}, T_{\text{stop}}]$ to get averaged values $\langle\,\cdot\,\rangle$. We use the following formula to average the quantities of the simulation,

$$\langle\, \phi\, \rangle \approx \langle\, \langle\, \phi\, \rangle_s\, \rangle_t = \frac{1}{N_x N_z (T_{\text{stop}} - T_{\text{start}})} \sum_{l > T_{\text{start}}}^{T_{\text{stop}}} \left(\sum_{k=1}^{N_z} \sum_{i=1}^{N_x} \phi(x_i, y, z_k, t_l) \right), \tag{5.28}$$

where ϕ is an arbitrary flow variable depending only on y, N_x, N_z are the numbers of sample points in x- and z-direction, T_{start} and T_{stop} are the time points of starting and stopping sampling. It is easy to show that the averaging procedure (5.28) fulfills the properties of Assumption 3.0.1. As an example, let us compute the root mean square (rms) value of the velocities using these properties:

$$\begin{aligned}
\langle\, u_i' u_j'\, \rangle &= \langle\, (\, u_i - \langle\, u_i\, \rangle\,)(\, u_j - \langle\, u_j\, \rangle\,)\, \rangle \\
&= \langle\, u_i u_j - u_i \langle\, u_j\, \rangle - \langle\, u_i\, \rangle u_j + \langle\, u_i\, \rangle\langle\, u_j\, \rangle\, \rangle \\
&= \langle\, u_i u_j\, \rangle - \langle\, u_i\, \rangle\langle\, u_j\, \rangle, \qquad\qquad \text{for } i = 1, 2, 3. \tag{5.29}
\end{aligned}$$

From this relation we see that the rms values can be computed only from suitable mean values.

The control flow of collecting statistics in the DLR-THETA-code is shown as follows:

$\boxed{\textbf{control flow of statistics}}$

- **Physical time steps: FOR** $\tau = 0, \ldots, T_{\text{stop}}$ **DO**

    - THETA Solver
    - **IF**$(\tau > T_{\text{start}})$
        · Sum up the interested quantities for each fixed y
    - **ENDIF**

- **ENDDO**

- Average over $N_x N_z$ and $T_{\text{stop}} - T_{\text{start}}$.

5.3 Test case setup

The computational domain is $[0, 2\pi] \times [0, 2] \times [0, \pi]$, i.e., $L = 2\pi$, $H = 1$ and $b = \pi$. To simulate fully developed region with a short channel, periodic boundary condition is imposed in streamwise x direction, no-slip condition for the walls in y direction and symmetric planes in the spanwise z direction. A Reynolds number based on the friction velocity and channel halfwidth $Re_\tau = 395$ is considered. For this flow, DNS data by Moser *et al.*, see [88], are available as reference data.

Initial conditions

Reichardt's law is adopted as the mean initial velocity

$$U_R(y) = U_R^+(y^+)u_\tau \tag{5.30}$$

with

$$U_R^+(y^+) = \frac{1}{\kappa}\ln(1 + 0.4y^+) + 7.8\left[1 - e^{-\frac{y^+}{11}} - \frac{y^+}{11}e^{-\frac{y^+}{3}}\right], \tag{5.31}$$

where $\kappa = 0.41$ is the von Karman constant and $B = 5.2$ the log-law constant. Therein, u_τ is given by the Reynolds number $u_\tau = Re_\tau \nu / H$, where we use $\nu = 1.53 \times 10^{-5}$ [ms^{-2}]. The velocity profile is plotted in Fig. 5.2 and is used in [12] as reference data. From Fig.

5.2 we can see that the mean initial data we start with is quite close to the DNS data. The perturbation of 10% of the bulk velocity is added to $U_R(y)$ to form the initial velocity:

$$u_0 = U_R(y) + 0.1U_{\text{bulk}}\psi_{\text{ran}}, \tag{5.32}$$

$$v_0 = 0.1U_{\text{bulk}}\psi_{\text{ran}}, \tag{5.33}$$

$$w_0 = 0.1U_{\text{bulk}}\psi_{\text{ran}}, \tag{5.34}$$

where ψ_{ran} is a random number in the interval [-1,1], and U_{bulk} is obtained from (5.1) with $U_R(y)$ instead of U. Although the initial velocity field is not divergence free, the equation of continuity is enforced immediately due to the projection scheme. The statistically converged solution is not affected by the particular choose of the initial perturbation.
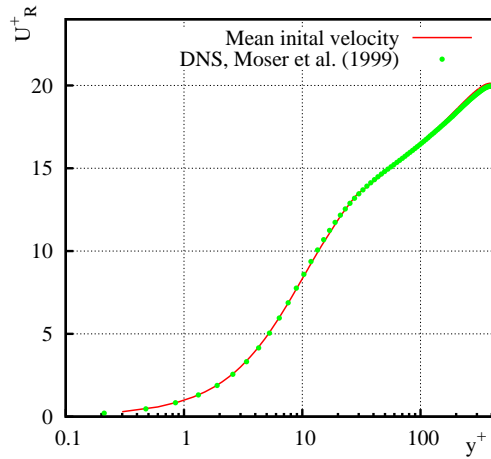
Figure 5.2: The mean initial velocity.

Computational grid

For the subgrid-scale model, we need a sufficiently fine grid resolution to capture the near-wall dynamics. Near the no-slip wall the mean free path of the molecules is small compared with the characteristic scales of the motion, it means that there exist steep gradients in this region. If the stress is computed with a finite-difference approximation, the distance of the first grid point away from the wall should not be too large. Usually, the first point is placed in the range $0 < y^+(1) \leq 1$ with $y^+ = yu_\tau/\nu$. The minimum resolution for representing the resolved scales is $\Delta x^+ < 80$ and $\Delta z^+ < 20$ as indicated by Zang [131]. Gravemeier [40] uses $\Delta x^+ = 57.92$ and $\Delta z^+ = 28.92$ for a simulation of the turbulent channel flow with the variational multiscale method.

The spatial discretization using $N_1 \times N_2 \times N_3 = 64 \times 64 \times 64$ control volumes in $x-$, $y-$ and $z-$direction, respectively, are employed. The mesh sizes in the streamwise x and spanwise
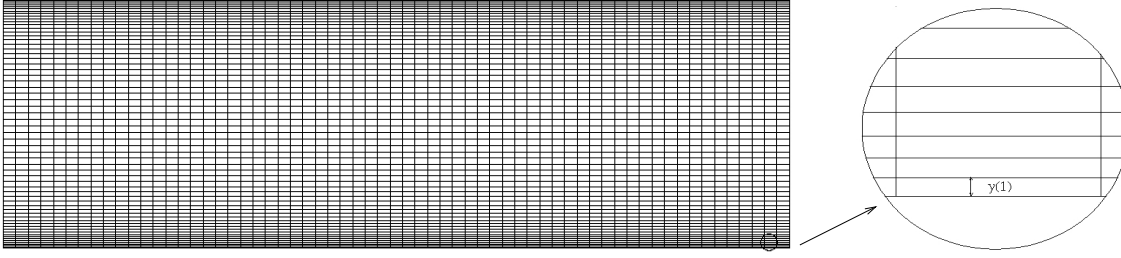
Figure 5.3: Mesh of a channel in *xy* plane.

z direction are uniform. The grid in wall normal direction is stretched using a hyperbolic-tangent function, as in [57, 87],

$$\frac{y(j)}{H} = \frac{\tanh[\gamma(2j/N_2 - 1)]}{\tanh(\gamma)} + 1.0, \qquad j = 0, \dots, N_2 - 1, \tag{5.35}$$

where $y(j) \in [0.0, 2.0]$ is the coordinate of *j*th grid point in *y* direction. The stretching parameter γ is taken to be 2.2, 1.72, 1.5 and 1.2, respectively. The wall unit length at shifted (first) wall point $y^+(1)$ =0.39(1.45), 0.79(2.92), 1.06(3.92) and 1.45(5.39), where the values in parentheses represent the first point away from the wall of the primary grid. Here the grid cells have $\Delta x^+ = 38.78$, $\Delta z^+ = 19.39$ and $\Delta y^+_{min}(\Delta y^+_{max}) = 0.39(29.26)$, 0.79(22.99) 1.06(20.77), 1.45(18.22). They are listed in Table 5.1.

γ	2.0	1.72	1.5	1.2
$y^+(1)$	0.39	0.79	1.06	1.45
Δy^+_{max}	29.26	22.99	20.77	18.22
Δx^+	38.78			
Δz^+	19.39			

Table 5.1: Grid resolution of channel flow at $Re_\tau = 395$.

Computational time step

The computational time step in wall units is defined as

$$\delta t^+ = \frac{u_\tau^2}{\nu} \delta t, \tag{5.36}$$

where u_τ is the friction velocity, ν the kinematic viscosity. It was discovered by Choi and Moin in [16] that for $\delta t^+ \geq 1.6$ the calculations result in laminar flow solutions for both the Crank-Nicolson and the backward Euler scheme. The viscous time scale in the sublayer (the so-called Kolmogorov time scale) is given by $\tau^+ = (u_\tau^4/\epsilon\nu)^{1/2} \approx 2.4$ (see [118]) in wall units,

where ϵ is the dissipation rate per unit mass. The computational time step of 1.6 is close to the Kolmogorov time scale, so they deduced that the computational time step should be less than the Kolmogorov time scale to maintain turbulence. Moreover, they observed that the turbulence fluctuations can only be sustained at $\delta t^+ = 0.4$ or smaller. However, in Ham *et al.* [46], it is reported that turbulent flow solutions over the entire range of computational time steps $\delta t^+ = 0.4$ to 5.0 can be achieved with fully conservative scheme (mass, momentum and energy discretely conserve in both space and time).

In [39], $\delta t^+ = 0.69 \sim 0.92$ is used for the channel flow at $Re_\tau = 590$ and the averaging period is up to 4600 steps. In this study the time step size in wall units is $\delta t^+ = 0.4$, which corresponds to $\delta t = 0.17$ [s]. 8000 time steps are performed to let the flow develop and reach the statistical steady state, statistics are collected in another 6000 steps.

Mass flux correction

If the flow is only driven by the pressure gradient given in (5.9), we can observe a decrease of the mass flux ρU_{bulk}, where ρ is the density of the flow. The mass flux is identical to the bulk velocity since $\rho = 1.0$. To keep the mass flux constant during simulation, a dynamical adjustment of the driving force is employed. Let $U_{\text{bulk,THETA}}(\delta t_n)$ be the bulk velocity of the computed solution of the DLR-THETA-code at time step δt_n and $U_{\text{bulk,DNS}}$ be the desired bulk velocity obtained from the DNS data. Then the modified source term of the Navier-Stokes equations is, as in [57],

$$\mathbf{f}(\delta t_{n+1}) = \begin{pmatrix} \frac{u_\tau^2}{H} \\ 0 \\ 0 \end{pmatrix} + \frac{1}{\delta t_n} \begin{pmatrix} U_{\text{bulk,DNS}} - U_{\text{bulk,THETA}}(\delta t_n) \\ 0 \\ 0 \end{pmatrix}, \tag{5.37}$$

where u_τ is computed from the Reynolds number Re_τ. The correction term enforces the mass flux conservation. When $U_{\text{bulk,THETA}}(\delta t_n)$ is larger than $U_{\text{bulk,DNS}}$, the source term will decrease to make the flow slow down, otherwise it will speed up.

5.4   Solver and model parameters affecting the solution

In Chapter 4, we compared some numerical schemes and parameters for DHIT. We cannot consider all those cases here, for the channel flow is much more complicated and more time consuming. Please note that this mesh with 64^3 grid points leads to a discrete problem with more than 10^6 degrees of freedom.

Within our calculation for DHIT (see Chapter 4), the QUDS with skew-symmetric form of the nonlinear term (QUDS_sk) gave in general better results than the divergence form. Moreover, the CDS scheme without skew-symmetric form gave the best results. So we will use here the CDS and QUDS_sk schemes.

The following parameters and schemes will be considered for the channel flow:

- solver parameter: discretization schemes, CDS and QUDS_sk,

- model parameters:

  - filter width Δ,
  - Smagorinsky constant C_S,
  - the wall distance of the nearest wall point $y^+(1)$.

As discussed in Section 3.3.2, we consider two choices for the filter width Δ and damping functions:

- SMG: $\Delta = V_c^{1/3}$, the cubic root of the volume of the cells, $D(y^+) = 1 - e^{-y^+/A^+}$ with $A^+ = 26$,

- SMG-MOD: $\Delta = \Delta_T$ from (3.54) and $D_3(y^+) = \left\{ 1 - \exp\left[-\left(\frac{y^+}{A^+}\right)^3 \right] \right\}^{1/2}$.

Only the classical Smagorinsky model is studied with variation of the constant C_S for both cases. C_S is the object value that we want to identify for the channel flow. All simulations are performed on a single processor with the DLR-THETA-code. Thus, the computations are quite time-consuming, each of them takes around one week.

5.5 Numerical results

The numerical results of time- and plane-averaged quantities are normalized by friction velocity u_τ, which is computed by a one-sided difference with averaged mean velocity at the walls,

$$u_\tau = \frac{1}{2}\left(\sqrt{\nu\frac{U_{w,b}}{y_w}} + \sqrt{\nu\frac{U_{w,t}}{y_w}} \right), \tag{5.38}$$

where $U_{w,b}$ ($U_{w,t}$) is the mean velocity at the bottom (top) wall and y_w is the wall distance of the first node. Fig. 5.4 shows the instantanous friction velocity at the bottom wall, where $u_{w,b}$ is the instantaneous space-averaged velocity at the bottom wall, and $U_{w,b} = \langle u_{w,b} \rangle_t$ is averaged in a time interval after the flow is fully developed.

The normalized quantities, we are interested in, are:

- the mean velocity $\langle u \rangle$ and the mean velocity in wall units $U^+ = \langle u \rangle / u_\tau$,

- the velocity fluctuations:

$$\langle u'u' \rangle^+ = \frac{\langle u'u' \rangle}{u_\tau^2}, \qquad \langle v'v' \rangle^+ = \frac{\langle v'v' \rangle}{u_\tau^2},$$

$$\langle w'w' \rangle^+ = \frac{\langle w'w' \rangle}{u_\tau^2}, \qquad \langle u'v' \rangle^+ = \frac{\langle u'v' \rangle}{u_\tau^2},$$
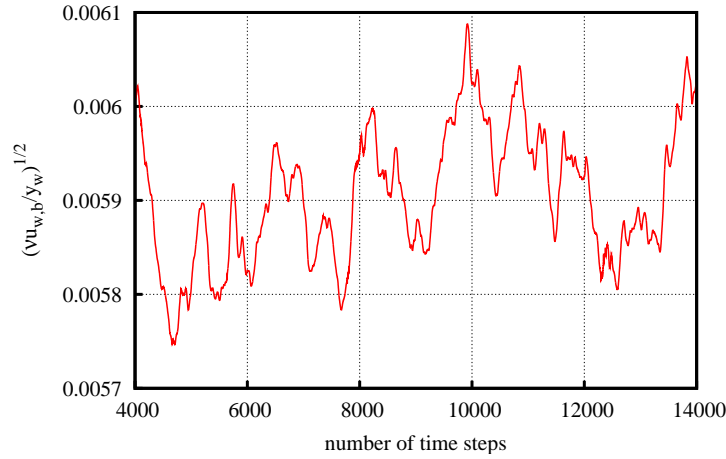
Figure 5.4: Time history of friction velocity at bottom wall for SMG-MOD at $C_S = 0.03$.

- the stresses:

$$S_{12}^{m,+} = \frac{\langle\, \nu_t \,\rangle\langle\, \mathrm{d}u/\mathrm{d}y \,\rangle}{u_\tau^2}, \qquad\qquad \text{the modeled stress}$$

$$S_{12}^{v,+} = \frac{\nu\langle\, \mathrm{d}u/\mathrm{d}y \,\rangle}{u_\tau^2}, \qquad\qquad \text{the viscous stress}$$

$$S_{12}^{t,+} = \frac{(\nu + \langle\, \nu_t \,\rangle)\langle\, \mathrm{d}u/\mathrm{d}y \,\rangle - \langle\, u'v' \,\rangle}{u_\tau^2}, \qquad \text{the total stress}$$

- the rms turbulence intensity (cf. [57] and [130]):

$$u_{rms}^+ = \langle\, u'u' \,\rangle^+ - \frac{1}{3}(\langle\, u'u' \,\rangle^+ + \langle\, v'v' \,\rangle^+ + \langle\, w'w' \,\rangle^+), \qquad (5.39)$$

- the turbulent kinetic energy:

$$k^+ = \frac{1}{2}(\langle\, u'u' \,\rangle^+ + \langle\, v'v' \,\rangle^+ + \langle\, w'w' \,\rangle^+). \qquad (5.40)$$

Since the mean values are either symmetric or antisymmetric to the center line of the channel, the average is also made on the two half channels. All results are only shown on half channel $[0, H]$.

Before we present the results, let us have a closer look at the damping function. For example, for the grid $y^+(1) = 0.39$ and $C_S = 0.05$ the mean velocities with and without damping function are shown in Fig. 5.5. Too much diffusion is produced by the Smagorinsky model, which leads to overprediction of the shear stress. Thus the mean velocity is normalized by a too large friction velocity. Hence, we keep the damping function in our simulations for this channel flow at moderate Reynolds number.
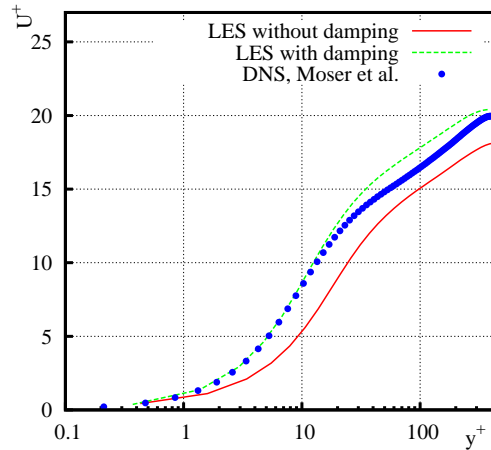
Figure 5.5: The mean velocity for the classical Smagorinsky model without and with damping function at $C_S = 0.05$ and $y^+(1) = 0.39$.

5.5.1 Influence of solver parameter

In this section, the Smagorinsky model with SMG and SMG-MOD using spatial discretization CDS and QUDS_sk is considered. The Smagorinsky constant C_S and grid parameter $y^+(1)$ of the shifted wall point are fixed. Let $C_S = 0.05$ with $\Delta/h = 2$ and $y^+(1) = 0.39$.

Fig. 5.6 and Fig. 5.7 present the corresponding quantities of CDS and QUDS_sk of these two cases, the mean velocities in (a) and mean velocity in wall units U^+ in (b), fluctuations scaled by friction velocity $\langle u'v' \rangle^+$ in (c) and $\langle u'u' \rangle^+$ in (d), u_{rms}^+ in (e) and the kinetic energy k^+ in (f). It is clearly shown that the resolution of CDS scheme has better agreement to DNS than QUDS_sk. So QUDS_sk is not a suitable discretization scheme in this LES computation, it will not be considered in following studies.

5.5.2 Influence of model parameters

Here we study the Smagorinsky model with the influence of grid parameter $y^+(1)$ and model coefficient C_S. The results of grid comparison, where C_S is fixed at 0.05, are plotted in Fig. 5.8-5.9. Very good agreement of the mean velocity and fluctuations are obtained compared with the DNS data, except the peak part of $\langle u'u' \rangle^+$. For the four values of $y^+(1)$, only slight differences can be observed concerning u_{rms}^+ in the middle of the channel in (e) of Fig. 5.8. However, the results of the four grids differ slightly from each other. The robustness with respect to the grid parameter $y^+(1) \in [0.0, 2.0]$ is shown.

In Fig. 5.10-5.11 the corresponding quantities at fixed $y^+(1) = 1.06$ for different values of C_S are reported. The mean velocity and fluctuations of SMG are effected obviously by the model constant C_S. On one hand, larger C_S, e.g. $C_S = 0.1$, provides larger deviation of the

(a): Mean velocity

(b): Mean velocity in wall units

(c): Fluctuation

(d): Fluctuation

(e): u_{rms}^+
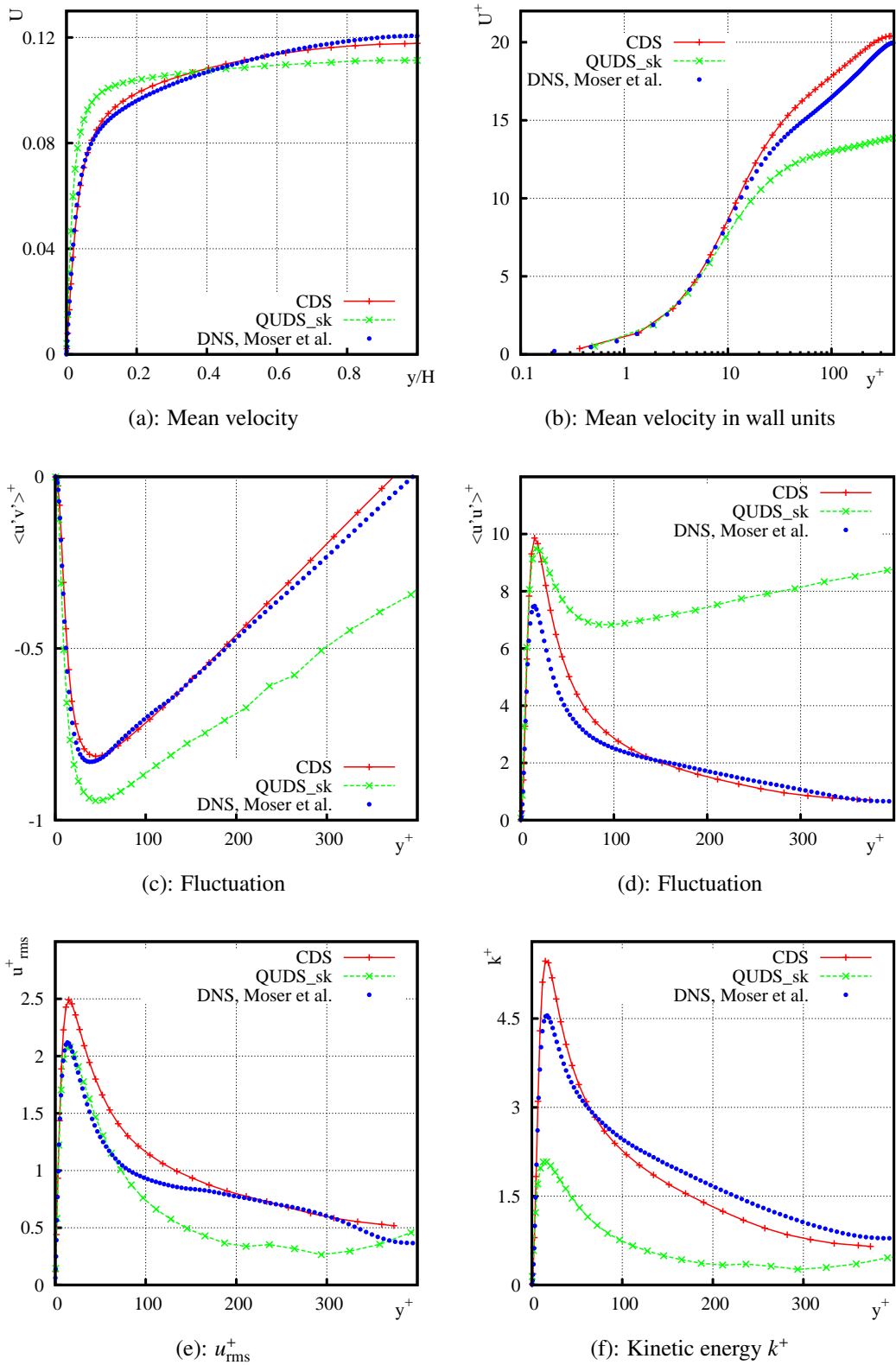
(f): Kinetic energy k^+

Figure 5.6: Comparison of CDS and QUDS_sk for SMG.
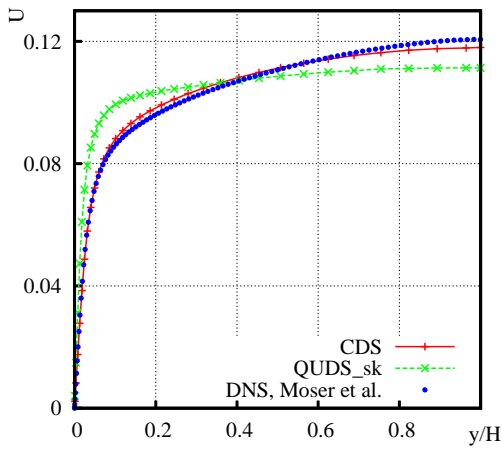
(a): Mean velocity
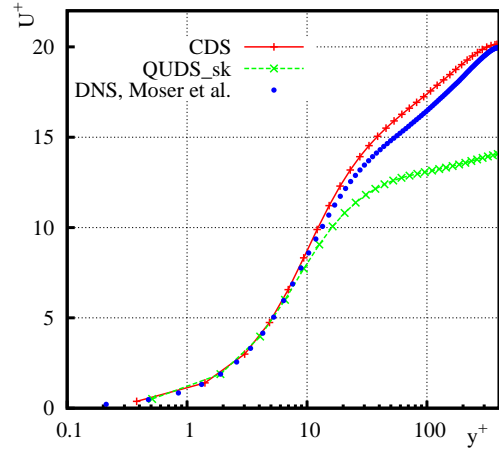
(b): Mean velocity in wall units
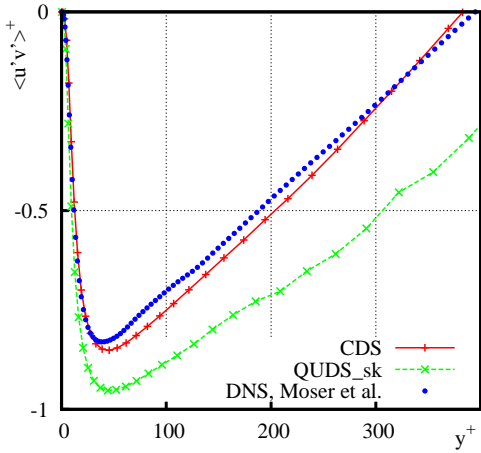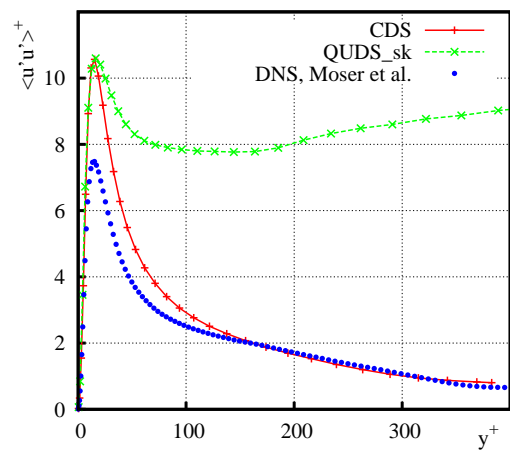
(c): Fluctuation

(d): Fluctuation
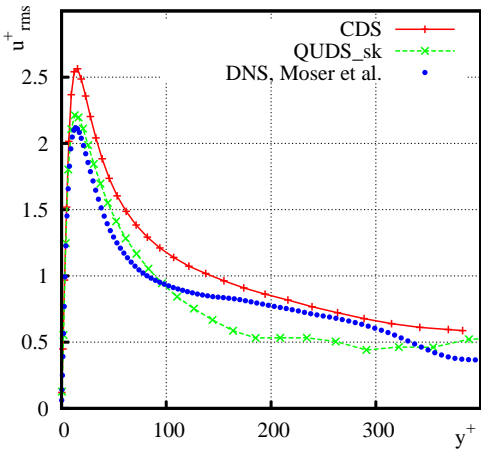
(e): u^+_{rms}
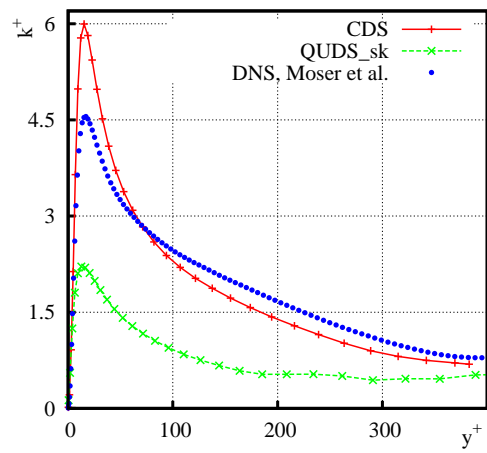
(f): Kinetic energy k^+

Figure 5.7: Comparison of CDS and QUDS_sk for SMG-MOD.

(a): Mean velocity

(b): Mean velocity in wall units

(c): Fluctuation

(d): Fluctuation

(e): u^+_{rms}

(f): Kinetic energy k^+

Figure 5.8: Comparison of results for SMG at $C_S = 0.05$ on different meshes.

(a): Mean velocity

(b): Mean velocity in wall units

(c): Fluctuation

(d): Fluctuation

(e): u_{rms}^{+}

(f): Kinetic energy k^{+}
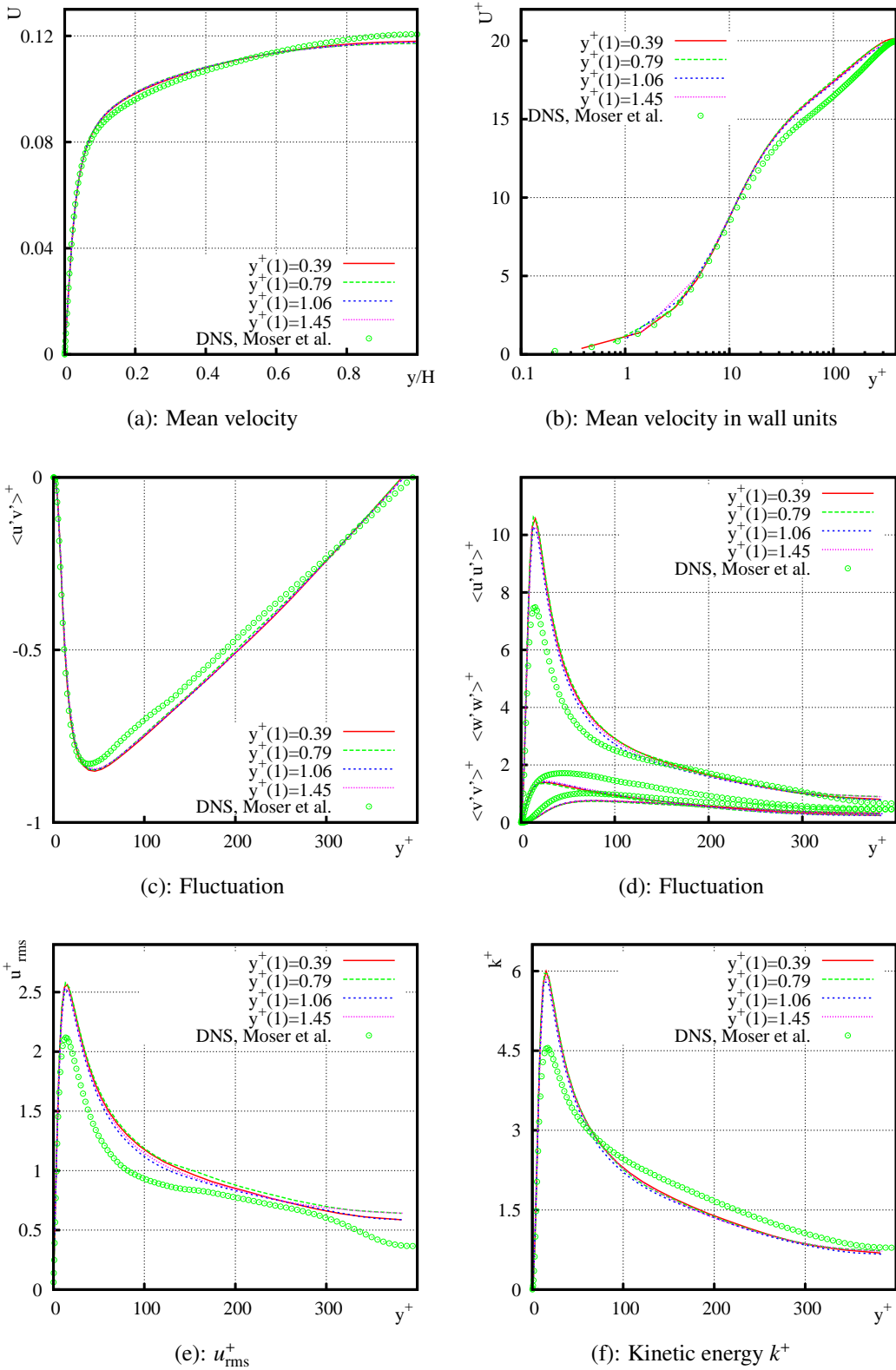
Figure 5.9: Comparison of results for SMG-MOD at $C_S = 0.05$ on different meshes.

(a): Mean velocity

(b): Mean velocity in wall units

(c): Fluctuation

(d): Fluctuation

(e): u^+_{rms}

(f): Kinetic energy k^+
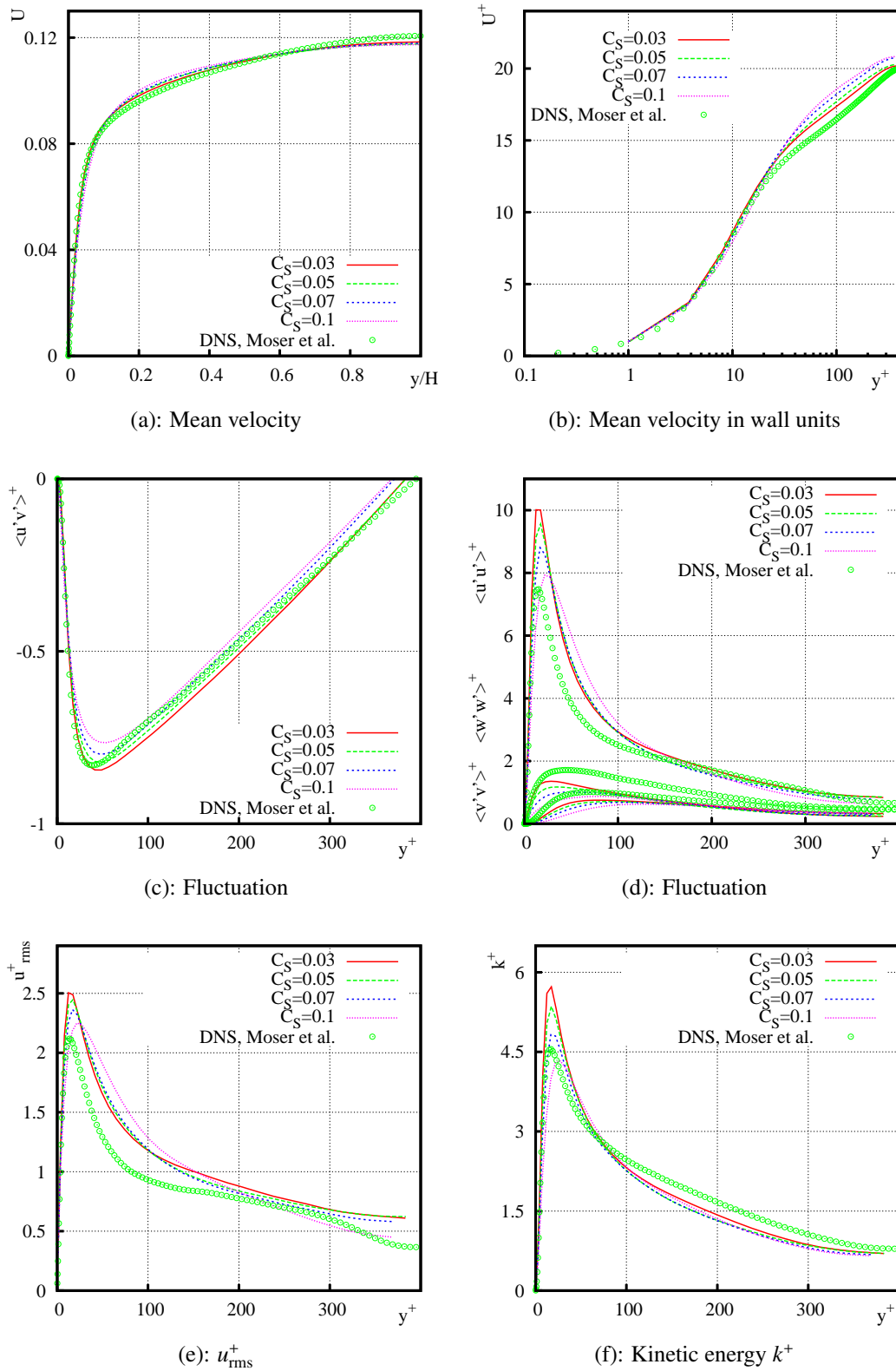
Figure 5.10: Comparison of results for SMG with different C_S on mesh $y^+(1) = 1.06$.

(a): Mean velocity

(b): Mean velocity in wall units

(c): Fluctuation

(d): Fluctuation

(e): u^+_{rms}

(f): Kinetic energy k^+
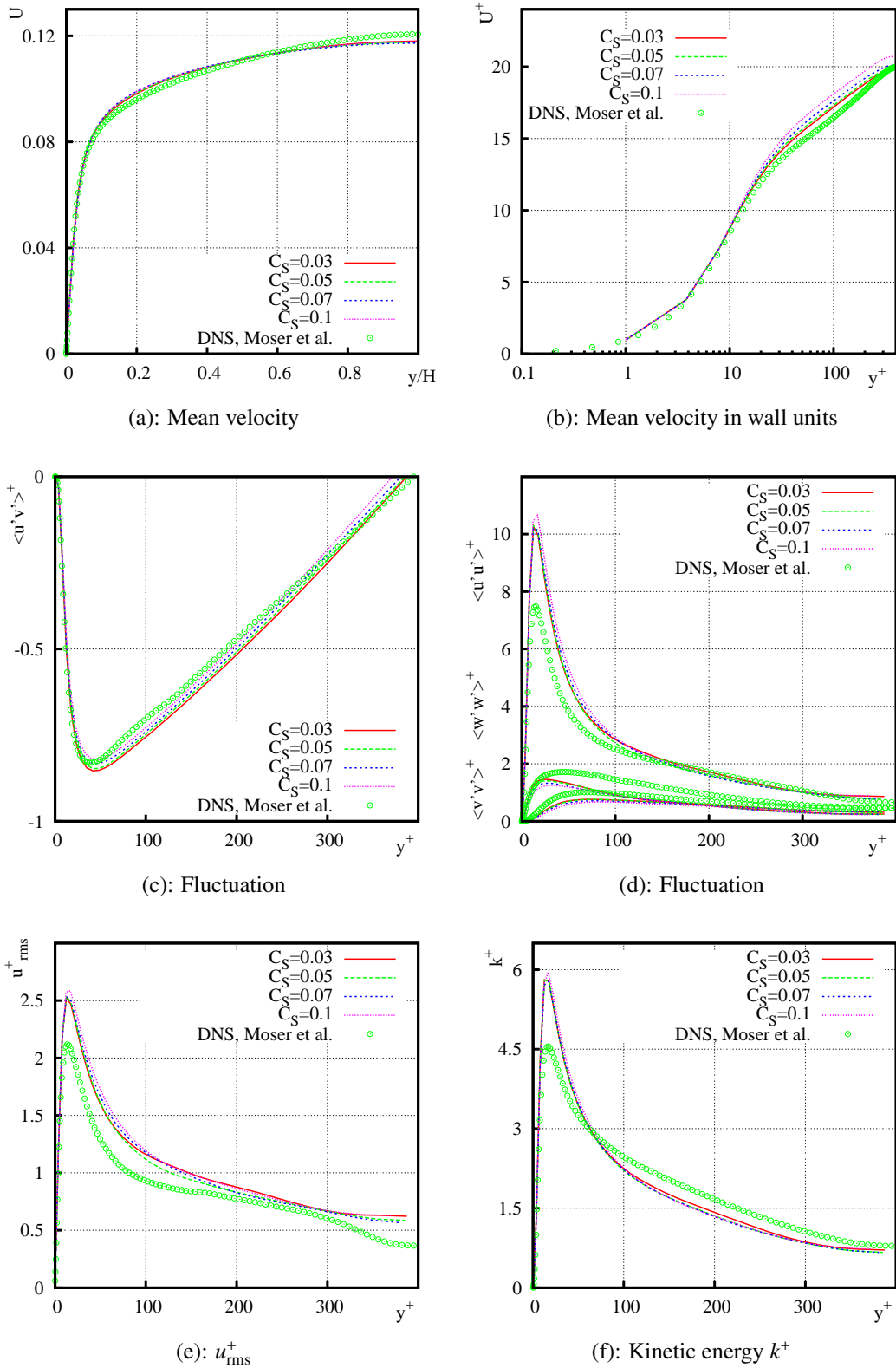
Figure 5.11: Comparison of results for SMG-MOD with different C_S on mesh $y^+(1) = 1.06$.

mean velocity U^+ and shear stress $\langle\, u'v'\, \rangle^+$ to the DNS data. On the other hand, the peak of $\langle\, u'u'\, \rangle^+$ is better predicted at $C_S = 0.1$. Moreover, SMG-MOD is not as sensitive as SMG to the constant C_S as it is stated by Travin *et al.* [122].

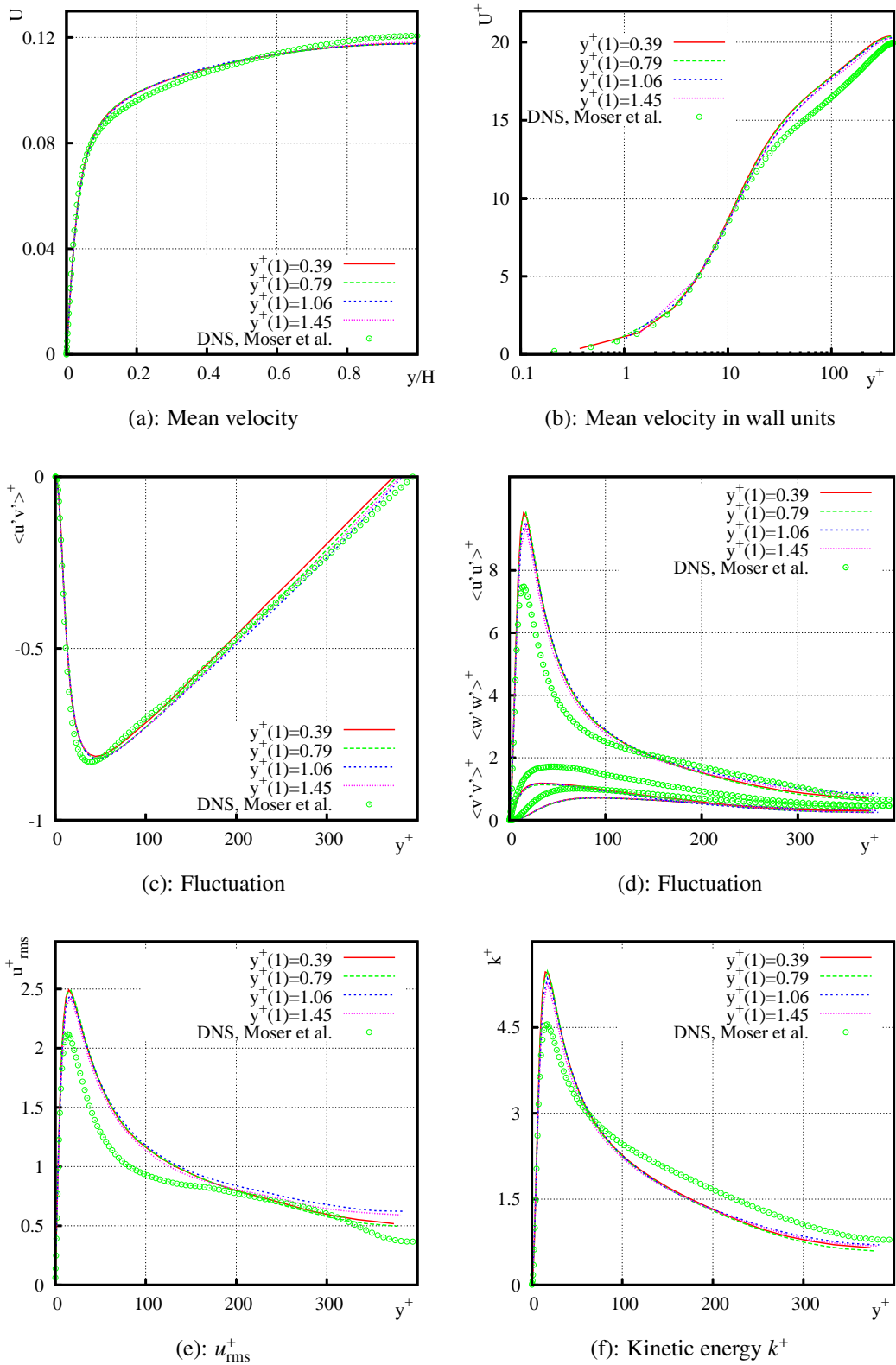For all cases, the near-wall peaks of $\langle\, u'u'\, \rangle^+$ are over-predicted. Concerning the other two components of the fluctuations $\langle\, v'v'\, \rangle^+$ and $\langle\, w'w'\, \rangle^+$, in general, some discrepancy between the numerical results and the DNS data is visible. With respect to the second order statistics, they can be considered more than satisfactory. Furthermore, they are predicted in the near-wall region better by SMG-MOD than by SMG.

5.5.3 Parameter identification

For this plane channel flow, we study the influence of the model parameter C_S and the grid parameter $y^+(1)$. There are two "measurements", the mean velocity and the kinetic energy produced from the DNS data [88], which correspond to the first order and second order statistics, respectively. The discrete L^2-error functionals of the LES results compared to the DNS data for the mean velocity and kinetic energy are defined as

$$J_u(y^+(1), C_S) \;=\; \left(\sum_{i=1}^{N} \left(U_i(y^+(1), C_S) - U_i(DNS) \right)^2 \Delta y_i \right)^{1/2}, \qquad (5.41)$$

$$J_k(y^+(1), C_S) \;=\; \left(\sum_{i=1}^{N} \left(k_i(y^+(1), C_S) - k_i(DNS) \right)^2 \Delta y_i \right)^{1/2}, \qquad (5.42)$$

where N is the number of grid points in the wall normal direction for half channel.

C_S	$y^+(1) = 0.39$	$y^+(1) = 0.79$	$y^+(1) = 1.06$	$y^+(1) = 1.45$
0.01	**1.174939e-03**	**1.491669e-03**	1.631961e-03	1.727693e-03
0.03	1.401019e-03	1.539358e-03	**1.401606e-03**	**1.654914e-03**
0.05	1.941480e-03	2.037467e-03	1.980393e-03	1.733179e-03
0.07	2.419876e-03	1.961264e-03	2.199981e-03	2.041513e-03
0.1	3.377118e-03	3.282331e-03	2.999015e-03	3.032605e-03
0.15	1.277990e-02	1.392222e-02	1.455811e-02	1.570244e-02

Table 5.2: Error functional (5.41) of the mean velocity in L^2-norm for SMG.

$J_u(y^+(1), C_S)$ in Eq. (5.41) does not change if we use U^+ and Δy^+ instead of U and Δy. However, $J_k(y^+(1), C_S)$ will be scaled by the friction velocity u_τ if the quantities in wall units are used. For simplicity, the mean velocity and kinetic energy without normalization by u_τ are considered in the error functionals. Otherwise we need to interpolate the values $U_i^+(DNS)$ and $k_i^+(DNS)$ of the DNS data at the corresponding Δy_i^+ for each single simulation due to the dependence of the friction velocity.

First the error functionals are given in Table 5.2-5.3 for SMG and in Table 5.4-5.5 for SMG-MOD. The values in bold face (also hereafter) are the local minimum of each column. For
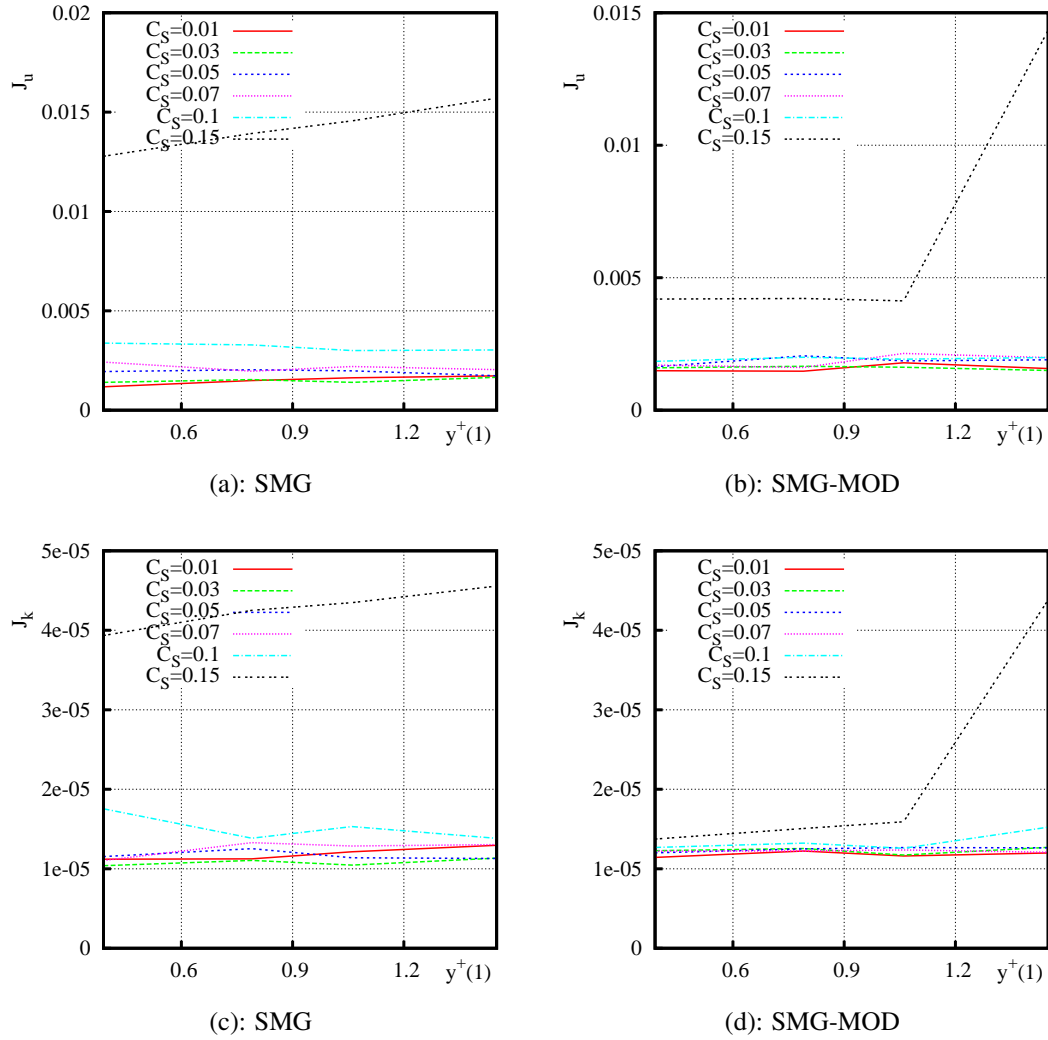
Figure 5.12: Error functionals J_u and J_k w.r.t $y^+(1)$.

C_S	$y^+(1) = 0.39$	$y^+(1) = 0.79$	$y^+(1) = 1.06$	$y^+(1) = 1.45$
0.01	1.120661e-05	1.124371e-05	1.214305e-05	1.295295e-05
0.03	**1.039050e-05**	**1.105665e-05**	**1.046828e-05**	1.134251e-05
0.05	1.153081e-05	1.252580e-05	1.138412e-05	**1.129620e-05**
0.07	1.103141e-05	1.329138e-05	1.286932e-05	1.304741e-05
0.1	1.754787e-05	1.384821e-05	1.530110e-05	1.382863e-05
0.15	3.934463e-05	4.250787e-05	4.348463e-05	4.556251e-05

Table 5.3: Error functional (5.42) of the turbulent kinetic energy in L^2-norm for SMG.

the kinetic energy the values are two orders smaller than those of the mean velocity as they
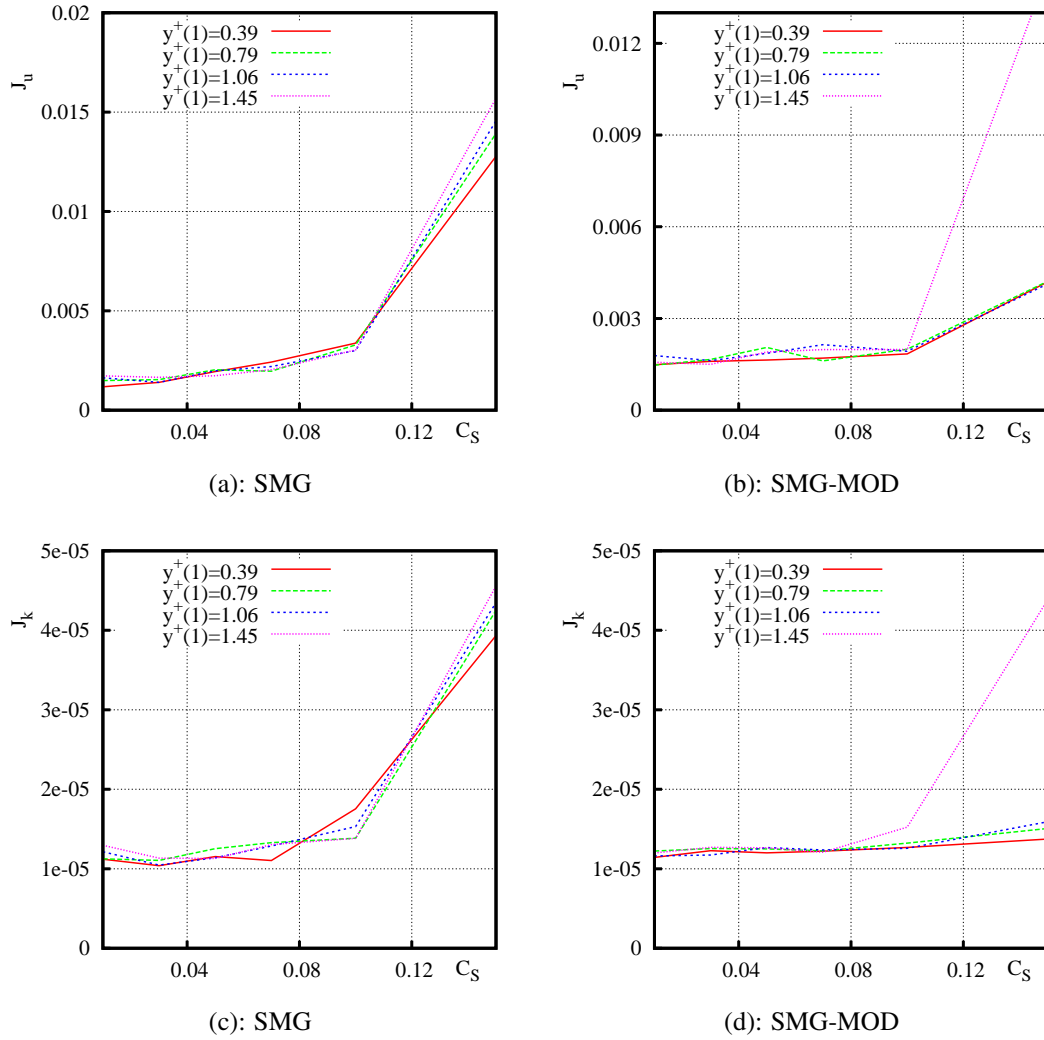
Figure 5.13: Error functionals J_u and J_k w.r.t C_S.

C_S	$y^+(1) = 0.39$	$y^+(1) = 0.79$	$y^+(1) = 1.06$	$y^+(1) = 1.45$
0.01	**1.489004e-03**	**1.472807e-03**	1.787553e-03	1.571086e-03
0.03	1.596579e-03	1.659347e-03	**1.619345e-03**	**1.500220e-03**
0.05	1.640767e-03	2.053577e-03	1.859769e-03	1.901873e-03
0.07	1.703799e-03	1.613097e-03	2.143838e-03	1.981984e-03
0.1	1.841989e-03	1.995355e-03	1.926328e-03	1.988063e-03
0.15	4.194576e-03	4.214954e-03	4.127977e-03	1.433722e-02

Table 5.4: Error functional (5.41) of the mean velocity in L^2-norm for SMG-MOD.

are second order statistics. The grid dependence of $y^+(1)$ is shown in Fig. 5.12. For most of the results except $C_S = 0.15$, the error functionals do not vary much with $y^+(1)$. As can been

C_S	$y^+(1) = 0.39$	$y^+(1) = 0.79$	$y^+(1) = 1.06$	$y^+(1) = 1.45$
0.01	**1.143229e-05**	**1.223304e-05**	**1.160898e-05**	**1.198000e-05**
0.03	1.227487e-05	1.254523e-05	1.172517e-05	1.269032e-05
0.05	1.200307e-05	1.250064e-05	1.266216e-05	1.264217e-05
0.07	1.221617e-05	1.223656e-05	1.235718e-05	1.207071e-05
0.1	1.267544e-05	1.322475e-05	1.257011e-05	1.523791e-05
0.15	1.373046e-05	1.506522e-05	1.591749e-05	4.383285e-05

Table 5.5: Error functional (5.42) of the turbulent kinetic energy in L^2-norm for SMG-MOD.

seen from Fig. 5.13 the lines are quite flat for $C_S \leq 0.1$. It is hard to say which C_S is the best. Actually, for smaller C_S the contribution of turbulence model becomes smaller, i.e. it tends to be no turbulence model, which might be due to the fact that the spatial and temporal resolution is close to be resolution used in a DNS. This is supported by the observation that the case $C_S = 0.0$, which is a DNS, is stable and gives good results. It can be seen from Fig.

(a): $C_S = 0.03$ (b): $C_S = 0.1$
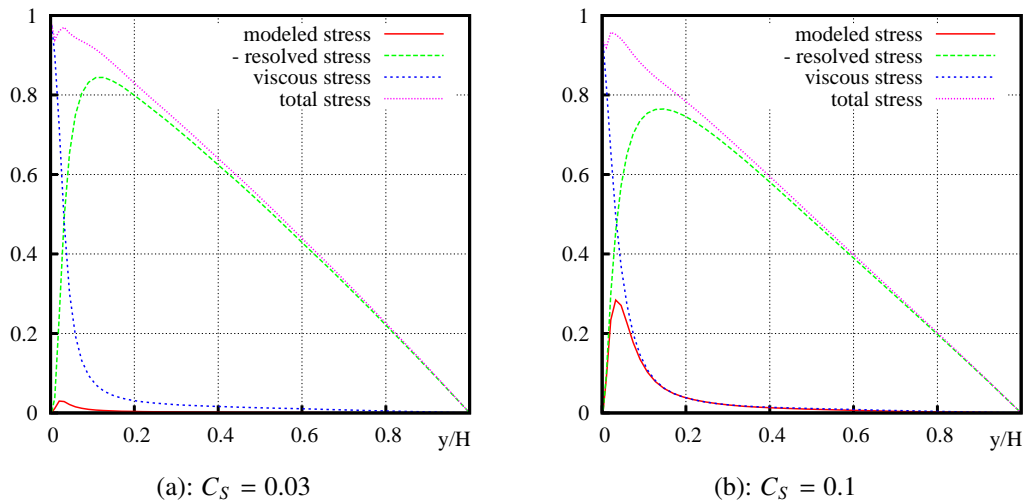
Figure 5.14: Stresses on grid $y^+(1) = 1.06$ at $C_S = 0.03$ and $C_S = 0.1$.

5.14 that the modeled stress becomes smaller with decreasing C_S. Thus the error is probably dominated by the numerical error. For a three-dimensional plot of the dependence on C_S and $y^+(1)$, we refer to Fig. 1.6.

Applying a Newton type method to channel flow could cause problems. For DHIT, there is one pronounced global minimum of the error functional and it is monotonously decreasing/increasing. But for channel flow, first there is no distinct global minimum. Moreover, J_u and J_k have several local minima, which may cause problems to a full Newton method.

In general, the results for SMG-MOD are slightly better than for SMG. The reason for robustness with respect to C_S and $y^+(1)$ could be the proper resolution of the boundary layer

using anisotropically refined meshes with appropriate $y^+(1)$.

In above L^2-fitting is used to evaluate the error functionals. Let us consider the L^∞-norm to the errors of the mean velocity and turbulent kinetic energy compared with the DNS data

$$J_u(y^+(1), C_S) = \max_{1 \le i \le N} |U_i(y^+(1), C_S) - U_i(DNS)|, \qquad (5.43)$$

$$J_k(y^+(1), C_S) = \max_{1 \le i \le N} |k_i(y^+(1), C_S) - k_i(DNS)|. \qquad (5.44)$$

C_S	$y^+(1) = 0.39$	$y^+(1) = 0.79$	$y^+(1) = 1.06$	$y^+(1) = 1.45$
0.01	**2.070800e-03**	2.471000e-03	2.641100e-03	2.866500e-03
0.03	2.282900e-03	**2.405840e-03**	**2.260500e-03**	**2.627500e-03**
0.05	2.973600e-03	3.188230e-03	3.075700e-03	2.808460e-03
0.07	4.657770e-03	5.161150e-03	5.608200e-03	5.301240e-03
0.1	9.794360e-03	8.453160e-03	8.889240e-03	8.902950e-03
0.15	3.368990e-02	3.511853e-02	3.578350e-02	3.677846e-02

Table 5.6: Error functional (5.43) of the mean velocity in L^∞-norm for SMG.

C_S	$y^+(1) = 0.39$	$y^+(1) = 0.79$	$y^+(1) = 1.06$	$y^+(1) = 1.45$
0.01	4.013550e-05	4.333530e-05	4.077330e-05	4.831930e-05
0.03	3.153040e-05	2.655930e-05	3.214270e-05	3.549140e-05
0.05	**1.707430e-05**	**1.759000e-05**	**1.649517e-05**	**1.556626e-05**
0.07	2.334691e-05	2.540660e-05	2.985434e-05	2.489390e-05
0.1	5.651433e-05	5.495002e-05	5.603390e-05	5.757332e-05
0.15	1.396430e-04	1.399473e-04	1.416503e-04	1.472540e-04

Table 5.7: Error functional (5.44) of the turbulent kinetic energy in L^∞-norm for SMG.

C_S	$y^+(1) = 0.39$	$y^+(1) = 0.79$	$y^+(1) = 1.06$	$y^+(1) = 1.45$
0.01	**2.527900e-03**	**2.546200e-03**	3.014500e-03	2.641900e-03
0.03	2.817200e-03	2.589200e-03	**2.642500e-03**	**2.520800e-03**
0.05	2.734100e-03	3.477500e-03	3.049500e-03	3.113600e-03
0.07	2.802900e-03	2.667700e-03	3.391300e-03	3.109700e-03
0.1	2.888100e-03	3.207300e-03	2.987360e-03	3.494210e-03
0.15	1.115313e-02	1.276633e-02	1.323239e-02	4.049765e-02

Table 5.8: Error functional (5.43) of the mean velocity in L^∞-norm for SMG-MOD.

The values of the error functionals in L^∞-norm are given in Table 5.6-5.7 for SMG and in Table 5.8-5.9 for SMG-MOD. As it can be seen that the results are not sensitive to the grid parameter $y^+(1)$, in this case we only plot the error functionals with respect to C_S. They are

C_S	$y^+(1) = 0.39$	$y^+(1) = 0.79$	$y^+(1) = 1.06$	$y^+(1) = 1.45$
0.01	4.400710e-05	4.445890e-05	4.536260e-05	4.618980e-05
0.03	4.241410e-05	4.144300e-05	4.377050e-05	4.667210e-05
0.05	3.982650e-05	4.116680e-05	4.101430e-05	4.400070e-05
0.07	3.341290e-05	3.496490e-05	3.345360e-05	3.281310e-05
0.1	**3.028630e-05**	**2.533120e-05**	**2.712490e-05**	**2.004818e-05**
0.15	3.940759e-05	4.836350e-05	4.973650e-05	1.481393e-04

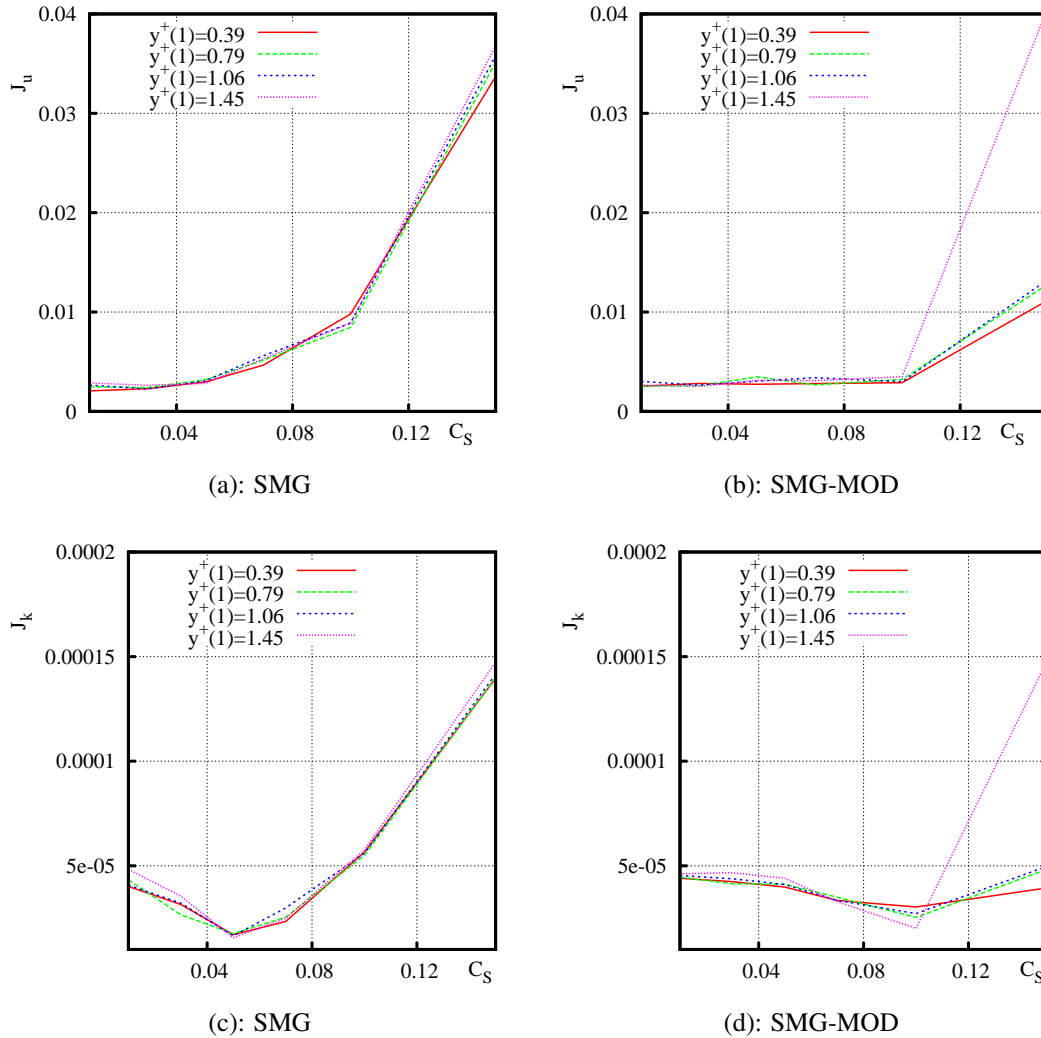Table 5.9: Error functional (5.44) of the turbulent kinetic energy in L^∞-norm for SMG-MOD.

Figure 5.15: Error functionals J_u and J_k in L^∞-norm w.r.t C_S.

shown in Fig. 5.15. Again, the dependence of SMG-MOD on C_S is not strong compared to SMG. For the turbulent kinetic energy there exists a certain minimum, however, at the

corresponding C_S the mean velocity behaviors differently.

In this chapter, two LES (the classical Smagorinsky and a modified Smagorinsky model) are considered for plane channel flow at $Re_\tau = 395$. We may draw the following conclusions:

- First, these two LES models are feasible for moderate Reynolds number with the DLR-THETA-code. For the high Reynolds number case we refer to Chapter 6.

- The robustness with respect to the grid parameter $y^+(1) \sim O(1)$ and $C_S < 1.5$ is shown given CDS and proper anisotropic layer-adapted grid. It does the job even for no turbulence model.

- A value of the Smagorinsky constant $C_S \geq 1.5$ is not appropriate for the two LES models.

- In general, the Smagorinsky model with modified filter width presents better results than the classical Smagorinsky model, and has weaker sensitivity to the parameters.

- Moreover, van Driest-damping is necessary in the case of moderate Reynolds number flow. However, it is difficult to implement for complex geometries.

- Finally, no optimal value is given from this study, an alternative choice could be to use the optimal C_S for DHIT.

Chapter 6

Numerical results for hybrid models

In this chapter we will consider hybrid methods for turbulent flows. Although LES is a routinely used approach to investigate turbulent flows, the near-wall resolution of wall-bounded flows has to be increased when the boundary layer thickness δ_{99} decreases with the increasing Reynolds number. In order to reduce the computational cost, a well-known approach is the detached-eddy simulation (DES) (see Section 3.4.1) which applies a RANS approach in the boundary layer and LES in the separation region. Another approach is to avoid resolving the near-wall layer by using wall models to provide wall stress boundary conditions to LES. Wall functions are used in the near-wall treatment. After a short overview we reconsider the benchmark problems of Chapters 4 and 5 and apply the hybrid methods. Then we study the plane channel flow at $Re_\tau = 4800$.

6.1   Overview

The basic principles of DES approach are first described by Spalart *et al.* [114]. Shur *et al.* [109] presented the first results of DES and derived the DES constant C_{DES} based on the simulation of DHIT. The plane channel flow in a wide range of Re_τ was investigated by Nikitin *et al.* [89]. Although friction velocity is underpredicted by up to 15% which leads to an overprediction of the velocity profile in the logarithmic law region, the results are stable up to very high Reynolds number on rather coarse grids. Another test case of the flow past a circular cylinder was studied by Travin *et al.* [123]. The values of drag, shedding frequency, pressure and skin friction have good agreement to the experimental data, however, large disagreements occur to the Reynolds stress and the length of the recirculation bubble. Moreover, Breuer *et al.* [11] made a comparison of DES, RANS and LES for the separated turbulent flow around a inclined flat plate. A good agreement of LES and DES is obtained after using a modified filter width and making some near-wall corrections.

Between RANS and LES lies a *gray region* (DES buffer layer), where the simulation of turbulence changes from fully modeled to almost fully resolved. That is the reason why Nikitin

et al. [89] obtained two logarithmic layers with no adjustment of the Spalart-Allmaras (SA) based DES model. The lower layer (modeled log layer) arises due to the RANS mode, while the upper layer (resolved log-layer) arises due to the LES mode. It implies an under-prediction of the skin-friction coefficient around by 15%. Travin *et al.* [122] proposed a blending of the RANS and LES length scale to the turbulent flow. It is shown that the resolved log-layer is adjusted with this new hybrid model, nevertheless, it is more complex. An alternative approach developed by Keating and Piomelli [62] is to use a dynamic stochastic forcing method coupled with DES, which assumes that the modeled and resolved Reynolds shear stress be approximately equal in the LES/RANS interface. It is found that the method removes the shift of the resolved log-layer and improves the prediction of the fluctuations for turbulent channel flow. However, new parameters are introduced in this approach, they need to be generalized.

Kalitzin *et al.* [61], Medic *et al.* [81] and Templeton *et al.* [117] proposed an eddy-viscosity-based near-wall treatment to enable the performance of LES on coarse grids. A correction is made to the eddy-viscosity in the near-wall region by adding the resolved turbulent stress to the RANS eddy-viscosity.

At high Reynolds number, the near-wall resolution requirements make the calculation of turbulent flows more expensive and not applicable to many practical problems. The simple way is to perform LES only in the outer layer by modeling the effect of the wall layer. One needs to provide the wall stress from the wall layer to the out layer flow. It is known as approximate boundary conditions. The wall stress can be determined from an algebraic relation for the turbulence model variables in the log-law region.

The idea of wall functions [107] method is to apply the approximate boundary conditions to turbulence models away from the wall, at a location in the log-law region. Thus, the first node can be located farther from walls, e.g. $y^+(1) \simeq 50$. The log-law has the form as (5.22),

$$U^+ = \frac{1}{\kappa}\ln y^+ + B, \qquad B = 5.2. \tag{6.1}$$

Here U^+ and y^+ are the nondimensionalized velocity and wall distance following (5.20), respectively. $\kappa = 0.41$ is the von Karman constant. Usually, a more complicated form can be used as wall function, such as Reichardt's law (5.23).

The wall function approach is quite attractive in application to complex flows because of its simplifications. Piomelli *et al.* [94] studied two broad classes of boundary condition approaches. Cabot and Moin [13] used a dynamic LES model together with using the law of the wall to predict the wall stress. For detailed review of wall functions till 2002, the reader is directed to Piomelli and Balaras [93].

6.2   Decaying homogeneous isotropic turbulence

For the hybrid approach SADES, we study the LES part with the same benchmark problem DHIT as in Chapter 4 in a cubic box.

6.2.1 SADES for DHIT

Since there is no boundary layer involved in this test case, the length scale $\tilde{d}$ in equation (3.58) is given by

$$\tilde{d} = C_{DES}\Delta, \quad \text{with} \quad \Delta = \max(\Delta x, \Delta y, \Delta z), \tag{6.2}$$

where C_{DES} is a model constant. Δ is the DES filter width related to the grid size $\Delta x, \Delta y, \Delta z$. Only LES mode is activated in this simulation.

In SADES, the turbulent viscosity is computed from the quantity $\tilde{\nu}$ which is the solution to the additional scalar equation (3.19), see Section 3.2.3 and 3.4.1. We use the velocity extracted from the experimental data at the initial time $t = 0.0$ as the initial condition. The kinetic energy decays with time. Thus, the initial condition of this scalar equation is of great importance to the solution. The idea is to use the kinematic viscosity as the initial guess and solve the scalar equation by freezing the velocity, that is, no momentum equation and pressure equation is solved in this process. After a convergent solution is obtained for the scalar equation, we solve the entire system, the momentum equation together with the pressure equation and scalar equation, with the solution to the scalar equation as the intial condition to it. The time step is $dt = 0.0001$ for the freezing velocity process and 50000 steps are carried out. Then the time is reset to zero and $dt = 0.0087$ is used to perform the simulation till $t = 0.87$ and $t = 2.0$.
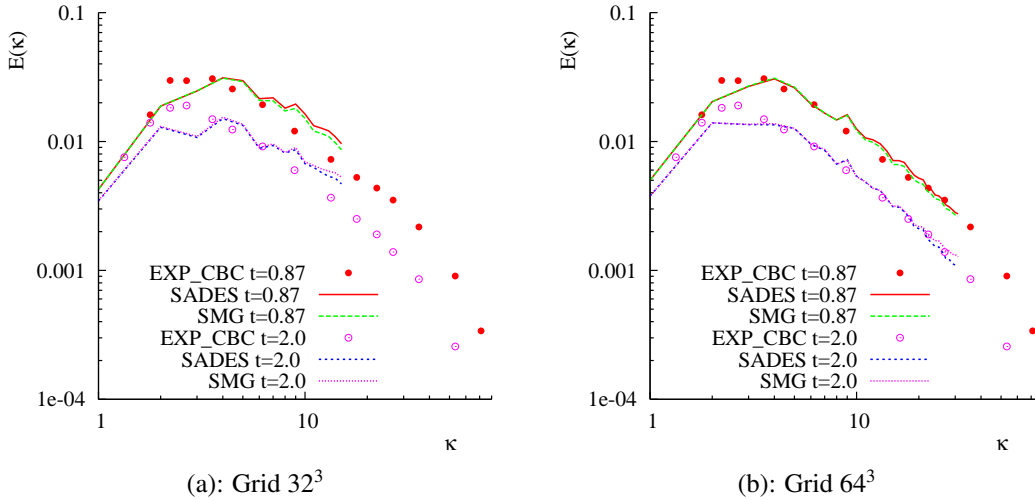

(a): Grid 32^3 (b): Grid 64^3

Figure 6.1: Energy spectra of DHIT for SADES and SMG.

In Fig. 6.1, both energy spectra of the Smagorinsky model (SMG) at the best $C_S = 0.094$ obtained in Chapter 4 and SADES with $C_{DES} = 0.65$ are shown in comparison with the experimental data (EXP_CBC, Comte-Bellot & Corrsin [19]) at time $t = 0.87$ and 2.0. SADES gives very good agreement to the results of the optimized SMG and the experimental data.

In the following, we will study the influence of the constant C_{DES} in this model. We consider only the fine grid 64^3 for the parameter identification. By setting $q = C_{DES}$, the error functional (4.17) is written as

$$J(C_{DES}) = \left(\sum_{i=1}^{N/2-1} \left[\left(E(\kappa_i, C_{DES}) - E_{exp}(\kappa_i) \right)^2_{t=0.87} + \left(E(\kappa_i, C_{DES}) - E_{exp}(\kappa_i) \right)^2_{t=2.0} \right] \right)^{1/2}, \quad (6.3)$$

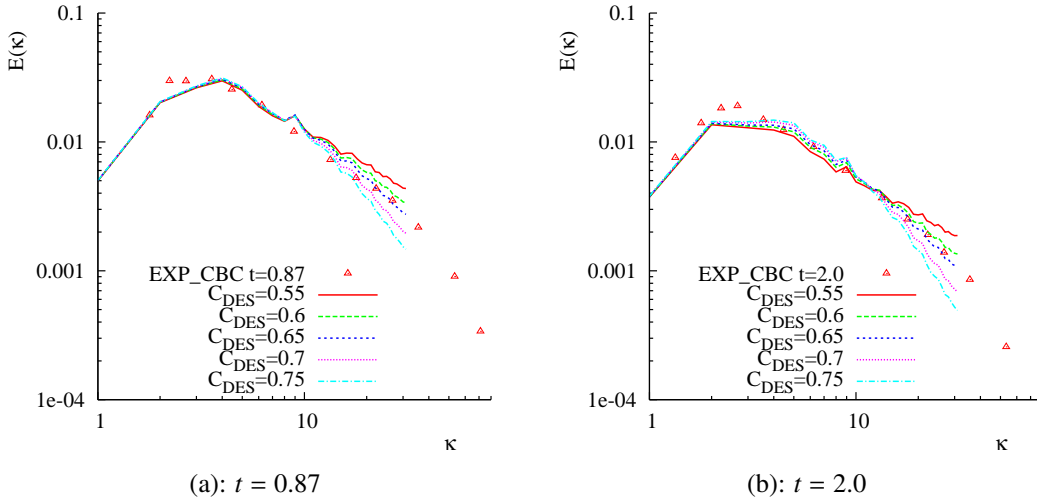with $N = 64$ the number of grid points in one spatial direction. The energy spectra of

(a): $t = 0.87$ (b): $t = 2.0$

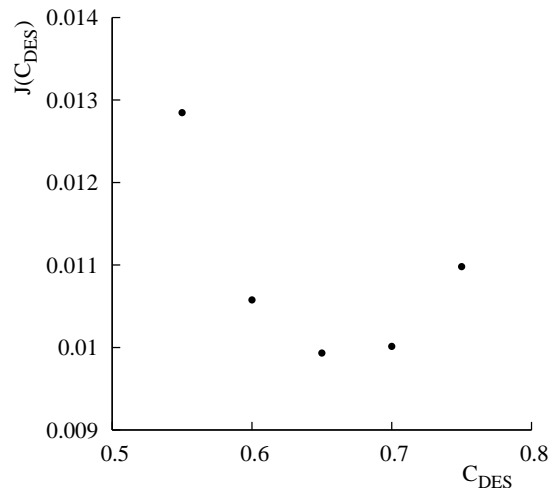Figure 6.2: Energy spectra of DHIT for SADES with different C_{DES}.

Figure 6.3: Error functional (6.3) of DHIT for SADES.

different constant C_{DES} are shown in Fig. 6.2. The main difference appears for the large wavenumbers which correspond to the small eddies. The values of the error functional are listed in Table 6.1 and plotted in Fig. 6.3. Taking $C_{DES} = 0.65$ as the starting value, we use the Newton type method as in Section 4.5.3 to search the C_{DES} which makes the error functional minimal. After a few iterations, the optimal value $C_{DES} = 0.67$ is obtained. It is very close to the value proposed by Shur *et al.* [109]. This, however, is not too much surprising as the DHIT case was used to calibrate C_{DES} in the mentioned paper.

C_{DES}	0.55	0.6	0.65	0.7	0.75
$J(C_{DES})$	1.284728e-02	1.057692e-02	9.932635e-03	1.001381e-02	1.098079e-02

Table 6.1: Error functional (6.3) of the energy spectrum for C_{DES}.

6.2.2 XLES for DHIT

An alternative hybrid approach is XLES proposed by Kok *et al* in [69]. In this model, a $k - \omega$ turbulence model is used in RANS region and a k-equation SGS model is used in LES region. Since DHIT is not a wall-bounded flow, only the LES part of XLES (see Section 3.4.2) is applied. The energy spectra with the parameter $C_1 = 0.07$ on two grids are plotted
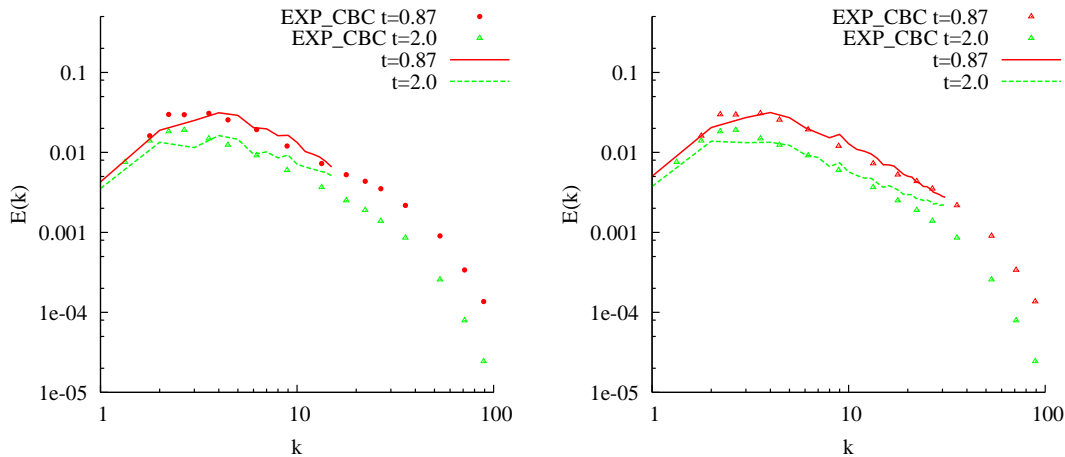

Figure 6.4: Energy spectra of DHIT for XLES on grid 32^3 and 64^3.

in Fig. 6.4 compared with the experimental data (EXP_CBC) [19]. They have very good agreement to the experimental data at the first time $t = 0.87$. At the second time $t = 2.0$ the energy is too dissipative at large wavenumbers. The reason could come from the parameter C_1. A different value $C_1 = 0.06$ is used in [69]. The initial value for the k-equation or the proper treatment of the dissipation and cross-diffusion terms could also cause problems. Due to time restriction of this thesis, we do not consider tuning of the parameter or other improvement of this turbulence model.

6.3 Channel flow at $Re_\tau = 395$

In the SADES model, the length scale $\tilde{d}$ defines the switch between RANS and LES. For the wall distance $d < C_{DES}\Delta$, the Spalart-Allmaras RANS (SA-RANS) mode is activated; otherwise, the LES mode is used. Within the near-wall region, a fine grid is also required for the RANS approach in the wall normal direction, such that a sufficient number of points are located in the near-wall region and the requirement $y^+(1) \simeq 1$ should also be satisfied. The switch between RANS and LES region therefore depends on Δx and Δz. In its original idea DES was conceived for flows with a clear (i.e. geometry-induced) separation point in a large region of separated flow, which is a large part ourside of the boundary layer. Then the entire boundary layer should be treated in RANS mode, which implies that Δx and Δz should be of the order of the boundary layer thickness. On the other hand, here the aim is to use DES as a wall-model for LES, see [89]. The boundary layer is treated in LES mode except for the near-wall region, where the RANS mode is active. According to [89], turbulent structures can be resolved (and hence proper LES solutions in the LES region ensured) provided $\Delta x = \Delta z \simeq 0.1H$. This issue will be discussed in Section 6.4 with emphasis on problem occurring at higher Reynolds numbers. According to the description of the grid resolution on page 83, $\Delta = \max(\Delta x, \Delta y, \Delta z) = \Delta x$.

Here we will study the plane channel flow at Reynolds number $Re_\tau = 395$ for SA-RANS and SADES. The test case setup is the same as in Chapter 5:

- computational domain $[0, 2\pi] \times [0, 2] \times [0, \pi]$,

- periodic boundary condition in streamwise direction, symmetric planes in spanwise direction and no-slip boundary condition at the walls,

- anisotropic grid $64 \times 64 \times 64$ with first grid node at $y^+(1) = 1.06$,

- time step size $\delta t = 0.17$,

- initial condition with perturbation (5.32),

- flow is driven by a pressure gradient $\mathbf{f} = (\frac{u_\tau^2}{H}, 0, 0)^{\mathrm{T}}$,

- mass flux correction (5.37),

- space discretization, CDS,

- time discretization, BDF(2),

- reference data, DNS data by Moser *et al.* (1999) [88].

Please note that in this hybrid SADES model, no damping function is adopted. The standard Spalart-Allmaras model is used in the near-wall region and the LES mode based on the modification of Spalart-Allmaras model is used away from the walls.

6.3.1 Spalart-Allmaras RANS

First the implementation of the SA model in URANS mode is validated by considering the channel flow problem. Fig. 6.5 shows the mean velocity profile when $\tilde{d} = d$ in the whole channel, which means the original Spalart-Allmaras model is used. The mean velocity
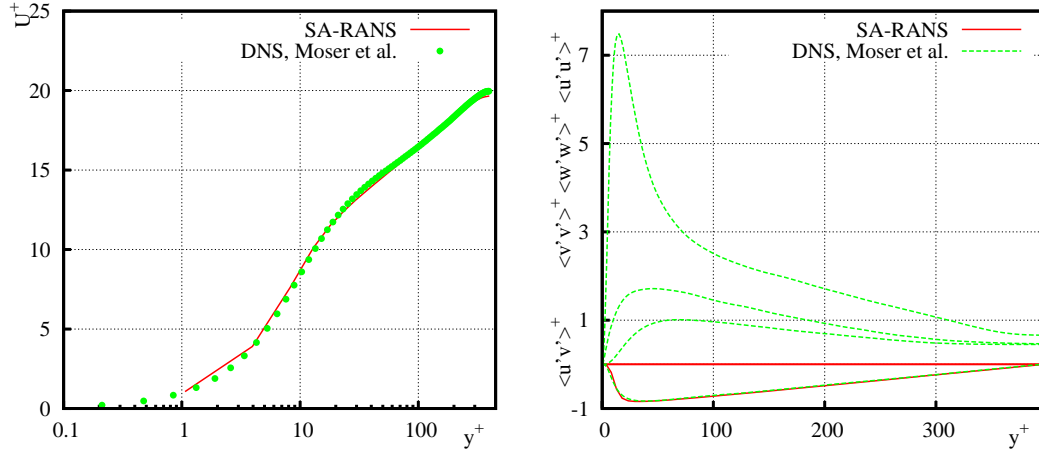

Figure 6.5: Mean velocity and fluctuations of channel flow for SA-RANS at $Re_\tau = 395$.

has a very good agreement with the DNS data. The modeled shear stress is close to the resolved shear stress in DNS. The SA model as a RANS model does not resolve any turbulent fluctuations and therefore the total stress is exactly equal to the modeled stress and there is no contribution from the resolved stresses.

6.3.2 Spalart-Allmaras model DES based (SADES)

In this section we present results of SADES for the plane channel flow at the moderate Reynolds number $Re_\tau = 395$. We compare the results of SADES with LES considered in Chapter 5. SMG of LES represents the classical Smagorinsky model and SMG-MOD is the Smagorinsky model with modified filter width where the wall distance is taken into account, cf. [123]. The computational domain and the test case setup are identical and thus LES and DES can be compared directly.

In Fig. 6.6, the profiles of mean velocity are very close for SMG and SADES, the best one is given by SMG-MOD, i.e. Smagorinsky model with modified filter width. There is improvement of SADES to the fluctuations compared to the LES results, especially at the peak of $\langle u'u' \rangle^+$. Thus u_{rms} has very good agreement with the DNS data in Fig. 6.7 and the turbulent kinetic energy k^+ is under-predicted due to the under-prediction of the other two fluctuations $\langle v'v' \rangle^+$ and $\langle w'w' \rangle^+$. The SADES with modification by Edwards and Chandra (see Section 3.2.3), denoted as SADES_ED, gives better $\langle v'v' \rangle^+$ and $\langle w'w' \rangle^+$ in the near-wall region. However, the peak of $\langle u'u' \rangle^+$ for SADES_ED is significantly larger than the
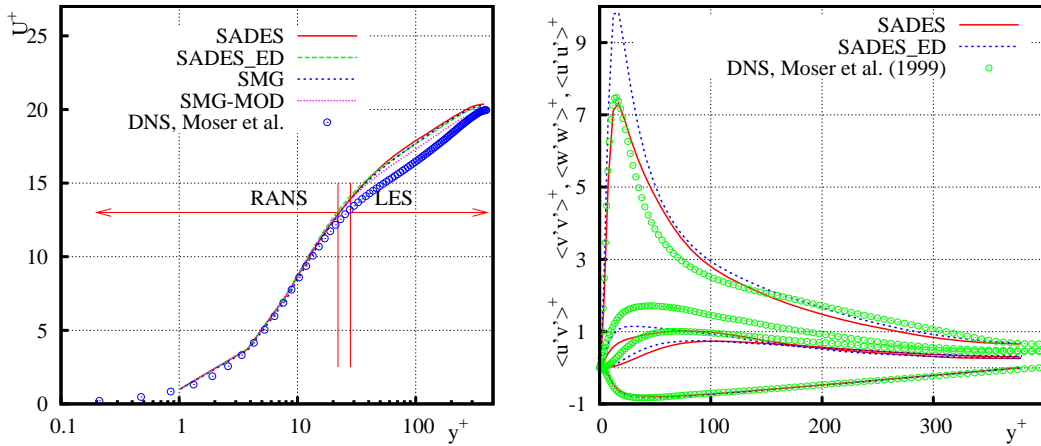
Figure 6.6: Mean velocity and fluctuations of channel flow for SADES at $Re_\tau = 395$.
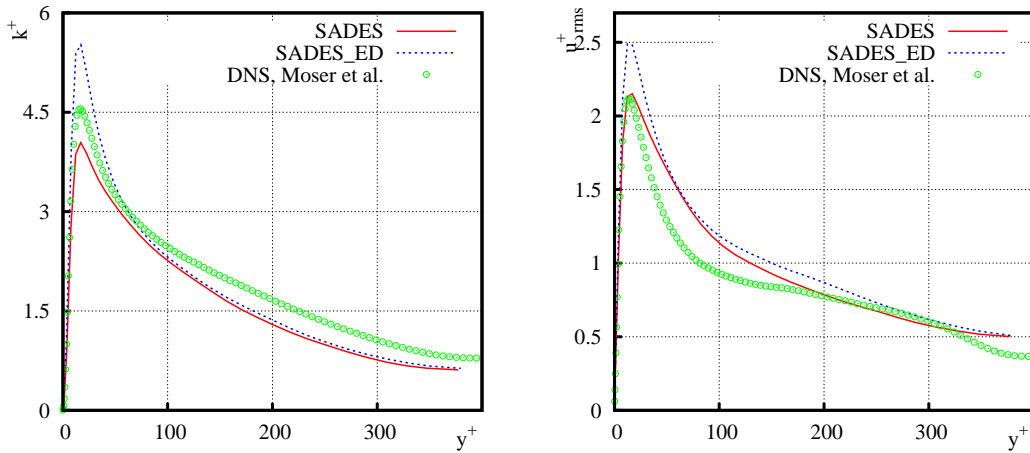

Figure 6.7: Kinetic energy k^+ and u_{rms} of channel flow for SADES at $Re_\tau = 395$.

DNS data. The shear stresses of these two models are given in Fig. 6.8. It should be noted that the modeled part of SADES is larger than that of SADES_ED.

Furthermore, the switch between RANS and LES happens at $y^+ \simeq 22 - 28$ as shown in Fig. 6.6, that is, RANS mode for $y^+ < 22$ and LES mode for $y^+ > 28$. There are 6 grid nodes in y direction involved in RANS mode in half channel. Still it is a very small region as compared to the whole channel (less than 8%).

Let us study the influence of the model parameter C_{DES} in this test case. Similar to (5.41) and (5.42), the discrete L^2-error functionals of the mean velocity and kinetic energy of SADES
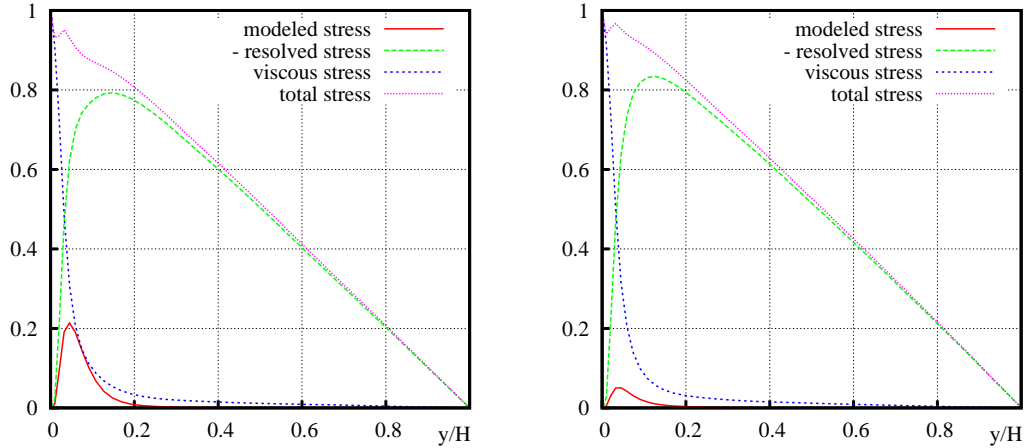
Figure 6.8: Stresses of channel flow for SADES (left) and SADES_ED (right) at $Re_\tau = 395$.

compared to the DNS data are defined as

$$J_u(C_{DES}) = \left(\sum_{i=1}^{N} (U_i(C_{DES}) - U_i(DNS))^2 \, \Delta y_i \right)^{1/2}, \tag{6.4}$$

$$J_k(C_{DES}) = \left(\sum_{i=1}^{N} (k_i(C_{DES}) - k_i(DNS))^2 \, \Delta y_i \right)^{1/2}. \tag{6.5}$$

The values of the error functionals are listed in Table 6.2 for different C_{DES}. Fig. 6.9

C_{DES}	$J_u(C_{DES})$	$J_k(C_{DES})$
0.55	2.028798e-03	1.116625e-05
0.57	1.576840e-03	1.123655e-05
0.59	1.653160e-03	1.205351e-05
0.61	1.718699e-03	1.071554e-05
0.63	1.715923e-03	1.135974e-05
0.65	1.788156e-03	1.138488e-05
0.67	1.745659e-03	1.008529e-05
0.69	1.831367e-03	1.214508e-05
0.71	1.904827e-03	1.081947e-05
0.73	1.856606e-03	1.075873e-05

Table 6.2: Error functionals (6.4) and (6.5) of channel flow for SADES at $Re_\tau = 395$.

gives the plot of the error functionals. The functionals are not monotonically increasing/decreasing. The local minimum for $J_k(C_{DES})$ is at $C_{DES} = 0.67$, which is the optimized value for DHIT. Regarding to the mean velocity, the value around $C_{DES} = 0.57$ gives local
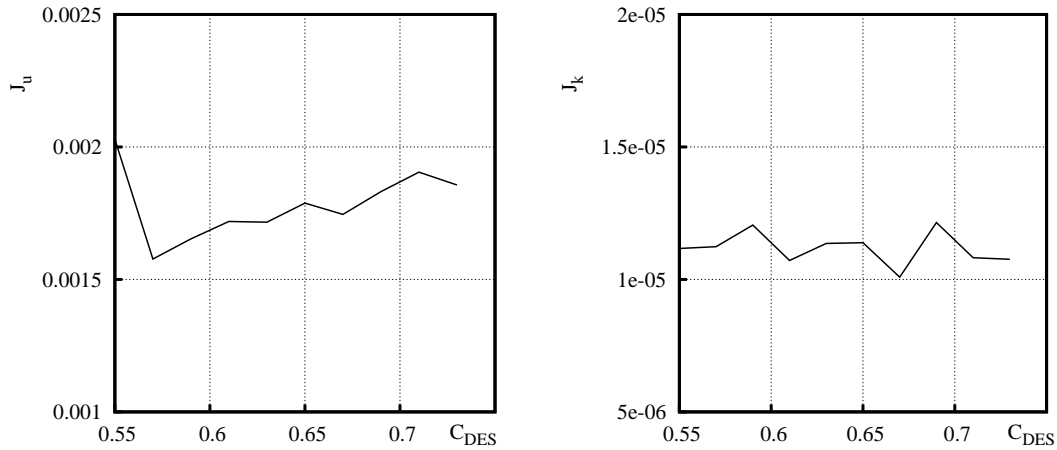
Figure 6.9: Error functionals (6.4) and (6.5) of channel flow for SADES at $Re_\tau = 395$.

minimum for $J_u(C_{DES})$. As it can been seen, the error functionals do not change much for given C_{DES}. Thus SADES is robust with respect to this parameter.

6.4   Channel flow at high Reynolds number $Re_\tau = 4800$

As mentioned in Chapter 1, one of the main goals of this work is to study the behavior of turbulence models in the DLR-THETA-code. We have considered DHIT and channel flow at moderate Reynolds number in previous work. Here we take Reynolds number $Re_\tau = 4800$ based on the friction velocity and channel half-width as a typical example at high Reynolds number flow, since there is some experimental data for this case available, e.g. by Comte-Bellot (1965) [20]. Regarding the quantity of the experimental data, it has to be remarked that the Comte-Bellot data are only for the log-layer and no data for the near-wall region ($y^+ < 100$) are measured. This is somewhat regrettable as the near-wall peak of the fluctuations cannot be used for comparison with the simulations. Moreover, friction velocity might suffer from deficiencies in the experiment, since the velocity profile in wall units deviates significantly from the theoretical log-law. It should be mentioned that Comte-Bellot performed experiments for three different Reynolds numbers, and for all experiments, different profiles for velocity in wall units are obtained, see Fig. 6.10. Moreover, due to a lack of data for the near-wall region, the bulk velocity cannot be determined accurately enough. As a remedy, data from a resolved LES are considered by Kravchenko *et al.* [71], although data are for a slightly different Reynolds number ($Re_\tau = 4000$).

For turbulent flows at high Reynolds numbers, the resolution depends crucially on the accurate modeling of the near-wall region, in which a rather fine grid is required to resolve the energy-carrying eddies. To avoid the high computational costs, hybrid approaches are proposed to use RANS mode or wall functions in the near-wall region and LES mode away
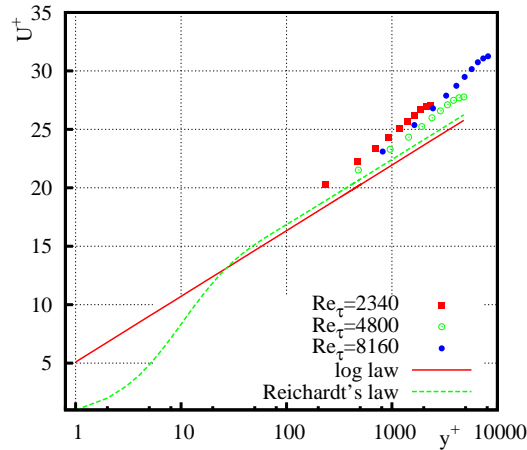
110

Figure 6.10: Mean velocity profiles of Comte-Bellot (1965).

from the wall. Thus, there is no need to use the damping function in the hybrid approaches.

We consider the same computational domain $[0, 2\pi] \times [0, 2] \times [0, \pi]$ as for $Re_\tau = 395$. Periodic boundary conditions are imposed in the streamwise direction, no-slip conditions at two walls and symmetric planes in the spanwise direction. The mass flux correction (5.37) is used. The central difference scheme as space discretization and BDF(2) as time discretization are applied. Moreover, the pressure gradient $(\frac{u_\tau^2}{H}, 0, 0)^T$ acts as the source term. Of course, the values of the corrected mass flux and pressure gradient are different from the case of $Re_\tau = 395$.

6.4.1 SADES

For the simulation of channel flow at high Reynolds number with application of SADES, to resolve the boundary layer we need enough points in such a narrow area. Grid $64 \times 96 \times 64$ is used with equidistant mesh in both streamwise and spanwise directions and stretched mesh in wall normal direction, where $y^+(1) \simeq 1$. In [62], CFL number of 0.3 is used for time-advancing scheme for NSE and 0.075 for the scalar transport equation. Here the time step is set to 0.002, which corresponds to CFL number of 0.043, to maintain stability. The mean velocity profiles of RANS and DES based on Spalart-Allmaras model are given in Fig. 6.11.

It should be mentioned that the computation is time-consuming due to the small time step and fine grid. The average is only performed in 3 'flow-through' times after 20000 step for flow developing. It is shown that the mean velocity in wall units is too large in the logarithmic law region compared with the experimental data or log-law. The friction velocity is around 20% underpredicted as reported by Keating & Piomelli [62] and Nikitin *et al.* [89]. One reason of the overprediction of the mean velocity could come from the grid resolution. A grid of $128 \times 128 \times 64$ is used for channel flow of DES at $Re_\tau = 4000$ in [62]. 64 points in
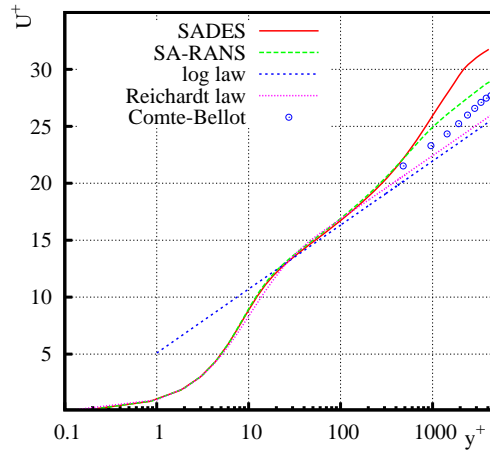
Figure 6.11: Mean velocity in wall units of channel flow at Re$_\tau$=4800.

streamwise and spanwise directions are not enough to resolve the near-wall turbulence (see Section 6.4.2). Since we cannot afford computations with high grid resolution, we turn to use the hybrid method with wall functions.

6.4.2   Hybrid LES and wall functions

In this section, the wall modeled LES using wall functions is applied to the channel flow at $Re_\tau = 4800$. Since wall functions are used in the near-wall region, we can use quite coarse grid in the wall normal direction and quite large y^+ for the first node above the wall. However, the grid spacing cannot be too coarse in streamwise (x) and spanwise (z) direction since the near-wall turbulent streaks need to be resolved. For instance, Piomelli [92] uses $\Delta x^+ \simeq 244$ in a simulation of a plane channel flow at $Re_\tau = 2000$.

Three grids used in the simulations consist of 64×24×64, 96×24×96 and 128×24×128 with $y^+(1) = 50$ and $\Delta x^+ = 2\Delta z^+ \simeq 470$, 314 and 235, respectively. Two models, the classical Smagorinsky model and SADES , are considered as the LES mode. We denote WSMG as the hybrid approach of the Smagorinsky model with wall functions and WSADES as SADES with wall functions.

The mean velocities and fluctuations are shown in Fig. 6.12 for WSMG and Fig. 6.13 for WSADES for three grids compared with the experimental data Comte-Bellot (1965) and LES data by Kravchenko *et al.* [71]. In general the mean velocities and the shear stresses have good agreement with the experimental data. A slight under-prediction of the mean velocity occurs close to the near-wall region for the coarsest grid $64 \times 24 \times 64$ for WSMG. Although there are 64 grid points in streamwise and spanwise directions, the grid resolution of 64×24×64 is still not fine enough to resolve the scales in the near-wall turbulent processes. $\langle u'u' \rangle^+$ is little overestimated and $\langle v'v' \rangle^+$ and $\langle w'w' \rangle^+$ are underpredicted, which is typical

Figure 6.12: Mean velocity and fluctuations of channel flow for WSMG $Re_\tau = 4800$.
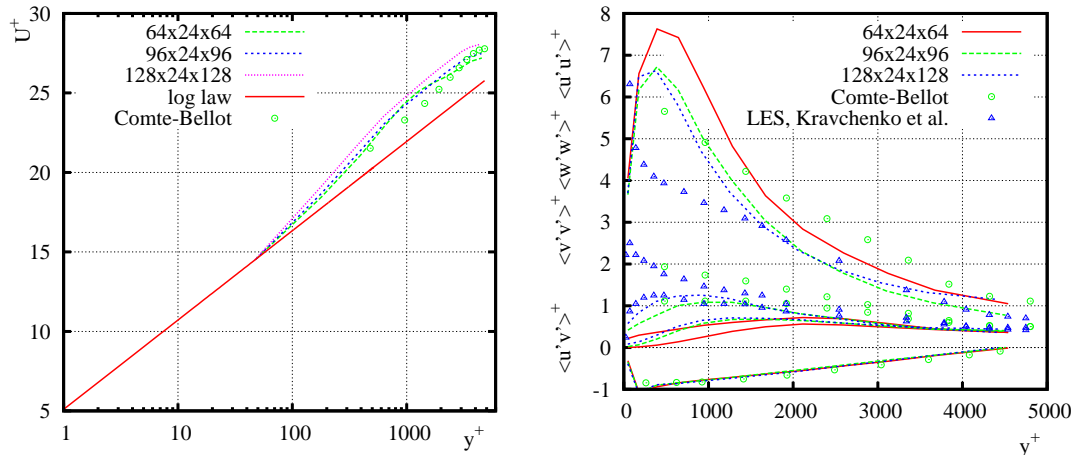
Figure 6.13: Mean velocity and fluctuations of channel flow for WSADES at $Re_\tau = 4800$.

for an underresolved LES (see [62]). This is more obvious when the results are compared with the LES data by Kravchenko *et al.*. With refinement of grids from 64 to 96 and even 128 in the streamwise and spanwise directions, the fluctuations of $\langle v'v' \rangle^+$ and $\langle w'w' \rangle^+$ increase and get closer to the experimental data. WSADES provides similar results and also requires finer grid resolution in streamwise and spanwise directions. However, the mean velocities have apparent deviation from the log-law.

An eddy-viscosity correction is proposed by Kalitzin *et al.* [61], Medic *et al.* [81] and Templeton *et al.* [117]. In the near-wall region, the SGS eddy-viscosity is replaced by a
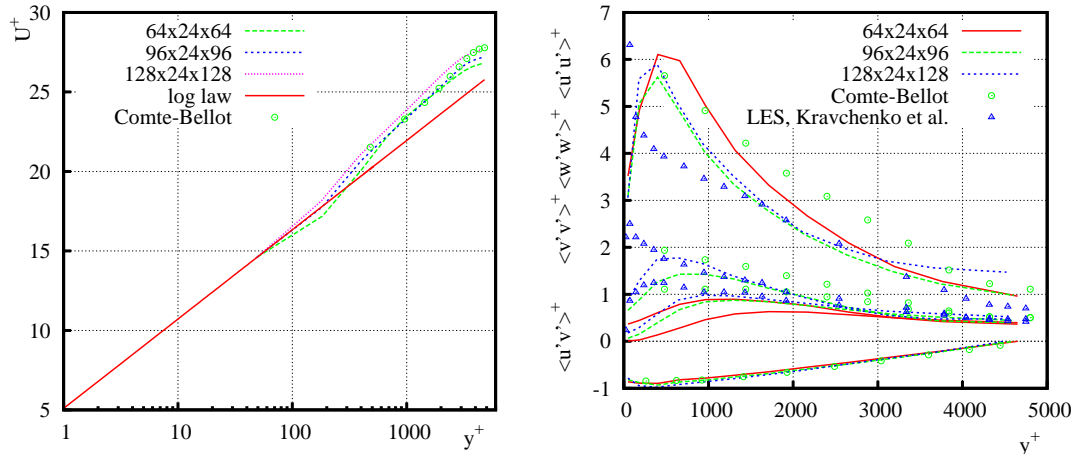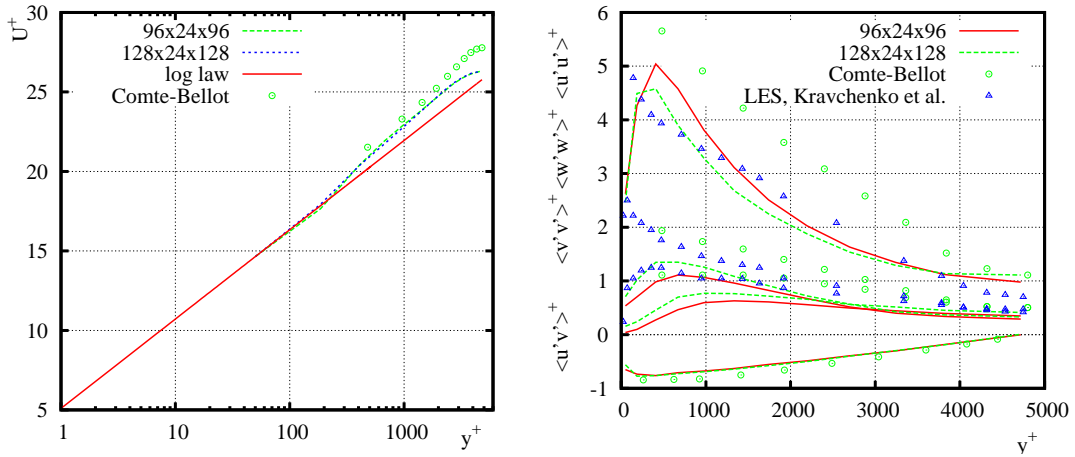
Figure 6.14: Mean velocity and fluctuations of channel flow for WSMG_CORR at $Re_\tau = 4800$.
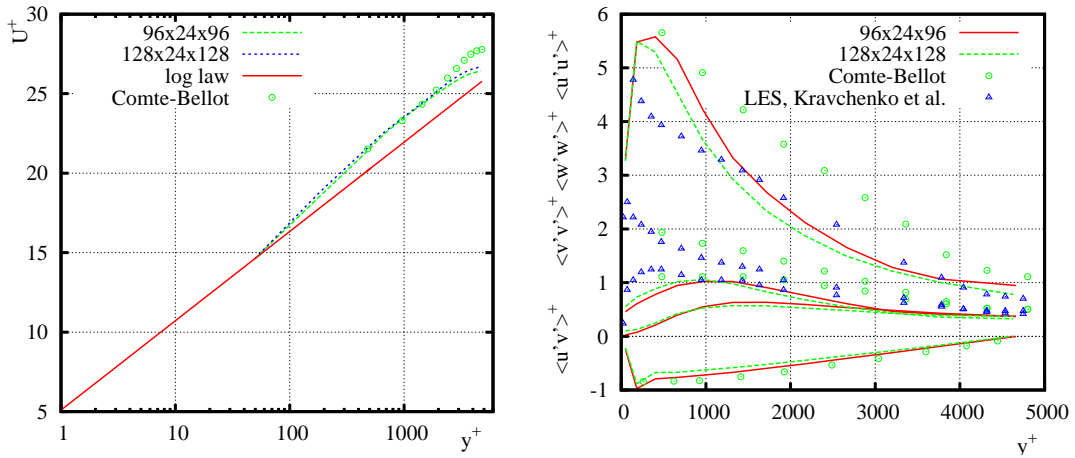
Figure 6.15: Mean velocity and fluctuations of channel flow for WSADES_CORR at $Re_\tau = 4800$.

RANS eddy-viscosity using the resolved turbulent stress

$$\nu_t^{SGS} = \nu_t^{RANS} + \langle\, u'v'\,\rangle / \langle\, \frac{\mathrm{d}u}{\mathrm{d}y}\,\rangle, \tag{6.6}$$

where $\langle\, u'v'\,\rangle$ and $\langle\, \frac{\mathrm{d}u}{\mathrm{d}y}\,\rangle$ are the resolved stress and velocity gradient obtained from the averaged LES velocity profile.

The results are presented in Fig. 6.14 and 6.15 with implementation of the correction (6.6) to the turbulent viscosity in the near-wall region of WSMG and WSADES, respectively, denoted as WSMG_CORR and WSADES_CORR. For clarity, the results for grid $64 \times 24 \times 64$

are not included. The mean velocities are better predicted in comparison with the log-law. Meanwhile, the fluctuations have good agreement with the experimental data, in particular with the LES Kravchenko *et al.* results. It is noted that the dependence of the mean velocity for both WSMG and WSADES on grid resolution is not well pronounced. The

	WSMG	WSADES	WSMG_CORR	WSADES_CORR
$96 \times 24 \times 96$	7.022318e-02	6.933079e-02	7.229627e-02	7.054821e-02
$128 \times 24 \times 128$	6.882198e-02	6.719955e-02	7.176496e-02	7.142692e-02

Table 6.3: Friction velocity u_τ^{THETA} of channel flow at $Re_\tau = 4800$.

	WSMG	WSADES	WSMG_CORR	WSADES_CORR
$96 \times 24 \times 96$	4.4%	5.6%	1.6%	3.9%
$128 \times 24 \times 128$	6.3%	8.5%	2.3%	2.7%

Table 6.4: Relative error of friction velocity u_τ^{THETA}.

averaged friction velocities u_τ^{THETA} are given in Table 6.3. With correction applied to the eddy-viscosity in the near-wall region friction velocities become closer to the theoretical value $u_\tau = Re_\tau \nu / H = 0.07344$. The relative error of the friction velocity is defined as

$$e(u_\tau) = \frac{|u_\tau^{THETA} - u_\tau|}{|u_\tau|}, \tag{6.7}$$

and they are given in Table 6.4. As it can be seen that the errors with corrected eddy-viscosity are much less than half of the ones without correction except for WSADES_CORR on grid $96 \times 24 \times 96$.
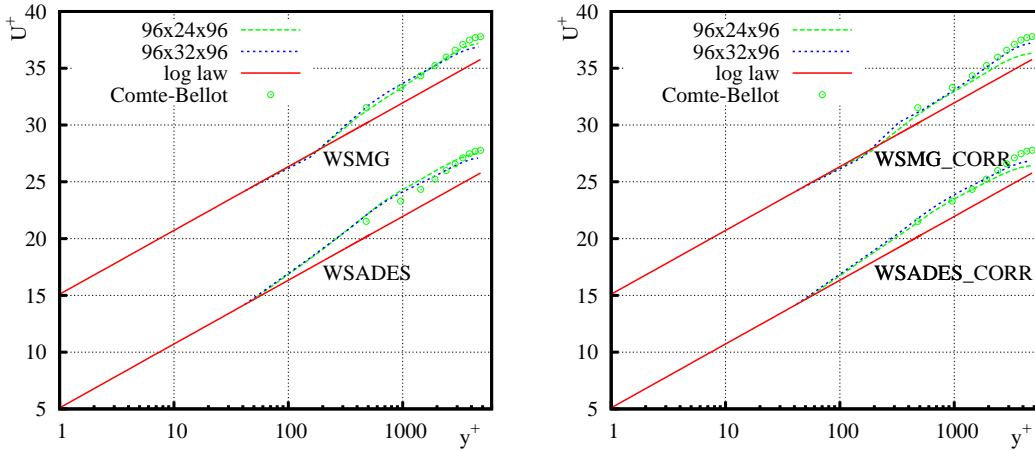

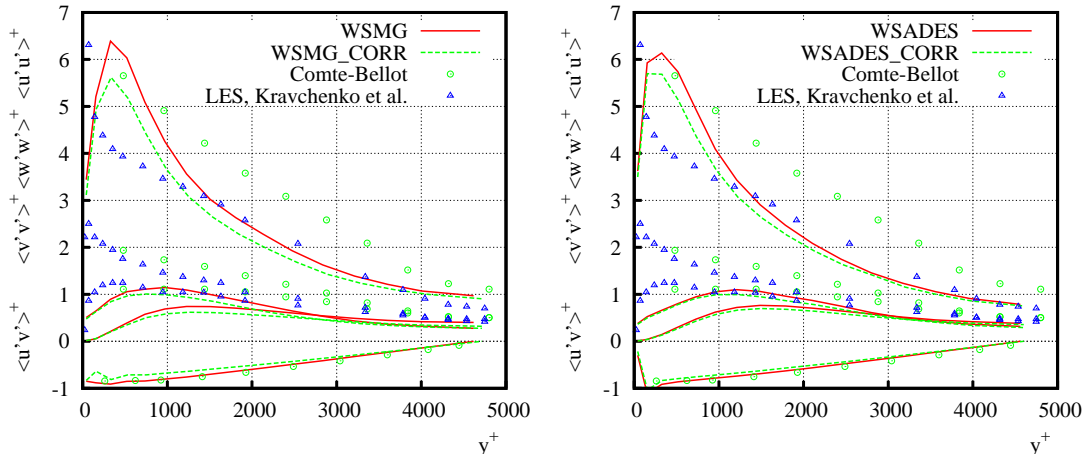Figure 6.16: Mean velocities of channel flow at $Re_\tau = 4800$.

Figure 6.17: Fluctuations of channel flow on grid $96 \times 32 \times 96$ at $Re_\tau = 4800$.

	WSMG	WSADES	WSMG_CORR	WSADES_CORR
u_τ	7.072795e-02	6.919573e-02	7.212636e-02	7.071905e-02
$e(u_\tau)$	3.7%	5.8%	1.8%	3.6%

Table 6.5: Friction velocity u_τ^{THETA} and relative error at $Re_\tau = 4800$ on grid $96 \times 32 \times 96$.

The effect of the grid refinement in wall normal direction is considered for grid $96 \times 24 \times 96$ and $96 \times 32 \times 96$, where $y^+(1) = 35$ for grid $96 \times 32 \times 96$. The mean velocities are shown in Fig. 6.16. Only slight difference can be observed in the core flow region. The fluctuations are given in Fig. 6.17. It is found that there is a clear logarithmic layer of WSMG which fits the log-law and the second layer fits the experimental data. However, the first layer does not exist in the case of WSADES. Moreover, from the friction velocities and their relative errors listed in Table 6.5 we can see that the results are very close to those on grid $96 \times 24 \times 96$.

As conclusion, the hybrid approach with wall functions requires fine grid resolution in streamwise and spanwise directions to resolve the near-wall turbulence. For WSMG the influence of grid resolution is more apparent than WSADES, in particular, to $\langle v'v' \rangle^+$ and $\langle w'w' \rangle^+$ in the near-wall region. However, there is little improvement of the refinement of the grid in wall normal direction.

Chapter 7

Conclusions

In this chapter we will present some first results with the Spalart-Allmaras model and the Smagorinsky model of the flow over a backward-facing step, which has only one homogeneous direction (spanwise direction), i.e. a statistically two-dimensional problem. It is more complex than the plane channel flow. Then a short discussion of the results presented in this thesis and some open questions will be addressed.

7.1   Flow over a backward-facing step

The Reynolds number we consider is $Re_h = 5100$ based on the step height h and the inlet free stream velocity. In this case, a strong adverse pressure gradient and the sudden expansion in the channel cause flow separations. The recirculation length after separation is a quantity of interest. A direct numerical simulation by Le and Moin [73] tells that the mean reattachment length is $6.28h$. It has very good agreement with the experimental data by Jovic & Driver (1994) [59]. Toschi *et al.* [121] use the backward-facing step as a test case to evaluate a shear improved Smagorinsky model.
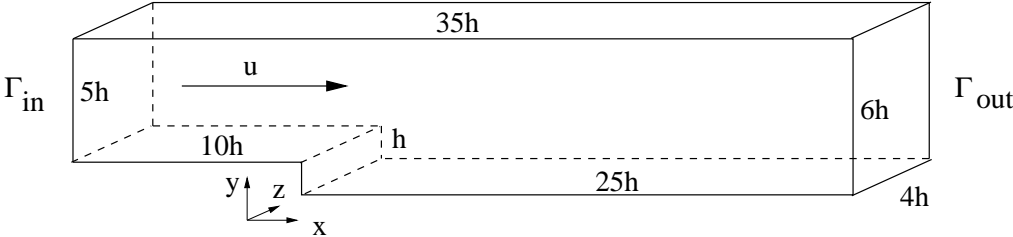

Figure 7.1: Backward-facing step.

The geometry of the backward-facing step in three-dimensional simulation is sketched in Fig. 7.1. The step is located at $x = 0$ with height h. The computational domain consists of

an inlet section of length $10h$ and an outflow part with length $25h$ in streamwise (x) direction, height $5h$ before the step and $6h$ afterwards in wall normal (y) direction, width $4h$ in spanwise (z) direction. No-slip boundary condition is imposed at the bottom wall, symmetric plane at the upper wall and periodic boundary condition in spanwise direction. The step-height Reynolds number is defined as

$$Re_h = \frac{U_0 h}{\nu},\qquad(7.1)$$

where U_0 is the free stream inlet velocity and kinematic viscosity ν. The expansion ratio is 1.2 as in [73].

A grid of $244 \times 88 \times 32$ is employed in x, y and z direction, respectively. An anisotropic grid spacing is used in y direction with fine grid near the bottom wall, equidistant mesh in z and large part of x direction, only a small stretching in the region near the outlet. The grid spacings in wall units are $\Delta x^+ \simeq 31 \sim 40$, $\Delta y^+ \simeq 0.4 \sim 26$ and $\Delta z^+ \simeq 23$. The central difference scheme for space discretization and BDF(2) for time discretization are used.

First we perform a simulation of Spalart-Allmaras RANS model with only two layers in spanwise direction. The profile of direct simulation from Spalart [112] for boundary layer is used as inflow data. It has to be adapted to the inlet profile,

$$\delta_{99} = 1.2h,\qquad(7.2)$$

where δ_{99} is the boundary layer thickness, at which the velocity equals 99% of the free-stream velocity U_0. For unsteady RANS (URANS) computation we take $\delta t = 2 \times 10^{-5}$. After 6000 steps the flow becomes steady. The velocity profile and streamtrace are shown in Fig. 7.2. Except the big recirculation bubbles after the step, some small bubbles can be seen
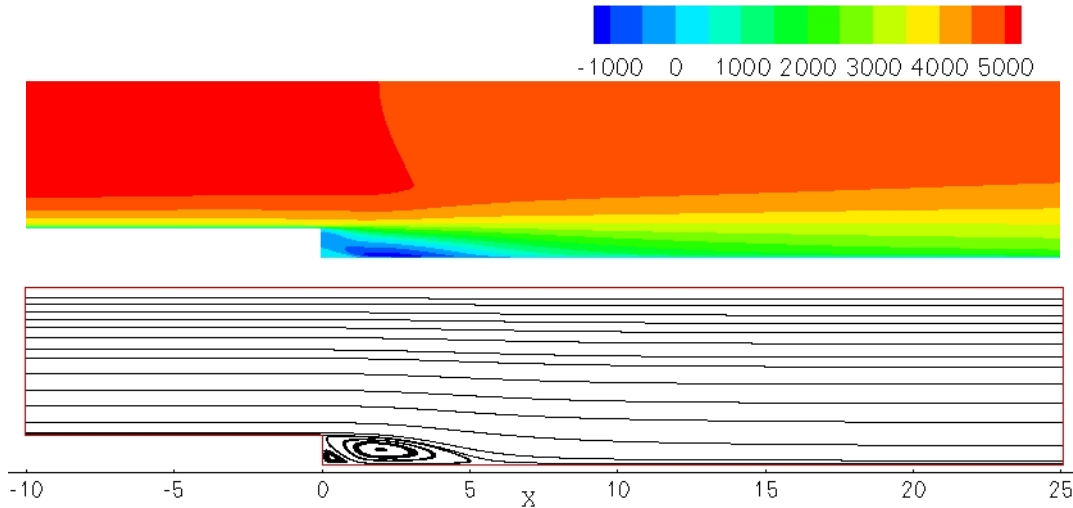

Figure 7.2: Velocity profile in streamwise direction of flow over a backward-facing step.

near the corner. Moreover, the recirculation length is around $6.5h$ which compares well with $6.28h$ in [73].

118

For LES, perturbations are required for the inflow boundary condition. A method of generating inflow fluctuations with a prescribed energy spectrum proposed by Lee, Lele & Moin [74] is used in the DNS by Le, Moin & Kim [73]. This method is rather complex and has some restrictions due to the use of the Fourier tansform. Klein *et al.* [64] presented a new approach which is based on digital filtering of random data. It is able to reproduce a prescribed first and second order statistics as well as autocorrelation functions. It was implemented to the DLR-THETA-code. By testing in a channel flow with inflow boundary condition it is found that the first and second order statistics have quite good agreement with the prescribed mean profiles. The data from Spalart [112] perturbed by the method of Klein *et al.* [64] is taken as our inflow boundary condition for LES.

The time step size used by Toschi *et al.* [121] is $\delta t = 0.01h/U_{bulk}$ with bulk velocity U_{bulk}, the time averaging window is around 5000 time steps. While $\delta t = 0.0018h/U_0$ is used in DNS [73] for a total simulation time $273h/U_0$ followed by an averaging time $109h/U_0$. In [80], the flow over a rectangular cylinder with vortex shedding using URANS and DES was investigated. In the DES, it takes more than ten non-dimensional time units, which is approximately the time it takes the flow to travel over the cylinder, for the flow to start to develop three-dimensional structures in the boundary layer and to reach a quasi-periodic time-dependent lift and drag coefficient. Here we set the time step size to be $\delta t = 0.02h/U_0 \simeq 4 \times 10^{-6}$.
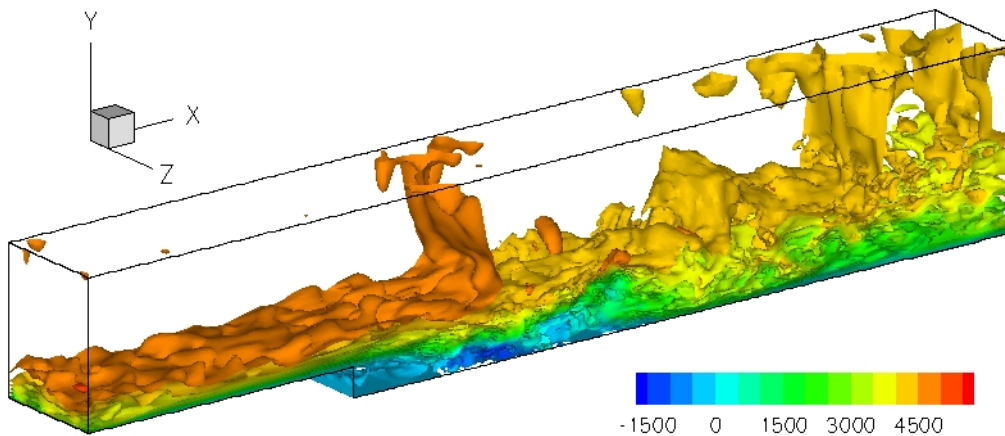
Figure 7.3: Isosurfaces of the instantaneous velocity of flow over a backward-facing step.

With the Smagorinsky SGS model we perform the simulation for 7000 steps. Fig. 7.3 shows isosurfaces of the instantaneous velocity in streamwise direction. The flow is strongly turbulent after the step. From the instantaneous velocity slice at the first wall nodes in Fig. 7.4 we can see the recirculation area where the velocity is negative. The three-dimensional character of the solution is obvious. The relatively large velocities in some small areas close to the wall might stem from eddies moving from a region of larger fluid velocity towards the wall.
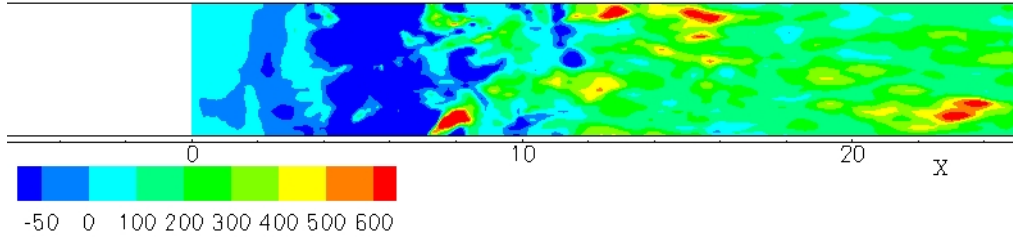
Figure 7.4: Slice of the instantaneous velocity of flow over a backward-facing step at the first wall node after the step.
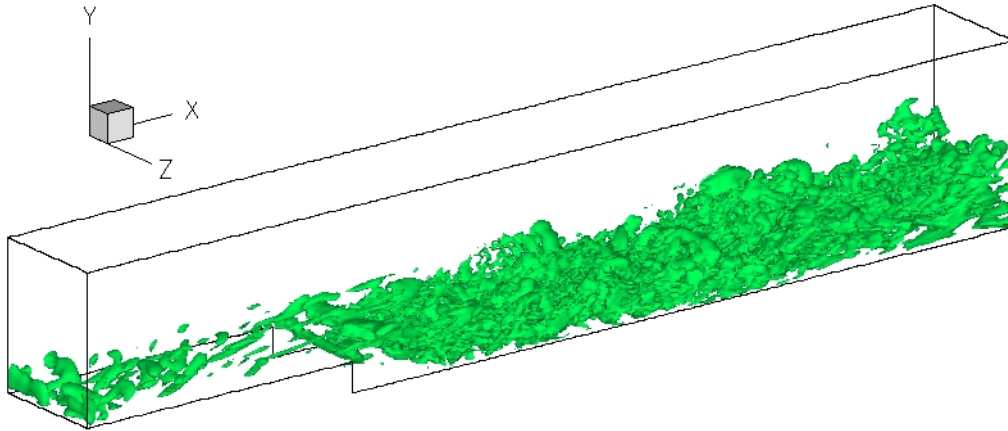
Figure 7.5: Isosurfaces of Q-invariant of flow over a backward-facing step at $Q = 1.4 \times 10^6$.

Due to the time restriction of this thesis no statistics will be presented for the flow over a backward-facing step here. We use a visualization tool to show the structures of the turbulent flow. The second invariant Q is defined as

$$Q = \frac{1}{2} \sum_{i,j=1}^{d} (\Omega_{ij}\Omega_{ij} - \mathbb{S}_{ij}\mathbb{S}_{ij}), \tag{7.3}$$

where $\Omega = (\nabla \mathbf{u} - \nabla \mathbf{u}^{\mathrm{T}})/2$ and $\mathbb{S} = (\nabla \mathbf{u} + \nabla \mathbf{u}^{\mathrm{T}})/2$ are respectively the antisymmetric and the symmetric part of the velocity gradient $\nabla \mathbf{u}$. It is the so-called *Q-criterion* proposed by Hunt *et al.* [52], see also [27]. The Q-invariant is a balance between the rotation rate Ω^2 and the strain rate $\mathbb{S}^2$. High positive values of Q imply vortex regions where the rotation rate is dominant compared to the strain rate. Another criterion developed by Jeong and Hussain [55] is the λ_2 criterion, which is the second eigenvalue of $\Omega^2 + \mathbb{S}^2$.

Fig. 7.5 reports the isosurface for the Q-invariant $Q = 1.4 \times 10^6$ and the isosurface for $\lambda_2 = -3.0 \times 10^{18}$ is plotted in Fig. 7.6. Cucitore *et al* [22] have shown that the definition of λ_2 is strongly related to the Q-criterion. From the figures, we can see that the structures are somehow similar for these two values. The rotational character of the turbulent flow is

120
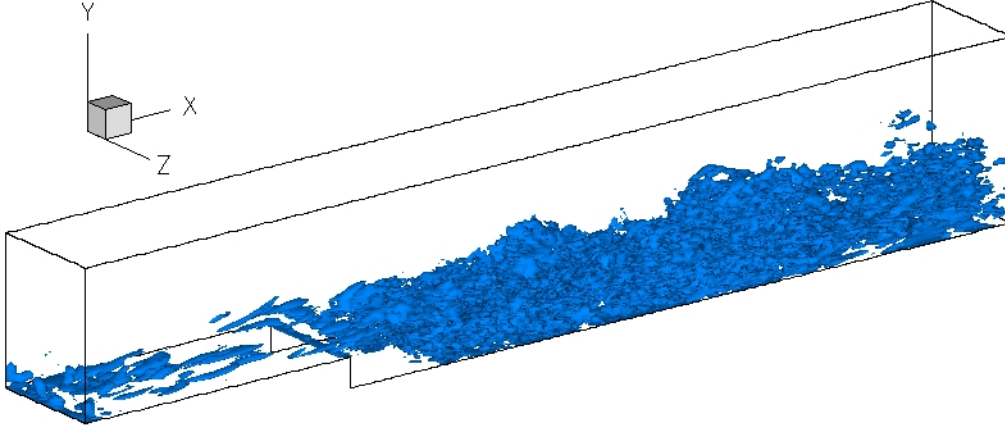
Figure 7.6: Isosurfaces of λ_2 of flow over a backward-facing step at $\lambda_2 = -3.0 \times 10^{18}$.

obvious.

For further research, we would like to compute the two-dimensional mean velocity field and second order statistics, which need to be averaged both on spanwise direction and on time. Moreover, the wall skin friction coefficient C_f given by

$$C_f = \frac{\tau_w}{\frac{1}{2}\rho U_0^2} \tag{7.4}$$

is also of interest. τ_w is the shear stress on the wall. Average on spanwise direction and on time is also required for C_f. The length from the step to the point where the averaged C_f turns from negative to positive is the averaged reattachment length.

7.2   Summary of the results

As stated in Chapter 1, the goal of this thesis is twofold,

- to test turbulence models and numerical schemes in the DLR-THETA-code, and

- to calibrate some model and grid parameters arising in LES and hybrid approaches.

Three benchmark problems with increasing complexity of homogeneity:

- decaying homogeneous isotropic turbulence (DHIT),

- plane channel flow, and

- flow over a backward-facing step,

are considered.

The performance of the DLR-THETA-code is addressed first. Given the exact solution in a unit square different spatial discretization schemes on Cartesian grids are studied. We found that:

- The convergence rate of UDS is lower than the other three (LUDS, QUDS and CDS).

- The temporal discretization scheme of BDF(2) performs well for constant time step.

- The incremental form of projection method gives good results, however, boundary layer occurs in pressure unless viscosity is very small. As a remedy, the rotational form by Timmermans *et al.* [120] is recommended.

- Furthermore, the stabilization term for pressure by Rhie and Chow [102] acts efficiently.

Large-eddy simulation (LES) with variants of the Smagorinsky model is carried out for two benchmark problems. First, DHIT as a flow with three homogeneous directions is studied on two equidistant grids. To compare with the experimental data (Comte-Bellot & Corrsin, 1966) the energy spectrum is generated, which is related to the turbulent kinetic energy. L^2-fitting of energy spectra compared with the experimental data is set up to calibrate the Smagorinsky constant C_S. It turns out that

- CDS and QUDS_sk with $\Delta/h = 2$ are clearly of preference.

- An optimized C_S is obtained to get the global minimum of the error functional.

Second, two variants of the Smagorinsky model of plane channel flow at the moderate Reynolds number $Re_\tau = 395$ are studied. In this wall-bounded flow, grid resolution in the near-wall region plays an important role, in particular, the location $y^+(1)$ of the first node away from the wall. The quantities we are interested in are the mean velocity profile and fluctuations (second order statistics). The DNS data of Moser *et al.* [88] are available to compare with. We draw the following conclusions.

- Studying the L^2-fitting of these quantities turns out that the DLR-THETA-code with the turbulence models is robust with respect to the grid parameter $y^+(1)$ and model parameter C_S with proper anisotropic mesh in the wall normal direction. Even with $C_S = 0$ (no turbulence model) the results are still convincing.

- It should be noticed that van Driest damping, which is used to reduce the influence of turbulence models in the near-wall region, cannot be avoided in the plane channel flow at moderated Reynolds numbers.

- It has good performance on anisotropic grids with aspect ratio up to 30.

122

Since LES is still too expensive when high Reynolds number flows are considered, hybrid approaches come into play. DES based on Spalart-Allmaras and XLES are two variants of them. In these hybrid approaches, the RANS mode is used in the near-wall region and the LES mode is applied to separation flows. For higher Reynolds number, requirement of grid resolution in the near-wall region is very high which leads to high computational cost. Instead, wall functions are used in the near-wall region to provide approximate boundary conditions for the core flow, where LES is applied to resolve large scales. Thus, $y^+(1)$ can be much larger, e.g. $y^+(1) = 50$. Following simulations are performed.

- By reconsidering DHIT with SADES, it is shown that LES part of SADES is able to give quite good results. Calibration of constant C_{DES} in SADES leads to an optimal value close to the one given by Shur *et al.* [109].

- Again for the channel flow at $Re_\tau = 395$, SADES produces quite appropriate results compared with the DNS data and LES results. The second order statistics are better predicted than the Smagorinsky model. It should be emphasized that there is no need to use a van Driest damping function in the hybrid approaches.

- As an example for high Reynolds number flow, the plane channel flow at $Re_\tau = 4800$ is surveyed with two models of hybrid approach, Smagorinsky model with wall functions and SADES with wall functions. Both cases present reasonable results compared with the experimental data by Comte-Bellot (1965) [20] and LES results from Kravchenko *et al.* [71].

- Moreover, a modification to the eddy-viscosity proposed by Kalitzin *et al.* [61] gives better prediction of the friction velocity.

7.3 Open questions

There is still work that could be done in the future, such as:

- It is worth studying the performance of the DLR-THETA-code on non-Cartesian grids, as all the simulations considered in this thesis are carried out on structured grids.

- There exists boundary layer for the pressure when the incremental pressure-projection scheme is applied. An aspect for future research is to implement the non-incremental projection scheme.

- Moreover, validation of the implementation of XLES could be done and tested by DHIT and plane channel flow.

- Finally, the study of the flow over a backward-facing step, as an interesting benchmark problem, is worth to complete. In particular, the two-dimensional velocity profile

and the reattachment length averaged on spanwise direction and on time seem to be interesting.

Appendix A

Properties of linear multistep methods

The transport step of projection schemes for the incompressible NSE leads to a large stiff and dissipative system of ordinary differential equations (ODE) of the form

$$\frac{d\mathbf{u}}{dt} = \mathbf{F}(t, \mathbf{u}), \qquad t \in [0, T]. \tag{A.1}$$

The standard assumption for the existence of a unique solution of (A.1) is the Lipschitz condition to $\mathbf{F}(t, \mathbf{u})$ with respect to the second argument $\mathbf{u}$. There exists a continuous function $L(t) > 0$, such that

$$|\mathbf{F}_i(t, \mathbf{u}) - \mathbf{F}_i(t, \tilde{\mathbf{u}})| \le L(t)\|\mathbf{u} - \tilde{\mathbf{u}}\|_\infty. \tag{A.2}$$

It turns out that often the weaker one-sided Lipschitz condition is sufficient: There exists a (piecewise) continuous function $l(t) : [0, T] \to \mathbb{R}$, such that

$$(\mathbf{F}_i(t, \mathbf{u}) - F_i(t, \tilde{\mathbf{u}}), \mathbf{u} - \tilde{\mathbf{u}}) \le l(t)\|\mathbf{u} - \tilde{\mathbf{u}}\|^2, \quad t \ge 0, \quad \forall \mathbf{u}, \tilde{\mathbf{u}} \in \mathbb{R}^n. \tag{A.3}$$

Here $(\cdot, \cdot)$ denotes a suitable scalar product on $\mathbb{R}^n$ and $\|\cdot\|$ the induced norm with $\|\mathbf{u}\|^2 = (\mathbf{u}, \mathbf{u})$.

System (A.1) is called *stiff* if

$$\int_0^T l(t)dt \ll \int_0^T L(t)dt. \tag{A.4}$$

An example is given by (A.7) below.

The linear p-step method of the initial value problem (A.1) is formulated as follows

$$\sum_{s=0}^{p} \alpha_s \mathbf{u}(t_{n+s}) = \delta t \sum_{s=0}^{p} \beta_s \mathbf{F}(t_{n+s}, \mathbf{u}(t_{n+s})), \tag{A.5}$$

where $t_n = n\delta t$ for $n = 0, 1, \ldots, N$, as we only consider equidistant discretization, $\alpha_0, \ldots, \alpha_p$ ($\alpha_p = 1$) and β_s for $s = 0, \ldots, p$ are constants. Later on we will use the following notation, $\mathbf{u}^{n+s} := \mathbf{u}(t_{n+s})$, $\mathbf{F}_{n+s} := \mathbf{F}(t_{n+s}, \mathbf{u}^{n+s})$. Then (A.5) is rewritten as

$$\sum_{s=0}^{p} \alpha_s \mathbf{u}^{n+s} = \delta t \sum_{s=0}^{p} \beta_s \mathbf{F}^{n+s}. \tag{A.6}$$

In this appendix we will present the stability, consistency and convergency of the linear multistep method.

A.1 Stability

Roughly speaking, a numerical solution method is said to be *stable* if it does not magnify the errors that appear in the course of numerical solution process. Stability is difficult to establish in absolute terms, especially when boundary conditions and nonlinearities are present.

To analyse the stability of the multistep method, one often considers the following scalar test problem with $F(t, u) = \lambda u$, i.e.,

$$u' = \lambda u, \qquad u(0) = 1 \quad \text{with } \mathrm{Re}\lambda \leq 0, \tag{A.7}$$

to which an exponential solution $u(t) = e^{\lambda t}$ exists. This is the simplest case of a stiff problem (A.1) since $L(t) = |\lambda|$ and $l(t) = 0$.

Applying the linear multistep method (A.6) to the test problem with $\alpha_p = 1$ and $F^{n+s} = \lambda u^{n+s}$, we get the following homogeneous linear differential equation

$$\sum_{s=0}^{p} (\alpha_s - \delta t \lambda \beta_s) u_{n+s} = 0. \tag{A.8}$$

The necessary condition for the discrete solution of the above equation to be bounded is that it is bounded in the limit case $\delta t \to 0$, that is, the solution of the following special differential equation

$$\sum_{s=0}^{p} \alpha_s u^{n+s} = 0 \tag{A.9}$$

must be bounded. We assume the solution of (A.9) has the form

$$u^k := v^k, \tag{A.10}$$

which leads (A.9) to

$$\sum_{s=0}^{p} \alpha_s v^{n+s} = 0. \tag{A.11}$$

We denote

$$\varrho(v) := \sum_{s=0}^{p} \alpha_s v^s = 0 \tag{A.12}$$

as the first characteristic polynomial.

Definition A.1 *The linear differential equation (A.8) is called zero-stable when all the solutions are bounded in case of $\delta t \to 0$.*

Lemma A.2 *The linear differential equation (A.8) is zero-stable, if* the root criterion *is satisfied: there are no zeros of the first characteristic polynomial (A.12) outside the closed unit disk, i.e., $|v| \leq 1$, and only simple zeros on the unit circle, i.e., $|v| = 1$.*

Proof is referred to the lecture note of Lube [77], Section 7.4.

For a one-step method, by taking $p = 1$, $\alpha_0 = -1$ and $\alpha_1 = 1$ in (A.12), we obtain

$$\varrho(v) = v - 1, \tag{A.13}$$

which satisfies the root criterion. Hence any one-step method is zero-stable, in particular the θ-scheme.

Definition A.3 *The linear multistep method (A.6) is called zero-stable, when the linear differential equation (A.8) is zero-stable.*

Definition A.4 *A discretization method with step size δt for approximating the test problem (A.7) is called absolutely stable if*

$$|u_n| \longrightarrow 0 \quad as \quad t_n \longrightarrow +\infty. \tag{A.14}$$

The numerical solution u_n depends on δt and λ. The *region of absolute stability* of the linear multistep method (A.6) is the subset of the complex plane

$$\mathcal{A} = \{u_n \in \mathbb{C} : (A.14) \text{ is satisfied}\}. \tag{A.15}$$

Definition A.5 *The stability region $\mathcal{S}$ of the linear multistep method (A.6) is the set of all complex values $\varsigma := \delta t \lambda \in \mathbb{C}$ which satisfy the root criterion, see Lemma A.2.*

Definition A.6 *(i) A method is called A-stable, if*

$$\mathbb{C}^- := \{\varsigma \in \mathbb{C} : Re(\varsigma) \leq 0\} \subset \mathcal{S}. \tag{A.16}$$

(ii) A method is called A(α)-stable with $\alpha \in [0, \frac{\pi}{2}]$, if

$$\{\varsigma \in \mathbb{C} : |arg(\varsigma) - \pi| \leq \alpha\} \subset \mathcal{S}. \tag{A.17}$$

Lemma A.7 (Second Dahlquist barrier) *An A-stable linear multistep method has the highest order $p = 2$.*

Proof is referred to Strehmel & Weiner [115]. According to this result, there is no A-stable linear multistep method with order greater than 2. Then one tries to find other A(α)-stable methods with higher order.

It can be shown that a linear multistep method (A.6) can be absolutely stable only if $\beta_0 = \ldots = \beta_{p-1} = 0$. In particular, the BDF-schemes (see (2.59)) are of this form.

Lemma A.8 (Cryer [21], 1972) *For $p = 1, \ldots, 6$, the methods of BDF are zero-stable, but for $p > 6$ the methods are all zero-unstable.*

Since BDF methods have relatively large stability regions, they are particularly suitable for solving stiff problems.

Lemma A.9 *The BDF method for $p = 1, \ldots, 6$ are $A(\alpha)$-stable with α in Table A.9.*

p	1	2	3	4	5	6
α	90°	90°	86.03^o	73.35^o	51.84^o	17.84^o

Table A.1: $A(\alpha)$-stability of BDF(p)

Details are referred to Hairer & Wanner [45]. It is shown in this table that $\alpha = 90^o$ for BDF(1) and BDF(2), thus they are A-stable. The implicit Euler scheme, i.e., BDF(1), also as θ-scheme with $\theta = 1$, is A-stable.

A.2   Consistency and convergency

Assume $\mathbf{u}(t)$ is the solution of the problem (A.1), the residual ϵ_{n+1} arising at the point t_{n+1}

$$\epsilon_{n+1} = \sum_{s=0}^{p} \alpha_s \mathbf{u}(t_{n+1} + s\delta t) - \delta t \sum_{s=0}^{p} \beta_s \mathbf{F}(t_{n+1} + s\delta t, \mathbf{u}(t_{n+1} + s\delta t)) \tag{A.18}$$

has the following relation

$$\tau_{n+1}(\delta t) = \frac{1}{\delta t} \epsilon_{n+1}, \tag{A.19}$$

where $\tau_{n+1}(\delta t)$ is called the *local truncation error* at the node t_{n+1}. The *global truncation error* is defined by

$$\tau(\delta t) = \max_{0 \leq n \leq N-1} |\tau_{n+1}(\delta t)|. \tag{A.20}$$

Definition A.10 *The linear multistep scheme is consistent if*

$$\tau_{n+1} \downarrow 0, \qquad as \qquad \delta t \downarrow 0. \tag{A.21}$$

Consistency means the local truncation error goes to zero as the mesh size tends to zero at any point. Moreover, the multistep method has consistency order p if there exists a constant K such that

$$|\tau(\delta t)| \leq K\delta t^p \quad \text{for all} \quad \delta t > 0. \tag{A.22}$$

Definition A.11 *The starting values* $\mathbf{u}^j$, $j = 0, \ldots, p - 1$ *are called consistent, if*

$$lim_{\delta t \to 0}\{\mathbf{u}^j(\delta t) - \mathbf{u}(t_j)\} = 0, \qquad j = 0, \ldots, p - 1.$$

The starting values have consistency order p, if there exists a constant K_A such that

$$|\mathbf{u}^j(\delta t) - \mathbf{u}(t_j)| \leq K_A \delta t^p, \qquad j = 0, \ldots, p - 1, \forall \delta t > 0.$$

Definition A.12 *A method is called convergent if the error fulfills*

$$|\mathbf{u}_n - \mathbf{u}(t_n)| \leq C(\delta t), \qquad \forall n = 0, \ldots, N,$$

where $C(\delta t)$ is an infinitesimal with respect to δt. It is said to be convergent with order p if $\exists C > 0$ such that $C(\delta t) = C\delta t^p$.

Lemma A.13 *A method is convergent (with order p) as $\delta t \downarrow 0$ if and only if it is zero-stable and consistent (with order p).*

Lemma A.14 *(i) If the linear multistep method (A.6) is consistent, zero-stable and satisfies the following condition:*

$$\left|\sum_{s=0}^{p}\beta_s\mathbf{F}(t, \mathbf{u}_s) - \sum_{s=0}^{p}\beta_s\mathbf{F}(t, \tilde{\mathbf{u}}_s)\right| \leq M\sum_{s=0}^{p}\left|\mathbf{u}_{n+s} - \tilde{\mathbf{u}}_{n+s}\right|, \tag{A.23}$$

for δt small enough, constant M and all $(t, \mathbf{u}_0), \ldots, (t, \mathbf{u}_p), (t, \tilde{\mathbf{u}}_0), \ldots, (t, \tilde{\mathbf{u}}_p)$. Moreover, if the starting values are consistent, the linear multistep is convergent.

(ii)If the consistency is of order p for the linear multistep method (A.6) and the starting values, then it has convergence order p.

Lemma A.15 *BDF(p) methods with $p \leq 6$ have consistency order p.*

Proof is referred to Hairer & Wanner [45].

A.3   CFL condition

The transport step in the projection method (see Section 2.3) leads to auxiliary problems of advection-diffusion type. The full discretization, i.e. in space and time, may lead to upper bounds for the time step δt. For the one-step θ-scheme, there exists a hybrid implicit/explicit treatment of different terms. Typical limitations of δt are based on the Courant-Friedrichs-Levy condition (CFL).

Appendix A. Properties of linear multistep methods

Here we briefly describe the problem for a finite difference discretization of a simple model problem. We consider the one-dimensional Cauchy initial value problem (IVP)

$$\partial_t u - \epsilon \partial_{xx} u + b \partial_x u = 0, \qquad (t, x) \in (0, T) \times \mathbb{R} \tag{A.24}$$
$$u(0, x) = u_0(x), \qquad x \in \mathbb{R} \tag{A.25}$$

with constant coefficients $\epsilon \in [0, 1]$ and $b > 0$. For simplicity, we use equidistant discretization in time $t^n = n\delta t$ with $n \in \mathbb{N}$ and in space $x_j = jh$ with $j \in \mathbb{N}$. Applying the one-step θ-scheme and central difference to (A.24) leads to

$$\frac{1}{\delta t}(u_j^{n+1} - u_j^n) + (1 - \theta)\left(\frac{b}{2h}(u_{j+1}^n - u_{j-1}^n) - \sigma \frac{\epsilon}{h^2}(u_{j+1}^n - 2u_j^n + u_{j-1}^n)\right)$$
$$\theta\left(\frac{b}{2h}(u_{j+1}^{n+1} - u_{j-1}^{n+1}) - \sigma \frac{\epsilon}{h^2}(u_{j+1}^{n+1} - 2u_j^{n+1} + u_{j-1}^{n+1})\right) = (1 - \theta)f_j + \theta f_j. \tag{A.26}$$

A properly chosen parameter $\sigma \geq 0$ will improve the stability and/or convergence. For $\sigma = 1$, one denotes the difference $\epsilon_h := (\sigma - 1)\epsilon$ as *numerical* or *artificial* viscosity. For better understanding, we consider the stationary case.

Example A.16 *After short computation, the formula (A.26) for $\delta t \to \infty$ and $\theta = 1$ reads*

$$-\epsilon \frac{u_{j+1} - 2u_j + u_{j-1}}{h^2} + b\left(\frac{1}{2} - \alpha\right)\frac{u_{j+1} - u_j}{h} + b\left(\frac{1}{2} + \alpha\right)\frac{u_j - u_{j-1}}{h} = f_j \tag{A.27}$$

with $\alpha := \frac{\sigma - 1}{2\rho}$ and the so-called grid-Peclet number $\rho := \frac{h|b|}{2\epsilon}$. By setting $\sigma = 1 + \rho$, i.e. $\alpha = \frac{1}{2}$, for $b > 0$, the simple upwind scheme is obtained

$$-\epsilon \frac{u_{j+1} - 2u_j + u_{j-1}}{h^2} + b\frac{u_j - u_{j-1}}{h} = f_j. \tag{A.28}$$

In this case, with the artificial viscosity ϵ_h it leads to a system which satisfies the discrete maximum principle.

This consideration motivates the choice of σ which depends on the grid-Peclet number. Back to the nonstationary problem, we have the following theorem.

Theorem A.17 *For $b > 0$ and $0 \leq \theta \leq 1$, if the parameters in (A.26) satisfy*

$$\sigma > \rho := \frac{hb}{2\epsilon}, \qquad \frac{2\epsilon\delta t(1 - \theta)\sigma}{h^2} \leq 1. \tag{A.29}$$

Then the method (A.26) is stable for all $\epsilon \geq 0$ in the discrete maximum norm.

In particular, the implicit scheme with $\theta = 1$ is unconditionally stable. For $\theta \in [0, 1)$ there must be an upper limit for the time step size. Inserting the lower bound of σ to the second inequality of (A.29), we obtain

$$(1 - \theta)\frac{\delta t b}{h} \leq 1, \tag{A.30}$$

where $\frac{\delta t b}{h}$ is exactly the CFL number. That is

$$\text{CFL} \leq \frac{1}{1 - \theta}, \qquad \theta \in [0, 1). \tag{A.31}$$

The time step δt is restricted to the CFL condition. For smaller θ the restriction gets looser.

Appendix B

Solvers for large linear algebraic problem

In this appendix, GMRES as one of the Krylov solvers and the multigrid method for solving the pressure Poisson equation are presented.

B.1 Krylov solver

The generalized minimal residual (GMRES) method (Saad and Schultz, 1986) is a method for solving large unsymmetric systems. It is an extension of the minimal residual method (MINRES), which is only applicable to symmetric systems. Like MINRES, it generates a sequence of orthogonal vectors, but in the absence of symmetry this can no longer be done with short recurrences; instead, all previously computed vectors in the orthogonal sequence have to be retained. For this reason, "restarted" versions of the method are used.

Consider a linear algebraic system

$$Ax = b. \tag{B.1}$$

In GMRES, an orthogonal basis is formed explicitly:

$$w^{(i)} = Av^{(i)}$$
$$\texttt{for } k = 1, \ldots, i$$
$$\quad w^{(i)} = w^{(i)} - (w^{(i)}, v^{(k)})v^{(k)}$$
$$v^{(i+1)} = w^{(i)}/|w^{(i)}|$$

The reader may recognize this as a modified Gram-Schmidt orthonormalization. Applied to the Krylov sequence $A^k r^{(0)}$ this orthogonalization is called the "Arnoldi method" (Arnoldi 1951). The inner product coefficients $(w^{(i)}, v^{(k)})$ and $|w^{(i)}|$ are stored in an upper Hessenberg matrix.

The GMRES iterates are constructed as

$$x^{(i)} = x^{(0)} + y_1 v^{(1)} + \ldots + y_i v^{(i)},$$

where the coefficients y_k have been chosen to minimize the residual norm $|b - Ax^{(i)}|$. The GMRES algorithm has the property that this residual norm can be computed without the iterate having been formed. Thus, the expensive action of forming the iterate can be postponed until the residual norm is deemed small enough.

The pseudocode for the restarted GMRES(m) algorithm with preconditioner M, see [99], is given as follows.

```
x⁽⁰⁾ is an initial guess
for j = 1, 2, ...
    solve r from Mr = b − Ax⁽⁰⁾
    v⁽¹⁾ = r/|r|₂
    s := |r|₂e₁
    for i = 1, 2, ..., m
        solve w from Mw = Av⁽ⁱ⁾
        for k = 1, ..., i
            h_{k,i} = (w, v⁽ᵏ⁾)
            w = w − h_{k,i}v⁽ᵏ⁾
        end
        h_{i+1,i} = |w|₂
        v⁽ⁱ⁺¹⁾ = w/h_{i+1,i}
        apply J₁, ..., J_{i−1} on (h_{1,i}, ..., h_{i+1,i})
        construct J_i, acting on ith and (i + 1)th component of h_{.,i}, such
        that (i + 1)th component of J_ih_{.,i} is 0
        s := J_is
        if s(i + 1) is small enough then UPDATE(x̃, i) and quit
    end
    UPDATE(x̃, m)
    check convergence, continue if necessary
end
```

In this scheme, UPDATE($\tilde{x}, i$) replaces the following computations:

```
 compute y as the solution of Hy = s̃, in which the upper i × i
triangular part of H has H_{i,j} as its elements (in least squares
sense if H is singular).  s̃ is the first i component of s.
x̃ = x⁽⁰⁾ + y₁v⁽¹⁾ + ... + y_iv⁽ⁱ⁾
s⁽ⁱ⁺¹⁾ = |b − Ax̃|₂
if x̃ is an accurate enough approximation then quit
else x⁽⁰⁾ = x̃
```

The generalized minimal residual method retains orthogonality of the residuals by using long recurrences, at the cost of a larger storage demand. The biconjugate gradient method (BCG) takes another approach, replacing the orthogonal sequence of residuals by two mutually orthogonal sequences, at the price of no longer providing a minimization.

B.2   Multigrid method

The Multigrid algorithm is a fast method of solving partial differential equations which have been discretized on a sequence mesh. For a general overview of the method the reader may consult, for instance, [127]. Let $\{\mathcal{G}^i : i = 1, 2, \ldots, I_C\}$ be a sequence of primary grids and $\{\mathcal{B}^i : i = 1, 2, \ldots, I_C\}$ be the corresponding dual grids with i denoting the grid level, i.e., $i = 1$ being the finest level and $i = I_C$ being the coarsest level.

Let $x^k \in X^k$ be the grid functions on grid level k. The linear problem (B.1) to be solved on $\mathcal{G}^k$ and $\mathcal{B}^k$ is denoted by

$$A^k x^k = b^k. \tag{B.2}$$

Let $\tilde{x}^k$ be an approximation solution on grid level k, and $c^k = x^k - \tilde{x}^k$ is the error or the correction. The residual or defect is defined as

$$r^k = A^k \tilde{x}^k - b^k. \tag{B.3}$$

Since A is linear, $A^k c^k = -r^k$. For the next fine grid $k - 1$, we have $A^{k-1} c^{k-1} = -r^{k-1}$. We need to define a fine-to-coarse grid transfer operator, I_{k-1}^k called a restriction operator, where $r^k = I_{k-1}^k r^{k-1}$. Now coarsen the grid and solve the new residual equation. Take the defect back to the fine grid via a prolongation or interpolation operator I_k^{k-1}, where $c^{k-1} = I_k^{k-1} c^k$.

Once an initial value is given, the first step is to perform relaxation on (B.2). Carefully chosen relaxation schemes will damp the oscillatory components of the error quickly. Thus, we see why relaxation is also called *smoothing*. the solution on the coarse grid is obtained, the correction c^k is transferred by prolongation operator to the fine grid. Then the new fine-grid solution is given by

$$x^{k-1} = \tilde{x}^{k-1} + I_k^{k-1} c^k. \tag{B.4}$$

With this correction, much of the low frequency error in the solution on the fine grid is removed, saving a lot of iterations on the fine grid. This process is continued until the solution on fine grid is converged. This gives us the following linear multigrid algorithm.

INPUT: x_0^k

OUTPUT: $MG(k, x_0^k, b^k)$ is defined by the recursion

IF $k = I_C$ **THEN**

(1) Determine (exact) solution c^k of $A^k c^k = b^k$

(2) **RETURN** c^k

ELSE

(1) Initial guess: x_0^k

(2) Perform N_1 relaxation/smoothing steps: $x_m^k = S_{N_1}(x_0^k, b^k)$

(3) Do recursion: compute correction on next coarse grid $c^{k+1} = MG(k + 1, x_0^{k+1},$
$I_k^{k+1}(b^k - A^k x_m^k))$

(4) Prolongation: $x_n^k = x_m^k + I_{k+1}^k c^{k+1}$

(5) Perform N_2 relaxation/smoothing steps: $x_o^k = S_{N_2}(x_n^k, b^k)$

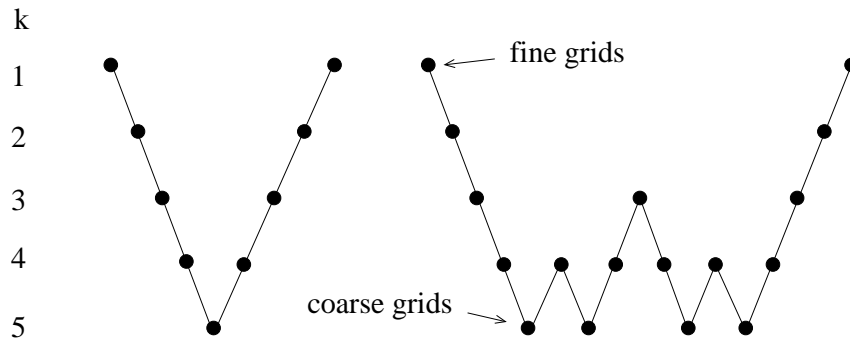(6) **RETURN** x_o^k

ENDIF

Figure B.1: V-, W-cycle diagrams.

There are two types of fixed cycle multigrid sequences, V-cycle and W-cycle as shown in Fig.B.1. For V-cycle the grid is coarsened to the lowest level once per iteration. That is, one could coarsen the grid by one level, perform a smoothing and restrict the residual to the next coarse grid, smooth again, and so on to the lowest level. Then one prolongates the coarsest grid values on the next level up, performs a smoothing, and so on until one is back on the finest grid. The number of smoothness done at each step can be varied infinitum and is a trade-off between solver work and error reduction. Some implementations use a W-cycle which is more efficient because each grid level has the chance to pass its residual down to the next coarse grid twice and receive the corrections twice.

Appendix C

The Fourier transform

C.1 The discrete Fourier transform

For a complex-valued function $u(x)$ defined on $(0, 2\pi)$, the Fourier transform of $u(x)$ is given by

$$\hat{u}_k = \frac{1}{2\pi} \int_0^{2\pi} u(x) e^{-ikx} dx, \qquad k = 0, \pm 1, \pm 2, \dots . \tag{C.1}$$

The integrals above exist if $u(x)$ is Riemann integrable, which is ensured, for instance, if $u(x)$ is bounded and piecewise continuous in $(0, 2\pi)$. More generally, the Fourier transform is defined for any function which is integrable in the sense of Lebesgue. The Fourier series for $u(x)$ is written in the form of

$$u(x) = \sum_{k=-\infty}^{\infty} \hat{u}_k e^{ikx}. \tag{C.2}$$

For any integer $N > 0$, consider the set of points

$$x_j = \frac{2\pi j}{N}, \qquad j = 0, \dots, N-1, \tag{C.3}$$

referred to as grid points. The *discrete Fourier transform* of function $u(x)$ in $[0, 2\pi]$ with respect to these points are

$$\hat{u}_k = \frac{1}{N} \sum_{j=0}^{N-1} u(x_j) e^{-ikx_j}, \qquad -N/2 \le k \le N/2 - 1. \tag{C.4}$$

The discrete Fourier series for $u(x)$ is written in the form of an inverse discrete Fourier transform

$$u(x) = \sum_{k=-N/2}^{N/2-1} \hat{u}_k e^{ikx}, \tag{C.5}$$

which is the $N/2$-degree trigonometric interpolant of $u(x)$ at the nodes (C.3).

C.2 Fast Fourier transform

The Fast Fourier Transform (FFT) is an efficient algorithm to compute the discrete Fourier transform (DFT) and its inverse, which was first discussed by Cooley & Tookey (1966). In numerical methods, the FFT and its inverse can be used to transform between time and frequency domains, and physical space and wavenumber space. In homogeneous turbulent flowsFFT is used extensively to transform between physical and wavenumber spaces.

Let $u_0, \ldots, u_{N-1}$ be complex numbers. The discrete Fourier transform is defined by

$$\hat{u}_k = \frac{1}{N} \sum_{n=0}^{N-1} u_n e^{-2\pi nki/N} \qquad k = 0, \ldots, N-1. \tag{C.6}$$

The inverse discrete Fourier transform (IDFT) is given by

$$u_n = \frac{1}{N} \sum_{k=0}^{N-1} \hat{u}_k e^{2\pi nki/N} \qquad n = 0, \ldots, N-1. \tag{C.7}$$

Evaluating these sums directly would take N^2 arithmetical operations.

Fast Fourier transform algorithms generally fall into two classes: decimation in time, and decimation in frequency. The Cooley-Tukey FFT algorithm first rearranges the input elements in bit-reversed order, then builds the output transform (decimation in time). The basic idea is to break up a transform of length N into two transforms of length $N/2$ using the identity

$$\sum_{n=0}^{N-1} u_n e^{-2\pi nki/N} = \sum_{n=0}^{N/2-1} u_{2n} e^{-2\pi(2n)ki/N} + \sum_{n=0}^{N/2-1} u_{2n+1} e^{-2\pi(2n+1)ki/N}$$

$$= \sum_{n=0}^{N/2-1} u_n^{even} e^{-2\pi nki/(N/2)} + e^{-2\pi ki/N} \sum_{n=0}^{N/2-1} u_n^{odd} e^{-2\pi nki/(N/2)}. \tag{C.8}$$

The first term in the right hand side of (C.8) is a DFT of the even-numbered elements, and the second of the odd-numbered elements. The first DFT is combined with the second multiplied by the complex exponential $e^{-2\pi ki/N}$. The half-length transforms are each evaluated at frequency indices $k = 0, \ldots, N-1$. Normally, the number of frequency indices in a DFT calculation ranges between zero and the transform length minus one.

The computational advantage of the FFT comes from recognizing the periodic nature of the discrete Fourier transform. The FFT simply reuses the computations made in the half-length transforms and combines them through additions and the multiplication by $e^{-2\pi ki/N}$, which is not periodic over $N/2$, to rewrite the length-N DFT. With the FFT algorithm, the number of operations is proportional to $N log_2 N$. Thus, for periodic data sampled at sufficiently small time intervals, the FFT is an efficient tool for evaluating Fourier coefficients, spectra and their inverse.

Appendix D

Nomenclature

Upper-case Roman

B	log law constant $B \in \{5.0, 5.2\}$ →(5.31)
$\mathcal{B}$	set of all control volumes of the dual grid
B_i	ith control volume
C_S	Smagorinsky constant → (3.52)
C_{DES}	constant in SADES model
$D(y^+)$	van Driest damping function, $D(y^+) = 1 - e^{-y^+/A^+}$ with $A^+ = 26$
$D_3(y^+)$	damping function, $D_3(y^+) = \left\{ 1 - \exp\left[-\left(\frac{y^+}{A^+}\right)^3 \right] \right\}^{1/2}$
$E(\kappa, t)$	spectrum of turbulent kinetic energy → (4.11)
H	channel halfwidth
I	time interval $I = [0, T]$
$\mathbb{I}$	unit tensor
J	cost functional
L	characteristic lengthscale
L	channel length in streamwise direction
L	side length of the cubic domain
N	number of grid points
P	averaged (filtered) pressure
R_{ij}	two-point correlation → (4.7)
Re_{bulk}	Reynolds number → (5.2)
Re_c	Reynolds number → (5.2)
Re_h	Reynolds number → (7.1)
Re_τ	Reynolds number based on friction velocity and channel half width, $Re_\tau = u_\tau H / \nu$
$\mathbb{S}(\mathbf{u})$	stress rate tensor → (1.3)
$\|S\|$	mean strain rate $\|S\| = (2 \sum_{i,j=1}^{d} \mathbb{S}_{ij}\mathbb{S}_{ij})^{1/2}$
T	final time
$\mathcal{T}$	scale separation operator → Section 3.1

Appendix D. Nomenclature

$\mathbf{U}$	averaged (filtered) velocity field
U	component of averaged velocity field in streamwise direction
U^+	normalized mean velocity $U^+ = U/u_\tau$
U_0	free-stream velocity
U_{bulk}	bulk velocity $U_{\text{bulk}} \equiv \frac{1}{H} \int_0^H U \mathrm{d}y$
U_c	centerline velocity
V	component of averaged velocity field in wall normal direction
W	component of averaged velocity field in spanwise direction

Lower-case Roman

b	channel width in spanwise direction
d	wall distance
$\tilde{d}$	length scale → (3.58)
$\mathbf{f}$	source term → (1.1)
h	grid spacing
k	kinetic energy
k^+	kinetic energy in wall unit
l_{DI}	lengthscale between the dissipation range and the inertial subrange
l_{EI}	lengthscale between the energy-containing range and smaller eddies
$\mathbf{n}$	unit outward normal vector
p	pressure
p'	pressure fluctuation
q	control parameter
t	time
$\mathbf{u}(\mathbf{x}, t)$	instantaneous velocity vector
$\langle \mathbf{u} \rangle$	statistically averaged velocity $\mathbf{U} = \langle \mathbf{u} \rangle$
$\mathbf{u}'(\mathbf{x}, t)$	fluctuating velocity vector
$\mathbf{u}^*(\mathbf{x}, t)$	intermediate velocity in projection method
$\hat{u}(\boldsymbol{\kappa}, t)$	Fourier transform of $\mathbf{u}(\mathbf{x}, t)$
u^+	rms turbulence intensity in wall unit
u_0	initial velocity in x direction
u_τ	friction velocity → (5.16)
v_0	initial velocity in y direction
w_0	initial velocity in z direction
$\mathbf{x}$	position variable
x	coordinate in streamwise direction
y	coordinate in wall normal direction
y^+	y in wall unit
$y^+(1)$	y in wall unit at the first node away from the wall
z	coordinate in spanwise direction

Upper-case Greek

140

Γ	boundary of domain Ω, $\Gamma = \partial\Omega$
Γ_{in}	inflow boundary
Γ_{out}	outflow boundary
Γ_W	wall boundary
Δ	filter width
Δx	grid size in x direction
Δx^+	Δx in wall units
Δy	grid size in y direction
Δy^+	Δy in wall units
Δz	grid size in z direction
Δz^+	Δz in wall units
Ω	$\Omega \subset \mathbb{R}^d$ a bounded domain $\rightarrow$ Section 1.1
Ω	vorticity
$\partial\Omega$	boundary of Ω

Lower-case Greek

γ	stretching parameter $\rightarrow$ (5.35)
δ_{99}	boundary layer thickness
δt	time step size
δt^+	time step size in wall unit $\rightarrow$ (5.36)
ϵ	dissipation rate
η	Kolmogorov lengthscale
$\boldsymbol{\kappa}$	wavenumber vector
κ	wavenumber
κ	von Karman constant $\kappa = 0.41$
λ	Taylor lengthscale
μ	dynamic viscosity
$\tilde{\nu}$	viscosity $\rightarrow$ Section 3.2.3
ν	kinematic viscosity
ν_t^+	nondimensionalized turbulent viscosity $\nu_t^+ = \nu_t/\nu$
ν_e	effective viscosity $\nu_e = \nu + \nu_t$
ν_t	turbulent viscosity
ρ	density of the flow
τ	Reynolds stress tensor
τ_w	wall shear stress
ω	weighting factor in projection scheme $\rightarrow$ Section 2.3.2
ω	model variable $\rightarrow$ Section 3.2.4

Abbreviations

BDF	backward differentiation formulae
CBC	experimental data of Comte-Bellot & Corrsin (1966) $\rightarrow$ Chapter 4

CDS	central difference scheme $\rightarrow$ Section 2.2.4
CFL	Courant-Friedrichs-Levy condition
CV	control volume
DES	detached-eddy simulation
DHIT	decaying homogeneous isotropic turbulence $\rightarrow$ Chapter 4
DNS	direct numerical simulation
$k - \omega$ model	$\rightarrow$ Section 3.2.4
LES	large-eddy simulation
LUDS	linear upwind difference scheme $\rightarrow$ Section 2.2.4
NSE	Navier-Stokes equations
PPE	pressure Poisson equation
QUDS	quadratic upwind difference scheme $\rightarrow$ Section 2.2.4
RANS	Reynolds averaged Navier-Stokes equations $\rightarrow$ Section 3.2.2
SA	Spalart-Allmaras model $\rightarrow$ Section 3.2.3
SADES	DES based on Spalart-Allmaras model
SGS	subgrid scale $\rightarrow$ Section 3.3
SMG	Smagorinsky model $\rightarrow$ 3.3.2
SMG-MOD	Smagorinsky model with modified filter width
DLR-THETA	the source code used in this thesis from DLR
UDS	upwind difference scheme $\rightarrow$ Section 2.2.4
WSADES	SADES with wall functions
WSMG	Smagorinsky model with wall functions
XLES	extra large-eddy simulation

Bibliography

[1] Anderson, J.D. (1995). Computational fluid dynamics, McGraw-Hill, Inc.

[2] Angermann, L. (2000). Error analysis of upwind-discretizations for the steady-state incompressible Navier-Stokes equations, Advances Comp. Math. 13, 167-198

[3] Arnoldi, W.E. (1951). The Principle of Minimized Iteration in the Solution of the Matrix, Eigenvalue Problem. Quart. Appl. Math. 9, 1729.

[4] Becker, R. and Vexler, B. (2004). A Posteriori Error Estimation for Finite Element Discretization of Parameter Identification Problems, Num. Math. vol. 96(3), 435-459

[5] Becker, R., Braack, M. and Vexler, B. (2005). Parameter Identification for Chemical Models in Combustion Problems, Appl. Num. Math. vol. 54(3-4), 519-536

[6] Berselli, L.C.,Iliescu, T. and Layton, W. J. (2005). Mathematics of large eddy simulation of turbulent flows, Springer-Verlag.

[7] Berselli, L.C. and Manfrin, R. (2004). On a theorem by Sohr for the Navier-Stokes equations, J. Evol. Equ., Birkhäuser Basel, 4, 193-211.

[8] Birkhoff, G.D. (1931). Proof of the ergodic theorem, Proceedings of the National Academy of Sciences USA, 17, 656-660.

[9] Blaisdell, G.A., Spyropoulos, E.T., Qin, J. H. (1996). The effect of the formulation of nonlinear terms on aliasing errors in spectral methods, Appl. Num. Math. vol. 21(3), 207219.

[10] Breuer, M. (2004). Direkte Numerische Simulation (DNS) & Large Eddy Simulation (LES), lecture note, university Erlangen.

[11] Breuer, M., Jovičić, N. and Mazaev, K. (2003). Comparison of DES, RANS and LES for the separated flow around a flat plate at high incidence, Int. J. Numer. Meth. Fluids 41, 357-388.

[12] Cabot, W., Jiménez, J. and Baggett J.S. (1999). On wakes and near-wall behavior in coarse large-eddy simulation of channel flow with wall models and second-order finite-difference methods. In. Annual Research Briefs, 343-354. Standford: Center for Turbulence Research.

[13] Cabot, W. and Moin, P. (1999). Approximate wall boundary conditions in the large-eddy simulation of high Reynolds number flow, Flow Turb. Combust. 63, 269-291.

[14] Canuto, C., Hussaini M.Y., Quarteroni A. and Zang, T.A. (1988). Spectral Methods in Fluid Dynamics, Springer-Verlag.

[15] Caretto, L.S., Gosman, A.D., Patankar, S.V. and Spalding, D.B. (1972). Two calculation procedures for steady, three-dimensional flows with recirculation, Proc, 3rd Int. Conf. on Numer. Methods Fluid Dyn., Paris.

[16] Choi, H. and Moin, P. (1994). Effects of the computational time step on numerical solutions of turbulent flow, J. Comput. Phys. 114, 1-4.

[17] Chorin, A.J. (1968). Numerical solution of the Navier-Stokes equations, Math. Comput. 22, 745-762.

[18] Chow, F.K. and Moin, P. (2003). A further study of numerical errors in large-eddy simulations, J. Comput. Phys. 184, 366-380.

[19] Comte-Bellot, G. and Corrsin, S. (1971). Simple Eulerian time correlation of full- and narrow-band velocity signals in grid-generated, 'isotropic' turbulence, J. Fluid Mech. vol. 48, part 2, 273-337.

[20] Comte-Bellot, G. (1965). Ecoulement turbulent entre deux parois paralleles. Publications Scientifiques et Techinques du Ministere de l'Air no. 419.

[21] Cryer, C.W. (1972). On the instability of high order backward-difference multistep methods, BIT 12, 17-25.

[22] Cucitore, R., Quadrio, M. and Baron, A. (1999). On the effectiveness and limitations of local criteria for the identification of a vortex, Eur. J. Mech. B 18 261-82.

[23] Dean, R.B. (1976). A single formula for the complete velocity profile in a turbulent boundary layer. ASME J. Fluids Eng. 98, 723-727.

[24] Davidson, L. and Peng, S.H. (2003). Hybrid LES-RANS modeling: a one-equation SGS model combined with a $k - \omega$ model for predicting recirculating flows, Int. J. Numer. Meth. Fluids 43, 1003-1018.

[25] Deardorff, J.W. (1970). A numerical study of three-dimensional turbulent channel flow at large Reynolds numbers, J. Fluid Mech. 41, 453-465.

[26] Doering, C.R. and Gibbon, J.D. (1995). Applied Analysis of the Navier-Stokes Equations, Cambridge University Press.

[27] Dubief, Y. and Delcayre, F. (2000). On coherent-vortex identification in turbulence, J.Turbulence 1, 011.

[28] Durbin, P.A. and Pettersson Reif, B.A. (2000). Statistical theory and modeling for turbulent flows, John Wiley & Sons.

[29] Dwight, R. (2007). Goal-Oriented Mesh Adaptation using a Dissipation-Based Error Indicator, International Journal of Numerical Methods in Fluids, DOI: 10.1002/fld.1582.

[30] E, W. and Liu, J.G. (2003). Gauge method for viscous incompressible flows, Commun. Math. Sci. 1(2), 317-332.

[31] Edwards, J.R. and Chandra, S. (1996). Comparison of eddy viscosity-transport turbulence models for three-dimensional, shock separated flowfields, AIAA Journal, Vol. 34, No. 4, 756-763.

[32] Ferziger, J.H., Perić, M. (1996). Computational Methods for Fluid Dynamics, Springer-Verlag.

[33] Galdi, G.P. (2000). An Introduction to the Navier-Stokes. Initial-Boundary Value Problem, Fundamental directions in mathematical fluid mechanics, Birkhäuser-Verlag, 1-70.

[34] Germano, M., Piomelli, U., Moin, P. and Cabot, W.H. (1991). A dynamic subgrid-scale eddy viscosity model, Phys. Fluids A 3(7), 1760-1765.

[35] Geurts, B.J. and Fröhlich, J. (2001). Numerical effects contaminating LES; a mixed story. Modern strategies for turbulent flow simulation, Ed: B.J. Geurts, Edwards Publishing. 317-347

[36] Ghosal, S. (1996). An analysis of numerical errors in large-eddy simulations of turbulence, J. Comput. Phys. 125, 187-206.

[37] Goda, K. (1979). A multistep technique with implicit difference schemes for calculating two- or three-dimensional cavity flows, J. Comput. Phys. 30, 76-95.

[38] Gravemeier, V. (2003). The variational multiscale method for laminar and turbulent incompressible flow, PhD thesis, Report No. 40, Institute of Structural Mechanics, University of Stuttgart.

[39] Gravemeier, V. (2006). Scale-separating operators for variational multiscale large eddy simulation of turbulent flows, J. Comput. Phys. 212, 400-435.

[40] Gravemeier, V. (2006). The variational multiscale method for laminar and turbulent flow, Arch. Comput. Meth. Engng. 13(2), 249-324.

[41] Guermond, J.-L. (1999). Un résultat de convergence d'ordre deux en temps pour l'approximation des équations de Navier-Stokes par une technique de projection incrémentale, M2AN Math. Model. Numer. Anal. 33 (1), 169-189

[42] Guermond, J.-L., Minev, P. and Shen, J. (2006). An overview of projection methods for incompressible flows, Comput. Methods Appl. Mech. Engrg. 196, 6011-6045.

[43] Guermond, J.-L.and Shen, J. (2003). Velocity-correction projection methods for incompressible flows, SIAM J. Numer. Anal. 41(1), 112-134.

[44] Guermond, J.-L.and Shen, J. (2003). A new class of truly consistent splitting schemes for incompressible flows, J. Comput. Phys. 192, 262-276.

[45] Hairer, E. & Wanner, G. (1991). Stiff and differential-algebraic problems, Springer.

[46] Ham, F.E., Lien, F.S. and Strong, A.B. (2002). A fully conservative second-order finite difference scheme for incompressible flow on nonuniform grids, J. Comput. Phys. 177, 117-133.

[47] Hinze, M. (2005). A variational discretization concept in control constrained optimization: the linear-quadratic case, Comp. Optim. Appl. 30, 45-61

[48] Hinze, M and Kunisch, K. (1999). Newton's method for tracking type control of the instationary Navier-Stokes equation, ENUMATH 99

[49] Hughes, T.J.R., Feijóo, G.R., Mazzei, L. and Quincy, J.B. (1998). The variational multiscale method - a paradigm for computational mechanics. Comput. Methods Appl. Mech. Engrg. 166, 2-24.

[50] Hughes, T.J.R., Mazzei, L. and Jansen, K.E. (2000). Large eddy simulation and the variational multiscale method. Comput. Visual Sci. 3, 47-59.

[51] Hughes, T.J.R., Mazzei, L., Oberai, A.A. and Wray, A.A. (2001). The multiscale formulation of large-eddy simulation: decay of homogeneous isotropic turbulence. Phys. Fluids 13(2), 505-512.

[52] Hunt, J.C. R., Wray, A.A. and Moin, P. (1988). Eddies, stream, and convergence zones in turbulent flows, Report CTR-S88, Center For Turbulence Research.

[53] Iliescu, T. and Fischer, P. (2003). Large eddy simulation of turbulent channel flows by the rational large eddy simulation model, Phys. Fluids, 15(10), 3036-3047.

[54] Issa, R.I. (1986). Solution of implicitly discretized fluid flow equations by operator-splitting, J. Comput. Phys. 62, 40-65.

[55] Jeong, J. and Hussain, F. (1995). On the identification of a vortex, J. Fluid Mech. 285, 69-94

[56] John, V. (2004). Large eddy simulation of turbulent incompressible flows: analytical and numerical results for a class of LES models, Springer-Verlag.

146

[57] John, V. and Roland, M. (2007). Simulations of the turbulent channel flow at Re_τ=180 with projection-based finite element variational multiscale methods, to appear.

[58] Johansson, H., Runesson, K. and Larsson F. (2007). Parameter identification with sensitivity assessment and error computation, GAMM-Mitteilungen, 30(2), p 430-457.

[59] Jovic, S. and Driver, D.M. (1994). Backward-facing step measurement at low Reynolds number, Re_h = 5000, NASA Tech. Mem. 108807.

[60] Kang, S.H., Chester, S. and Meneveau, C. (2003). Decaying turbulence in an active-grid-generated flow and comparisons with large-eddy simulation, J. Fluid Mech. vol. 480, 129-160.

[61] Kalitzin, G., Templeton, J.A. and Medic, G. (2005). A near-wall eddy-viscosity formulation for LES, In Symposium on Complex Effects in LES, Limassol, Cyprus.

[62] Keating, A. and Piomelli, U. (2006). A dynamic stochastic forcing method as a wall-layer model for large-eddy simulation, J. Turbulence, vol. 7, 12.

[63] Kim, D. and Choi, H. (2000). A second-order time-accurate finite volume method for unsteady incompressible flow on hybrid unstructured grids, J. Comp. Phys. 162, 411-428.

[64] Klein, M., Sadiki, A. and Janicka, J. (2003). A digital filter based generation of inflow data for spatially developing direct numerical or large eddy simulations, J. Com. Phys. 186, 652-665.

[65] Knabner, P. and Angermann, L. (2003). Numerical Methods for Elliptic and Parabolic Partial Differential Equations, Springer-Verlag.

[66] Knopp, T. (2003). Finite-element simulation of buoyancy-driven turbulent flows, PhD thesis, University of Göttingen.

[67] Knopp, T. (2007). Discontinuous-Galerkin Finite-Element Methods and Applications in Fluid Mechanics, lecture notes.

[68] Kok, J.C. (2000). Resolving the dependence on freestream values for the k-omega turbulence model. AIAA J. v38. 1292-1295.

[69] Kok, J.C., Dol, H.S., Oskam, B., van der Ven, H. (2004). Extra-large eddy simulation of massively separated flows, AIAA, 2004-264, 42nd AIAA Aerospace Sciences Meeting and Exhibit, Reno, Nevada, Jan. 5-8.

[70] Kolmogorov, A.N. (1941). The local structure turbulence in an incompressible viscous fluid. at very large Reynolds number, Dokl. Akad. Nauk SSSR 30, 301-305.

[71] Kravchenko, A.G., Moin, P. and Moser, R. (1996). Zonal embedded grids for numerical simulations of wall-bounded turbulent flows, J. Comp. Phys. 127, 412-423.

[72] Langtangen, H.P. (1999). Computational partial differential equations: numerical methods and Diffpack programming, Springer-Verlag.

[73] Le, H., Moin, P. and Kim J. (1997). Direct numerical simulation of turbulent flow over a backward-facing step, J. Fluid Mech. vol. 330, 349-374.

[74] Lee, S., Lele, S. and Moin, P. (1992). Simulation of spatially evolving compressible turbulence and the application of Taylors hypothesis, Phys. Fluids A 4, 1521-1530.

[75] Lilly, D.K.(1967). The representation of small-scale turbulence in numerical simulation experiments. In H. H. Goldstine (Ed.), Proc. IBM Scientific Computing Symp. on Environmental Science, pp. 195-210. Yorktown Heights, NY:IBM.

[76] Lilly, D.K.(1992). A proposed modification of the Germano subgrid-scale closure method, Phys. Fluids, A 4(3), 633-635.

[77] Lube, G. (1999). Theorie und Numerik gewöhnlicher Differentialgleichungen, lecture note, university Göttingen.

[78] Lube, G. (2006). Theorie und Numerik instationaerer Differentialgleichungen, lecture note, university Göttingen.

[79] Mahnken, R. (ed) (2007). Parameter Identification: From efficient numerical methods to representative engineering applications, GAMM-Mitteilungen, 30(2), p 350-505.

[80] Mannini, C. (2006). Flutter Vulnerability Assessment of Flexible Bridges, Ph.D. thesis, University of Florence - TU Braunschweig.

[81] Medic, G., Daeninck, G., Templeton, J.A. and Kalitzin, G. (2005). A framework for near-wall RANS/LES coupling, Annual Research Briefs, center for Turbulence Research.

[82] Meidner, D. and Vexler, B. (2007). Adaptive space-time finite element methods for parabolic optimization problems, SIAM Journal on Control and Optimization 46(1), S. 116142.

[83] Meister, A. (1999) Numerik linearer Gleichungssysteme: eine Einfhrung in moderne Verfahren, Braunschweig: Vieweg-Verlag.

[84] Menter, F.R. (1993). Zonal two equation k/ω turbulence models for aerodynamic flows. AIAA Paper 1993-2906.

[85] Mohamed, M.S. and LaRue, J.C. (1990). The decay power law in grid-generated turbulence, J. Fluid Mech. vol. 219, 195-214.

[86] Mohammadi, B. and Pironneau, O. (1994). Analysis of the K-Epsilon Turbulence Model, John Wiley & Sons, Masson.

[87] Morinishi, Y. and Vasilyev, O. (2001). A recommended modification to the dynamic two-parameter mixed subgrid scale model for large eddy simulation of wall bounded turbulent flow. Phys. Fluids 13, 3400-3410.

[88] Moser, T.D., Kim, J., Mansour, N.N. (1999). Direct numerical simulation of turbulent channel flow up to $Re_\tau = 590$. Phys. Fluids, 11, 943-946.

[89] Nikitin, N.V., Nicoud, F., Wasistho, B., Squires, K.D., Spalart, P.R. (2000). An approach to wall-modeling in large-eddy simulations. Phys. Fluids 12, 1629-1632.

[90] Park, N., Yoo, J.Y. and Choi, H. (2004). Discretization errors in large eddy simulation: on the suitability of centered and upwind-biased compact difference schemes, J. Comput. Phys. 198, 580-616.

[91] Patel, V.C., Head, M.R. (1969). Some observations on skin friction and velocity profiles in fully developed pipe and channel flows. J. Fluid Mech. 38, 181-201.

[92] Piomelli, U. (1993). High Reynolds number calculations using the dynamic subgrid-scale stress model. Phys. Fluids A 5(6), 1484-1490.

[93] Piomelli, U. and Balras, E. (2002). Wall-layer models for large-eddy simulation, Annu. Rev. Fluid Mech. 34: 349-374.

[94] Piomelli, U., Ferziger, J. and Moin, P. (1989). New approximate boundary conditions for large eddy simulations of wall-bounded flows, Phys. Fluids A 1(6), 1061-1068.

[95] Piomelli, U., Moin, P. and Ferziger, J. (1988). Model consistency in large-eddy simulation of turbulent channel flows, Phys. Fluids 31, 1884-1894.

[96] Pope, S.B. (2000). Turbulent flows, Cambridge University Press.

[97] Pruett, C.D. (2001). Toward the De-Mystification of LES, DNS/LES progress and challenges. C. Liu, L. Sakell and T. Beutner(eds.), Greyden Press, Columbus, OH, 231-238.

[98] Quarteroni, A., Sacco, R. and Saleri, F. (2000). Numerical mathematics, Springer-Verlag.

[99] Quarteroni, A. and Valli, A. (1997). Numerical Approximation of Partial Differential Equations, Springer-Verlag.

[100] Rannacher, R. and Vexler, B. (2005). A Priori Error Estimates for the Finite Element Discretization of Elliptic Parameter Identification Problems with Pointwise Measurements, SIAM Journal on Control and Optimization, vol. 44(5), 1844-1863.

[101] Reichardt, H. (1951). Vollstandige Darstellung der turbulenten Geschwindigkeitsverteilung in glatten Leitungen, Zeitschrift für Angewandte Mathematik und Mechanik, 31, 208-219.

[102] Rhie, C.M. & Chow, W.L. (1983). Numerical study of the turbulent flow past an airfoil with trailing edge separation, AIAA J. 21, 1525-1532.

[103] Roos, H.G., Stynes, M. and Tobiska, L. (1996). Numerical methods for singularly perturbed differential equations, Springer.

[104] Saad, Y. and Schultz, M. (1986). GMRES: A Generalized Minimal Residual Algorithm for Solving Nonsymmetric Linear Systems, SIAM J. Sci. Statist. Comput. 7, 856-869.

[105] Sagaut, P. (1998). Large Eddy Simulation for incompressible flows, Springer-Verlag.

[106] Sagaut, P., Deck, S. and Terracol, M. (2006). Multiscale and Multiresolution Approaches in Turbulence, Imperial College Press.

[107] Schumann, U. (1975). Subgrid-scale Model for Finite Difference Simulations of Turbulent Flows in Plane Channels and Annuli, J. Comp. Phys. 18, 376-404.

[108] Shen, J. (1996). On error estimates of projection methods for the Navier-Stokes equations: second-order schemes, Math. Comput. 65 (215), 1039-1065.

[109] Shur, M., Spalart, P.R., Strelets, M. and Travin, A. (1999). Detached-eddy simulation of an airfoil at high angle of attack, Fourth International Symposium on Engineering Turbulence Modeling and Experiments, Corsica, 24-26 May 1999, edited by Rodi, W. and Laurence, D. (Elsevier, New York, 1999).

[110] Smagorinsky, J. (1963). General circulation experiments with the primitive equations, I. The basic experiment, Mon. Weather Rev. 91, 99-152.

[111] Sohr, H. (2001). The Navier-Stokes Equations, An Elementary Functional Analytic Approach, Birkhäuer Advanced Texts, Birkhäuser-Verlag.

[112] Spalart, P.R. (1988). Direct simulation of a turbulent boundary layer up to $R_\theta = 1410$, J. Fluid Mech., vol. 187, pp. 61-98

[113] Spalart, P.R. and Allmaras, S.R. (1992). A One-Equation Turbulence Model for Aerodynamic Flows, AIAA Paper 1992-0439.

[114] Sparlart, P.R., Jou, W.H., Strelets, M. and Allmaras, S.R. (1997). Comments on the feasibility of LES for wings, and on a hybrid RANS/LES approach. First AFOSR Int'l Conference on DNS/LES, Ruston, LA. In Advances in DNS/LES, Liu C, Liu Z (eds). Greyden Press: Columbus, OH.

[115] Strehmel, K. & Weiner, R. (1995). Numerik gewöhnlicher Differentialgleichungen, Teubner-Studienbücher, Stuttgart.

[116] Temam, R. (1969). Sur l'approximation de la solution des équations de Navier-Stokes par la méthode des pas fractionnaires ii, Arch. Ration. Mech. Anal. 33, 377-385.

[117] Templeton, J.A., Medic, G. and Kalitzin, G. (2005). An eddy-viscosity based near-wall treatment for coarse grid large-eddy simulation, Phys. Fluids, 17, 105101.

[118] Tennekes, H. and Lumley, J.L. (1972). A first course in Turbulence, MIT press, Cambridge, MA.

[119] Tessicini, F., Temmerman, L. and Leschziner, M.A. (2006). Approximate near-wall treatments based on zonal hybrid RANS-LES methods for LES at high Reynolds numbers, Proceedings of Engineering Turbulence Modeling and Measurements (ETMM6), Sardinia.

[120] Timmermans, L.J.P., Minev, P.D. and Van De Vosse, F.N. (1996). An approximate projection scheme for incompressible flow using spectral elements, Int. J. Numer. Methods Fluids 22, 673-688.

[121] Toschi, F., Kobayashi, H., Piomelli, U. and Iaccarino, G. (2006). Backward-facing step calculations using the shear improved Smagorinsky model, Center for Turbulence Research, Proceedings of the Summer Program 2006.

[122] Travin, A.K., Shur, M.L., Spalart, P.R. and Strelets, M.Kh. (2006). Improvement of delayed detached-eddy simulation for LES with wall modeling European Conference on Computational Fluid Dynamics, TU Delft, the Netherlands.

[123] Travin, A.K., Shur, M.L., Strelets, M.Kh. and Spalart, P.R. (1999). Detached-Eddy Simulation Past a Circular Cylinder, Flow Turb. Combust. 63, 293-313.

[124] Doormal, J.P., Raithby, G.D. (1984). Enhancements of the SIMPLE method for predicting incompressible fluid flow, Numer. Heat Transfer, 7, 147-163.

[125] van Driest, E.R. (1956). On turbulent flow near a wall, J. Aerospace Sci. 23, 1007-1011.

[126] Weinman, K., van der Ven, H., Mockett, C.R., Knopp, T.A., Kok, J.C., Perrin, R.T.E. and Thiele, F.H. (2006). A study of grid convergence Issues for the simulation of the massively separated flow around a stalled airfoil using DES and related methods, EC-COMAS CFD 2006 conference, TU Delft, the Netherlands.

[127] Wesseling, P. (1992). An introduction to multigrid methods, John Wiley & Sons.

[128] Wilcox, D.C. (1988). Reassessment of the Sacale Determining Equation for Advanced Turbulence Models, AIAA J. Vol 26, No. 11, 1299-1310.

[129] Wilcox, D.C. (1998). Turbulence Modeling for CFD, second edition, DCW industries.

[130] Winckelmans, G.S., Jeanmart, H. and Carati, D. (2002). On the comparison of turbulent intensities from large-eddy simulation with those from experiment or direct numerical simulation, Phys. Fluids, 14: 1809-1811.

[131] Zang, T.A. (1991). Numerical simulation of the dynamics of turbulent boundary layers: Perspectives of a transition simulator. Philos. Trans. R. Soc. Lond. Ser. A 336, 95-102.

Acknowledgments

Lebenslauf

Name:	Xiaoqin Zhang
Geburtsdatum:	Jiangsu, China
Geburtsort:	06. Oct. 1976
Staatsangehörigkeit:	chinesisch
Familienstand:	ledig
Eltern:	Xingbai Zhang
	Qilan Zhao

1983-1989:	Grundschule Qiliu, Jiangsu
1989-1992:	Mittelschule Sanlian, Jiangsu
1992-1995:	Hauptschule Dongtai, Jiangsu
1995-1999:	Mechanik, Hohai Universität, Nanjing, China
July 1999:	Bachelor of Engineering, Hohai Universität
1999-2000:	Ingenieurin, Changjiang Institute of Survey, Planning, Design and Research of Changjiang Water Resource Committee, Wuhan, China
2000-2001:	Mechanik, Masterstudiengang, Hohai Universität
2001-2003:	Computational Engineering, Ruhr-Universität Bochum, Deutschland
Nov. 2003:	Master of Science, Ruhr-Universität Bochum
2002-2004:	Wissenschaftliche Hilfskraft am Lehrstuhl für Technische Mechanik, Ruhr-Universität Bochum
2004-2007:	Promotion am Institut für Numerische und Angewandte Mathematik bei Prof. Dr. G. Lube, Georg-August-Universität Göttingen Stipendiatin des Graduiertenkolleg 1023 "Identifikation in mathematischen Modellen: Synergie stochastischer und numerischer Methoden"